Bergische Universität Wuppertal
Fakultät für
Mathematik und Naturwissenschaften
Fachgruppe Physik

Analysis of a combined measurement of $W^{\pm} \to \ell^{\pm}\nu$ ($\ell = e, \mu$) cross sections differential in m_T^W and $m_T^W \otimes |\eta|$ at high transverse masses at $\sqrt{s} = 13$ TeV with the ATLAS detector

Thesis zur Erlangung des akademischen Grades Master of Science (M.Sc.) im Studiengang Physik der Bergischen Universität Wuppertal

vorgelegt von

Tim Frederik Beumker

Erstgutachter: Herr PD Dr. Frank Ellinghaus
Zweigutachter: Herr Prof. Dr. Christian Zeitnitz

Abgabedatum: 20. Juni 2023

Contents

Chapter 1

Introduction

Physicists from different disciplines study various phenomena in nature. One such discipline is particle physics. It describes the most fundamental constituents of matter and their interactions. To provide a complete theory, the Standard Model of elementary particle physics has been developed. It is able to describe and predict most of the observed effects very accurately. Its most recent success was the discovery of the Higgs boson in 2012.
However, there are also some phenomena that cannot be explained by the Standard Model. One of these phenomena is the nature of dark matter. Furthermore, the observation of neutrino oscillation contradicts the Standard Model [1, 2, 3]. Another very important aspect is that it does not include the gravitational force. Therefore, it is important to precisely test the predictions of the Standard Model to find deviations, which can lead to explanations for such undescribed effects.
Many of these tests are carried out by analysing data taken from high-energy collisions at particle accelerators. The largest accelerator is the “Large Hadron Collider” (LHC)[4] located at the “Conseil Européen pour la Recherche Nucléaire” (CERN) in Geneva. It is a circular accelerator with a circumference of 27 km, which was designed to accelerate protons to energies of up to 7 TeV. Several experiments study proton-proton collisions in the LHC. In this thesis, data recorded by the ATLAS detector will be analysed.
This thesis is part of a double-differential measurement in m_T^W and $|\eta(\ell)|$ [5] of the cross section of the process $q\bar{q}' \to W^\pm \to \ell^\pm\nu_\ell$ ($\ell = e, \mu$), called the charged-current Drell-Yan process [6, 7]. The measurement focusses on high transverse masses of the W boson. While the inclusive cross section has been precisely measured [8], a differential measurement at high transverse masses is done for the first time. The analysed dataset corresponds to the LHC Run-2, which ran from 2015 to 2018, and yields an integrated luminosity of $\mathcal{L} = (140.1 \pm 1.2)$ fb^{-1} [9]. The measurement can provide constraints on parton distribution functions of the proton as it explores a phasespace where they have large uncertainties [10]. It is also sensitive to the running of the electroweak coupling constant [11]. In addition, an effective field theory interpretation is possible. Finally, the measurement can also be used as a test of lepton universality. Such a test is presented in this thesis: The separate measurements for an electron and a muon final state are combined to obtain a cross section for the process $q\bar{q}' \to W^\pm \to \ell^\pm\nu_\ell$. This is done via a χ^2-minimisation method using HAVERAGER. It also indicates how well the two measurements fit together. Furthermore, the combined cross section benefits from better statistics compared to the single electron and muon channel measurements, since data corresponding to both electron and muon final states are used.
This thesis is structured as follows. First, an overview of the theoretical and experimental context of the measurement is presented. Here, the Standard Model and the facilities used are introduced and a brief theoretical description of the physics of proton-proton collisions is given (Chapter 2). Then the underlying measurements of the two channels of the charged-current

Drell-Yan process are shortly described (Chapter 3). After that, the combination of the electron and muon channel measurements, which is the main part of this thesis, is performed and studied (Chapter 4). At first, the general minimisation procedure of the HAverager tool is briefly described. This is followed by a detailed investigation of the combined results of the single- and double-differential measurements in m_T^W and $m_T^W \otimes |\eta(\ell)|$. In addition, several studies concerning the performance of the combination are presented. Finally, an overview of the obtained results together with a short outlook is given (Chapter 5).

Chapter 2

Theoretical and experimental background

This chapter describes the theoretical background as well as the experimental facilities used for data acquisition. First, a brief overview of the Standard Model of particle physics is given (Section 2.1). After that, the Large Hadron Collider (Section 2.2) and the ATLAS detector (Section 2.3) are introduced, ending with a basic description of the analysis of *pp*-collisions (Section 2.4).

2.1 The Standard Model of particle physics

The Standard Model (SM) of elementary particle physics [12, 13, 14, 15] represents the current understanding of the fundamental particles and their interactions. Figure 2.1 shows an overview of the elementary particles according to the Standard Model. These particles are classified into two groups depending on their spin. Particles with spin $S = n + \frac{1}{2},\ n \in \mathbb{N}_0$ are called fermions, while particles with spin $S = n,\ n \in \mathbb{N}_0$ are referred to as bosons.
The Standard Model contains twelve fermions, each of which has a corresponding antifermion. Antiparticles are characterised by having the same mass as the particle but the opposite charge. A further distinction is made between quarks and leptons. The quarks can be divided into particles with a charge of $q = +\frac{2}{3}e$ ("up-type quarks") and $q = -\frac{1}{3}e$ ("down-type quarks"), where e' is the elementary charge. The three up-type quarks are called up- (u), charm- (c) and top-quark (t), while the down-type quarks are called down- (d), strange- (s) and bottom-quark (b). A similar classification is made for leptons according to their charge: There are three charged leptons ($q = -1e$) - the electron (e), the muon (μ) and the tau (τ) - and three charge-neutral lepton-neutrinos - the electron-neutrino (ν_e), muon-neutrino (ν_μ) and tau-neutrino (ν_τ). All fermions are sorted into three generations depending on their mass. The first generation consists of the lightest fermion of each type (u, d, e, ν_e), followed by the heavier second generation (c, s, μ, ν_μ) and the third generation, which is composed of the heaviest fermions (t, b, τ, ν_τ). In fact, the SM predicts that the neutrinos are massless. However, it has already been discovered that their mass cannot be exactly zero, although it is very small [1, 2].

There are four fundamental forces that act between particles. Three of them are described by the SM: The strong interaction (SI), the electromagnetic interaction (EMI) and the weak interaction (WI). The remaining fundamental force is the gravitation. However, its influence on the observed energy scales is negligible because its strength is much smaller (~ 30 orders of magnitude at a distance of 1 fm) than that of the other forces. The forces described by the Standard Model are mediated by so-called gauge bosons. These are the gluons (g) for the SI,

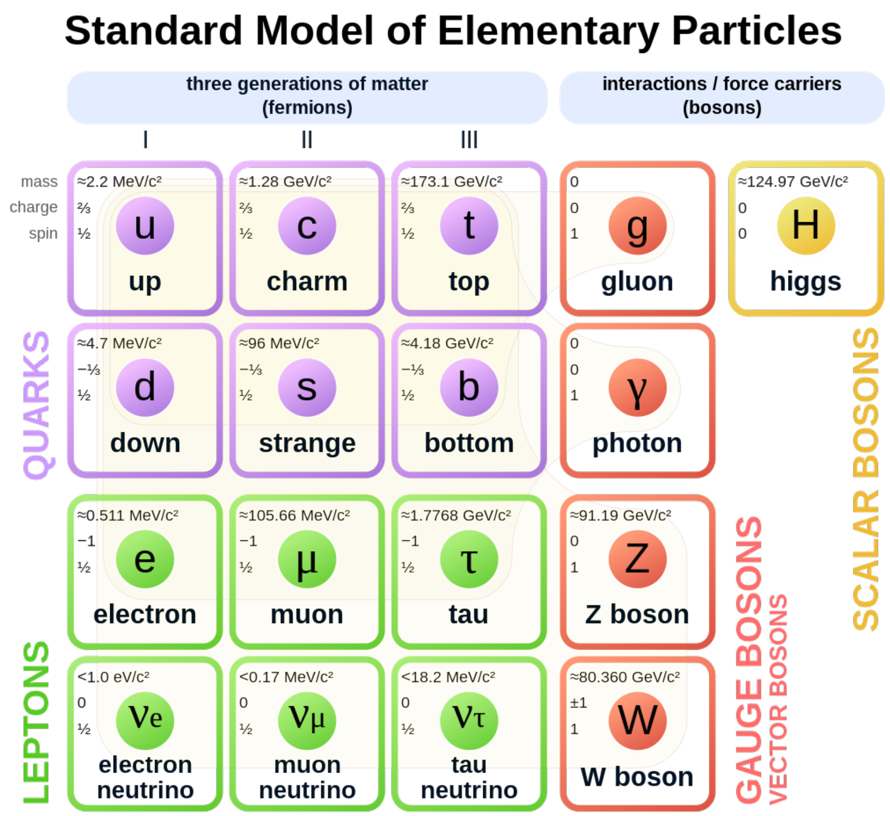

Figure 2.1: Overview of the fundamental particles of the Standard Model of elementary particle physics [16].

the photon (γ) for the EMI and the Z^0- and $W^{\pm}$-bosons for the WI. A measure of the strength of the fundamental interactions is given by their coupling constant α.
The strongest force in the Standard Model is the strong interaction with a coupling constant of $\alpha_s \sim 1$ at a distance of 1 fm [17]. It is sensitive to the colour charge, which is carried by quarks and gluons. The colour can be either red, green or blue (for a quark), antired, antigreen or antiblue (for an antiquark) or a combination of colour and anticolour (for a gluon). Since the gluons mediate the SI and are also coloured, they can interact directly with each other. The strength of the SI is closely related to the distance between two interacting particles. At small distances, the SI is comparatively weak. This leads to the effect that quarks at small distances ($\hat{=}$ large energy scales) behave as "quasi-free" particles, which is called asymptotic freedom. On the other hand, the increasing strength of the SI with distance leads to the impossibility of observing free coloured particles. This is called "colour confinement". As a result, a single quark is forced to form a bound state with at least one other quark. Such bound states are known as hadrons. Depending on its quark content, a hadron is either classified as a baryon (containing three (anti-)quarks with (anti-)red + (anti-)green + (anti-)blue = white) or as a meson (containing quark and antiquark with colour + anticolour = white).
The second strongest force is the electromagnetic interaction with a coupling constant of $\alpha_{em} \sim 10^{-3}$ at a distance of 1 fm [17]. The EMI is mediated by the photon and couples to particles with an electromagnetic charge. Unlike gluons the photon cannot couple to itself because it does not carry an electromagnetic charge. The photon is a massless particle. Together with the absence of self-couplings, this results in an infinite range of the EMI.
Finally, the weak interaction is the weakest force described by the Standard Model. Its coupling constant is of the order of $\alpha_w \sim 10^{-8}$ at a distance of 1 fm[17]. The WI couples to the weak

charge, carried by all fermions. It is mediated by the Z^0- and $W^{\pm}$-bosons. These are the only gauge bosons whose mass is not zero. Like gluons, the Z^0- and $W^{\pm}$-bosons can interact with themselves. The most famous effect of the weak interaction is the radioactive β-decay. Thereby, a W-boson mediates the decay of an $d(u)$-quark in a $u(d)$-quark and decays than into an electron (positron) and a neutrino.
The last remaining boson included in the Standard Model is the Higgs boson. In contrast to the gauge bosons, the Higgs is a scalar particle, meaning that its spin is $S = 0$. The Higgs boson was introduced into the Standard Model as a consequence of the Higgs mechanism [18, 19, 20] and couples to all massive particles. It was discovered in 2012 by the experiments ATLAS and CMS at CERN [21, 22].

2.1.1 The W-boson

The underlying analyses measure properties of the W-boson. For this reason, the current knowledge about this boson is now summarised in more detail. The W-boson has a charge of $q = \pm 1e$ and its measured mass is $m_W = (80.377 \pm 0.012)\,\text{GeV}$. Its full decay width is experimentally determined to be $\Gamma_W = (2.085 \pm 0.042)\,\text{GeV}$ [23].
The basic vertices of a W-boson are shown in Figure 2.2. In principle, the W-boson can couple either leptonically to a pair of a charged lepton and the corresponding neutrino (Figure 2.2a) or hadronically to an up-type quark U and the corresponding down-type quark D' (Figure 2.2b). However, the weak eigenstate $D' \in \{|d'\rangle, |s'\rangle, |b'\rangle\}$ shown in Figure 2.2b is not exactly equal to

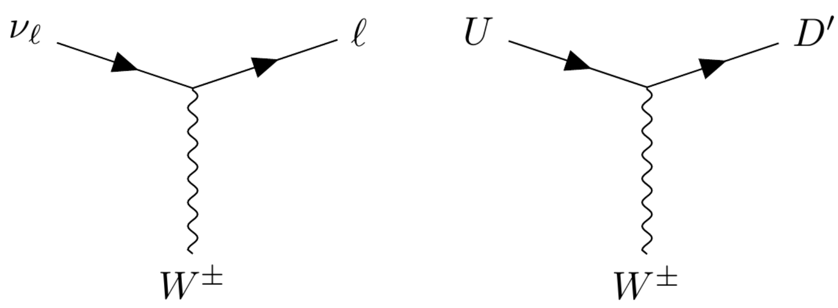

a) leptonic vertex **b)** hadronic vertex

Figure 2.2: Decay/Production vertices of the W-boson.

the mass eigenstates $|d\rangle$, $|s\rangle$ and $|b\rangle$. The connection between the weak and the mass eigenstates is given by the Cabibbo-Kobayashi-Maskawa matrix (CKM matrix) [24]:

$$\begin{pmatrix} |d'\rangle \\ |s'\rangle \\ |b'\rangle \end{pmatrix} = V_{CKM} \cdot \begin{pmatrix} |d\rangle \\ |s\rangle \\ |b\rangle \end{pmatrix} = \begin{pmatrix} V_{ud} & V_{us} & V_{ub} \\ V_{cd} & V_{cs} & V_{cb} \\ V_{td} & V_{ts} & V_{tb} \end{pmatrix} \cdot \begin{pmatrix} |d\rangle \\ |s\rangle \\ |b\rangle \end{pmatrix}. \tag{2.1}$$

The magnitudes of the elements of the CKM matrix are given by

$$V_{CKM} = \begin{pmatrix} |V_{ud}| = 0.97373 & |V_{us}| = 0.2243 & |V_{ub}| = 3.82 \cdot 10^{-3} \\ |V_{cd}| = 0.221 & |V_{cs}| = 0.975 & |V_{cb}| = 40.8 \cdot 10^{-3} \\ |V_{td}| = 8.6 \cdot 10^{-3} & |V_{ts}| = 41.5 \cdot 10^{-3} & |V_{tb}| = 1.014 \pm 0.029 \end{pmatrix}, \tag{2.2}$$

with uncertainties ranging from 0.003% (V_{ud}) to 5.3% (V_{ub}) [23].
Consequently, a W-boson most likely couples to quarks of the same generation, although couplings to quarks of different generations are possible too. In this analysis, leptonic decays of

the W boson are studied, since they produce a cleaner detector signature than hadronic decays. Their branching ratios are experimental determined to be:

$$\mathcal{BR}(W \to \ell\nu_\ell) = \begin{cases} (10.71 \pm 0.16)\% & W \to e\nu_e \\ (10.63 \pm 0.15)\% & W \to \mu\nu_\mu \\ (11.38 \pm 0.21)\% & W \to \tau\nu_\tau \end{cases} [23]. \tag{2.3}$$

The fact that the measured branching ratios for the three leptonic decays are very close to each other follows from the principle of lepton universality. It says that the weak couplings are the same for all three lepton flavours.

2.2 The Large Hadron Collider

The **L**arge **H**adron **C**ollider[4] (LHC) is a hadron accelerator and collider located at CERN. It is the successor to the electron-positron collider LEP (**L**arge **E**lectron **P**ositron collider), which was decommissioned in the year 2000. The LHC uses the former LEP-tunnel, which is 26.7 km long and lies 45 m-170 m below the surface [4].
An overview of the accelerator complex at CERN is shown in Figure 2.3. First, the linear accelerator LINAC4 accelerates H^--ions up to an energy of 160 MeV. The H^-- ions are then stripped of their two electrons and the remaining protons move on to the following stages. These are the circular accelerators PSB (**P**roton **S**ynchrotron **B**ooster), PS (**P**roton **S**ynchrotron) and SPS (**S**uper **P**roton **S**ynchrotron). In the PSB, the protons are boosted to 2 GeV, then in the PS to 26 GeV and finally in the SPS to 450 GeV. These 450 GeV-protons are injected into the LHC [25].

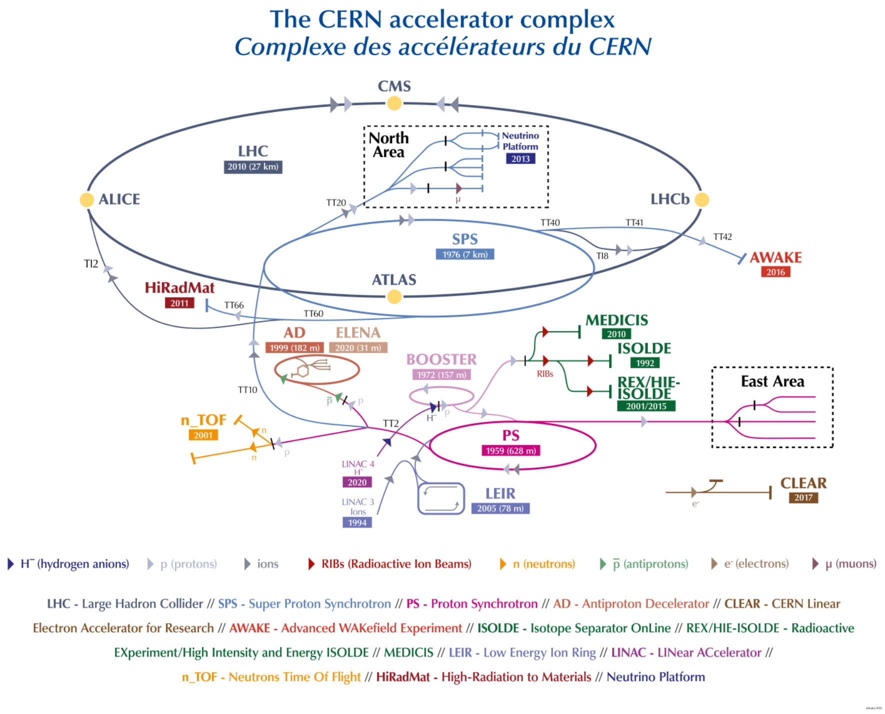

Figure 2.3: The CERN accelerator complex with the LHC (grey) and its pre-accelerators SPS (blue), PS (magenta), PSB (shaded purple) and LINAC4 (purple) [26].

Similar to the PSB, the PS and the SPS, the LHC is a synchrotron. A synchroton is a circular accelerator, where a particle is accelerated in every circulation. This provides, in principle, an

infinite acceleration length. In the LHC, the protons are accelerated using radio-frequency-cavities (RF-cavities). In these cavities, the protons are accelerated by a RF-voltage, which re-pools while the protons are outside the cavity. To keep the beam on its circular trajectory, superconducting magnets with NbTi Rutherford cables are used. These are also needed to focus the beams. The magnets are operated at a temperature of 2 K and can generate a magnetic field of more than 8 T. The centre-of-mass energy achieved in Run-3 is about $\sqrt{s} = 13.6\,\text{TeV}$, which corresponds to an energy of 6.8 TeV per proton beam. The data analysed was taken during Run-2, when the LHC was operating at a centre-of-mass energy of $\sqrt{s} = 13$ TeV. The instantaneous design luminosity of the LHC is $L = 10^{34}\,\text{cm}^{-2}\text{s}^{-1}$. This is to be realised by filling the LHC with 2808 proton bunches with $1.15 \cdot 10^{11}$ protons per bunch. At the design luminosity the bunches are spaced by 25 ns. This corresponds to about $40 \cdot 10^{6}$ collisions per second [4].
There are several experiments at CERN that collect data from *pp*-collisions. The most important ones are ATLAS[27] (**A** **T**oroidal **L**HC **A**pparatu**S**), CMS[28] (**C**ompact **M**uon **S**olenoid) and LHCb[29]. The LHC can also accelerate heavy ions like lead nuclides. The largest experiment analysing such collisions is ALICE[30] (**A** **L**arge **I**on **C**ollider **E**xperiment).

2.3 The ATLAS detector

The ATLAS detector is a multi-purpose detector built to collect *pp*-collision data from the LHC. A sketch of the detector is shown in Figure 2.4. It has a cylindrical form with a length of 44 m, a height of 25 m and a weight of 7000 t. In order to be able to detect a wide variety of particles, ATLAS consists of three different subdetectors layered around the beam pipe. The innermost detector is the so-called Inner Detector, which is covered by the calorimeters and the Muon Spectrometer [27].

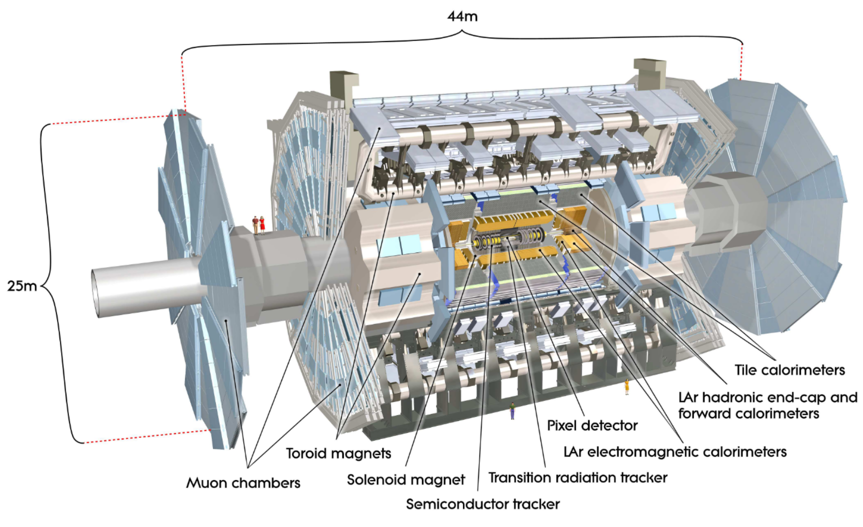

Figure 2.4: Sketch of the ATLAS detector with its different sub-detectors and magnet systems [27].

2.3.1 Coordinate system and observables

A general coordinate system is defined to describe trajectories and geometries within the detector. Its origin lies at the nominal interaction point (IP). The z-axis is parallel to the beam pipe, while the other axes point from the IP towards the centre of the LHC-ring (x-axis) and vertically upwards (y-axis). An azimuthal angle $\phi \in [-\pi, \pi]$ is defined in the x-y-plane. The

x-axis corresponds to $\phi = 0$. The polar angle $\theta \in [-\frac{\pi}{2}, \frac{\pi}{2}]$ of a trajectory refers to the angle to the z-axis ($\hat{=}$ beam pipe).
The polar angle is usually replaced by the so-called pseudorapidity, which is defined as follows:

$$\eta = -\ln\left(\tan\left(\frac{\theta}{2}\right)\right) \in (-\infty, \infty). \tag{2.4}$$

Here $\eta = 0$ corresponds to $\theta = 0$, while and $\eta > 0$ corresponds to $\theta > 0$ and $\eta < 0$ corresponds to $\theta < 0$. Some important marks are given by $|\eta| = 1.0$ ($\hat{=}\ \theta \approx 20°$), $|\eta| = 1.0$ ($\hat{=}\ \theta \approx 13°$) and $|\eta| = 2.4$ ($\hat{=}\ \theta \approx 5°$). Another important quantity is given by:

$$\Delta R = \sqrt{(\Delta\eta)^2 + (\Delta\phi)^2}. \tag{2.5}$$

It can be used as a distance measure in the η-ϕ-plane between different trajectories in the detector.
Since the z-axis is parallel to the beam direction and the total transverse momentum is conserved, the momentum deposited in the x-y-plane must sum to zero. Consequently, by adding the momenta of all measured objects, one can infer the transverse momentum of undetected particles. This leads to the definition of the missing transverse momentum:

$$\vec{p}_T^{\,miss} = -\sum_{\text{objects } i} \vec{p}_T^{\,i}. \tag{2.6}$$

Usually, the missing transverse energy (MET or E_T^{miss}) is used instead of the missing transverse momentum. It is given by:

$$E_T^{miss} = |\vec{p}_T^{\,miss}|. \tag{2.7}$$

Furthermore, one often looks at the projection of the detected objects in the transverse plane. These observables are labelled with the index $_T$ [27].

2.3.2 Inner Detector

The most central subsystem of ATLAS is the Inner Detector (ID) [31]. It consists of three different tracking detectors to obtain a precise reconstruction of the trajectories of charged particles. The ID is located in a magnetic field with $B = 2$ T generated by a solenoid magnet. This allows a reconstruction of the charges and the momenta of the detected particles. The magnetic field forces every charged particle into a circular path. From the radius of this path, the momentum of the corresponding particle can be reconstructed. Furthermore, the direction of the curvature of this path depends on the charge of the particle, so that this can be reconstructed too. The innermost part of the ID is a silicon pixel detector. In 2014, it was extended by the Insertable B-Layer[32]. The pixel detector is followed by a silicon strip detector (SCT) and a transition radiation tracker (TRT) based on straw tubes filled with a $Xe/CO_2/O_2$ gas mixture. The semiconductor detectors of the ID cover a range of $|\eta| < 2.5$, while the coverage of the TRT ends at $|\eta| = 2.0$. With this combined system a resolution of $\frac{\sigma_{p_T}}{p_T} = 0.05\% \frac{p_T}{\text{GeV}} \oplus 1\%$ can be achieved [27].

2.3.3 Calorimeters

The ID is followed by a system of different calorimeters. These measure the energy of an incoming particle by absorbing it. In the ATLAS detector, so-called sampling calorimeters are used. They consist of several layers of passive absorbers and active materials. Thereby, the

absorbers are used to stop the incoming particles by causing a particle shower. These particle excite the active material, which then emits scinitillation light. Its amount is proportional to the energy of the incoming particle.
The most central calorimeter is the electromagnetic calorimeter (ECAL), which measures the energy of electrons and photons. It uses lead as absorber and liquid argon as active material. The ECAL covers the range $|\eta| < 3.2$ and has a resolution of $\frac{\sigma_E}{E} = 10\%\frac{\sqrt{\mathrm{GeV}}}{\sqrt{E}} \oplus 0.7\%$.
It is followed by the hadronic calorimeter (HCAL), which measures the energy of hadronic objects. In the central region (Barrel), covering $|\eta| < 1.7$, steel absorbers and scintillating tiles are used, while in the outer part (End-Cap, $1.5 < |\eta| < 3.2$) a copper/liquid-argon calorimeter is installed. In addition, the high-eta region ($3.1 < |\eta| < 4.9$) is covered by the Forward Calorimeter (FCAL). It has an absorber of copper and tungsten, while liquid argon is used as active detector material. The resolution achieved by the hadronic calorimeters, is given by $\frac{\sigma_E}{E} = 50\%\frac{\sqrt{\mathrm{GeV}}}{\sqrt{E}} \oplus 3\%$ (barrel and end-caps) and $\frac{\sigma_E}{E} = 100\%\frac{\sqrt{\mathrm{GeV}}}{\sqrt{E}} \oplus 10\%$ (FCAL) [27].

2.3.4 Muon Spectrometer

The outermost part of the detector is the Muon Spectrometer (MS) [33]. Since a muon interacts as a minimum ionizing particle with the detector material, it is not stopped in the calorimeters. Consequently, an additional detector is needed to identify muons. The MS consists of a series of drift chambers that allow the tracking of particles that are not absorbed by the calorimeters. The drift chambers are arranged in cylindrical layers around the beam pipe (barrel, $|\eta| < 1.05$) and in discs perpendicular to the beam pipe (end-caps, $1.05 < |\eta| < 2.7$). A magnetic field is generated in the MS, using an air-core toroidal magnet system. This results in a curvature of the measured tracks. Because the MS is the outermost part of the detector, it has a reduced acceptance caused by the detector architecture. For example, the detector has feet, which reach into the MS and lead to measurement inefficiencies. In addition, a small gap at $\eta = 0$ is included in the MS, which is needed for cables and services for the inner detector parts. The measurement resolution of the MS is in the order of $\frac{\sigma_{p_T}}{p_T} = 10\%$ for particles with a transverse momentum of $p_T = 1$ TeV [27].

2.3.5 Trigger system

The event rate in the ATLAS detector is of the order of 40 MHz. It has to be reduced to 1 kHz, since the data acquisition system can only store events at this frequency.
For that reason, ATLAS has a trigger system consisting of two levels: The hardware-based Level-1 (L1) trigger and the software-based high-level trigger (HLT). The L1 trigger reduces the event rate to 100 kHz. It uses data from special trigger chambers and reduced granularity information from the calorimeters. The trigger favours events with high E_T^{miss}, a high total E_T and objects with high p_T. Finally, the L1 trigger defines a Region of Interest (RoI). This region is used in the subsequent trigger stage. After an event has passed the L1 trigger, it is analysed by the HLT, which reduces the event rate to 1 kHz. Therefore, more detailed information, which is not available for the L1 trigger is used, such as higher granularity information from the calorimeters, precision measurements from the MS and tracking information from the ID. Typically, a two-step approach is used where the majority of events are discarded with an initial fast reconstruction followed by a slower but more accurate reconstruction of the remaining events. This is done to reduce processing time [27, 34].

2.4 Proton-proton-collisions

Proton-proton collisions can be described with the reaction $p+p \to F+X$. Two protons interact with each other and form an observed final state F together with possible unobserved states X. At small energies, the substructure of the proton is not relevant for the scattering process. However, a proton consists of three valence quarks (uud). These quarks exchange gluons, which can split into quark-antiquark pairs again ("sea-quarks"). Since the LHC provides pp-collisions at very high energies, the protons interact as a bound state of their constituents, called partons. The process $p+p \to F+X$ is thus composed of all possible sub-processes $i+j \to F+X$, where i and j refer to partons of the first and the second proton, respectively. The cross section for such a process can be calculated via:

$$\sigma_{p_A+p_B\to F+X} = \sum_{i,j}\int \mathrm{d}x_A \mathrm{d}x_B f_i^A(x_A,\mu_F^2) f_i^B(x_B,\mu_F^2)\sigma_{i+j\to F}(x_A,x_B,\sqrt{s},\mu_R^2) \text{ [35]}. \tag{2.8}$$

To determine the total cross section, all possible combinations of partons i and j from protons A and B that can produce a final state F (i.e. the partonic cross section $\sigma_{i+j\to F}$ is not zero) are considered. Each parton carries a fraction x of the momentum of the corresponding proton. This quantity is called Bjoerken-x. Since the partonic cross section usually depends on the momentum of the partons, one has to integrate over all possible momentum fractions $x_A, x_B \in [0,1]$. The integral is weighted with the parton distribution functions (PDF) $f_i^{A/B}(x)$. They give the probability of finding a parton i in proton A (B) that carries a fraction x of the protons momentum. Some examples of parton distribution functions for a proton are shown in Figure 2.5. The distributions shown refer to u-, $\bar{u}$-, d-, $\bar{d}$-, s-, $\bar{s}$-quarks and gluons. Thereby, the s-quark distribution is the same as for $\bar{s}$-quarks, since they have the same mass and can appear as sea-quarks only. One can see that the valence quarks carry the largest part of the protons momentum at small energy scales (Figure 2.5a). When the energy scale increases, the momentum carried by the gluons and sea-quarks become more important. Since parton distribution functions cannot be calculated from theory only, measurements of e.g. cross sections are very important to constrain them. The scales μ_F (factorisation scale) and μ_R (renormalisation scale) in Equation 2.8 are theory parameters, which, in principle, can be freely chosen. A common choice is the mass of the Z-boson $m_Z = 90\,\mathrm{GeV}$. They are needed to avoid non-converging sums in the perturbative calculation of $\sigma_{i+j\to F}$ and f_i^A.

For the analysis of collider experiments, a measure of the number of possible interactions is needed. This is given by the instantaneous luminosity, which can be determined by:

$$L = \frac{N_1 \cdot N_2}{A}\cdot f \tag{2.9}$$

$$N_1,\ N_2 \hat{=} \text{ number of particles in the crossing particle bunches,} \tag{2.10}$$

$$A \hat{=} \text{ beam cross section,} \tag{2.11}$$

$$f \hat{=} \text{ bunch crossing frequency.} \tag{2.12}$$

It is related to the event rate via

$$\dot{N} = \sigma \cdot L \tag{2.13}$$

for an interaction with cross section σ. Integration of Equation 2.13 yields:

$$N = \sigma\cdot\mathcal{L},\ \mathcal{L} = \int \mathrm{d}t L. \tag{2.14}$$

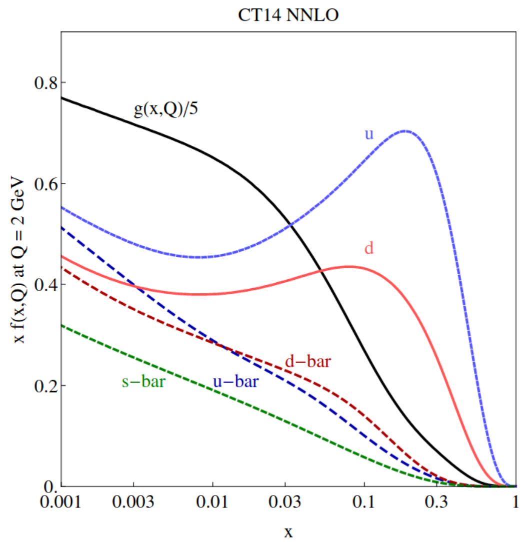

a) $Q = 2$ GeV

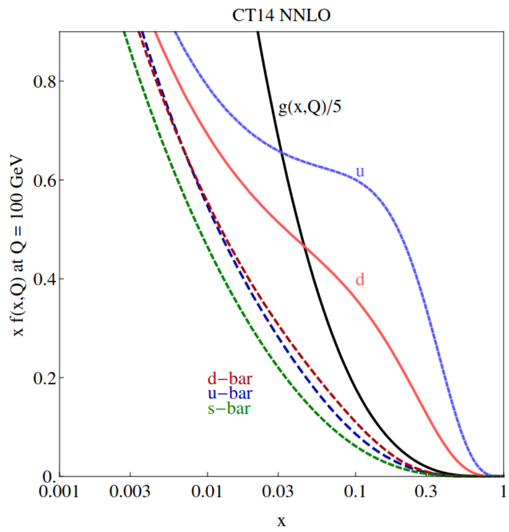

b) $Q = 100$ GeV

Figure 2.5: Parton distribution functions provided by the CT group at the energy scales $Q = 2$ GeV and $Q = 100$ GeV [36].

The quantity $\mathcal{L}$ is called integrated luminosity and usually measured in b^{-1} ($1\text{b}^{-1} = (10^{-28}\text{m}^2)^{-1}$). For simplicity, $\mathcal{L}$ will be referred to as luminosity in the following.

In fact, a real detector will not be able to detect every event generated in a collision, e.g. due to mismeasurements. Therefore, Equation 2.14 becomes

$$N = \epsilon \cdot \sigma \cdot \mathcal{L} \tag{2.15}$$

with a detector efficiency ϵ. It corrects for events that are not detected by the detector. Based on Equation 2.15, the cross section σ can be determined from a measured number of events N. This process is called unfolding. For a differential measurement, migrations between different bins have to be taken into account, too. In this case, the cross section can be determined via:

$$\frac{\mathrm{d}\sigma}{\mathrm{d}x_j} = \frac{1}{\Delta x_j \cdot \mathcal{L} \cdot \epsilon_j} \sum_{\text{bins } i} R^{-1}_{ij} \cdot f^i_{in} \cdot (N^i_{data} - N^i_{bkg}). \tag{2.16}$$

$(N^i_{data} - N^i_{bkg})$ is identified with the number of signal events recorded in bin i. This number is corrected by the acceptance correction factor f^i_{in} for events migrating into bin i from outside the measurement range. The migration matrix R_{ij} then gives the probability for an event generated in bin i migrating into bin j. By inverting this matrix one can calculate the number of events, which are measured in bin j, but produced in bin i. Consequently, the term $R^{-1}_{ij} \cdot f^i_{in} \cdot (N^i_{data} - N^i_{bkg})$ corresponds to the number of signal events, which are reconstructed in bin j, but originally located in bin i. Summation over j then gives the number of reconstructed events, which are generated in bin i. Finally, the efficiency correction factor ϵ_j corrects for events that were not reconstructed by the detector. This results in a corrected estimate of the signal events that were produced in bin j. Division by the luminosity $\mathcal{L}$ and the bin width Δx_j gives the final differential cross section $\frac{\mathrm{d}\sigma}{\mathrm{d}x_j}$.

A Feynman diagram of the measured process is shown in Figure 2.6. Two quarks produce a

W-boson, which decays into a pair of a charged lepton and a corresponding lepton neutrino[1]. Knowing the properties of the decay products, one can calculate the mass of the produced W-boson by finding the invariant mass of the lepton and the neutrino:

$$m_W^2 = m_{inv}^2 = (P_\ell + P_\nu)^2, \tag{2.17}$$

where P_ℓ and P_ν are the momentum four-vectors. However, since the neutrino interacts only

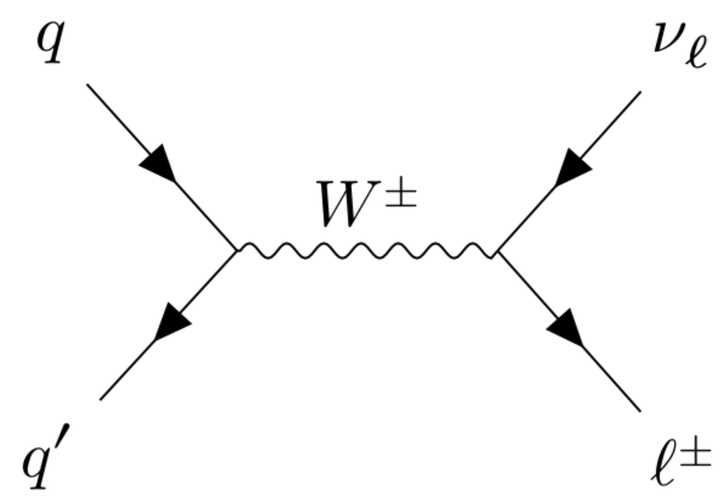

Figure 2.6: Feynman diagram of the observed process.

very weakly with the detector, it cannot be measured and its four-vector is unknown. This problem can be solved by taking into account the plane perpendicular to the beam. Because the neutrino is not detected, it appears as part of the E_T^{miss} as defined in Section 2.3.1. Assuming that all particles produced have been correctly measured and identified, the E_T^{miss} can be associated with the projection of P_ν into the transverse plane. Thus, the transverse projections of P_ℓ and P_ν can be used to reconstruct a transverse mass of the W-boson:

$$m_T^W = \sqrt{2p_T(\ell)E_T^{miss}(1 - \cos(\Delta\phi(\ell, E_T^{miss})))}. \tag{2.18}$$

Thereby $p_T(\ell)$ and E_T^{miss} correspond to the magnitudes of the transverse projections of P_ℓ and P_ν.

[1]In the following, the charged lepton and the lepton neutrino will be referred to as lepton and neutrino, respectively.

Chapter 3

Underlying measurements

The underlying analyses provide cross section measurements of the charge current Drell-Yan process ($q\overline{q'} \to W \to \ell\nu_\ell$) at high transverse masses ($m_T^W > 200$ GeV) [5]. While the total inclusive cross section has been studied, this is the first measurement at high masses. The cross section is measured both differentially in m_T^W and double-differentially in $m_T^W \otimes |\eta(\ell)|$. Two decay channels are considered: $W \to e\nu_e$ and $W \to \mu\nu_\mu$. Furthermore, a separation between charges is made for both lepton flavours.

This chapter gives a brief overview of the underlying measurement. First, the data and Monte-Carlo (MC) samples used (Section 3.1) as well as the object reconstruction (Section 3.2) are introduced. The event selection with the resulting MC-data comparisons is then shown (Section 3.3) followed a by a presentation of the considered systematic uncertainties (Section 3.4). Finally, a short discussion of the unfolded results is given in Section 3.5.

3.1 Data and simulated samples

The dataset analysed was recorded by the ATLAS detector during LHC Run-2, i.e. between 2015 and 2018. The recorded pp-collisions were performed at a centre-of-mass energy of $\sqrt{s} = 13$ TeV. Only data where it is ensured that all parts of the detector worked properly are used. This is done by considering only data from a so-called GoodRunList. In total, data corresponding to a luminosity of $\mathcal{L} = (140.1 \pm 1.2)$ fb^{-1} [9] is analysed.

Since the detector signature of the signal process is not unique, many other processes produce events, which cannot be separated from the signal events in the data. These are called background events. The signal process and most of the background process are modelled using Monte-Carlo simulations. Some Feynman diagrams contributing to these processes are presented in Figure 3.1. The charged-current DY process is shown in Figure 3.1a. It can contribute both as a signal and as a background. On the one hand, the W can decay into an electron or a muon and a neutrino, which results in the signal process. However, the W can decay into a tau and a neutrino as well. As this tau is unstable and decays within the detector, it can produce an electron or a muon, so that it has a signature similar to the signal. Most of the other backgrounds involve processes that produce at least one W-boson. If this boson decays leptonically and no further leptons are produced, it has also a detector signature similar to the signal. This is the case for the diboson- (Figure 3.1b), the $t\bar{t}$- (Figure 3.1c) and the single-t-production (Figure 3.1e). In addition, backgrounds can arise from mismeasurements. An example for such a background process is the Z+jets production, as shown in Figure 3.1d.

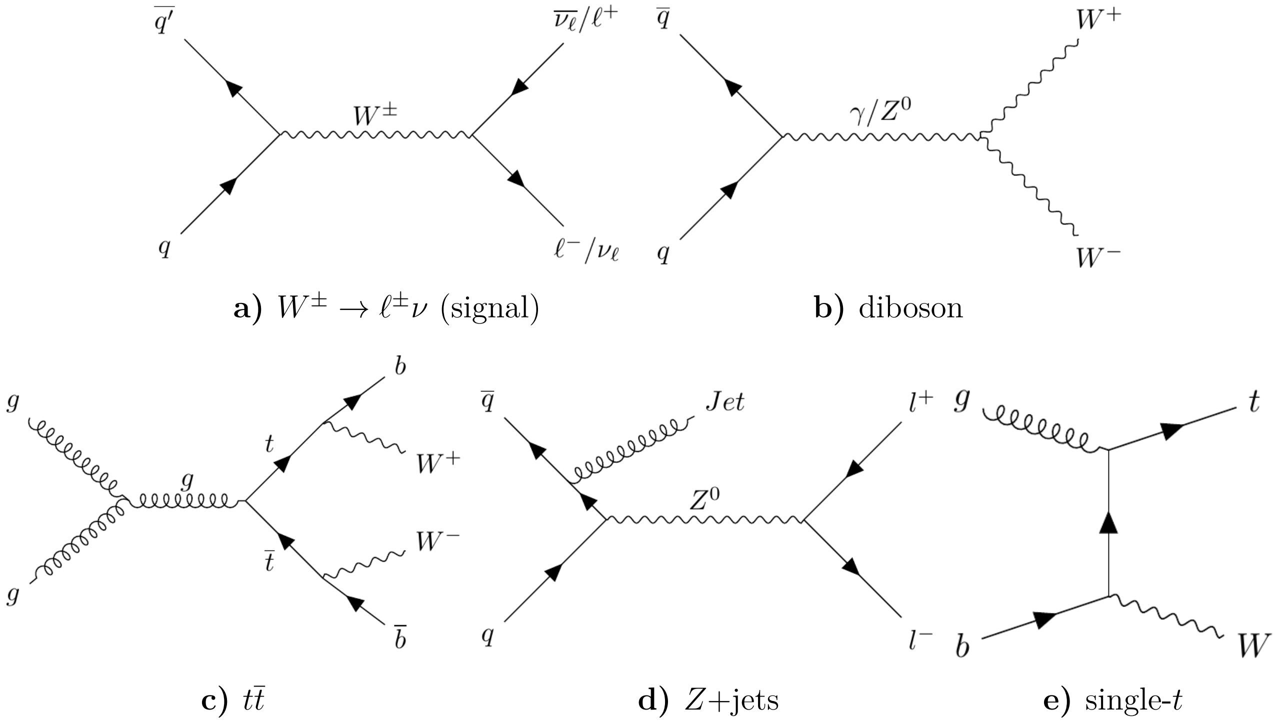

Figure 3.1: Feynman diagrams for the signal and background processes. Only an examples of the contributing processes are shown.

This process can only contribute to the background if one of the two leptons in the final state is not detected. Since no neutrinos are produced, a non negligible amount of E_T^{miss} must arise from mismeasurements like e.g. the not detected lepton.
The MC simulations consist of several steps. First, the matrix element of the process is calculated using a proton PDF. Then the hadronisation and final state radiation is simulated (showering). This forms the simulated event, before it interacts with the detector material. It is called the truth-level. Finally, the detector response is determined. This involves calculating the interaction of the event with the detector and the resulting signal. This level is called the reconstruction level and agrees with the level of the measured data. All these steps are done with different MC-generators. An overview of the generators used is given in Table 3.1. For the simulation of the $W \to \ell\nu$ and the Z+jets processes, a mass-dependent k-factor obtained with the `LPXkfactorTool` is used. It corrects the default CT10NLO PDF to CT14NNLO and applies NLO EW as well as NNLO QCD corrections. All MC are further corrected using lepton scale factors. These provide correction factors for lepton trigger, identification and isolation. In addition, a muon TTVA and an electron reconstruction scale factor is applied. Lastly, the data in the muon channel is corrected using a sagitta bias correction. It accounts for distortions of the detector geometry and is anticorrelated between charges.

Table 3.1: Simulated processes with the PDF and the generators used.

	PDF	matrix element	showering	detector
$W \to \ell\nu$	CT14NNLO [37]	Powheg-Box[38]	Pythia8[39]	GEANT4[40]
$t\bar{t}$	NNPDF3.0[41]	Powheg-Box	Pythia8	GEANT4
single-t	NNPDF3.0	Powheg-Box	Pythia8	GEANT4
Z+jets	CT14NNLO	Powheg-Box	Pythia8	GEANT4
diboson	NNPDF3.0	Sherpa[42]	Sherpa	GEANT4

3.2 Object reconstruction

The multiple components of the ATLAS detector allow the reconstruction of a large number of different particles and objects. For this purpose, complex algorithms combine the data from the ID, the calorimeters and the MS to reconstruct the type, energy and momentum of a particle. The reconstruction for the most important objects considered in this analysis is described below.

3.2.1 Electrons

Since an electron is a charged particle, it leaves a track in the Inner Detector. In addition, electrons are stopped in the calorimeter, so that their energy is deposited there. These are also the main requirements for an object to be identified as an electron: A track in the ID, a cluster in the ECAL and a close $(\eta \times \phi)$-matching of the track and the cluster. Once these basic requirements are met, the object can be further classified, depending on how certain it is that it is an electron. This is done using the electron identification criteria. It is based on a likelihood, that takes into account several variables from the tracking detector and the calorimeter. Its output is related to the probability that the analysed object is an electron. A cut is then set on this output to decide, whether an object is classified as electron or not. The different identification working points `VeryLoose`, `Loose`, `Medium` and `Tight` correspond to increasingly strict cuts on this likelihood discriminant. Furthermore, an additional working point `LooseAndBLayer` is given by requiring the `Loose` cut on the likelihood and a hit in the innermost layer of the pixel detector. Another important variable in deciding whether an object is an electron or not is the isolation. It is also helpful to separate electrons that originate directly from the signal process from those that originate from e.g. hadron decays. The isolation corresponds to an upper limit on the amount of energy that is deposited in a ΔR-cone of a certain size around the reconstructed object. This can be done either on the basis of the calorimeter or the tracker information [43].
In this analysis, electrons are classified as tight and loose based on the identification and isolation criteria. Thereby, a tight electron always fulfils the criteria for a loose electron, while a loose level electron does not need to fulfil the criteria for the tight level. The detailed identification and isolation requirements are given in Table 3.2.

Table 3.2: Identification and isolation requirements for a lepton to fulfil the loose and the tight level, respectively.

lepton	level	identification	isolation
electron	loose	`LooseAndBLayerLH`	`FCLoose`
	tight	`TightLH`	`FCHighPtCaloOnly`
muon	loose	`Medium`	-
	tight	`HighPt`	`FCTightTrackOnly_FixedRad`

3.2.2 Muons

In contrast to electrons, muons interact with the calorimeter material as minimum ionizing particles, so that they do not deposit any relevant amount of energy there. However, a muon is a charged particle, which leads to tracks in both the ID and the MS. Consequently, the most important reconstruction requirements for a muon are close tracks in the ID and the MS. The calorimeters are used to correct for the rare cases of large energy losses, to determine track parameters and for MS-independent muon reconstruction. Different identification criteria are

provided, depending on how accurately the reconstructed object could be classified as a muon. A dedicated working point is defined for muons with high p_T, since their tracks become very straight, making a precise momentum measurement difficult. Thereby, the muon is also required to be tracked in both the MS and the ID. Furthermore, a muon isolation is defined by setting a condition on the amount of energy deposited in a ΔR-cone around the reconstructed track [44].
Similar as for electrons, the identification and isolation criteria are used to define a loose and tight level for muons (see Table 3.2).

3.2.3 Jets

Due to the principle of colour confinement, a quark or a gluon cannot exist in an unbound state. If such a quark or gluon is part of the final state of an event, it starts a series of strong interactions that produce many strong interacting particles. These form a jet of hadrons, carrying the energy and the momentum of the original particle. This process is called hadronisation and causes the typical detector signature of a quark or a gluon, a so-called "jet". Jets are reconstructed by clustering energy deposits in the hadronic calorimeter. Here, this is done with the anti-k_t [45] algorithm.

3.2.4 E_T^{miss}

Finally, the reconstruction of the E_T^{miss} (see Section 2.3.1) is very important in this analysis. The reason for this is that the neutrino, which is produced in the leptonic decay of a W, cannot be detected and therefore only appears in the E_T^{miss}. The E_T^{miss} is based on the measured energy contribution of all reconstructed objects, such as electrons, muons, photons, tauons and jets, whereby taus and photons are not considered in this analysis. In addition, energy clusters that are not associated to a reconstructed object are also taken into account. This is done in the so-called soft-term. Thus, the $x(y)$-component of the E_T^{miss} is calculated by:

$$E_{x(y)}^{miss} = E_{x(y)}^{miss,e} + E_{x(y)}^{miss,\gamma} + E_{x(y)}^{miss,\tau} + E_{x(y)}^{miss,jets} + E_{x(y)}^{miss,\mu} + E_{x(y)}^{miss,soft}. \tag{3.1}$$

From this, the final E_T^{miss} is determined:

$$E_T^{miss} = \sqrt{(E_x^{miss})^2 + (E_y^{miss})^2}. \tag{3.2}$$

It is worth noting that the way objects are reconstructed plays an important role in the determination of the E_T^{miss}. For example, one can decide whether a loose level electron should be classified as a jet or an electron. As the energies of jets and electrons are calibrated differently, this would result into different energy contributions in the terms $E_{x(y)}^{miss,e}$ and $E_{x(y)}^{miss,jets}$, respectively. For the underlying analyses it was decided to treat loose level electrons as electrons and not as jets [46, 47].

3.3 Event selection and MC-data comparisons

First of all, the events must be triggered as described in Section 2.3.5. Since the final state of the signal contains exactly one lepton, single-lepton triggers are used. The triggers selected for this analysis are shown in Table 3.3. These are the lowest unprescaled triggers available.
Since the signal process consists of one lepton and one neutrino in the final state, the event selection filters for events with a similar signature. Furthermore, kinematic cuts are applied to improve the signal-background ratio. An event passing the signal selection must satisfy the following conditions:

Table 3.3: Triggers in the electron and muon channel.

channel	year	trigger
electron	2015	HLT_e24_lhmedium_L1EM20VH HLT_e60_lhmedium HLT_e120_lhloose
	2016-18	HLT_e26_lhtight_nod0_ivarloose HLT_e60_lhmedium_nod0 HLT_e140_lhloose_nod0
muon	2015	HLT_mu20_iloose_L1MU15 HLT_mu50
	2016-18	HLT_mu26_ivarmedium HLT_mu50

- exactly one lepton in the event fulfilling:
  - lepton is tight (see Table 3.2),
  - $p_T(\ell) > 65$ GeV,
  - $|\eta(\ell)| < 2.4$;
- no further leptons with $p_T(\ell) > 20$ GeV fulfilling the loose level criteria;
- $E_T^{miss} > 85$ GeV;
- $m_T^W > 200(150)$ GeV[1];
- special vetos depending on lepton flavour:
  - no electron with $1.37 < |\eta| < 1.52$,
  - no muon with $1.0 < |\eta| < 1.01$.

While the $p_T(\ell)$-cut is chosen such that the trigger with a p_T-cut close to this limit have already reached their full efficiency, the cuts on E_T^{miss} and m_T^W are mainly used to reduce the background. Here, the relation between the E_T^{miss} and m_T^W is roughly oriented towards a high-mass-W-boson that transfers its energy equally to the lepton and the neutrino. The flavour-dependent veto regions are the transition regions between the barrel and the end-cap of the electromagnetic calorimeter (electrons) and the muon spectrometer (muons), respectively.

The cuts above define a signal region, where the measurement is done. Then the remaining background and the expected signal contribution have to be estimated. Most of the backgrounds as well as the signal are simulated with MC as described in Section 3.1. However, one background, the fake lepton background or multijet (MJ), is estimated with the data-driven Matrix Method. This background arises from jets misidentified as leptons or leptons originating from decays in hadronic jets. These are called “fake leptons”, in contrast to “real leptons” that originate directly from the decay of a W- or Z-boson. Although the fake leptons are very unlikely to pass the signal selection, they are a non-negligible part of the background. This is due to the high jet production cross section.
For the Matrix Method, the leptons must be classified as either loose or tight, whereby a tight

[1]During the unfolding, the m_T^W-cut is lowered to 150 GeV, in order to allow the usage of a shadow bin that stabilises the unfolding.

level lepton also fulfils the loose level criteria. Such a classification is provided with the levels shown in Table 3.2. For muons the loose level is increased, so that a loose level muon has to satisfy the `HighPt` identification instead of the `Medium` identification. From the numbers of leptons fulfilling these two levels, one can conclude on the number of real and fake leptons. This is done using the following relation:

$$\begin{pmatrix} N^{tight} \\ N^{loose-not-tight} \end{pmatrix} = \begin{pmatrix} \epsilon_R & \epsilon_F \\ 1-\epsilon_R & 1-\epsilon_F \end{pmatrix} \cdot \begin{pmatrix} N^{loose}_{real} \\ N^{loose}_{fake} \end{pmatrix}. \tag{3.3}$$

Thereby, $\epsilon_{R/F}$ are called real/fake efficiencies and are determined by

$$\epsilon_{R/F} = \frac{N^{tight}_{real/fake}}{N^{loose}_{real/fake}}. \tag{3.4}$$

These efficiencies correspond to the probability that a real/fake lepton passing the loose level will pass the tight level, too. Since the number of real/fake leptons that fulfil the loose and tight level criteria are accessible in the data, the contributing multijet background can be estimated. It consists of the fake leptons that pass the tight level, i.e. $\epsilon_F N^{loose}_{fake}$, which can be extracted by inverting the matrix in Equation 3.3:

$$\epsilon_F N^{loose}_{fake} = \frac{\epsilon_F}{\epsilon_R - \epsilon_F}(\epsilon_R(N^{loose-not-tight} + N^{tight}) - N^{tight}). \tag{3.5}$$

This can be converted into event weights that are applied to the loose level data, depending on whether an event passes the tight level or not:

$$w^{tight}_{MM} = \frac{\epsilon_F(\epsilon_R - 1)}{\epsilon_R - \epsilon_F}, \qquad w^{loose-not-tight}_{MM} = \frac{\epsilon_F \epsilon_R}{\epsilon_R - \epsilon_F}. \tag{3.6}$$

The main challenge of this method is the experimental determination of the real and fake efficiencies. The determination of the efficiencies is done in regions that are, on the one hand, close to the signal region and, on the other hand, enriched in real and fake leptons, respectively. For the determination of the real efficiencies, the following event selection with respect to the signal selection is used:

- the cuts on m_T^W and E_T^{miss} are omitted.
- a truth-matching is required: $\Delta R(\ell, \ell_{truth}) < 0.1$.

Then, the number of real leptons on the loose and tight level is estimated using the signal MC. Thereby, the real efficiencies are binned in four $|\eta(\ell)|$-bins and eight (electron channel) and six (muon channel) $p_T(\ell)$-bins, respectively. In case of the fake efficiencies, the following changes with respect to the signal region are made:

- The m_T^W requirement is omitted.
- The E_T^{miss}-cut is inverted to $E_T^{miss} < 65\,\mathrm{GeV}$.

In addition, two cuts are required in the muon channel only:

- at least one jet with $p_T > 40\,\mathrm{GeV}$ and $\Delta R(\mu, jet) > 0.2$.
- d_0[2] significance greater than 1.5.

[2]The d_0 significance describes the shortest distance between the vertex of a track and the beam line [48].

Here, the number of fake leptons is estimated by subtracting the contributions from the electroweak backgrounds and the signal, which are simulated by MC, from the data. The fake efficiencies are binned in twelve equidistant $\Delta\phi(\ell, E_T^{miss})$-bins, four $|\eta(\ell)|$-bins and eleven $p_T(\ell)$-bins in the electron channel. In the muon channel, six $\Delta\phi(\ell, E_T^{miss})$-bins, three $|\eta(\ell)|$-bins and six $p_T(\ell)$-bins are used. The extracted real and fake efficiencies can be found in the appendix (Appendix A.1).

The resulting measurement distributions in the 1D measurement binning in m_T^W and the 2D measurement binning in $m_T^W \otimes |\eta(\ell)|$ are shown in Figure 3.2 and Figure 3.3, respectively. The vertical lines in the 2D-distributions separate different m_T^W-bins, while the corresponding $|\eta(\ell)|$-distribution is shown between the lines. Separate plots per m_T^W-bin can be found in the appendix (see Appendix A.2). The regions $1.37 < |\eta(e)| < 1.52$ and $1.01 < |\eta(\mu)| < 1.1$ are

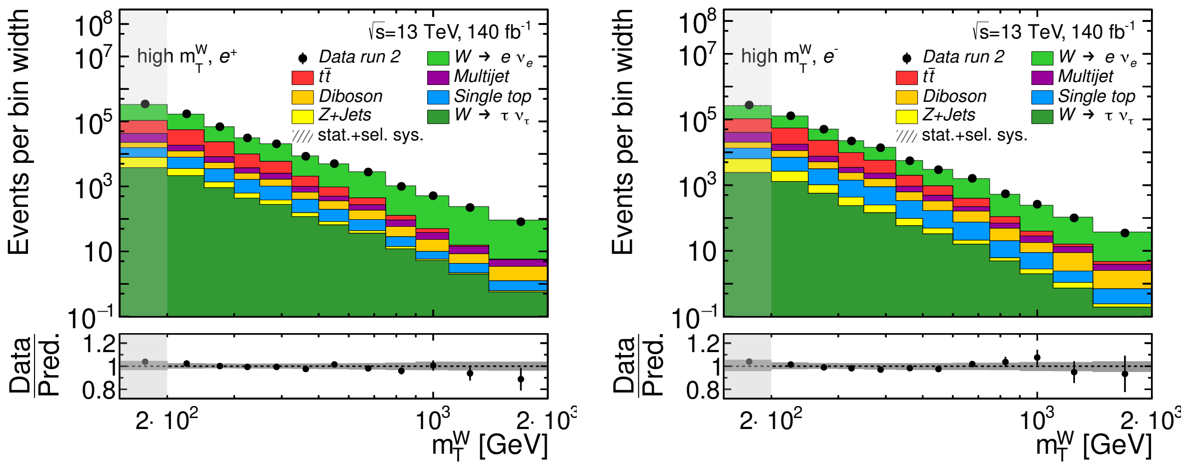

a) e^+-channel **b)** e^--channel

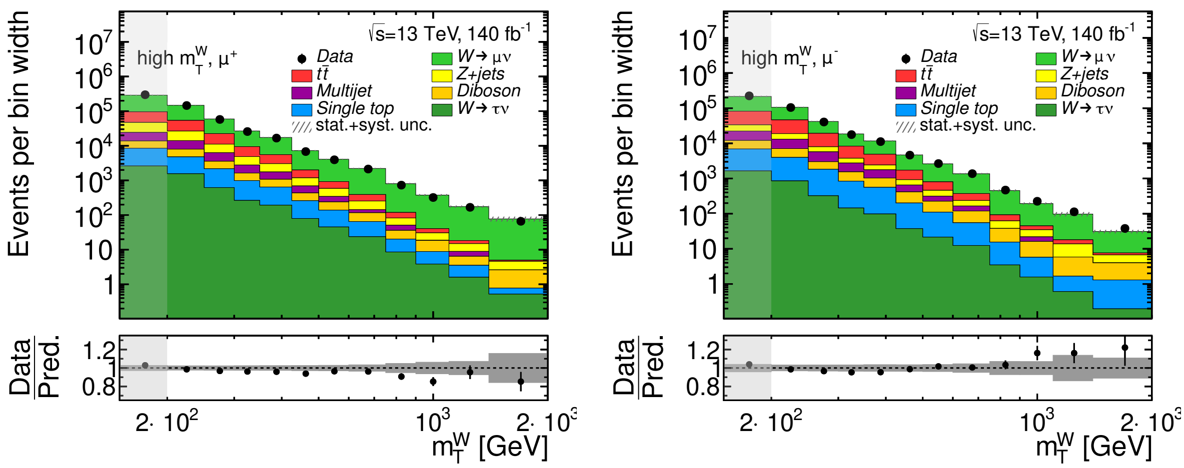

c) μ^+-channel **d)** μ^--channel

Figure 3.2: Data-MC comparison in m_T^W in the 1D measurement binning. The shaded area corresponds to the shadow bin in the range 150 GeV $< m_T^W <$ 200 GeV. All systematic uncertainties with a contribution of at least 0.5% in at least one bin of the measurement distributions are included in the uncertainty band [5].

affected from the barrel-end-cap transition in the ECAL and the MS, respectively. Since events where the lepton is reconstructed in this region are vetoed, no events are present in this ranges.

Therefore, single empty bins are introduced to cover these regions. The shaded area in the plots marks a shadow bin in m_T^W (150 GeV $< m_T^W <$ 200 GeV), which is used to stabilise the unfolding. In particular the insmearing factor f_{in} in Equation 2.16 can be handled better if the shadow bin is used. However, it will not be part of the unfolded results. The uncertainty band includes all systematics with a contribution of at least 0.5% in at least one bin of one of the measurement distributions. For each variable, the distributions in the e^+-, e^--, μ^+- and μ^--channel are shown.

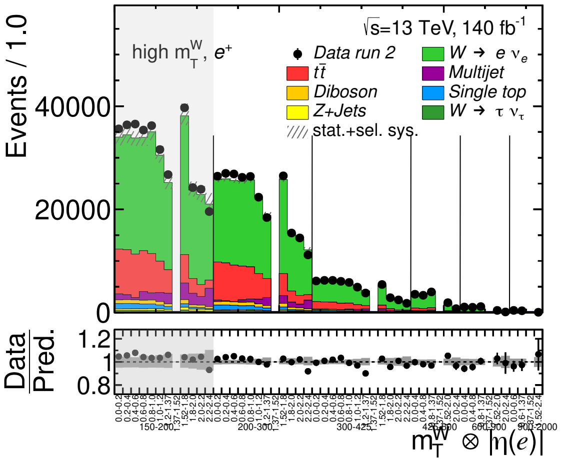

a) e^+-channel

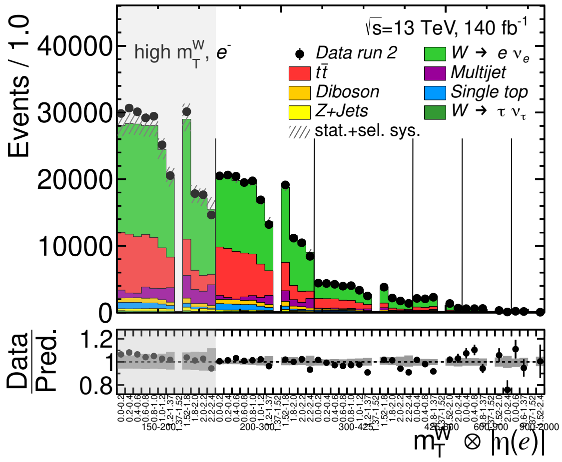

b) e^--channel

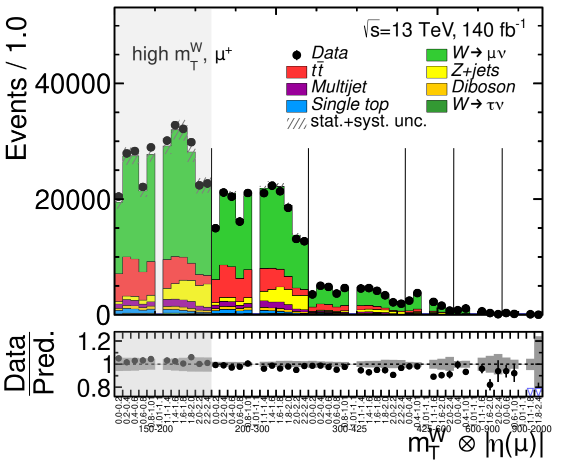

c) μ^+-channel

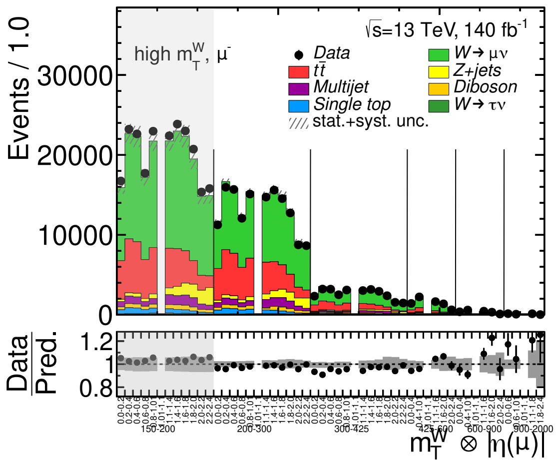

d) μ^--channel

Figure 3.3: Data-MC comparison in $m_T^W \otimes |\eta(\ell)|$ in the measurement binning. The vertical lines in the 2D-distributions separate different m_T^W-bins, while the corresponding $|\eta(\ell)|$-distribution is shown between the lines. Separate plots per m_T^W-bin can be found in the appendix (see Appendix A.2). The shaded area corresponds to the shadow bin 150 GeV $< m_T^W <$ 200 GeV. All systematic uncertainties with a contribution of at least 0.5% in at least one bin of the measurement distributions are included in the uncertainty band [5].

Overall, the agreement between data and prediction in 1D in m_T^W is very good. This holds for the electron channel as well as for the muon channel and both charges. In the electron channel all differences between data and prediction are covered by the statistical and systematic uncertainties. For a muon final state, only two bins in the μ^+-channel (750 GeV $< m_T^W <$ 900 GeV and 900 GeV $< m_T^W <$ 1100GeV) and one bin in the μ^--channel (900 GeV $< m_T^W <$ 1100GeV) have a deviation of up to 20% that is not covered by the systematic uncertainties. All of them are part of an opposite trend, which is observed in the two charges. This trend is probably caused by a sagitta bias correction that may not give perfect results in the high-m_T^W-region. In the 2D measurement distribution in $m_T^W \otimes |\eta(\ell)|$, one can see in principle the same behaviour. In most of the bins, the differences between data and prediction are well covered by the uncertainties. However, there are also a few bins with larger deviations. In the electron channel, these are in particular the bins before the LAr-crack ($1.2 < |\eta(e)| < 1.37$) and the last $|\eta(e)|$-bin ($2.2 < |\eta(e)| < 2.4$). This behaviour is seen across all m_T^W-bins and provides differences of up to 10% while the uncertainties are well below 5%. Considering the distributions of the signal and the different backgrounds, these discrepancies are caused by the multijet background, which has a relative event yield in these particular bins. This can be seen in Figure 3.3a and Figure 3.3b and separated per m_T^W-bin in Figure A.6 and Figure A.7 in the appendix. Two bins that show significant deviations in the muon channel, are the first two $|\eta(\mu)|$-bins in the second m_T^W-bin for a μ^--final state. These show discrepancies of $5\% - 10\%$, while the total uncertainty is smaller than 5%. These deviations are so far not fully understood. In addition some discrepancies are visible for $|\eta(\mu)| > 1.1$, which are not fully covered by the uncertainties. These deviations are increasing with larger m_T^W and large $|\eta(\mu)|$ and point in opposite directions for the two charges. Thus, these are most likely due to a non-perfect sagitta bias correction.

3.4 Systematic uncertainties

Beside statistical uncertainties, systematic uncertainties also occur in physic measurements. The main difference between statistical and systematic uncertainties is that the latter cannot be reduced by repeating the experiment. Several systematic uncertainties are considered in the analysis. They account for uncertainties in the measurement and reconstruction of detected objects, theory uncertainties in the simulation of the background processes and uncertainties in the estimation of the fake lepton background. To reduce statistical fluctuations, the `ROOT` smoothing algorithm is applied to all systematic uncertainties. This is done by smoothing the whole m_T^W-range in 1D and each m_T^W-bin in 2D, respectively. If an uncertainty is two-sided and it is not known to be asymmetric, it is also symmetrised. The systematic uncertainties are also propagated through the unfolding. If they are associated to background processes only, the value of N^i_{bkg} in Equation 2.16 is varied. The experimental systematic uncertainties are taken into account for the signal process as well as for the largest background, namely $t\bar{t}$. These are considered by replacing $N^i_{data} - N^i_{bkg}$ with $N^i_{signal,syst} + N^i_{t\bar{t},syst} - N^i_{t\bar{t},nom}$, where $N^i_{signal,syst}$ and $N^i_{t\bar{t},syst}$ denote the systematically varied signal and $t\bar{t}$ background and $N^i_{t\bar{t},nom}$ describes the nominal $t\bar{t}$ background.

3.4.1 Experimental systematic uncertainties

Experimental uncertainties regarding the energy scale and resolution are taken into account for all reconstructed objects. These are jets [49], electrons [50], muons [51] and the E_T^{miss} [52]. Moreover, the uncertainties of the lepton scale factors are included too. The experimental uncertainties are considered for both the signal and the $t\bar{t}$ background. They are treated in a correlated way during the unfolding. The experimental uncertainties with a contribution of at least 0.5% in any bin in any of the measurement distributions are shown in Figure 3.4 exemplarily for a ℓ^+ final state and the 2D measurement variable. The uncertainties on the 1D measurement variables as well as the other charges can be found in the appendix in Figure A.10-A.13. The by far most important uncertainty in the muon channel is the MU SAGITTA RESBIAS systematic. It is one of two systematic uncertainties related to the sagitta bias correction described in Section 3.1 and corresponds to a variation of the momentum scale in the determination of this correction. At small m_T^W, it is in the order of $\sim 1\%$ and thus of the same size as the other muon related uncertainties. With higher m_T^W, the MU SAGITTA RESBIAS systematic increases up to $\sim 30\%$. Furthermore, it can be seen that the uncertainty is also larger for $|\eta(\mu)| > 1.0$ than for $|\eta(\mu)| < 1.0$. This behaviour is plausible, since the correction becomes more important at high $|\eta(\mu)|$ and m_T^W, too. For the muon scale factors, two-sided uncertainties are provided by the MCP group. The largest of them is related to the identification scale factor. Similar to the MU SAGITTA RESBIAS systematic, it increases with larger $|\eta(\mu)|$ and m_T^W. It ranges from $\sim 1\%$ in the first m_T^W-bin to 5% for $1.8 < |\eta(\mu)| < 2.4$ and $900\,\text{GeV} < m_T^W < 2000\,\text{GeV}$. Furthermore the uncertainties MU MS, corresponding to the track resolution in the MS, and MU SCALE, corresponding to the muon momentum scale have a non-negligible impact on the analysis. They extend to $\sim 1.5\%$ in the last measurement bin.

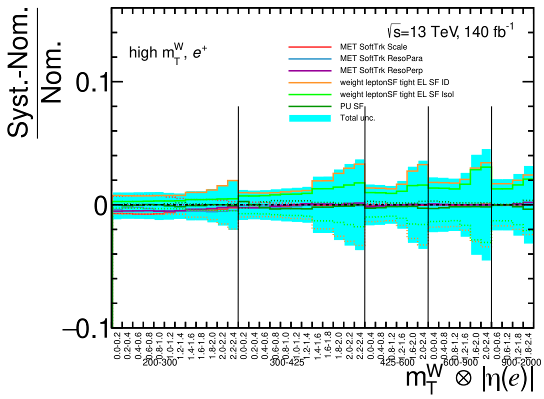

a) e^+-channel

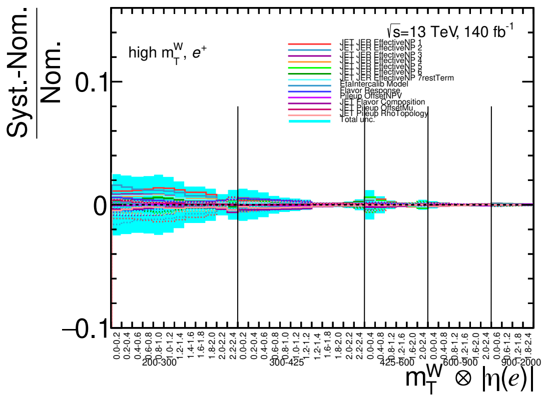

b) e^+-channel

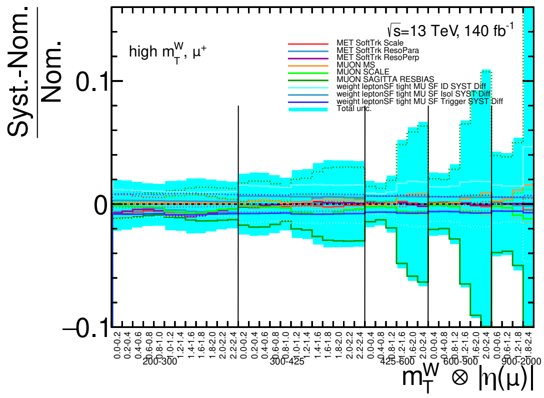

c) μ^+-channel

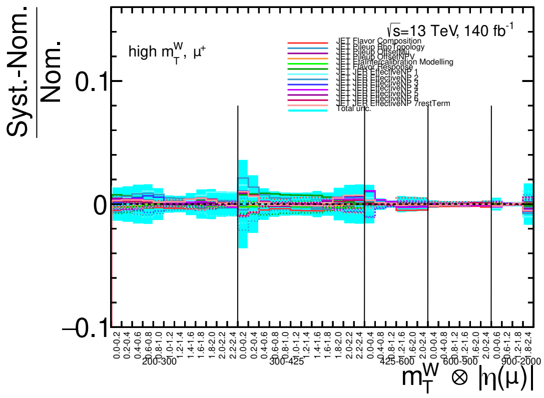

d) μ^+-channel

Figure 3.4: Experimental systematics in the measurement variable in $m_T^W \otimes |\eta(\ell)|$ exemplarily for an e^+ and a μ^+ final state. The lepton and MET systematics are shown in the left column and the JET systematics in the right column. A complete overview of all charges and measurement distributions can be found in the appendix (Appendix A.3, Figure A.10-A.13) Shown are the systematic uncertainties after the unfolding normalised to the unfolded cross section [5].

The largest electron uncertainties are related to the identification and isolation scale factors. They are relatively constant in the barrel of the ECAL ($|\eta(e)| < 1.37$) and increase in the end-caps. At maximum, values of $3\% - 4\%$ are achieved. Furthermore, the egamma group provides uncertainties on the energy resolution and scale of the electron. A scheme with 34 nuisance parameter is used. The largest of them extend to $\sim 1\%$ at small $|\eta(e)|$ and m_T^W.
Three nuisance parameters are considered to cover uncertainties on the E_T^{miss}. They account for

uncertainties in the momentum scale and resolution of the soft term of the E_T^{miss}. Compared to the other systematic uncertainties, their impact is small (up to $\sim 5\%$). The E_T^{miss}-systematics become most important at small $|\eta(\ell)|$ and m_T^W.
Lastly, uncertainties in the energy scale and resolution of jets are taken into account. Since the underlying analyses are inclusive in jets, their effects are only considered through the E_T^{miss}. The largest JET systematics are related to the jet energy resolution. They increase up to 1.5% for small $|\eta(e)|$ and m_T^W.

3.4.2 Theory systematic uncertainties

The Monte-Carlo simulations are based on theoretical calculations. These have uncertainties as well. Therefore, the generator used is varied to obtain uncertainties in the simulation of the matrix element and the hadronisation. Furthermore, uncertainties in the initial and final state radiation, the factorisation and renormalisation scales, and the PDF used are taken into account. These uncertainties are considered only for the $t\bar{t}$-background [53], since it is the largest one. In Figure 3.5a and Figure 3.5c the uncertainties with an impact of at least 0.5% in at least one measurement bin are presented, exemplarily for a ℓ^+ final state and the 2D measurement variable. A complete overview of all charges and measurement distributions is given in the appendix (Figure A.14+A.15). The largest of them are the systematic uncertainties covering the matrix element (TTBAR HARDSCATTER), the showering (TTBAR HADRONIZATION) and the factorisation and renormalisation scales (TTBAR SCALEMUR5MUF5 and TTBAR SCALEMUR2MUF1). They extend to $\sim 2\%$ in the e^+-channel and $\sim 1\%$ in the μ^+-channel.
Another important effect is the interference between the tW and the $t\bar{t}$-background [53]. Since the b-quark in Figure 3.1e is produced by a gluon splitting into a $b\bar{b}$ pair and the t-quark decays into a W-boson and another b-quark, it has a $WbWb$ signature in the final state. The same signature originates from the $t\bar{t}$-process, because both top quarks decay into a W-boson and a b-quark. Consequently, the two processes interfere with each other and this interference needs to be addressed. Two methods are provided to remove the interference: The diagram-removal (DR)[54] and the diagram-subtraction (DS)[55] scheme. While the DR scheme is used as default, the difference to the DS scheme provides a one-sided uncertainty on the single-t-background. This uncertainty is among the largest theory uncertainties and extends to $\sim 2\%$ in both channels.
Lastly, flat cross section uncertainties are applied to the smaller electroweak backgrounds. The values used are 5% for $W \to \tau\nu$ and Z+jets [56], 6% for the diboson background [57] and 4% for single-t [58]. These are presented in Figure 3.5b and Figure 3.5d for the ℓ^+-channels and the 2D measurement distribution. The other channels and distributions can be found in the appendix (Figure A.17+A.16). The most relevant impact is given by the Z+jets background at high $|\eta(\mu)|$ and small m_T^W in the muon channel. This is caused by the fact that this background becomes relatively large in this regions.

3.4.3 Uncertainties associated to the fake lepton background

The most difficult part in the determination of the fake lepton background is the calculation of the fake efficiencies. Thus, systematics associated to this background are extracted by varying the fake enriched region, where these efficiencies are calculated.
Two uncertainties are applied on both the electron and muon fake lepton background:

- MJ EL/MU MC SCALING: varying the estimated real lepton background in the fake-enriched region by $\pm 6\%$;

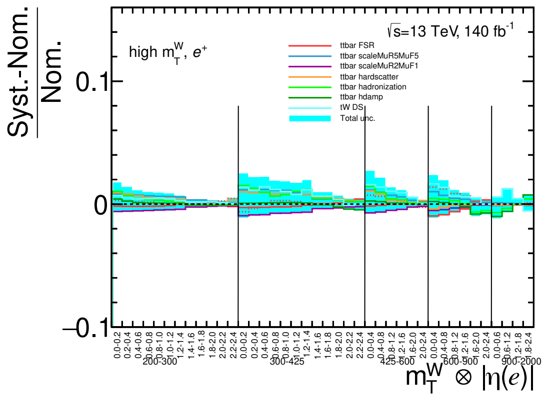

a) e^+-channel

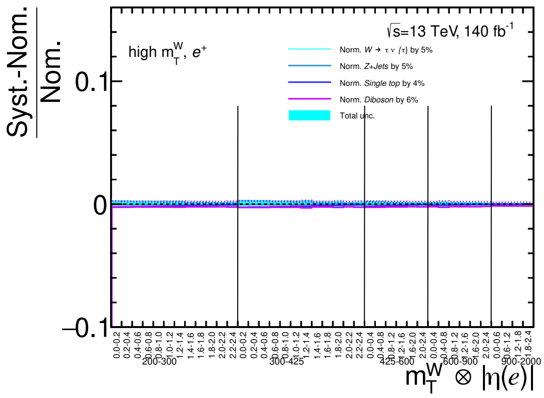

b) e^+-channel

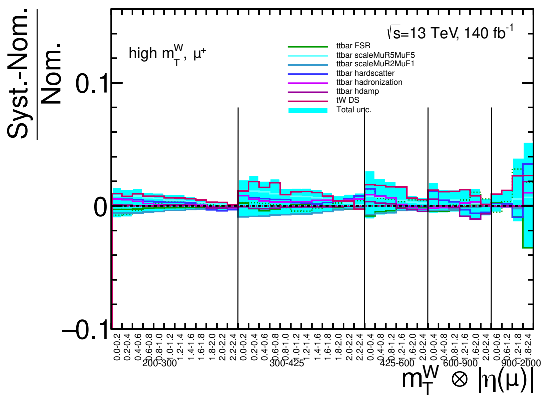

c) μ^+-channel

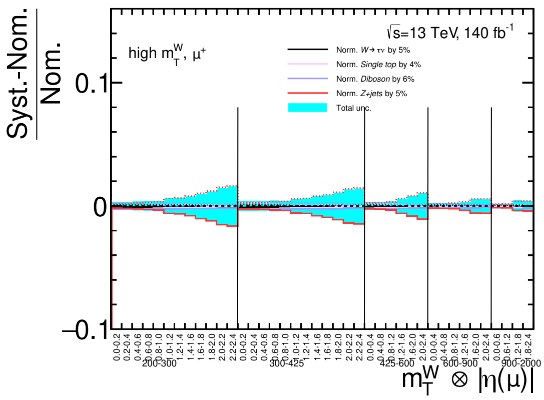

d) μ^+-channel

Figure 3.5: Theory systematics in the measurement variable in $m_T^W \otimes |\eta(\ell)|$ exemplarily for an e^+ and a μ^+ final state. The cross section uncertainties are shown in the right column and the other theory systematics in the left column. A complete overview of all charges and measurement distributions can be found in the appendix (Appendix A.3, Figure A.14-A.17) Shown are the systematic uncertainties after the unfolding normalised to the unfolded cross section [5].

- MJ EL/MU MET: replacing the nominal E_T^{miss}-range by a low-E_T^{miss} ($0\,\text{GeV} < E_T^{miss} < 30\,\text{GeV}$) and a high-$E_T^{miss}$ range ($30\,\text{GeV} < E_T^{miss} < 65\,\text{GeV}$).

Furthermore, some uncertainties are taken into account only for the electron multijet:

- MJ EL 1JET: requiring at least one jet;
- MJ EL MIXMET: varying the definition of the E_T^{miss}.

For the MJ EL MIXMET systematic, the multijet template is composed of two different templates using either the loose or the tight E_T^{miss} definitions. The difference between the two definitions is, whether loose level electrons are considered as jets or electrons in the E_T^{miss} calculation. The uncertainties, which are considered for the muon multijet only, are:

- MJ MU NOJET: do not require a jet;
- MJ MU D0CUT: varying the applied $d0$cut by $\Delta d0 = 0.5$.

In Figure 3.6, one can see the resulting uncertainties for the 2D measurement distribution and an e^+ or μ^+ final state. Shown are only uncertainties with a contribution of at least 0.5%

in one bin of the 1D or 2D measurement distributions. The other charges and distributions are presented in the appendix (Figure A.18+A.19). One can see that the behaviour of the uncertainties is quiet different in the electron and muon channel. For an electron final state, sharp peaks are observed in the MJ EL MC scaling and the MJ EL MET systematic. These are located in the bins before the LAr-crack and in the last $|\eta(e)|$-bin and extend up to $\sim 5\%$. The peaks are probably related to the large multijet background in these bins. The MJ EL mixMET systematic tends to decrease the cross section and has a maximum size of $\sim 4\%$. In the muon channel, the MJ MU MC scaling and MJ MU MET systematics do not show such peaks as in the electron channel. They decrease starting from $|\eta(\mu)| = 0$ until the end of the MS barrel. The same structure is seen in the MS end-cap: The uncertainties reach their maximum at $|\eta(\mu)| \approx 1.0$ and decrease for larger $|\eta(\mu)|$. Finally, the MJ MU d0cut uncertainty also has large impact on the measurement. It reaches its maximum at $|\eta(\mu)| \approx 2.0$ in each m_T^W-bin.

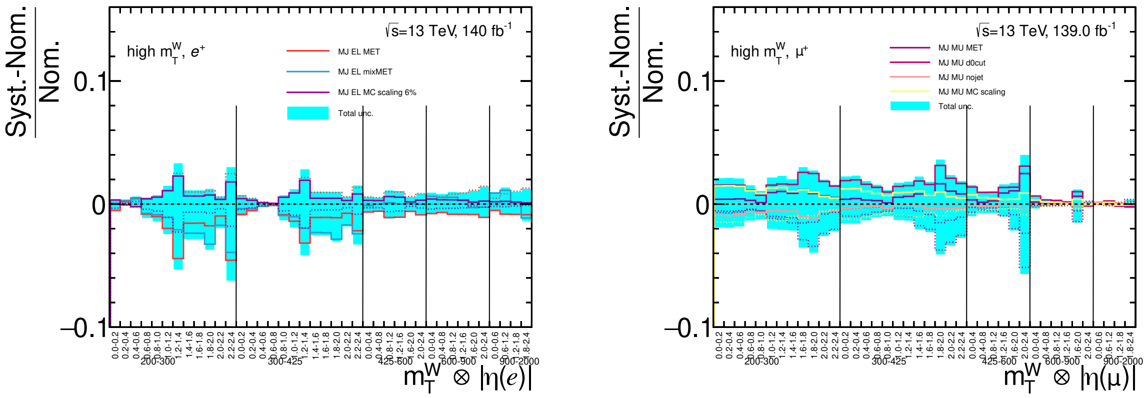

a) e^+-channel **b)** μ^+-channel

Figure 3.6: Uncertainties associated to the fake lepton background in the measurement variable in $m_T^W \otimes |\eta(\ell)|$ exemplarily for an e^+ and a μ^+ final state. A complete overview of all charges and measurement distributions can be found in the appendix (Appendix A.3, Figure A.18+A.19). Shown are the systematic uncertainties after the unfolding normalised to the unfolded cross section [5].

3.5 Unfolded cross sections

Finally, the data is unfolded as described in Equation 2.16. In Figure 3.7 (m_T^W) and 3.8 ($m_T^W \otimes |\eta(\ell)|$), one can see the resulting unfolded cross sections where the shadow bin is no longer shown. The unfolding is done to the born lepton level, i.e. before any final state radiation. The error bars give the statistical uncertainty of the data, the signal and the backgrounds and the light blue (blue) uncertainty bands represent the systematic (total=statistical+systematic) uncertainty. In addition to the unfolded cross section, the MC theory prediction is also presented (red markers).
The largest uncertainties at low m_T^W are the multijet and the scale factor systematics with a size of up to 5% in single bins. At large m_T^W, the uncertainties are dominated by the data statistics. They are in the order of $\sim 20\%$ for the electron channel and $\sim 30\%$ for the muon channel. In addition, the MU SAGITTA RESBIAS systematic extends up to 3% at high m_T^W and high $|\eta(\mu)|$ in the muon channel. Overall, the measurement precision is in the order of $\sim 5\%$ at small m_T^W. At large m_T^W, a precision of about $\sim 20\%$ in the electron channel and $\sim 30\%$ in the muon channel is achieved.

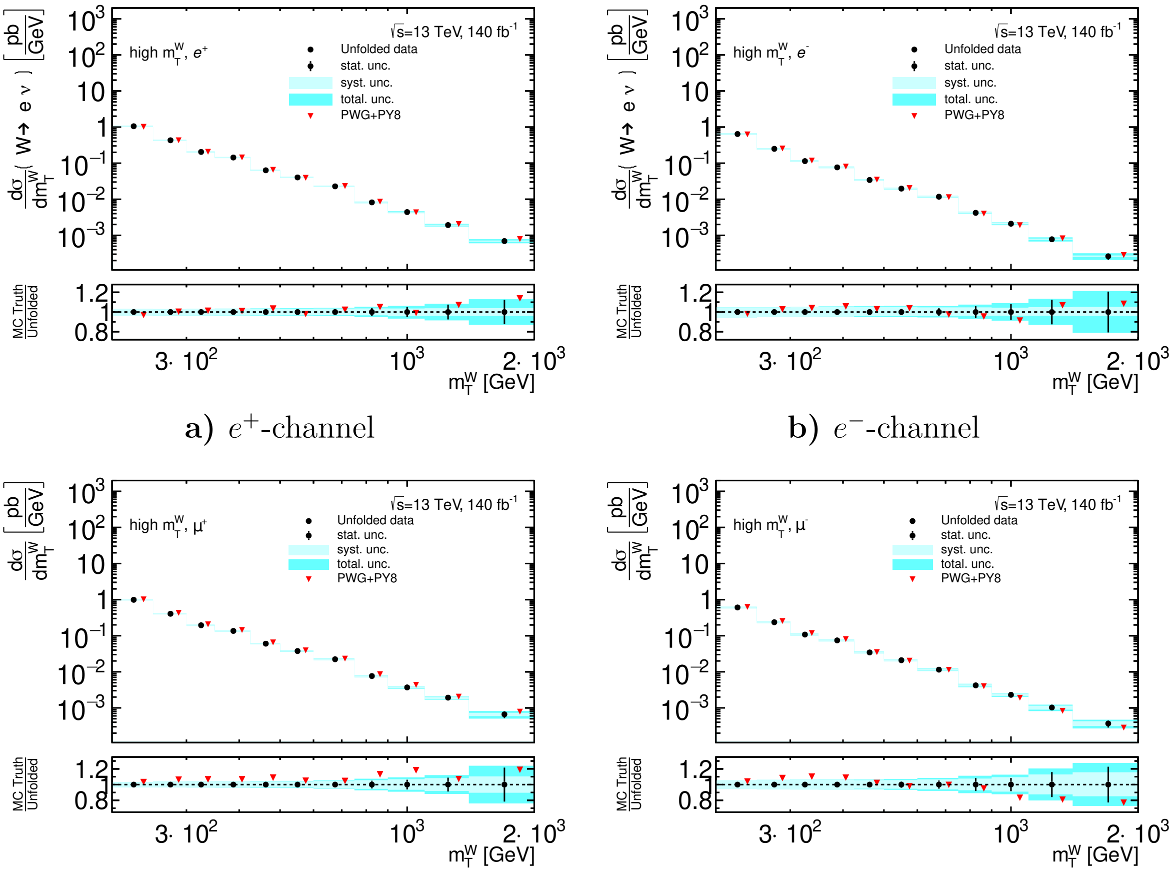

a) e^+-channel

b) e^--channel

c) μ^+-channel

d) μ^--channel

Figure 3.7: Unfolded results in m_T^W. The black markers show the unfolded uncertainty, while the red markers correspond to the MC prediction. The light blue uncertainty band corresponds to the systematic uncertainty and the error bars to the statistical uncertainties. The total uncertainty is indicated with the blue uncertainty band. Only systematics uncertainties with a contribution of at least 0.5% in at least one measurement bin are taken into account [5].

The unfolded cross sections in m_T^W show basically the same trends as the MC-data comparisons in Figure 3.2. Overall, the MC agrees with the unfolded data within the total uncertainty in most of the bins. However, it is noteworthy that the deviations that occurred in the MC-data comparison, are more pronounced after the unfolding.
Similar effects can be observed after the unfolding of the $m_T^W \otimes |\eta(\ell)|$-distribution. The deviations at high $|\eta(\ell)|$ and in the bin before the barrel-end-cap transitions are larger than before the unfolding by roughly a factor of 2. Furthermore, they are still not covered by the systematic uncertainties. This holds for discrepancies in the μ-channel as well. The disagreements between the MC and the unfolded data at $|\eta(\mu)| < 0.4$ and 300 GeV $< m_T^W <$ 425 GeV are increased by a factor of 2 and not covered by the systematic and statistical uncertainties.
In general, it can be observed that the measured cross section decreases with increasing m_T^W. This is as expected, since the measurement starts well above the mass peak. Therefore, the probability of producing a W-boson should become smaller with increasing mass. It can also be seen that the cross section in the ℓ^+-channels is higher than in the ℓ^--channels. This is expected due to the fact that the LHC is a pp-collider. Since a proton contains more up-type valence quarks than down-type valence quarks, it is more likely that a W^+-boson will be produced.

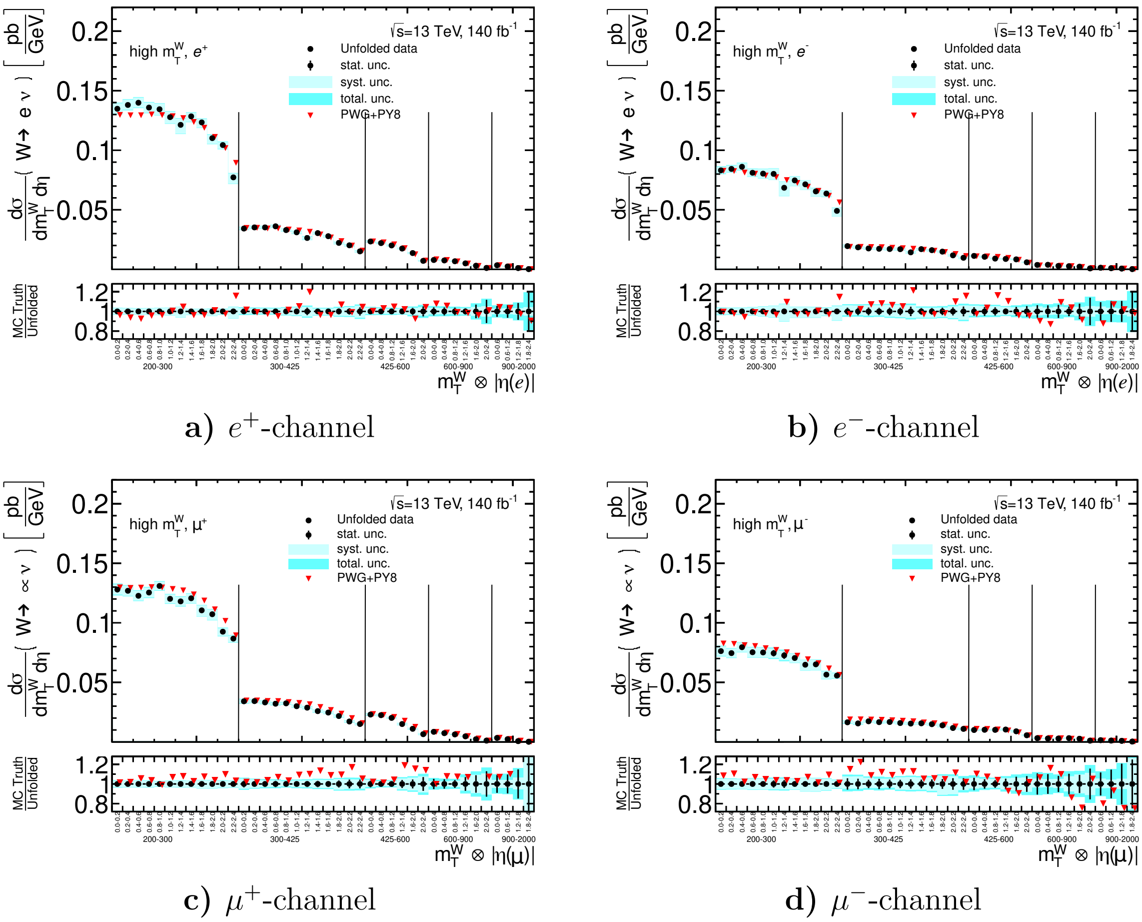

a) e^+-channel **b)** e^--channel

c) μ^+-channel **d)** μ^--channel

Figure 3.8: Unfolded results in $m_T^W \otimes |\eta(\ell)|$. The black markers show the unfolded uncertainty, while the red markers correspond to the MC prediction. The light blue uncertainty band corresponds to the systematic uncertainty and the error bars to the statistical uncertainties. The total uncertainty is indicated with the blue uncertainty band. Only systematics uncertainties with a contribution of at least 0.5% in at least one measurement bin are taken into account [5].

Chapter 4

Combination of the electron and muon channel measurements

In the following, the main part of this thesis, the combination of the electron and muon channel measurements (see Chapter 3) is described and analysed. Due to the concept of lepton universality (see Section 2.1.1), the measured cross sections should agree within the uncertainties at the born level. Thus, a well-defined average between the electron and the muon channels would underpin the consistency of the measurements. In addition, the better statistics when using both electron and muon data can lead to a $W \to \ell\nu$ measurement with higher precision. First, the combination procedure of the used HAVERAGER [59] tool is described. Then the combinations of the differential and double-differential cross section measurements are performed. Finally, the obtained results are analysed in more detail. First of all, different studies concerning the phase space, which is considered in the combination, are performed. Decorrelations are performed in both m_T^W and $|\eta(\ell)|$, as well as in the charge of the leptons. In addition, the multijet estimate in the electron channel is further investigated, since it is probably related to the largest differences between data and prediction in the unfolded results of the electron channel. Moreover, the systematic uncertainties that are considered in the combination are also further discussed. Finally a short summary of the performed combinations and studies is given.

4.1 HAverager combination procedure

In the following, a condensed overview of the HAVERAGER combination procedure is given, according to the more detailed descriptions in the HAVERAGER manual [59].
The averaging is based on a χ^2-minimisation with the following χ^2-function:

$$\chi^2(\vec{\mu}_{aver}, \vec{\beta}) = \sum_{e=1}^{N_e} \sum_{i=1}^{N_b} \frac{\left(\mu_{i,aver} - \mu_{i,e} - \sum_{j=1}^{N_s} \Gamma_{i,e}^j \beta_j\right)^2}{\Delta_{i,e}^2} W_{i,e} + \sum_{j=1}^{N_s} \beta_j^2 \tag{4.1}$$

with N_e the number of the combined measurements, N_b the number of the bins and N_s the number of the considered bin-to-bin-correlated systematic uncertainties. Here $\mu_{i,e}$ denotes the measurement result of measurement e in bin i and $\Delta_{i,e}$ its bin-to-bin uncorrelated uncertainty. In this case, $\Delta_{i,e}$ corresponds in particular to the statistical uncertainty of the input measurement. $\Gamma_{i,e}^j$ represents the magnitude of the symmetric bin-to-bin uncertainty j. These are systematic uncertainties of the input measurements. The parameters $\mu_{i,aver}$ and β_j are free-floating and used to minimise the χ^2. Thereby, $\mu_{i,aver}$ corresponds to the final combined average, while β_j represents a shift in the central value of the systematic uncertainty j relative to their magnitude. Finally, the parameter $W_{i,e}$ is either 1 ore 0, depending on whether measurement

e contributes in bin i. The term $\sum_{j=1}^{N_s} \beta_j^2$ constrains the shifts of the systematic uncertainties. In order to deal with asymmetric systematic uncertainties, an iterative procedure is used. It is based on a variation of each systematic depending on its shift. The applied value of $\Gamma_{i,e}^j$ in iteration k is given by

$$\Gamma_{i,e}^{j,k} = \begin{cases} \frac{\Gamma_{i,e}^{j,+} - \Gamma_{i,e}^{j,-}}{2} & , \ k = 1 \\ \frac{\Gamma_{i,e}^{j,+} - \Gamma_{i,e}^{j,-}}{2} + \frac{\Gamma_{i,e}^{j,+} + \Gamma_{i,e}^{j,-}}{2} \beta_j^{k-1} & , \ else \end{cases} \tag{4.2}$$

with $\Gamma_{i,e}^{j,+(-)}$ the up(down)-variation of the systematic j and β_j^{k-1} the systematic shift of iteration $k-1$. Thus, a symmetrised value of the uncertainty is used in the first iteration. This value is corrected in the following iterations depending on the shift of the previous iteration. Thereby the uncertainty is increased if β_j shifts into the direction of the larger variation and decreased if it does not. An uncertainty is convergent if its shift varies by less than 5% between the last two iterations.

A further correction is made for multiplicative uncertainties, which are proportional to the measured value. Thus, these uncertainties increase if the average is higher than the input cross section and decrease if it is smaller. This behaviour is taken into account by replacing the absolute uncertainty $\Gamma_{i,e}^j$ by the relative uncertainty $\gamma_{i,e}^j := \frac{\Gamma_{i,e}^j}{\mu_{i,e}}$ and applying it to the averaged cross section. Equation 4.1 then transforms to:

$$\chi^2(\vec{\mu}_{aver}, \vec{\beta}) = \sum_{e=1}^{N_e} \sum_{i=1}^{N_b} \frac{\left(\mu_{i,aver}\left(1 - \sum_{j=1}^{N_s} \gamma_{i,e}^j \beta_j\right) - \mu_{i,e}\right)^2}{\Delta_{i,e}^2} W_{i,e} + \sum_{j=1}^{N_s} \beta_j^2. \tag{4.3}$$

Once the optimal shifts have been determined, the averaged measurement in bin i can be calculated via:

$$\mu_{i,aver} = \frac{\sum_{e=1}^{N_e} \left(\mu_{i,e} + \sum_{j=1}^{N_s} \Gamma_{i,e}^j \beta_j\right) \frac{W_{i,e}}{\Delta_{i,e}^2}}{\sum_{e=1}^{N_e} \frac{W_{i,e}}{\Delta_{i,e}^2}}. \tag{4.4}$$

Thus, the combined measurement corresponds to a weighted average of the input cross sections shifted by the parameters β_j. The uncorrelated uncertainty is then given by:

$$\Delta_{i,aver}^2 = \frac{1}{\sum_{e=1}^{N_e} \frac{W_{i,e}}{\Delta_{i,e}^2}}. \tag{4.5}$$

Besides the shifts β_j, another parameter that describes the behaviour of the systematics in the fit is given by their reduction. It represents, how much the systematic was reduced during the combination. Thus, it can indicate whether the initial uncertainties were overestimated.

Finally, the compatibility of the two channels is also measured by the pull of the central value of measurement e in bin i:

$$p^{i,e} = \frac{\mu_{i,aver}\left(1 - \sum_{j=1}^{N_s} \frac{\Gamma_{i,e}^j}{\mu_{i,aver}} \beta_j\right) - \mu_{i,e}}{\sqrt{\Delta_{i,e}^2 - \Delta_{i,aver}^2}}, \tag{4.6}$$

which can be rewritten as follows:

$$p^{i,e} = \frac{\mu_{i,aver} - \left(\mu_{i,e} + \sum_{j=1}^{N_s} \Gamma_{i,e}^j \beta_j\right)}{\sqrt{\Delta_{i,e}^2 - \Delta_{i,aver}^2}}. \tag{4.7}$$

The pull is a measure of the significance of the difference between the shifted input values and the final average. Large pulls suggest that the input measurements, corrected by the systematic shifts, do not agree well. In cases, where only two measurements contribute to a bin the sum over all pulls equals 0: $p^{i,1} + p^{i,2} = 0$ (see Appendix B.1 for mathematical proof).

4.2 Systematic uncertainties considered in the combination

Only systematic uncertainties with a contribution of at least 1% in at least one bin of any of the single- or double-differential measurement distributions are considered in the combination. In principle, this choice is arbitrary, but small systematic uncertainties do not have relevant impact on neither the χ^2 nor the obtained average so that they can be neglected. A complete overview of the considered uncertainties is given in Table 4.1.

Table 4.1: Systematic uncertainties considered in the combination. The type indicates whether a systematic is symmetric (s), asymmetric (a) ore one-sided (o). Uncertainties with names containing EG (applied to the e-channel), EL (applied to the e-channel) or MU (applied to the μ-channel) are not correlated between the lepton flavours. All uncertainties are correlated between lepton charges.

type	uncertainty	type	uncertainty
s	MET SoftTrk Scale New Diff	a	ttbar FSR
o	MET SoftTrk ResoPara	a	ttbar scaleMuRMuF
o	MET SoftTrk ResoPerp	o	ttbar hardscatter
s	EG SCALE S12	o	ttbar hadronisation
s	EG SCALE L1GAIN	o	ttbar hdamp
s	EG SCALE L2GAIN	a	MJ EL MET
s	JET JER EffectiveNP 1	o	MJ EL mixMet
s	JET JER EffectiveNP 2	s	MJ MC scaling
s	JET JER EffectiveNP 3	o	tW DS
s	JET JER EffectiveNP 4	s	Norm. W tau
s	JET JER EffectiveNP 5	s	Norm. ZJets
s	JET JER EffectiveNP 6	s	Norm. Single top
s	JET JER EffectiveNP 7restTerm	s	Norm. Diboson
s	JET Flavor Composition	s	MU MS
s	JET Pileup RhoTopology	s	MU SAGITTA RESBIAS
s	JET Pileup OffsetMu	s	MU SF ID SYST Diff
s	EL SF ID	a	MJ MU MET
s	EL SF Isol	a	MJ MU d0cut
		o	MJ MU nojet

The systematics are labelled according to whether they are symmetric (s), asymmetric (a) or one-sided (o). Thereby, one-sided uncertainties are treated as asymmetric uncertainties with a down-variation set to zero. Uncertainties with names containing EG (applied to the e-channel), EL (applied to the e-channel) or MU (applied to the μ-channel) are only available in the one respective channel and thus are not correlated between the lepton flavours. All other systematic uncertainties are treated correlated between electron and muon channel measurements. The ttbar scaleMuRMuF is an asymmetric uncertainty composed of the two one-sided systematics ttbar scaleMuR5MuF5 and ttbar scaleMuR2MuF1. The combination is done correlated between the lepton charges. Therefore, an additional charge-bin is introduced so that both measurements can be combined in a simultaneous fit. All systematics are treated correlated between the charges. i.e. only one nuisance parameter per systematic is used for both channels. Ten iterations are used to correct for asymmetric uncertainties[1]. The multiplicative

[1]Different numbers of iterations were studied, but it was seen that the effect on the combination is negligible.

model is used for all systematics[2].

4.3 Combination of the single-differential cross section measurements

The result of the combination of the single differential measurement in m_T^W are shown in Figure 4.1. The charge-correlated fit of the ℓ^+- and ℓ^--channel is given in Figure 4.1a and 4.1b, while Figure 4.1c presents the combination of the $\ell^\pm$-channel.
The latter is performed as a cross check, since charge dependent effects cancel out if the sum of both lepton charges is considered. In both cases, all systematic uncertainties converge during the combination. The obtained averaged cross section is presented with the black markers. In addition, the input measurements of the electron (red triangles) and muon (blue triangles) are shown. The blue (light blue) uncertainty bands represent the systematic (total) uncertainty of the average, while the error bars correspond to the statistical uncertainties. In the middle panel, the ratio of the input measurements with respect to the average is shown, while the bottom panel gives the pull of the central values according to Equation 4.6.

The charge-correlated combination results in a $\chi^2/NDF = 11.04/22$. This shows that the measured cross sections in 1D fit very well together. However, a $\chi^2 < NDF$ also suggests that the uncertainties might be overestimated. This is supported by the fact that the input cross sections agree with the combined cross section within the total uncertainties in almost all bins. At high m_T^W, even the statistical uncertainty is sufficient to cover the differences, which also underlines the good agreement between electron and muon channel measurements. Thus, the principle of lepton universality is confirmed by this combination.
The differences between the averaged cross sections and the MC theory prediction can be obtained by comparing the ratios in Figure 4.1a and Figure 4.1b, with the ratio $\frac{\sigma_{MCtruth}}{\sigma_{unf}}$ in Figure 3.7. Considering the difference between combined cross section and unfolded cross section on the one hand, and unfolded cross section and MC truth level on the other hand, one can see that the averaged cross section is in most bins closer to the MC truth level than the unfolded ones. This underlines the agreement between the electron and muon channel and suggests that the observed differences between the MC truth level and the unfolded results (see Section 3.5 Figure 3.7) are caused by imperfect corrections like e.g. the sagitta bias correction. The pulls (see Equation 4.6) of the central values as shown in the bottom panel are - except for one bin - all less than one, which also indicates a good agreement between the input measurements. In addition, the sign of the pulls often fluctuates from positive to negative and vice versa. This is a behaviour one would expect if the differences between the input cross sections were mainly due to statistical fluctuations and not due to systematic effects.
A similar picture is drawn by the corresponding shifts of the systematics (Figure 4.2a). Thereby, the black marker represents the shift of the systematic uncertainty relative to its size, while the error bar corresponds to its reduction. For comparison the areas corresponding to a shift smaller than 1σ (2σ) are marked in green (yellow). Most of the shifts fluctuate around zero and are well below 0.5σ. This behaviour underlines the good compability of electron and muon channel measurements. The only systematics with a shift close to 1σ are MJ EL MIXMET and MU SAGITTA RESBIAS. The shift in the MJ EL MIXMET systematic indicates that the mixed scheme of loose and tight E_T^{miss} works better for the MJ estimation in the

[2]The alternative additive model was also studied, but it was seen that the multiplicative model provides better agreements, indicated by a smaller χ^2/NDF.

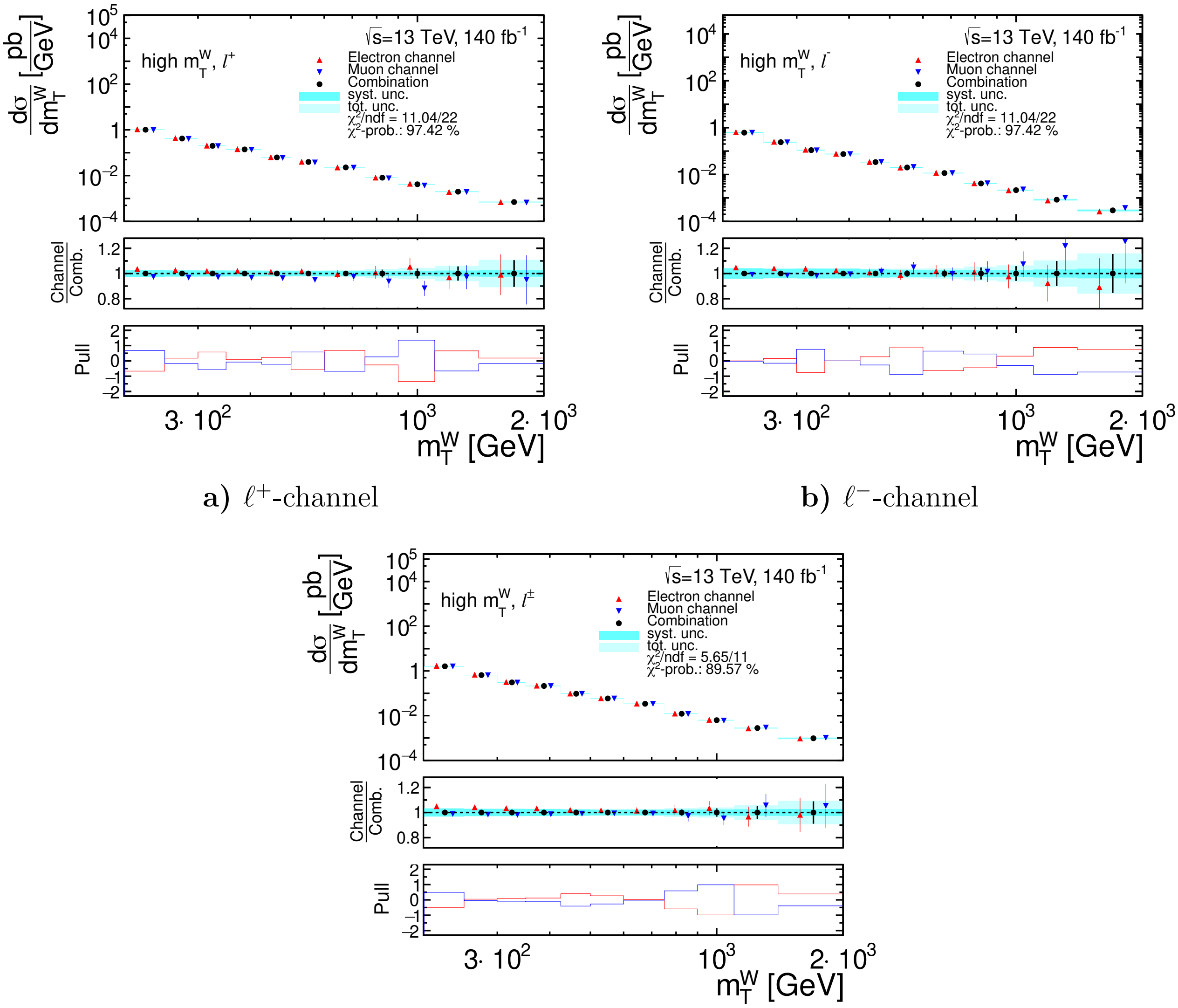

a) ℓ^+-channel **b)** ℓ^--channel

c) $\ell^\pm$-channel

Figure 4.1: Combined cross section (black) of the single-differential measurement in m_T^W together with the input cross sections of electron- (red triangles) and muon- (blue triangles) channel. The blue (light blue) uncertainty band gives the systematic (total=statistical+systematic) uncertainty of the average. The error bars represent the statistical uncertainty only. The middle panel shows the ratio of the initial measurements with respect to the combined cross section. The bottom panel shows the pulls of the electron (red) and muon (blue) channel, according to Equation 4.6. The averages in (a) and (b) are obtained with a simultaneous fit of both the ℓ^+- and ℓ^--channels.

single-differential measurement in m_T^W. The shift on MU SAGITTA RESBIAS reflects the differences between unfolded muon channel cross section and theory prediction, which were observed when analysing the high m_T^W region of the measured spectrum. With the exception of the MU SAGITTA RESBIAS systematic, no significant reductions are observed. Since the systematic shifts do not reflect the size of a systematic, the largest shift does not necessarily correspond to the largest effect on the input cross section. For this reason, it is also useful to look directly at the effect on the input measurement. It is given by

$$\beta_j \Gamma_{i,e}^j \tag{4.8}$$

for a systematic j in bin i on measurement e. The uncertainties with a effect of more than

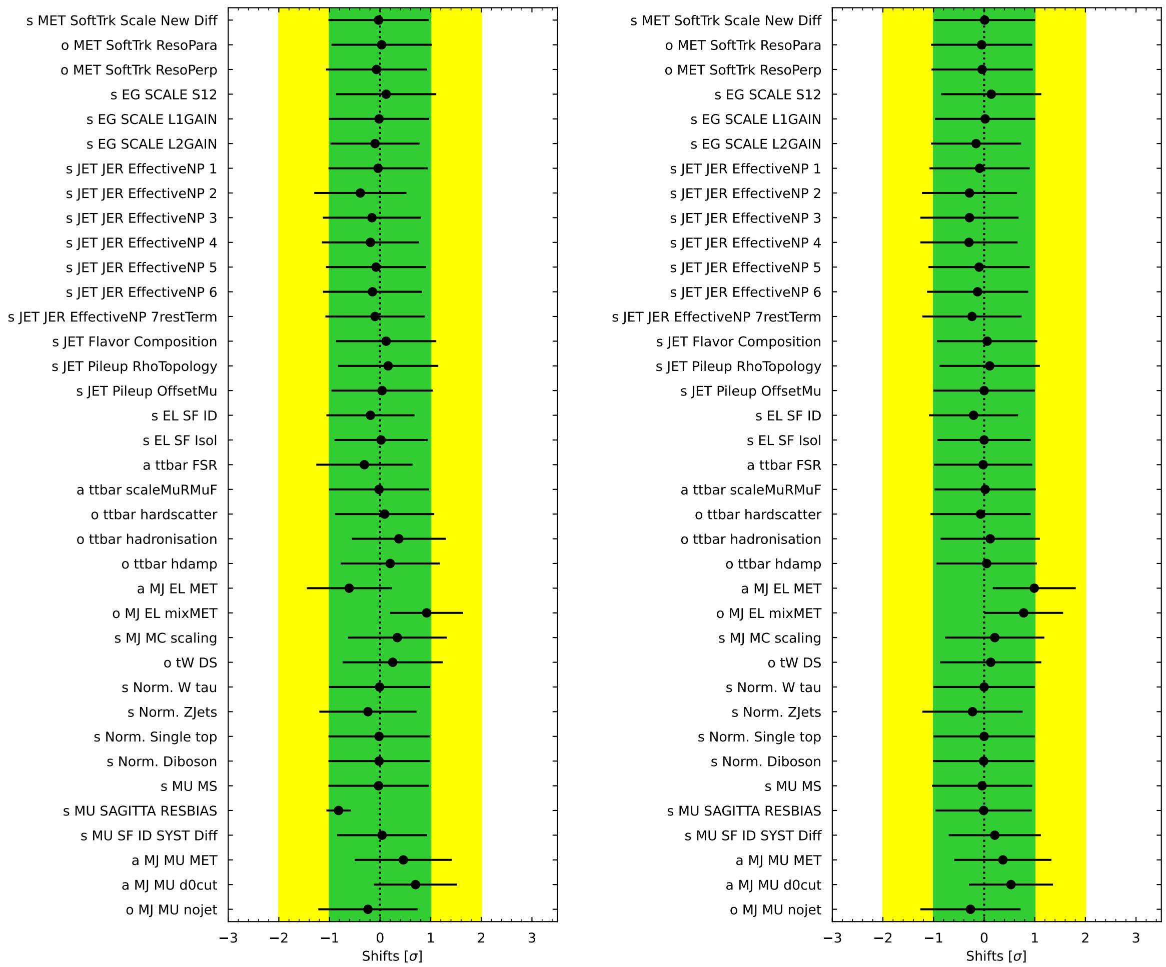

a) $(\ell^+ + \ell^-)$-channel **b)** $\ell^\pm$-channel

Figure 4.2: Systematic shifts β_j for the charge correlated combination of ℓ^+- and ℓ^--channel (a) and the combination of the $\ell^\pm$-channels (b) in m_T^W. The error bars represent the reduction of the uncertainties by the combination. The areas corresponding to a shift smaller than 1σ (2σ) are marked in green (yellow). The uncertainties are labelled depending on whether they are symmetric (s), asymmetric (a) or one-sided (o).

0.5% on the input cross sections are shown in Figure 4.3. It can be seen that by far the largest impact is due to the MU SAGITTA RESBIAS systematic with $\sim 10\%$ at maximum. This is plausible, since it is relatively large and additionally shifted by $\sim 1\sigma$. All other shifts, both in the electron and in the muon channel have a maximum effect on the cross section of the order of $\sim 2\%$.

To remove and understand charge dependent effects, e.g. the sagitta bias correction, a combination of the $\ell^\pm$-channel is performed. The resulting combined cross section is given in Figure 4.1c, while the corresponding shifts are shown in Figure 4.2b. Compared to the charge-correlated combination, the divergent trends at high m_T^W are no longer visible. This is expected, since the effects are probably related to the sagitta bias correction, which is anti-correlated between the two lepton charges. Therefore, they cancel out when the ℓ^+- and ℓ^--channel are summed up. This can also be seen from the shift of the MU SAGITTA RESBIAS systematic, which is very close to zero in the $\ell^\pm$-combination. Moreover, the fluctuations of the systematic shifts are smaller than for the charge correlated fit of ℓ^+- and ℓ^--channel. The only systematic with a

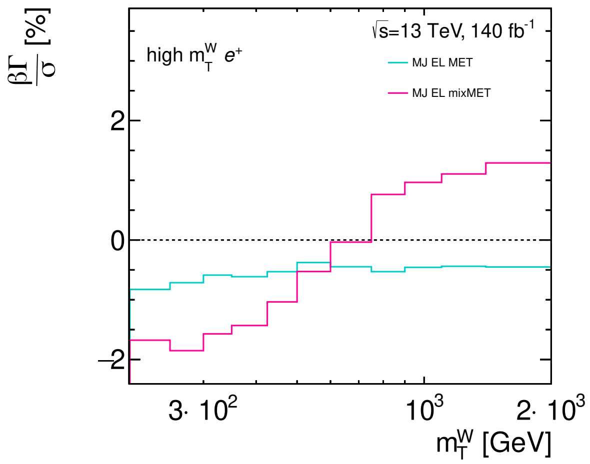

a) e^+-channel

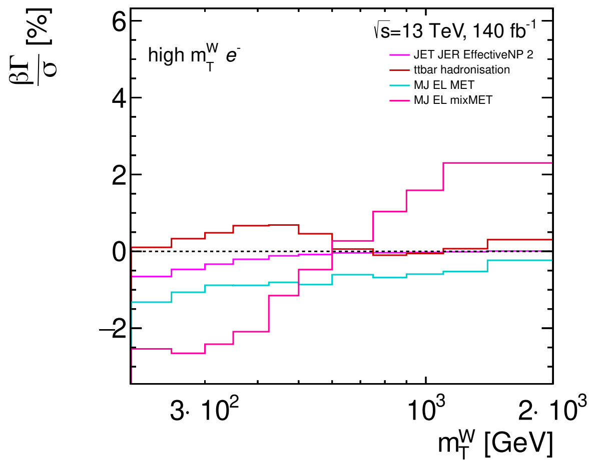

b) e^--channel

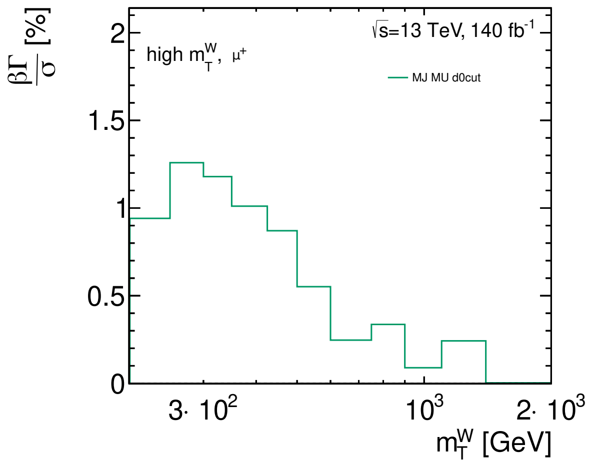

c) μ^+-channel

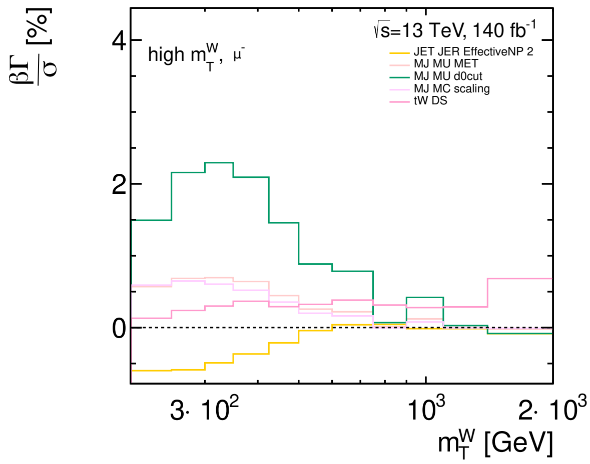

d) μ^--channel

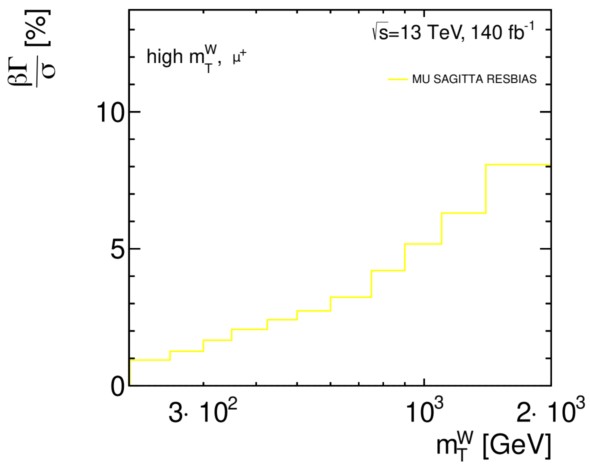

e) μ^+-channel - MU SAGITTA RESBIAS

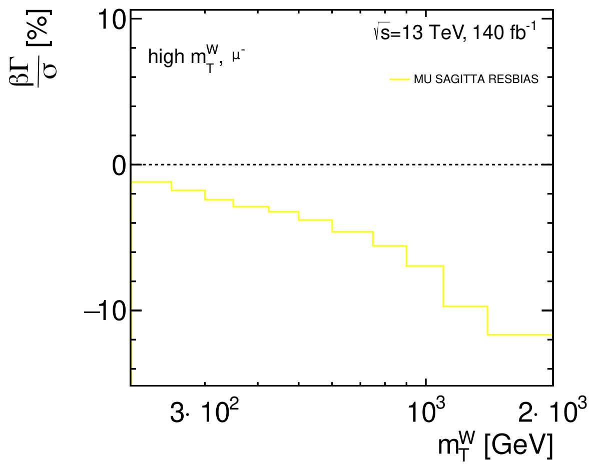

f) μ^--channel - MU SAGITTA RESBIAS

Figure 4.3: Effect of the systematic shifts (Equation 4.8) normalised to the input cross sections in %, for the charge correlated fit of ℓ^+- and ℓ^--channel. Shown are only those systematics, with an effect of at least 0.5% in at least one bin in the given channel. For better visibility, the effect of the MU SAGITTA RESBIAS systematic is shown in an extra plot.

significantly larger shift is MJ EL MET. Its shift of about $+1\sigma$ corresponds to the low-E_T^{miss}-region for the determination of the fake efficiencies.
Lastly, the direct effects on the cross sections are shown in Figure 4.4. All systematics with a contribution of at least 0.5% in at least one bin are plotted. It can be seen, that the impact on the input measurements are less than 2% for all systematics and all bins. This reflects the fact that most of the systematics shifts became smaller when combining the summed $\ell^{\pm}$-channel instead of the simultaneous combination of the ℓ^{+}- and the ℓ^{-}-channel.

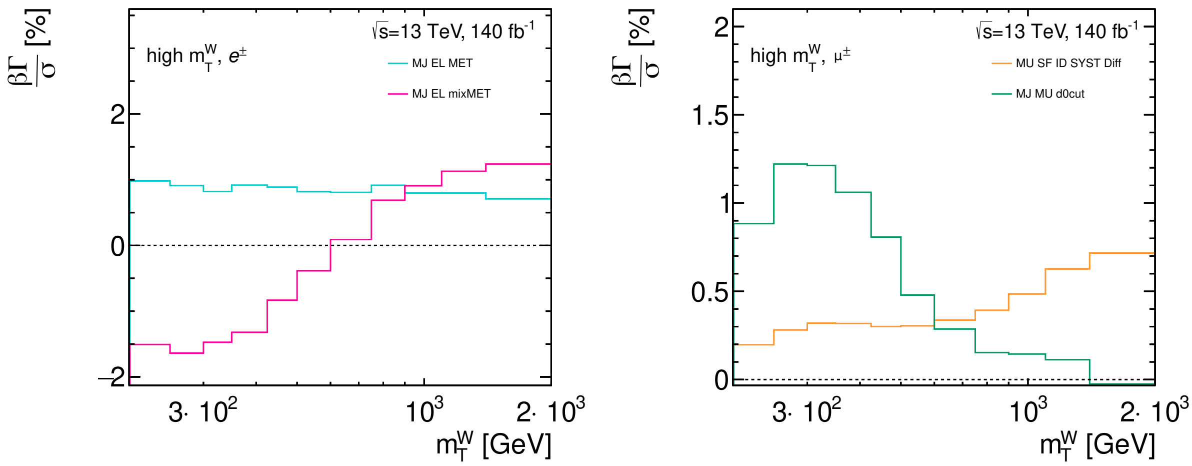

a) $e^{\pm}$-channel **b)** $\mu^{\pm}$-channel

Figure 4.4: Effect of the systematic shifts (Equation 4.8) normalised to the input cross sections in %, for the fit in the $\ell^{\pm}$-channel. Shown are only those systematics, with an effect of at least 0.5% in at least one bin in the given channel.

All in all, the combination of the single-differential measurements provides reasonable results and shows a good agreement between the unfolded cross sections in the electron and muon channel. Some uncertainties might be overestimated, which is indicated by the small χ^2/NDF.

4.4 Combination of the double-differential cross section measurements

The combination is also performed for the double-differential measurements in $m_T^W \otimes |\eta(\ell)|$. In Figure 4.5, one can see the obtained average values for this combination. The charge-correlated (simultaneous) combination of the separate ℓ^{+}- and ℓ^{-}-channels is presented in Figure 4.5a and Figure 4.5b. Again, the combination of the summed $\ell^{\pm}$-channel is shown in Figure 4.5c, as a cross check. The corresponding shifts of the systematic uncertainties are given in Figure 4.6. Three systematic uncertainties (EG SCALE L2GAIN, JET JER EffectiveNP 7RestTerm, MJ EL mixMet) do not converge during the combination. However, different numbers of iterations were tested and found not to have an effect on the number of converging uncertainties.

With a $\chi^2/NDF = 105.82/80$, the combination in $m_T^W \otimes |\eta(\ell)|$ shows still a relatively good agreement between electron and muon channel measurements. However, it also indicates that there a some non-negligible differences between the unfolded cross sections.

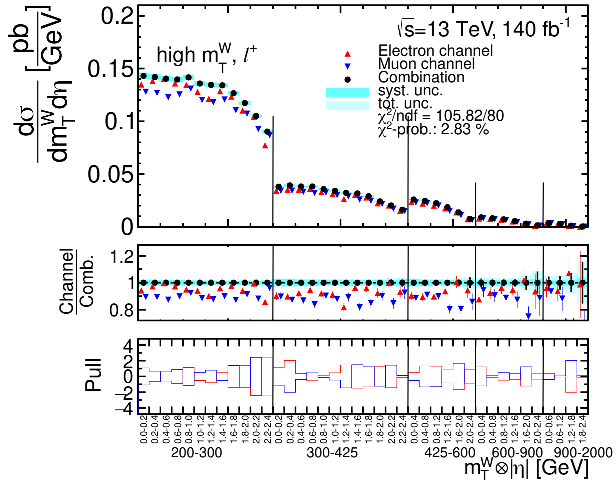

a) ℓ^+-channel

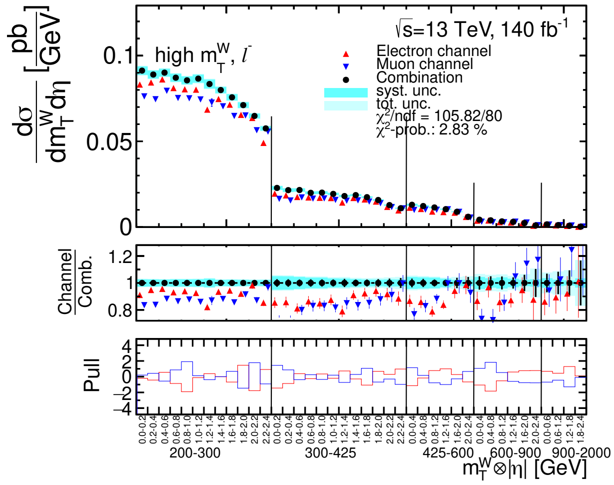

b) ℓ^--channel

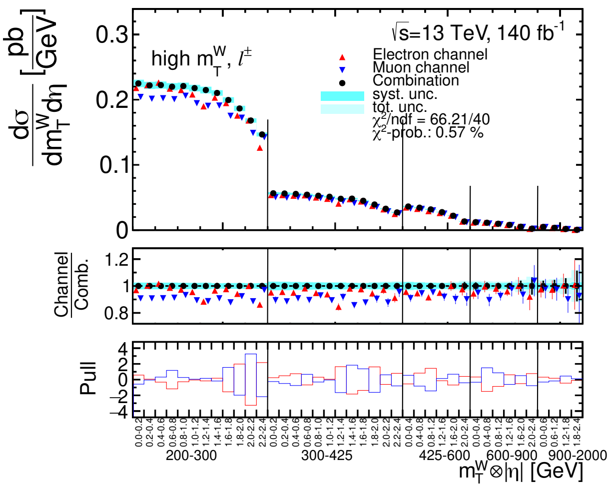

c) $\ell^\pm$-channel

Figure 4.5: Combined cross section (black) in $m_T^W \otimes |\eta(\ell)|$ together with the input cross sections of electron (red) and muon (blue) channel. The blue (light blue) uncertainty band gives the systematic (total) uncertainty. The error bars represent the statistical uncertainty. The middle panel shows the ratio with respect to the combined cross section. The bottom panel shows the pulls of the electron (red) and muon (blue) channel, according to Equation 4.6.

One striking behaviour of the combination is the difference between the averaged cross section and the input cross sections across all $|\eta(\ell)|$-bins in the first three m_T^W-bins (200 GeV $< m_T^W <$ 600 GeV): In most bins, the averaged cross section is higher than both the measured cross sections in the electron and muon channel. This can happen due to large shifts β_j on the input cross sections, which cause a large shift in the input measurements before the average is calculated (see Equation 4.4). This observation is most pronounced in the second m_T^W-bin in the ℓ^--channel and extends up to $\sim 20\%$. Such an overall shift could by triggered by individual bins with poor agreement between the input measurements. Since these bins have relative large differences between electron and muon channel ($\sim 20\%$), large shifts are needed to correct this differences. However, such shifts usually have also a substantial effect in the other bins. Consequently, an overall shift on the input cross sections is observed. If the average between those shifted cross sections is calculated, the combined cross section can become larger than both of the (unshifted) input measurements. Furthermore, the differences between electrons and muons

increase in the last two m_T^W-bins. It can be seen, that this behaviour is more pronounced at higher $|\eta(\ell)|$, i.e. the region $2.0 < |\eta(\ell)| < 2.4$. A comparison with the unfolded cross section in Figure 3.8 shows that these are bins, where the muon channel deviates significantly from the MC prediction.
These observations are also supported by the pulls of the central values, which are much higher than for the combination in m_T^W. Some bins show a pull $\gtrsim 2$. Moreover, the signs of these large pulls are fluctuating, e.g in the last two $|\eta(\ell)|$-bins ($2.0 < |\eta(\ell)| < 2.4$) of the first m_T^W-bin (200 GeV $< m_T^W <$ 300 GeV) in the ℓ^+-channel. Because of the magnitude of theses pulls and the fact that they are located in a region with small statistical uncertainties, this cannot be explained by statistical fluctuations. This may be due to the fact that the shapes of the systematic uncertainties do not fit very well to the disagreements between the electron and muon channel. Since the quadratic behaviour of the minimised χ^2-function (see Equation 4.1) prefers many small to fewer large deviations, shifts are also introduced, when they add new (smaller) discrepancies, while reducing the large ones.
The corresponding systematic shifts are shown in Figure 4.6a. In contrast to the 1D-combination, several shifts greater than 1σ are visible here. Most striking are the shifts of the MJ MC SCALING and the TW DS systematic uncertainty, both of which are larger than 2σ. These systematic uncertainties are among the largest ones for small to intermediate m_T^W with about $\sim 5\%$ on the cross section (see Figure A.15+A.19 in the appendix). In addition, the MJ EL MET and the EG SCALE L1GAIN also have substantial shifts larger than 1σ. In comparison to the combination in m_T^W, the shift of the MJ EL MIXMET systematic becomes smaller and changes sign. For a one-sided systematic, a negative shift correponds to a reduction of the uncertainty, since its down-variation is zero (see Equation 4.2). This behaviour indicates that the use of the mixMET-multijet-template would no longer lead to a better combination. However, the fact that most of the largest shifts are related to the fake electron background is an indication that it is not well modelled. The shift applied to the TW DS systematic suggests that the DS scheme (see Section 3.4.2) is preferred to the DR scheme, which is used by default. However, this would correspond to a shift of 1σ, while the shift of 2σ leads to a region that does not correspond to any of the schemes provided. However, it is still possible that the use of the DS scheme as default improves the agreement between electron and muon channel, since it would correspond to approximately half of the effect that is achieved with this shift. On the other hand, the TW DS systematic would be replaced by a TW DR systematic, which points in the opposite direction. Consequently, the cross section could no longer be shifted beyond the DS scheme. Due to time constraints, this study was not done within the scope of this thesis. The last systematic with a shift greater than 1σ is the MU SAGITTA RESBIAS systematic. Similar to the combination of the 1D measurement, it covers for the deviations observed at high m_T^W and high $|\eta(\ell)|$ and does not significantly affect the shift of the combined cross section at small m_T^W. Figure 4.7 shows the effects of the systematic shifts on the input measurements (see Equation 4.8). In the electron channel, the largest impacts are visible in the bin before the LAr-crack ($|\eta(\ell)| < 1.4$) and in the last $|\eta(\ell)|$-bin of the first two m_T^W-bins ($200\,\text{GeV} < m_T^W < 425\,\text{GeV}$). The shifts of the MJ MC SCALING, MJ EL MET and EG SCALE L1GAIN systematics are pronounced in these single bins. The multijet systematics cause the largest shift in the bin before the LAr-crack ($1.2 < |\eta(\ell)| < 1.4$) and a slightly smaller shift in the last $|\eta(\ell)|$-bin. In contrast, the effect of EG SCALE L1GAIN is greatest in the last $|\eta(\ell)|$-bin. Considering the differences between the theory prediction and the unfolded results in the electron channel in Figure 3.8a and Figure 3.8b, these shifts are plausible as they try to cover exactly these deviations. The TW DS systematic causes large shifts at small $|\eta(\ell)|$, which decrease for $|\eta(\ell)| > 1.2$. The overall effect on the cross section is positive (in an order of $\sim$ 5%-10%), which matches to the expectations arising from the general shift of the averaged cross section.

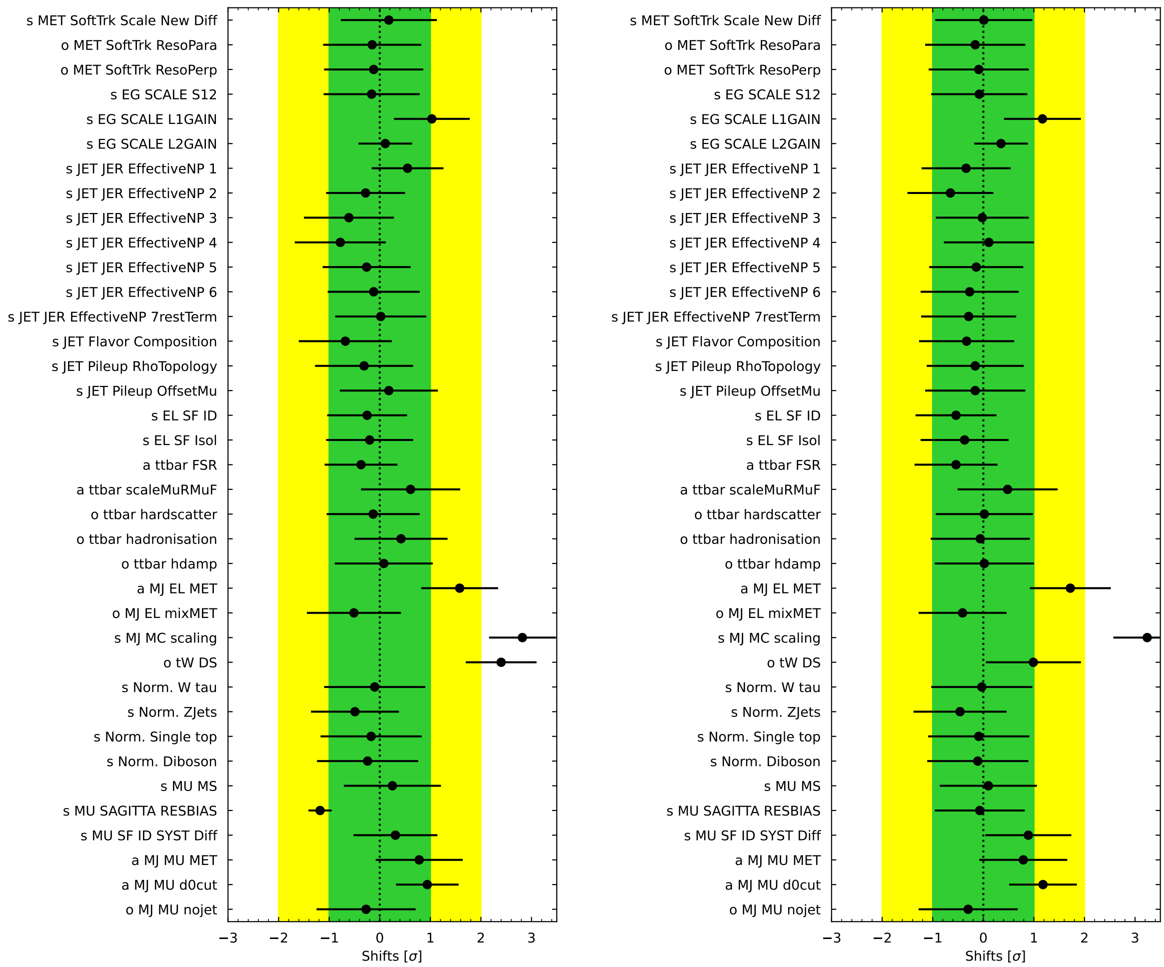

a) $(\ell^+ + \ell^-)$-channel **b)** $\ell^{\pm}$-channel

Figure 4.6: Systematic shifts β_j for the charge correlated combination of ℓ^+- and ℓ^--channel (a)) and the combination of the $\ell^{\pm}$-channels (b)) in $m_T^W \otimes |\eta(\ell)|$. The error bars represent the reduction of the uncertainties by the combination.

The effects in the muon channel are not as extremely pronounced in single bins as in the electron channel. At low to intermediate m_T^W and small $|\eta(\ell)|$ the most dominant systematics are the multijet systematics and the TW DS systematic. They shift the cross section upwards by about 5%-10% (μ^+-channel) and 10%-15% (μ^--channel). This is also in line with what is expected from the total shift of the combined cross section. At high m_T^W and high $|\eta(\ell)|$, by far the most dominant shift is due to the MU SAGITTA RESBIAS systematic. It extends up to $\sim -30\%$ in the μ^--channel and $\sim +35\%$ in the μ^+-channel for $1.8 < |\eta(\mu)| < 2.4$ and $900\,\text{GeV} < m_T^W < 2000\,\text{GeV}$. This systematic shift thus tries to correct for the deviations between unfolded and prediction observed at high m_T^W and high $|\eta(\ell)|$ in the μ-channel (see Figure 3.8c and Figure 3.8d).

Analogous to the 1D-combination, an average was also calculated for the summed $\ell^{\pm}$-channel (Figure 4.5c). This fit gives a χ^2/NDF of 66.21/40. As can be seen from the χ^2-probability of 0.57%, this indicates a worse agreement than in the simultaneous combination of the ℓ^+- and the ℓ^--channel. Thus, the most dominant issues are not coming due to effects that are anti-correlated between the two charges and do not cancel out in the summed channel.
This is also underlined by the pulls of the central values which are larger than the pulls in the

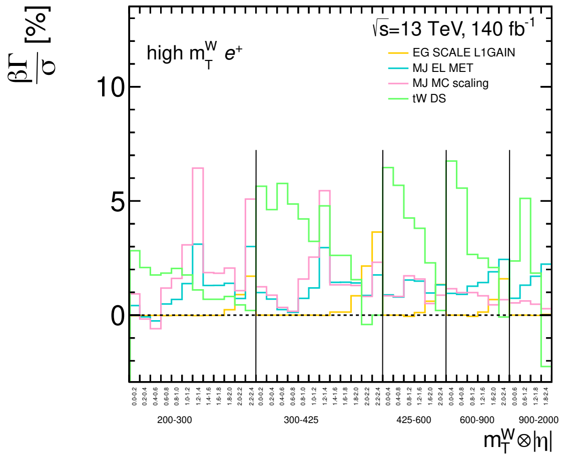

a) e^+-channel

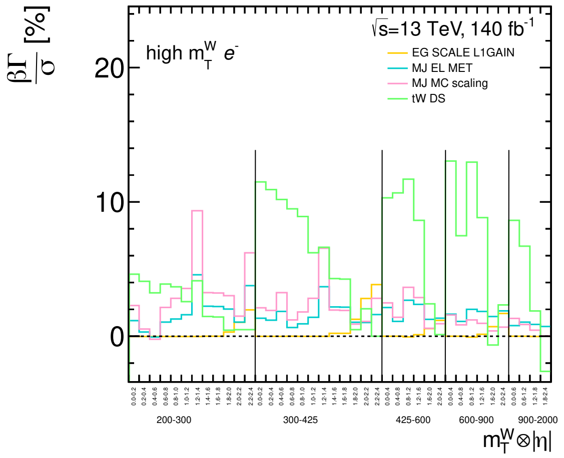

b) e^--channel

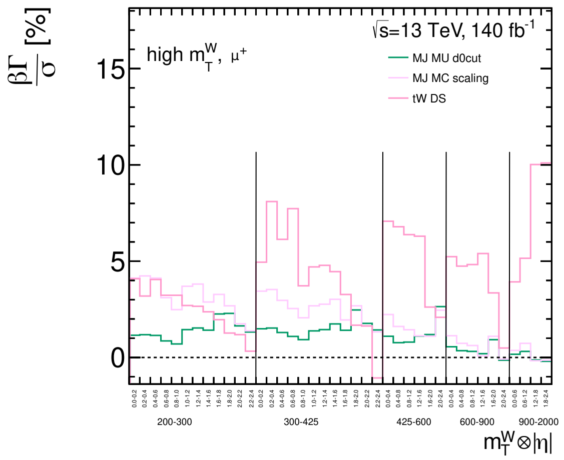

c) μ^+-channel

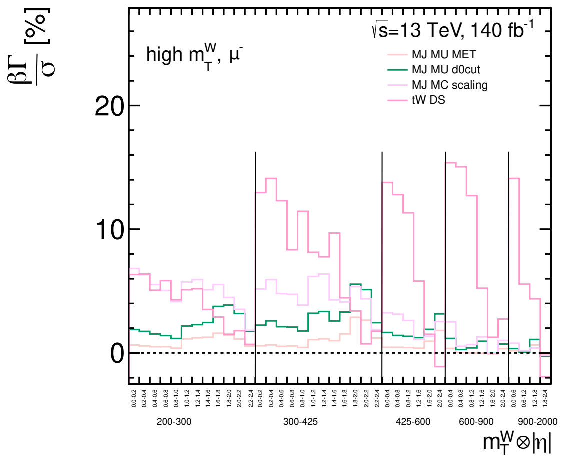

d) μ^--channel

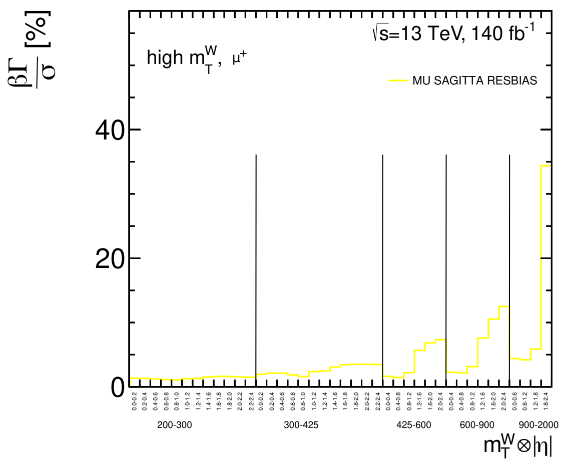

e) μ^+-channel - MU SAGITTA RESBIAS

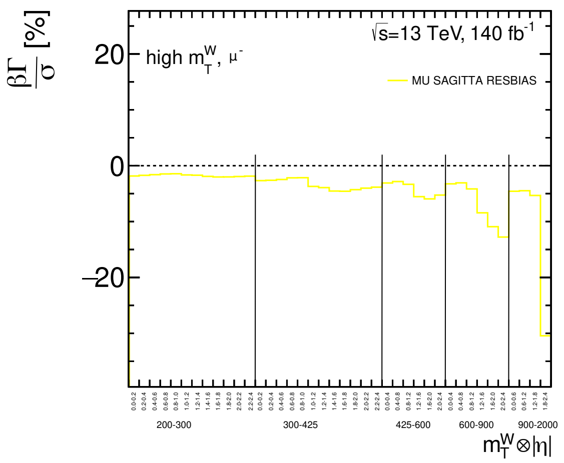

f) μ^--channel - MU SAGITTA RESBIAS

Figure 4.7: Effect of the systematic shifts normalised to the input cross sections in %, for the charge correlated fit of ℓ^+- and ℓ^--channel. Shown are only those systematics, with an effect of at least 0.5% in at least one bin in the given channel. For better clarity, the effect of the MU SAGITTA RESBIAS systematic is shown in an extra plot.

charge-separated combination and extend up to more than 3. An exception of this behaviour is observed in the last m_T^W-bin, where the pulls in the $\ell^\pm$-channel are smaller. Since the discrepancies at high m_T^W are triggered by the charge-anti-correlated sagitta bias correction, this is expected.

Furthermore, this holds for the systematic shifts (Figure 4.6b) too. While the shift of the MU SAGITTA RESBIAS systematic is reduced close to zero, the shifts of the multijet systematics are increased. The MJ MC SCALING shift even extends to more than 3σ. A final interesting behaviour is shown by the TW DS systematic. Its shift reduces close to 1σ, which, as mentioned above, corresponds exactly to the use of the DS scheme. This suggests that at least a part of the previous TW DS-shift are caused by side effects due to charge correlation and that the DS scheme may be more suitable for this analysis.

The effects on the input cross sections of the $e^\pm$- and the $\mu^\pm$-channel are shown in Figure 4.8. In principle, the same behaviour can be observed as in the charge-correlated fit, except for the MU SAGITTA RESBIAS systematic, which is no longer relevant.

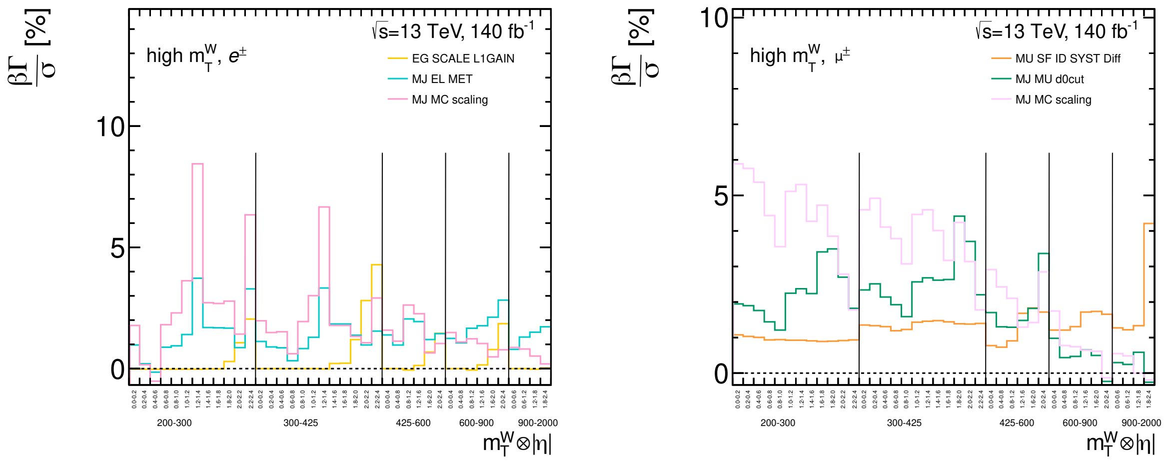

a) $e^\pm$-channel **b)** $\mu^\pm$-channel

Figure 4.8: Effect of the systematic shifts normalised to the input cross sections in %, for the fit in the $\ell^\pm$-channel. Shown are only those systematics, with an effect of at least 0.5% in at least one bin in the given channel.

Overall, the combination of the double-differential electron and muon channel measurements shows relative good agreement. However, some systematic uncertainties are significantly shifted during the fit. This leads to the fact that the averaged cross section is larger than both electron and muon channel measurements.

4.5 Combinations in different phase spaces

In contrast to the combination of the single-differential measurements, large shifts are observed in the 2D combination. To understand whether these large shifts are caused by individual regions or by correlations between different regions in $|\eta(\ell)|$ and m_T^W, several studies were carried out. Thereby, the considered phase space was varied in different ways. At first, the total phase space is decorrelated in the lepton charges, in m_T^W and in $|\eta(\ell)|$. Furthermore, individual bins are excluded from the combination to test their impact on the obtained systematic shifts. Lastly, the dataset is divided into different periods, which were combined separately.

4.5.1 Charge-decorrelated combination

First, the effects of the correlation between the different lepton charges were investigated. Therefore, the combination was done decorrelated between charges, i.e. two separate fits were performed, one for each charge. The resulting averaged cross sections are given in Figure 4.9. Figure 4.10 shows the most important systematic shifts, while a complete overview of all systematics shifts can be found in the appendix (Figure B.1).

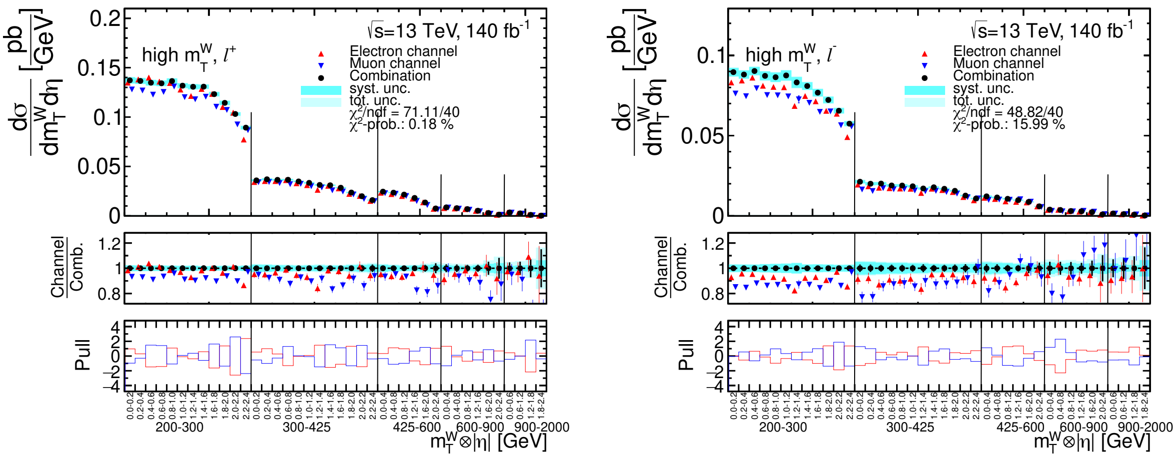

a) ℓ^+-channel **b)** ℓ^--channel

Figure 4.9: Averaged cross section (black) in $m_T^W \otimes |\eta(\ell)|$ together with the input cross sections of electron (red) and muon (blue) channel for the charge-decorrelated combination. The blue (light blue) uncertainty band gives the systematic (total) uncertainty. The error bars represent the statistical uncertainty. The middle panel shows the ratio with respect to the combined cross section. The bottom panel shows the pulls of the electron (red) and muon (blue) channel, according to Equation 4.6.

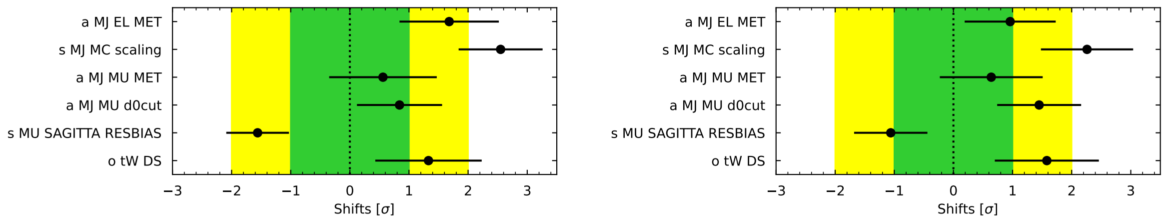

a) ℓ^+-channel **b)** ℓ^--channel

Figure 4.10: Important systematic shifts β_j for the charge decorrelated combination of ℓ^+- (a)) and ℓ^--channel (b)) in $m_T^W \otimes |\eta(\ell)|$. The error bars represent the reduction of the uncertainties by the combination. A complete overview of all systematic shifts are shown in the appendix in Figure B.1.

The shift of the averaged cross section with respect to the input cross sections as seen in the middle panel is more pronounced in the ℓ^--channel than in the ℓ^+-channel. However, the χ^2/NDF of 48.82/40 corresponding to a χ^2-probability of 15.99% shows that the agreement is much better than for a ℓ^+ final state (71.11/40, 0.18%). Thus, the systematic uncertainties can correct the differences between electron and muon cross section measurements more accurately in the ℓ^--channel. Both fits provide a smaller total shift of the combined cross section than the charge correlated average. Consequently, the systematic shifts are at least partly driven by the correlation between the charges. The fact that the cross sections are still significantly shifted shows that the origin of the large systematic shifts is an issue in both channels in a similar way. Furthermore, the shifts of the main systematics also show a slightly different behaviour between the two charges. Comparing Figure 4.10a and Figure 4.10b, it can be seen that the shifts of MJ EL MET and MJ MC SCALING are smaller for a negatively charged lepton, while in particular the shift of MJ MU D0CUT is enlarged. This suggests that the systematic uncertainties of the muon channel multijet fit better to the differences between electrons and muons for a ℓ^- final state. In addition, the shift of the TW DS systematic is slightly larger in the ℓ^--channel. Combined with the fact that the uncertainty is larger for a ℓ^- final state, this explains the larger shift of the combined cross section, especially in the second m_T^W-bin. Finally, the shift of the MU SAGITTA RESBIAS systematic is larger for a ℓ^+ than than a ℓ^- final state. There are two possible explanations for this: First, the systematic in the μ^+-channel is simply smaller than in the μ^--channel. Therefore, a larger shift is required to achieve the same effect on the cross section. On the other hand, diverging trends between the e^+- and μ^+-channels are observed for $1.2 < |\eta(\ell)| < 2.4$ in the last two m_T^W-bins. For this reason, a large shift of the MU SAGITTA RESBIAS systematic is needed to correct for the non perfect sagitta bias correction.

Overall, these combinations show that the disagreements between electrons and muons are much better covered by the systematic uncertainties for a negatively charged lepton believing the large difference in the χ^2 (71.11 vs. 48.82). However, there are in principle discrepancies in both channels that trigger systematic shifts in the combination. The correlation between the charges then causes a further increase of these shifts.

4.5.2 Combination decorrelated per m_T^W-bin

Since the measurement in $m_T^W \otimes |\eta(\ell)|$ is two-dimensional, correlations in both $|\eta(\ell)|$ and in m_T^W play a role in the default 2D combination. To separate and study these correlations, the averaging was further decorrelated in m_T^W: Separate fits were performed for the first m_T^W-bin (200 GeV $< m_T^W <$ 300 GeV), the second m_T^W-bin (300 GeV $< m_T^W <$ 425 GeV) and the last three m_T^W-bins (425 GeV $< m_T^W <$ 2000 GeV). Because a sufficient number of bins is important for a reasonable combination, the latter was not further decorrelated. Correlations between the lepton charges were taken into account to keep things close to the nominal combination. The resulting averaged cross sections are shown in Figure 4.11 with the corresponding systematic shifts in Figure B.2 in the appendix. An overview of the largest systematic shifts is given in Figure 4.12.

The agreement between electron and muon channel is strongly m_T^W-dependent. This is particularly evident from the χ^2-probability, which increases with larger m_T^W (0.24%/3.70%/10.74%). Thereby, the probability for the combination in the second m_T^W-bin is of the same order as for the combination over the entire phase space (2.83%), while the probabilities for the combination in the first m_T^W-bin and the last three m_T^W-bins are significantly lower and higher, respectively. Furthermore, the total shift of the averaged cross section with respect to the input cross sections is smaller for all sub-spaces than for the total phase space. In the second m_T^W-bin for a negatively charged lepton, this effect is strongest. It can be identified with the shift of the TW DS systematic, which mainly drives the shift of the total cross section in this region see

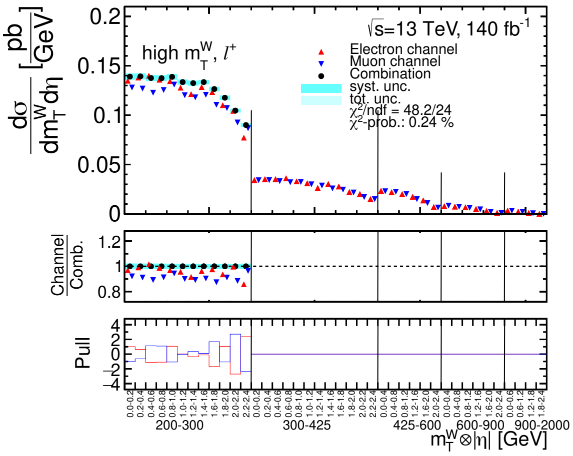

a) ℓ^{+}-channel 200 GeV $< m_T^W <$ 300 GeV

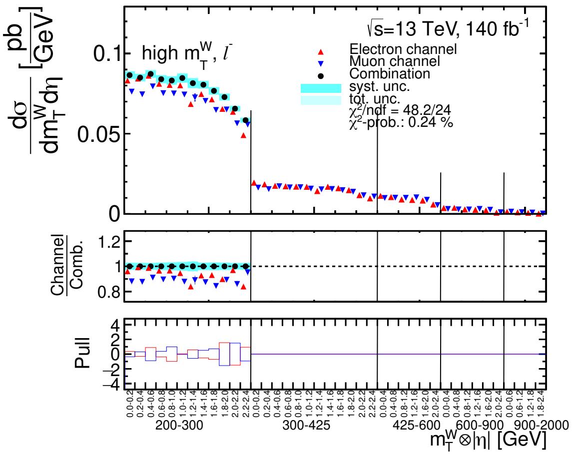

b) ℓ^{-}-channel 200 GeV $< m_T^W <$ 300 GeV

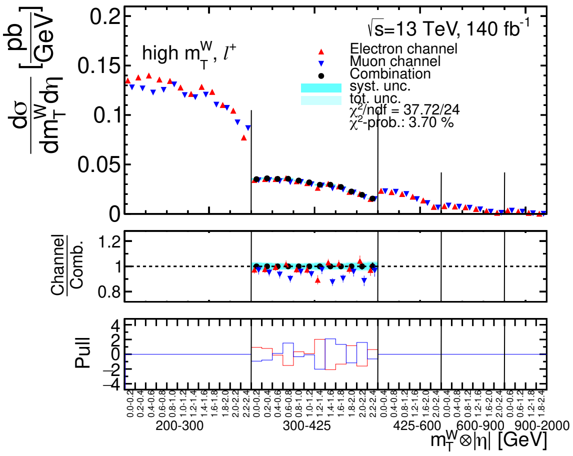

c) ℓ^{+}-channel 300 GeV $< m_T^W <$ 425 GeV

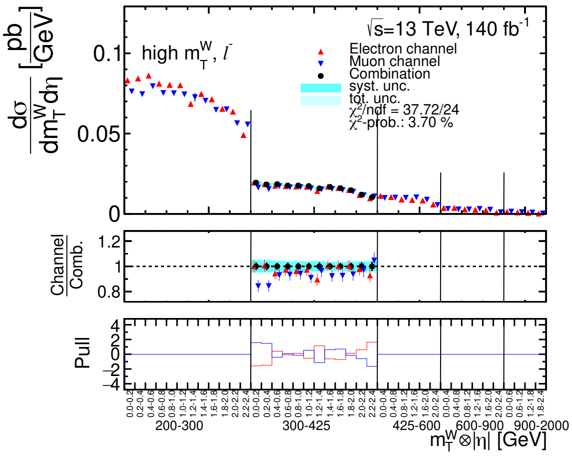

d) ℓ^{-}-channel 300 GeV $< m_T^W <$ 425 GeV

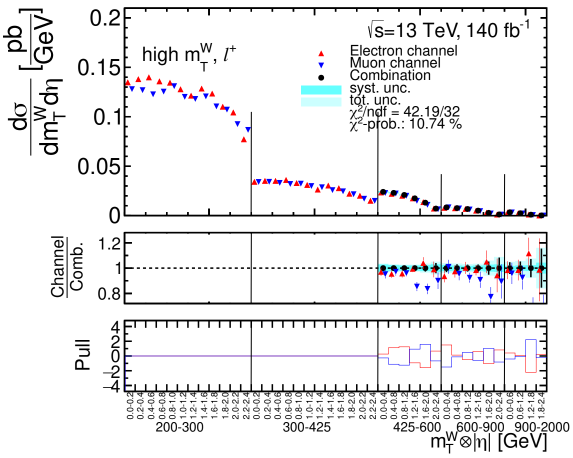

e) ℓ^{+}-channel 425 GeV $< m_T^W <$ 2000 GeV

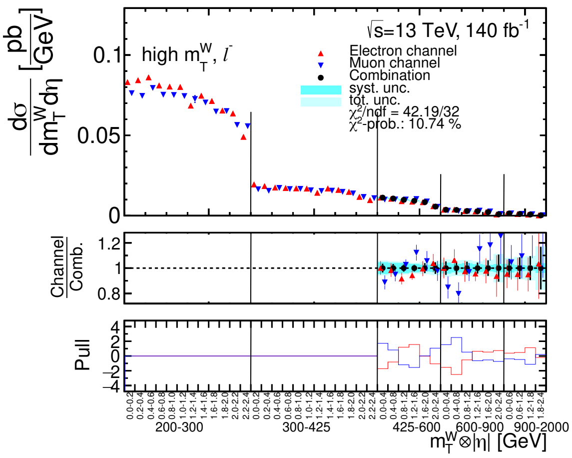

f) ℓ^{-}-channel 425 GeV $< m_T^W <$ 2000 GeV

Figure 4.11: Averaged cross section (black) in $m_T^W \otimes |\eta(\ell)|$ together with the input cross sections of electron (red) and muon (blue) channel for the combination per m_T^W-bin. The blue (light blue) uncertainty band gives the systematic (total) uncertainty. The error bars represent the statistical uncertainty. The middle panel shows the ratio with respect to the combined cross section. The bottom panel shows the pulls of the electron (red) and muon (blue) channel, according to Equation 4.6.

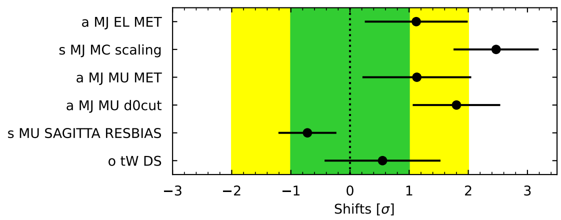

a) 200 GeV $< m_T^W <$ 300 GeV

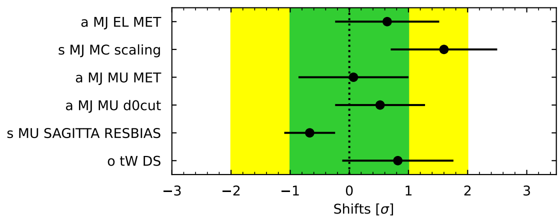

b) 300 GeV $< m_T^W <$ 425 GeV

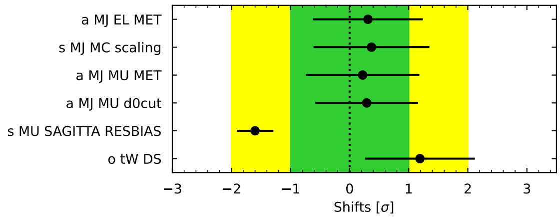

c) 425 GeV $< m_T^W <$ 2000 GeV

Figure 4.12: Important systematic shifts β_j for the combination in $m_T^W \otimes |\eta(\ell)|$ separated per m_T^W-bin. The error bars represent the reduction of the uncertainties by the combination. All systematic shifts are shown in the appendix in Figure B.2.

Figure 4.7d. Since its shift is reduced by $\sim 1.5\sigma$ compared to the combination over the whole phase space, the total shift of the combined cross section is also reduced with respect to the default combination. The systematic shifts show a different behaviour for the three sub-regions. Comparing the shifts in the first and second m_T^W-bin, i.e. Figure 4.12a and Figure 4.12b, their structure is similar. However, the absolute magnitude of the shifts of the shown multijet systematics is about $\sim 1\sigma$ larger in the first m_T^W-bin. Probably this is an important part of the explanation of the higher χ^2/NDF in the first m_T^W-bin. Firstly, larger shifts β_j directly increase the χ^2, because of the term $\sum_{j=1}^{N_S} \beta_j^2$ in Equation 4.1. Secondly, larger shifts are a consequence of larger deviations between the initial measurements.
For the combination of the last three m_T^W-bins, the shifts of the multijet systematics are close to zero and thus do not significantly shift the averaged cross section. The most dominant shift in this range is due to the MU SGAITTA RESBIAS systematic. This is also to be expected as it covers for the sagitta bias correction, which is particularly important at large $p_T(\mu)$ and hence large m_T^W.
Finally, the TW DS shift is reduced to $\sim 1\sigma$, compared to the previously observed shift of $\sim 2.4\sigma$. This shows that its shift is also driven by correlations across the different m_T^W-bins. The remaining shift of $\sim 1\sigma$ is another indication that the DS-scheme may be more appropriate for this analysis.

Summarising, the correlation in m_T^W increases the total shift of the combined cross section, since the deviations between electrons and muons are strongly dependent on m_T^W. The fact that the shapes and the magnitudes of the systematic shifts are very different in the three regions suggests that the modelling of these uncertainties over m_T^W is not optimal. However, one can also see that there are significant deviations between the electron and the muon channel in all three regions, as all fits provide significant systematic shifts.

4.5.3 Combination decorrelated at $|\eta(\ell)| = 1.0$

Similar to the decorrelation in m_T^W (Section 4.5.2), a decorrelation in $|\eta(\ell)|$ was performed, to study the effects arising from correlations between different $|\eta(\ell)|$-regions. For this purpose, two separated fits were calculated, one for $|\eta(\ell)| < 1.0$ and one $|\eta(\ell)| > 1.0$. This threshold is roughly motivated by the transition between the barrel and the end-caps of the Muon Spectrometer. Furthermore, the muon channel shows a much better agreement with the theory predictions in the barrel region of the MS, i.e. $|\eta(\mu)| < 1.0$ than in the end-caps, which is probably due to a non-perfect sagitta bias correction. For technical reasons, the separation was based on the unfolded, i.e. truth-level, $\eta(\ell)$ of the leptons. Bins covering the transition region were ignored in both combinations. Figure 4.13 and Figure 4.14 show the obtained averaged cross sections together with the main systematic shifts. An overview of all systematic shifts can be found in the appendix (Figure B.3).

The combination restricted to $|\eta(\ell)| < 1.0$ shows a very good agreement between the electron and muon channel with a $\chi^2/NDF = 35.66/30$ and the resulting probability of 21.94%. This is probably due to the fact that most of the observed deviations between the unfolded data and the theory prediction are present at $|\eta(\ell)| > 1.0$. The fact that the averaged cross section is shifted shows that there are still discrepancies present that need to be corrected. However, the good χ^2/NDF demonstrates that the systematics can compensate for these discrepancies. Another observation can be made by looking at the pulls of the central values. These are much smaller for a negatively charged lepton than for a positively charged one, as can be seen, for example, in the first m_T^W-bin. This again underlines that better agreement can be obtained in the ℓ^- channel. Moreover, most of the systematic shifts are reduced with respect to the combination considering the full phase space. Thereby, the shift of the MU SAGITTA RESBIAS systematic is close to zero. In principle, this is to be expected, since the sagitta bias correction is more important at high $|\eta(\mu)|$ values. On the other hand, the multijet systematics are important at lower $|\eta(\ell)|$ values. Consequently, a shift of these systematics has also for $|\eta(\ell)| < 1.0$ relevant effects on the cross section. Similar to the previous tests, the TW DS systematic is shifted by $\sim 1\sigma$.
A quiet different picture is shown by the combination of the region $|\eta(\ell)| > 1.0$. The χ^2/NDF of 71.32/44 is much worse than for $|\eta(\ell)| < 1.0$. This is also underlined by the χ^2-probability of 0.57%. Furthermore, the total shift of the averaged cross section is larger than for the combination at central $|\eta(\ell)|$, whereby all important systematic shifts are enlarged. In the case of the MU SAGITTA RESBIAS systematic, this behaviour can be explained by the fact that the sagitta bias correction becomes more important at high $|\eta(\mu)|$. The enlargement of the shifts of the multijet systematics indicates that they are mainly caused by disagreements at $|\eta(\ell)| > 1.0$. Since the most relevant discrepancies between the unfolded results and the theory predictions are present for $|\eta(\ell)| > 1.0$, this is also plausible. Finally, the bins with the largest pulls of the central values in the nominal combination in $m_T^W \otimes |\eta(\ell)|$ are in the region $|\eta(\ell)| > 1.0$ too. These pulls are also visible in the combination restricted to the high-$|\eta(\ell)|$ region. This is especially true for the last two $|\eta(\ell)|$-bins in the first m_T^W-bin, where large pulls in different directions are observed. These pulls are thus not (predominantly) triggered by the correlations between the barrel and the end-cap region but by deviations between the electron and muon channel, which are not well covered by the systematics.

In summary, the combination decorrelated at $|\eta(\ell)| = 1.0$ shows a much better agreement between electron and muon channel measurements for the central $|\eta(\ell)|$ region than for high $|\eta(\ell)|$. There are two reasons for this. On the one hand, the largest deviations between the

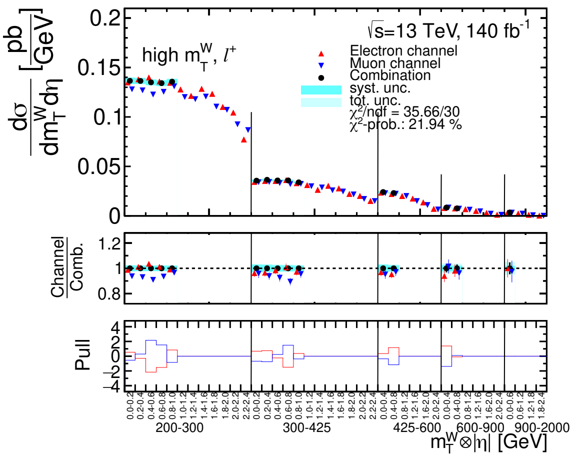

a) ℓ^+-channel $|\eta(\ell)| < 1.0$

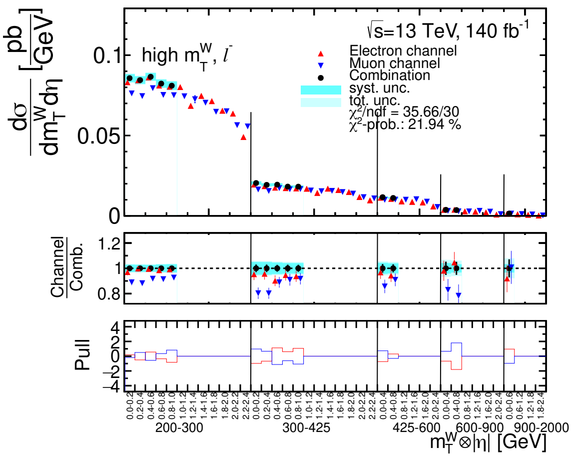

b) ℓ^--channel $|\eta(\ell)| < 1.0$

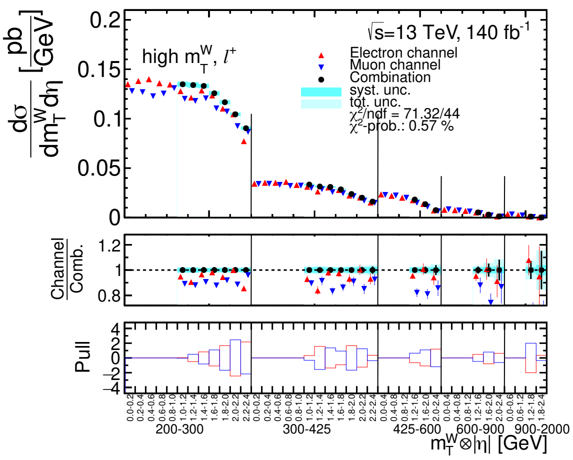

c) ℓ^+-channel $|\eta(\ell)| > 1.0$

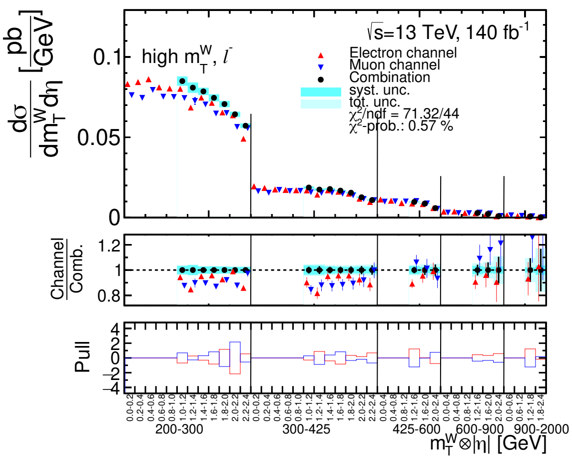

d) ℓ^--channel $|\eta(\ell)| > 1.0$

Figure 4.13: Averaged cross section (black) in $m_T^W \otimes |\eta(\ell)|$ together with the input cross sections of electron (red) and muon (blue) channel for the combination decorrelated at $|\eta(\ell)| = 1.0$. The blue (light blue) uncertainty band gives the systematic (total) uncertainty. The error bars represent the statistical uncertainty. The middle panel shows the ratio with respect to the combined cross section. The bottom panel shows the pulls of the electron (red) and muon (blue) channel, according to Equation 4.6.

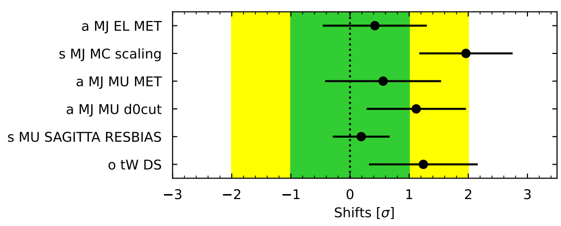

a) $|\eta(\ell)| < 1.0$

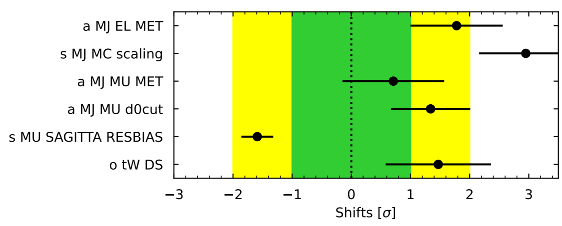

b) $|\eta(\ell)| > 1.0$

Figure 4.14: Important systematic shifts β_j for the combination in $m_T^W \otimes |\eta(\ell)|$ decorrelated at $|\eta(\ell)| = 1.0$. The error bars represent the reduction of the uncertainties by the combination. All systematic shifts are shown in the appendix in Figure B.3.

unfolded data and the theory expectation in the electron channel are observed for $|\eta(\ell)| > 1.0$. These are likely to play an important role in the shifts of the multijet systematics. On the other hand, the shift of the MU SAGITTA RESBIAS systematic is much more pronounced in the high-$|\eta(\ell)|$ region, due to a more important sagitta bias correction.

4.5.4 Removing individual bins in combination

Some individual bins, e.g. $1.2 < |\eta(\ell)| < 1.4$ and $2.2 < |\eta(\ell)| < 2.4$ in the first two m_T^W-bins in the electron channel, show substantial deviations between the unfolded data and the theory prediction. In Figure 4.7a and Figure 4.7b it was seen that these are also the bins, which are strongly shifted by the fit. It is therefore reasonable to assume that these shifts are caused by individual bins with poor agreement between data and prediction. For this reason, a combination was performed in which individual bins with such large deviations were ignored. The following bins were removed:

- 200 GeV $< m_T^W <$ 300 GeV:
  - ℓ^+: $2.0 < |\eta(\ell)| < 2.2$, $2.2 < |\eta(\ell)| < 2.4$;
  - ℓ^-: $2.0 < |\eta(\ell)| < 2.2$, $2.2 < |\eta(\ell)| < 2.4$;
- 300 GeV $< m_T^W <$ 425 GeV:
  - ℓ^+: $1.2 < |\eta(\ell)| < 1.4$, $1.4 < |\eta(\ell)| < 1.6$, $2.0 < |\eta(\ell)| < 2.2$;
  - ℓ^-: $0.0 < |\eta(\ell)| < 0.2$, $0.2 < |\eta(\ell)| < 0.4$, $1.2 < |\eta(\ell)| < 1.4$, $2.2 < |\eta(\ell)| < 2.4$;
- 425 GeV $< m_T^W <$ 600 GeV:
  - ℓ^+: $1.2 < |\eta(\ell)| < 1.6$, $1.6 < |\eta(\ell)| < 2.0$;
  - ℓ^-: $0.8 < |\eta(\ell)| < 1.2$;
- 600 GeV $< m_T^W <$ 900 GeV:
  - ℓ^+: $1.6 < |\eta(\ell)| < 2.0$;
  - ℓ^-: $1.6 < |\eta(\ell)| < 2.0$.

The results of this combination are presented in Figure 4.15. The most important shifts are shown in Figure 4.16, while an overview over all shifts can be found in the appendix (Figure B.4).

The χ^2/NDF of 64.96/64 corresponds to a $\chi^2_{red} = 1.015$. This shows a very good agreement between the electron and the muon channel after the corrections due to the systematic shifts. The χ^2-probability of 44.30% underlines this observation. Thus, these bins are the main reasons for the larger χ^2 in the nominal combination in $m_T^W \otimes |\eta(\ell)|$.
However, the main purpose of this combination was to eliminate the large systematic shifts. As it can be seen in the middle panels of Figure 4.15, the averaged cross section is still significantly shifted compared to the input cross sections. This shows that there are still large shifts needed in the combination. This is consistent with the systematic shifts shown in Figure 4.16. In particular the MJ MC SCALING and the TW DS systematic are still significantly shifted. The shifts of the MU SAGITTA RESBIAS and the MJ EL MET systematic become smaller. In the case of the MU SAGITTA RESBIAS systematic this is probably due to the removal of the $1.6 < |\eta(\ell)| < 2.0$-bin in the fourth m_T^W-bin. The shift of the MJ EL MET systematic is probably necessary to correct for the deviations at $1.2 < |\eta(\ell)| < 1.4$ and $2.2 < |\eta(\ell)| < 2.4$

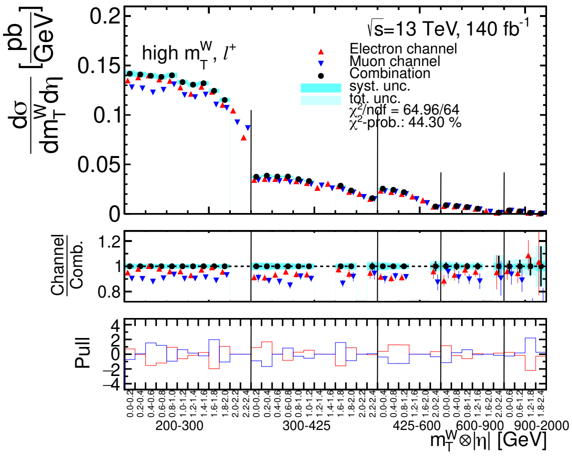

a) ℓ^+-channel

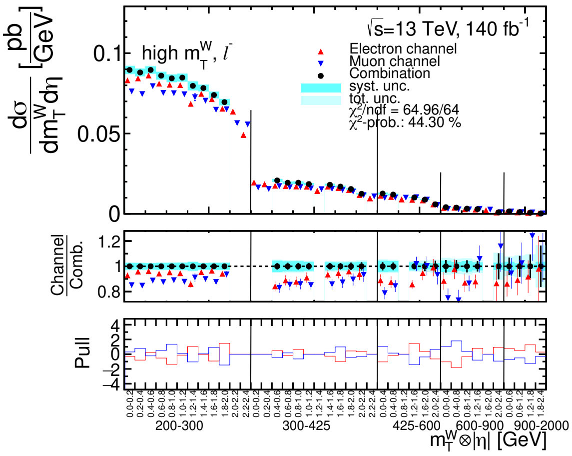

b) ℓ^--channel

Figure 4.15: Averaged cross section (black) in $m_T^W \otimes |\eta(\ell)|$ together with the input cross sections of electron (red) and muon (blue) channel for the combination when some single bins are ignored in the combination. The blue (light blue) uncertainty band gives the systematic (total) uncertainty. The error bars represent the statistical uncertainty. The middle panel shows the ratio with respect to the combined cross section. The bottom panel shows the pulls of the electron (red) and muon (blue) channel, according to Equation 4.6.

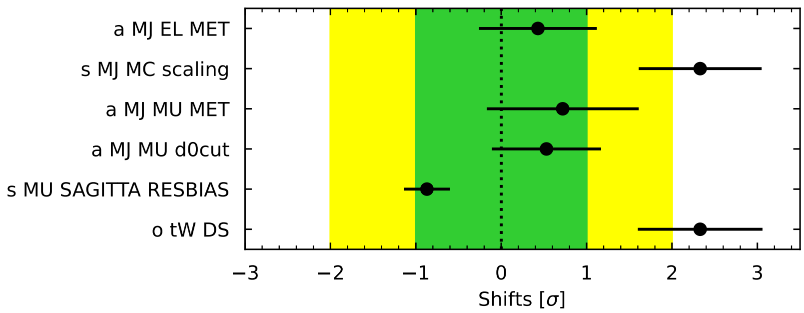

Figure 4.16: Important systematic shifts β_j for the combination in $m_T^W \otimes |\eta(\ell)|$ when some single bins are ignored in the combination. The error bars represent the reduction of the uncertainties by the combination. All systematic shifts are shown in the appendix in Figure B.4.

in the electron channel (see Figure 3.8). Removing these bins strongly reduces the shift. The deviations in the other bins are sufficiently covered by the MJ MC SCALING and the TW DS systematic.

The fact that the χ^2 of this combination is much better than for the nominal combination, shows that the removed bins are the ones with significant residual differences between electrons and muons after applying the systematic shifts. However, the large systematic shifts are also induced by bins where the deviations between data and prediction are not extremely large.

4.5.5 Combination per data taking period

The analysed dataset is divided into three different periods, corresponding to different years of data taking: mc16a for 2015 and 2016, mc16d for 2017 and mc16e for 2018. A comparison of the unfolded results separated per data taking period is shown in Figure 4.17. The unfolded result is marked with the black dots, while the red and blue lines represent the cross sections on truth and reconstruction level. The error bars correspond to the statistical uncertainties. In the bottom panel, the ratio unfolded over truth is presented. Comparing the different periods, one can see that the agreement between data and prediction is much better for mc16a than for mc16d and mc16e. In particular, the bins with the largest deviations for full Run-2 are closer to the prediction in mc16a, e.g. the last $|\eta(e)|$-bin in the shadow bin ($2.2 < |\eta(e)| < 2.4$, 150 GeV $< m_T^W <$ 200 GeV). While the deviations in these bins are in the order of $\sim 20\%$ for mac16d and mc16e, the deviations in mc16a are well below 10%. Differences between the periods may occur due to different scale factors for e.g. pileup[3] and triggers, but these are smaller than the deviations observed between the different periods. Furthermore, a bug in the reconstruction scale factor was found, which only affected mc16d and mc16e. However, its impact on the analysis was tested and found to be negligible (see Appendix C). A combination per period was performed to test the impact on the averaged cross section. This also provides a consistency test for the nominal combination, since the data from the different periods should give in principle the same results. Figure 4.18 shows the different averaged cross sections. The important shifts are given in Figure 4.19 and a complete overview of all shifts can be found in Figure B.5 in the appendix.

Comparing the obtained values of the χ^2/NDF (mc16a: 84.73/80, mc16d: 99.82/80, mc16e: 86.79/80) with those of the full Run-2 combination (105.82/80), it can be seen that all combinations per period give a better agreement between the electron and the muon channel. This can be explained especially by the larger statistical uncertainties, when using only a subset of the data. In principle, this should be accompanied by larger fluctuations that increase the χ^2 again. However, large statistical uncertainties can also cover for deviations that are not well modelled by the considered systematic uncertainties. Since the Run-2 combination results in a high χ^2 along with still large shifts, this is probably the case. The behaviour with a better agreement in mc16a is no longer seen in the combination. While the fit in mc16d shows a significantly worse χ^2/NDF than the one in mc16a, the χ^2/NDF for mc16e is similar to mc16a.
The ratio between the averaged and the input measurement shows that the averaged cross section tends to be more shifted in periods with a lower χ^2/NDF. This again underlines that the large systematic shifts in the multijet systematics, the tW DS systematic and the MU SAGITTA RESBIAS indeed improve the agreement between electrons and muons.
The main important systematic shifts are even larger in mc16d than in mc16a. The smaller total shift can be explained by more smaller shifts (see Figure B.5 in the appendix) to higher cross sections in mc16a than in mc16d. Otherwise the shifts in mc16a and mc16d are relatively similar. A quiet different behaviour can be observed in mc16e, where the systematic shifts of MJ EL MET and MJ MC SCALING are increased, while the shifts for MJ MU MET and MJ MU D0CUT are relatively close to 0.

[3]Pileup denotes the fact that several collision can take place at the same time in the ATLAS detector.

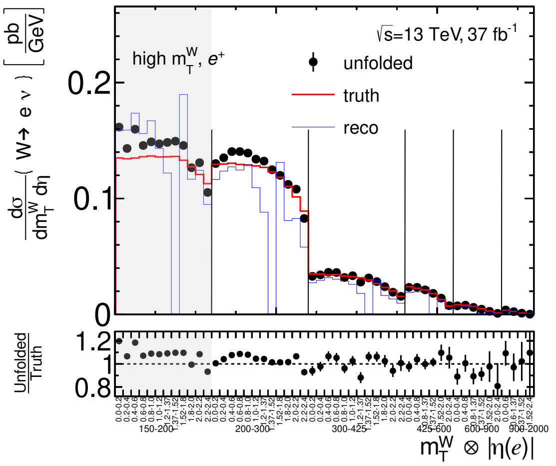

a) e^+-channel - mc16a

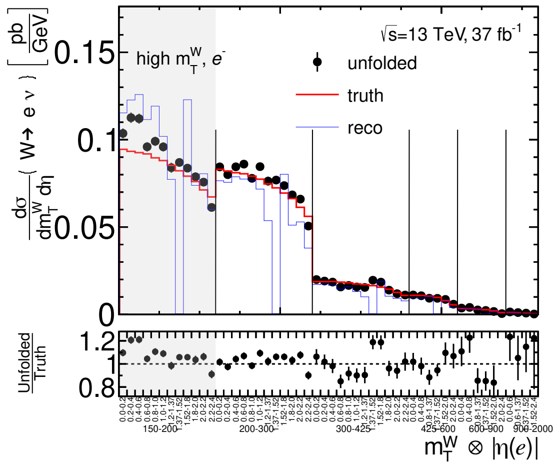

b) e^--channel - mc16a

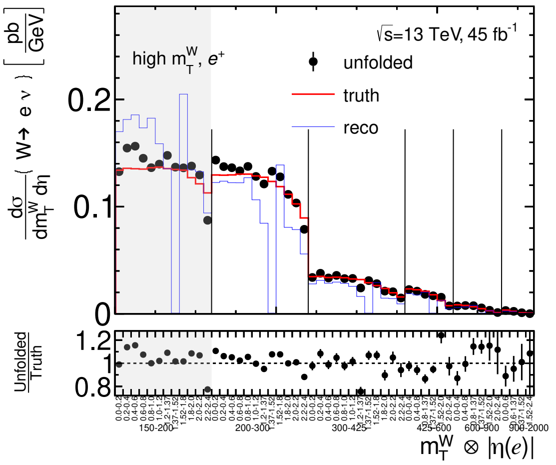

c) e^+-channel - mc16d

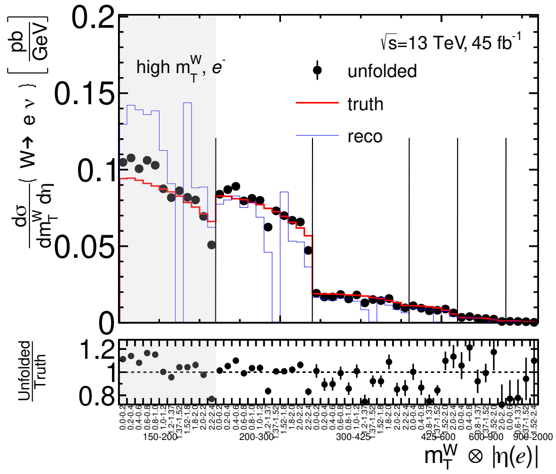

d) e^--channel - mc16d

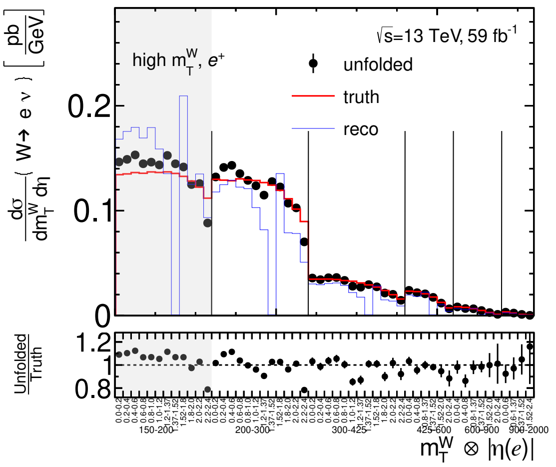

e) e^+-channel - mc16e

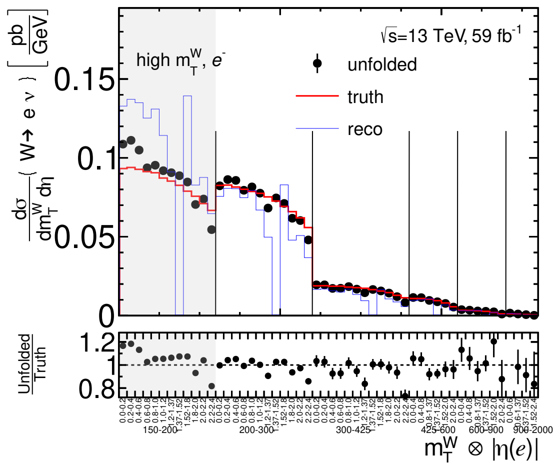

f) e^--channel - mc16e

Figure 4.17: Unfolded cross section (black) in $m_T^W \otimes |\eta(\ell)|$ together with the truth (red) and reconstruction (blue) level cross sections in the electron channel per data taking period. The bottom panel shows the ratio unfolded over truth level cross section. The uncertainty bars represent the data statistic only.

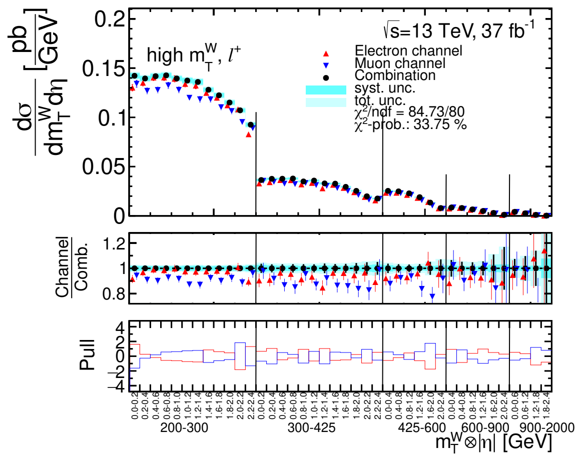

a) ℓ^+-channel - mc16a

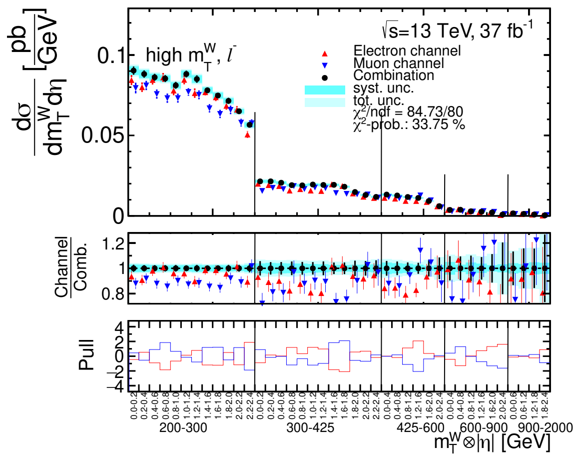

b) ℓ^--channel - mc16a

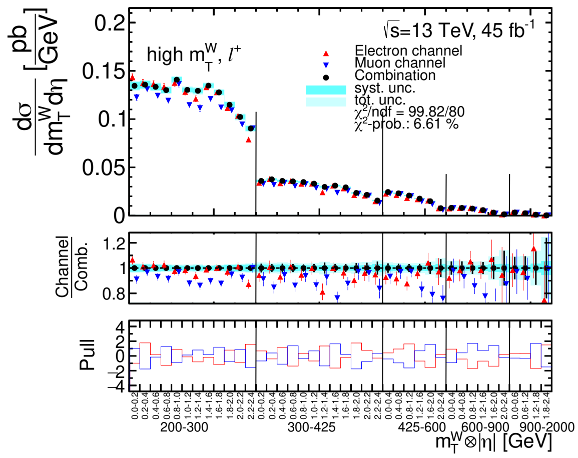

c) ℓ^+-channel - mc16d

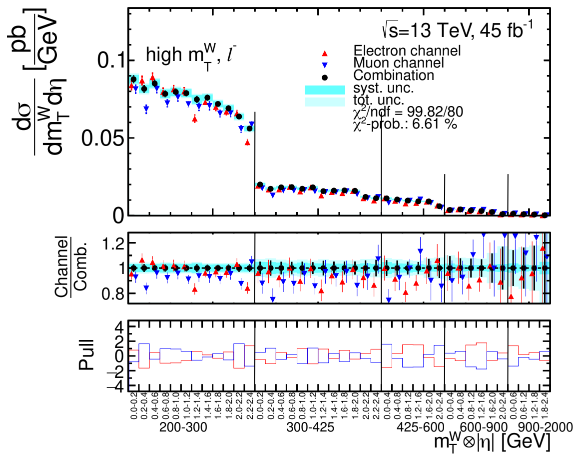

d) ℓ^--channel - mc16d

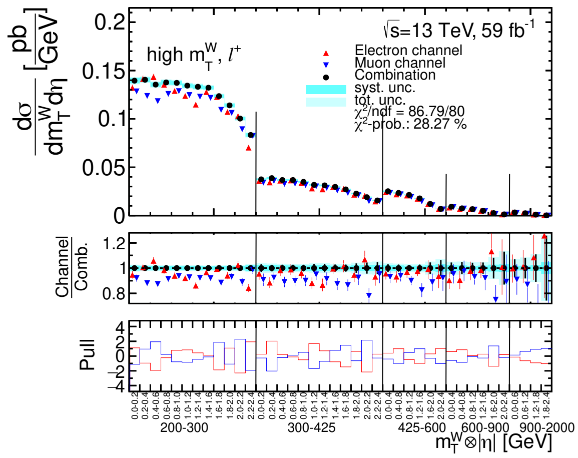

e) ℓ^+-channel - mc16e

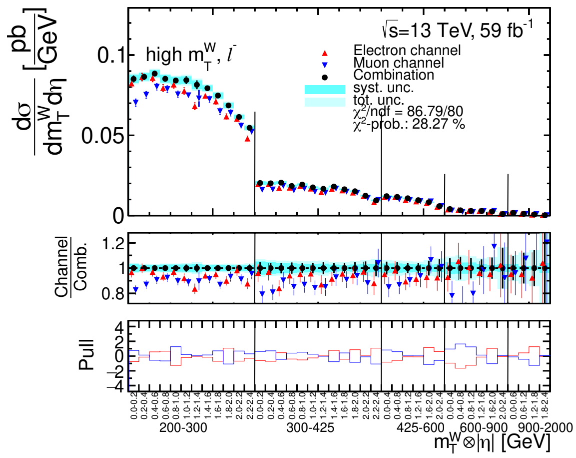

f) ℓ^--channel - mc16e

Figure 4.18: Averaged cross section (black) in $m_T^W \otimes |\eta(\ell)|$ together with the input cross sections of electron (red) and muon (blue) channel for the combination per data taking period. The blue (light blue) uncertainty band gives the systematic (total) uncertainty. The error bars represent the statistical uncertainty. The middle panel shows the ratio with respect to the combined cross section. The bottom panel shows the pulls of the electron (red) and muon (blue) channel, according to Equation 4.6.

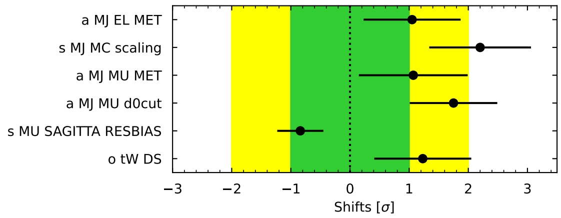

a) mc16a

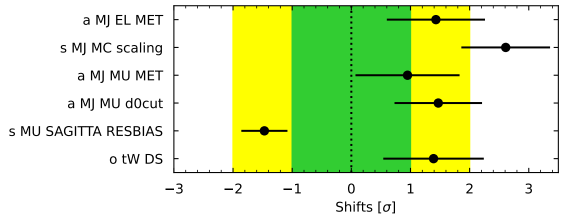

b) mc16d

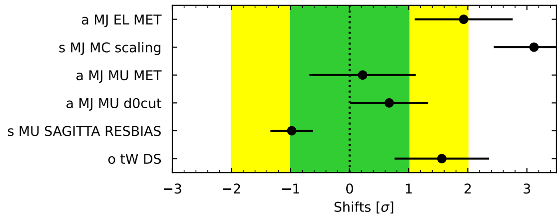

c) mc16e

Figure 4.19: Important systematic shifts β_j for the combination in $m_T^W \otimes |\eta(\ell)|$ separated per data taking period. The error bars represent the reduction of the uncertainties by the combination. All systematic shifts are shown in the appendix in Figure B.5.

No extremely large differences were found between the three periods. In particular, no period with significantly better or worse agreement between electrons and muons could be identified. While mc16d has the highest χ^2/NDF of the three periods, its shifts are relatively similar to those of mc16a. On the other hand, the combination in mc16e gives the largest shifts in the MJ MC SCALING and MJ EL MET systematic, while resulting in a still very good χ^2/NDF of 86.79/80.

4.6 Studies regarding the fake electron background

When the bins with the largest deviations between unfolded cross section and theory prediction in the electron channel were analysed, an interesting behaviour was observed. As can be seen in Figure A.6 and Figure A.7 in the appendix, the bins with a relatively low data-over-MC ratio, like e.g. $1.2 < |\eta(e)| < 1.37$ and $2.2 < |\eta(e)| < 2.4$ in the first two m_T^W-bins, the contribution of the fake leptons is significantly higher than in the neighbouring bins. Furthermore, the combination in $m_T^W \otimes |\eta(\ell)|$ results in relatively large shifts on the MJ MC SCALING and the MJ EL MET systematic. These shifts significantly reduce the fake electron background, especially in these bins, as can be seen in Figure 4.7a and 4.7b. Thus, it is reasonable to assume that the multijet estimate is not perfect especially in these particular bins. Therefore, several studies have been carried out to test the calculation of this background in the electron channel.

4.6.1 Finer $|\eta|$-binning of fake efficiencies

This study was conducted at an earlier state of the analysis, where, in particular, the tW DS systematic was not included in the combination. This systematic had a rather large effect on the combination. In addition, two bugs were found concerning the trigger scale factors and the MU SAGITTA RESBIAS systematic was decorrelated between charges, which had a smaller influence on the combination. The nominal combination before adding the tW DS systematic and correcting the trigger scale factor bugs can be found in the appendix (Appendix B.3).

One important part of the estimation of the fake electron background is the calculation of the fake efficiencies. These correspond to the probability of a fake electron, e.g. a misidentified jet, that passes the loose level to pass the tight level as well. The fake efficiencies used are binned in $|\eta(e)|$, $|\Delta\phi(e, E_T^{miss})|$ and $p_T(e)$. This binning is varied in the following. Since the large deviations in the measurement variable were observed only in $m_T^W \otimes |\eta(e)|$, but not in m_T^W, a variation of the $|\eta(e)|$-binning would probably have the biggest effect. Indeed, the $|\eta(e)|$-binning currently in use is much coarser than the reconstruction level binning. It consists of four bins dividing both the region before and after the LAr-crack into two bins of approximately equal size:

- $|\eta(e)| = [0.0, 0.6, 1.4, 2.0, 2.4]$.

A binning that is closer to the one of the measurement and provides a finer resolution in the crucial $|\eta(e)|$-regions, may have a relevant impact on the multijet estimate. A finer $|\eta(e)|$-binning was tested. It is defined via:

- $|\eta(e)| = [0.0, 0.2, 0.4, 0.6, 0.8, 1.0, 1.2, 1.37, 1.52, 1.8, 2.01, 2.2, 2.4]$.

Thereby, an empty bin was introduced covering the region around the LAr-crack, such as in the measurement binning on reconstruction level. The only difference to the reconstruction level binning is the boundary at $|\eta(e)| = 2.01$ instead of $|\eta(e)| = 2.0$. It is motivated by the end of the TRT-tracker in the Inner Detector.
If one increases the number of $|\eta(e)|$-bins, one also has to take care of the available statistics. For this reason, the number of $|\Delta(\phi(e, E_T^{miss}))|$-bins was reduced by merging bins. Thus, the applied $|\Delta(\phi(e, E_T^{miss}))|$-binnings are given by:

- default: $|\Delta(\phi(e, E_T^{miss}))| = [0.0, 0.26, 0.52, 0.78, 1.05, 1.31, 1.57, 1.83, 2.09, 2.36, 2.62, 2.88, 3.14]$,
- varied: $|\Delta(\phi(e, E_T^{miss}))| = [0.0, 1.05, 2.09, 2.62, 2.88, 3.14]$.

An example of the resulting fake efficiencies is given in Figure 4.20 for the last $|\Delta\phi|$-bin. Thereby, only the $|\eta(e)| > 1.4$-region is shown, as no major differences are observed for $|\eta(e)| < 1.4$. All other bins can be found in the appendix (see Appendix B.3). Similar to the region $|\eta(e)| < 1.4$, no large differences are observed in the high $|\eta(e)|$ range $|\eta(e)| > 2.0$ (Figure 4.20b and Figure 4.20d). Thus, the fake efficiencies do not have a large slope in $|\eta(e)|$ in this region. In contrast, such a slope in $|\eta(\ell)|$ can be observed in the region behind the LAr crack. The fake efficiencies in the interval $1.8 < |\eta(e)| < 2.01$ are larger than those for $1.4 < |\eta(e)| < 2.0$, while the efficiencies for $1.52 < |\eta(e)| < 1.8$ are smaller. This could therefore result in a significant effect on the multijet in the region $1.4 < |\eta(e)| < 2.0$. However, these bins are not the ones where the largest discrepancies between the unfolded result and the theory prediction occur.

These fake efficiencies are used to estimate the multijet background as described in Section 3.3. The resulting multijet estimates for the measurement variable $m_T^W \otimes |\eta(e)|$ are presented in Figure 4.21a and Figure 4.21b. The uncertainties shown in the ratios in the bottom panel are not reasonable, since the two estimates are statistically fully correlated. In general, the effects observed in the fake efficiencies are transferred to the multijet itself. In most bins, the multijet varies within 5%, which would lead to a probably negligible effect on the cross section, since the overall multijet contribution is only in the order of 5%. Most of the larger deviations are found in bins with a very small multijet contribution, i.e. at high transverse masses and low pseudorapidities. Apart from this, the two $|\eta(e)|$-bins behind the LAr-crack also show larger

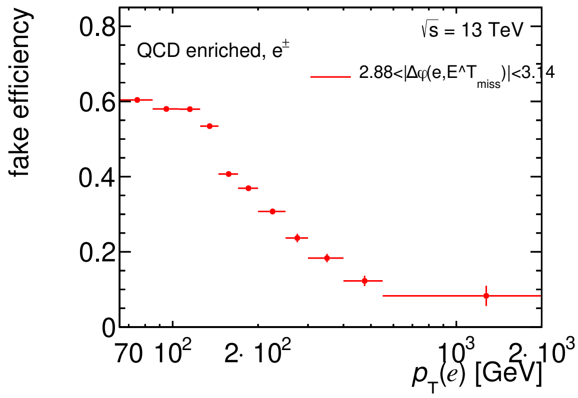

a) nominal: $1.4 < |\eta(\ell)| < 2.0$

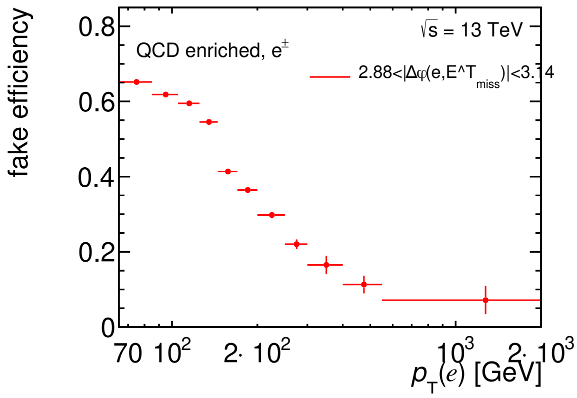

b) nominal $2.0 < |\eta(\ell)| < 2.4$

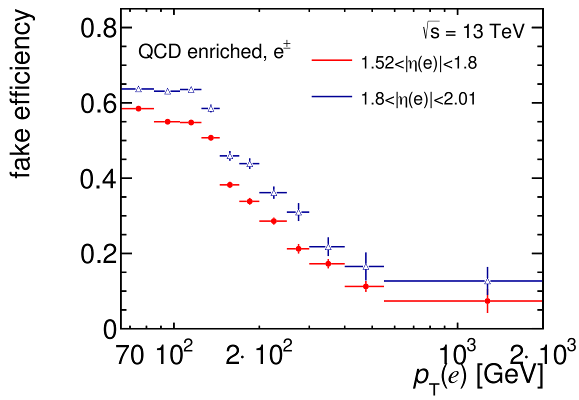

c) finer bins: $1.4 < |\eta(\ell)| < 2.01$

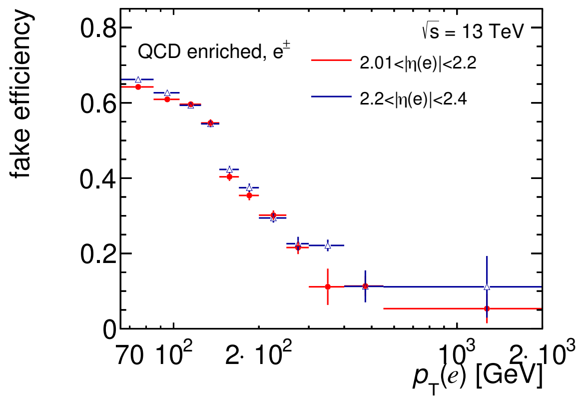

d) finer bins: $2.01 < |\eta(\ell)| < 2.4$

Figure 4.20: Fake efficiencies in the nominal (top row) and the finer (bottom row) $|\eta|$-binning. Only the last $|\Delta\phi|$-bin ($2.88 < |\Delta(\phi(e, E_T^{miss}))| < 3.14$) and the region $|\eta(e)| > 1.4$ is shown. All other bins can be found in the appendix (Appendix B.3).

changes in the order of $\sim 10\%$. However, this is consistent with the calculated fake efficiencies. Since the new efficiencies are smaller for $1.52 < |\eta(e)| < 1.8$ and larger for $1.8 < |\eta(e)| < 2.0$, a smaller ($1.52 < |\eta(e)| < 1.8$) and larger ($1.8 < |\eta(e)| < 2.0$) multijet background should be calculated, respectively. This is exactly the behaviour that can be observed in the comparisons. Furthermore, the multijet is enhanced by about 5% in the last $|\eta(e)|$-bin of the shadow bin. However, this effect is less pronounced in the measurement bins and would further reduce the unfolded cross section. In contrast, another observation is made which is more pronounced for $m_T^W > 200$ GeV. The multijet contribution in the bin before the LAr crack is reduced with respect to the nominal multijet background, by $\sim 10\%$. This increases the unfolded cross section and thus probably improve the agreement between data and prediction in this bin. The influence of the finer $|\eta(e)|$-binning on the statistical uncertainty of the multijet background was also tested and found to be negligible. This can be seen by comparing Figure B.20 and Figure B.21 in the appendix.
Figure 4.21c and Figure 4.21d compare the resulting unfolded cross sections using the two multijet estimates. As can be seen, the differences are well below 1% in most of the bins. The largest differences are observed in the region $1.2 < |\eta(e)| < 2.0$ with $\lesssim 5\%$. Here, the cross section increases in the interval $1.2 < |\eta(e)| < 1.8$, while it decreases for $1.8 < |\eta(e)| < 2.0$. This improves the agreement between data and theory especially in the bin before the LAr-crack ($1.2 < |\eta(e)| < 1.4$). However, the agreement in the bins after the crack ($1.4 < |\eta(e)| < 1.8$) was relatively good with the nominal multijet and deteriorates when the varied multijet is applied.

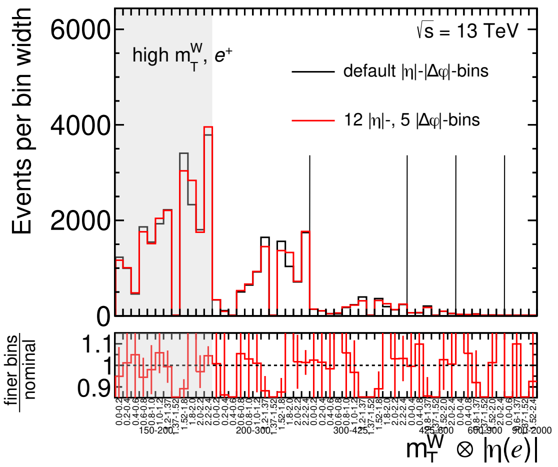

a) multijet - e^+-channel

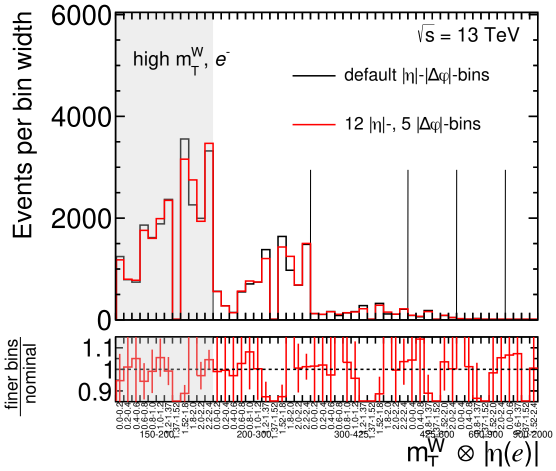

b) multijet - e^--channel

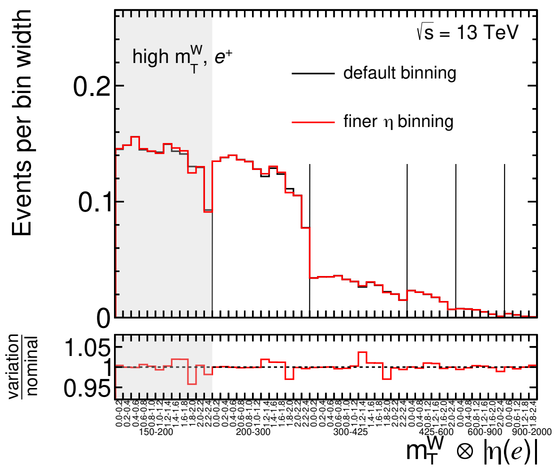

c) unfolded - e^+-channel

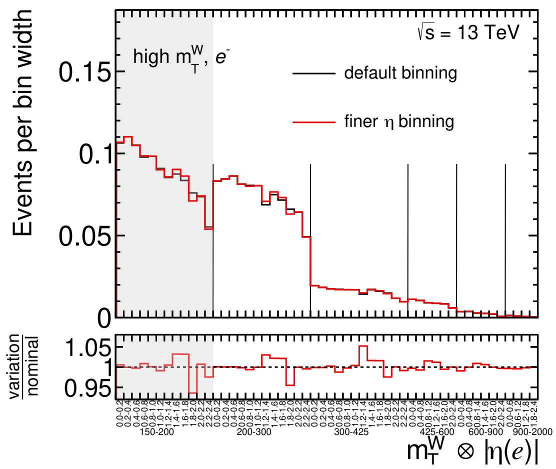

d) unfolded - e^--channel

Figure 4.21: Comparisons of the obtained multijet (top row) and the unfolded results (bottom row) for the e^+- (left column) and the e^--channel (right column), respectively. The multijet corresponding to the finer $|\eta(e)|$-binning is shown in red and the default multijet is shown black. The uncertainties shown in the bottom panels of (a) and (b) are not reasonable, since the two estimates are statistically fully correlated.

In addition, the deviation observed at $1.8 < |\eta(e)| < 2.0$ is further increased by the use of the finer binned fake efficiencies.

To check, whether the new efficiencies help in the electron-muon agreement, a combination was also performed for each of the multijet estimates. This involved recalculating the electron multijet systematics using the different binning of the fake efficiencies. The resulting averaged cross sections are presented in Figure 4.22, the main systematic shifts in Figure 4.23. All other shifts can be found in the appendix (Figure B.22).
In general, there are no major differences, when comparing the two combinations. The χ^2/NDF of 132.9/80 for the combination with the varied multijet is slightly higher than for the nominal combination ($\chi^2/NDF = 128.91/80$). Thus, the increased differences behind the LAr-crack have a greater impact than the improved agreement before the crack. This is also plausible, since the original deviation of up to 20% is only slightly reduced by using the varied multijet. A similar picture emerges by the pulls of the central values, which are very similar between the

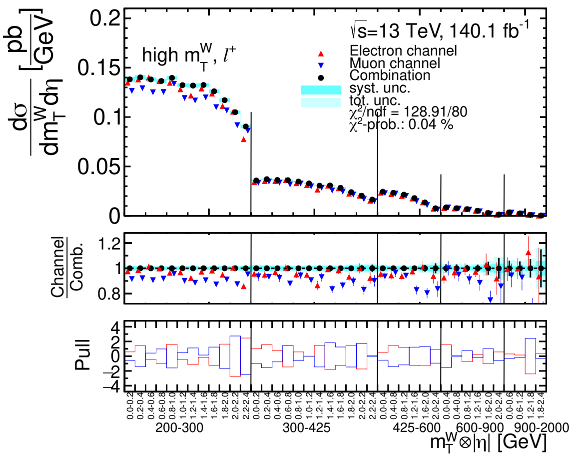

a) nominal multijet

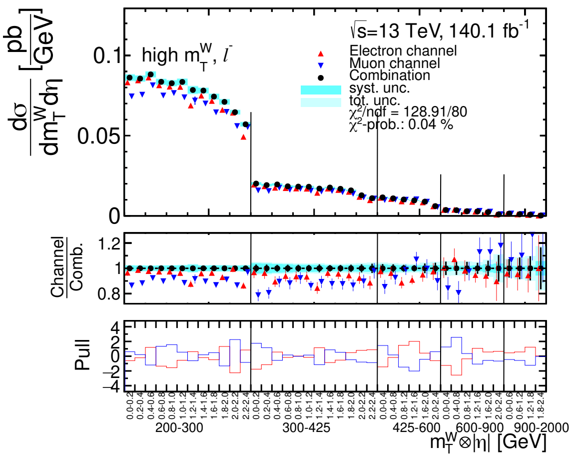

b) nominal multijet

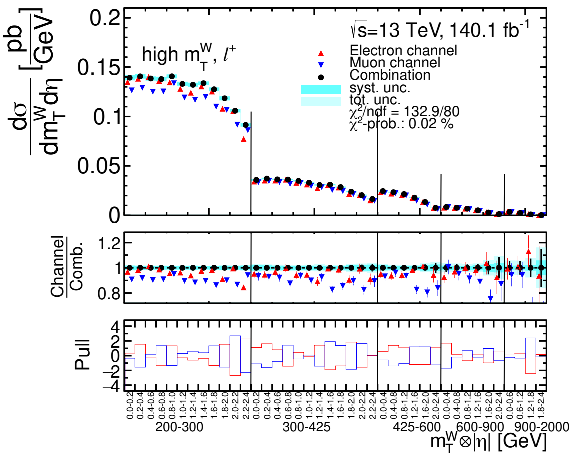

c) varied multijet

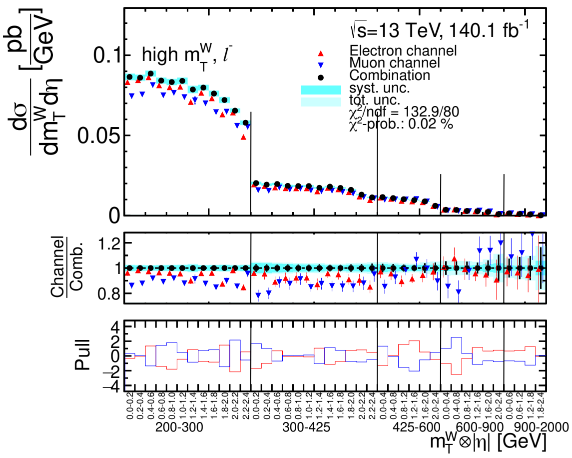

d) varied multijet

Figure 4.22: Averaged cross section (black) in $m_T^W \otimes |\eta(\ell)|$ together with the input cross sections of electron (red) and muon (blue) channel for the combination using the nominal or the varied electron multijet. The blue (light blue) uncertainty band gives the systematic (total) uncertainty. The error bars represent the statistical uncertainty. The middle panel shows the ratio with respect to the combined cross section. The bottom panel shows the pulls of the electron (red) and muon (blue) channel, according to Equation 4.6.

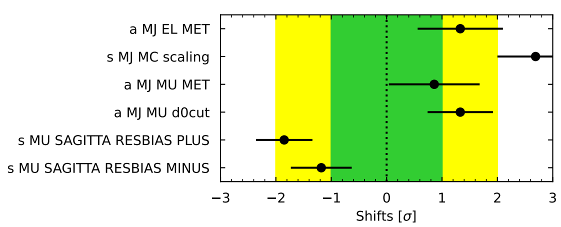

a) nominal multjet

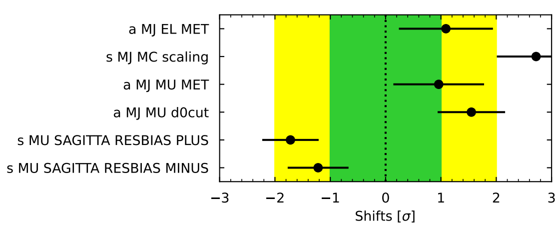

b) varied multijet

Figure 4.23: Important systematic shifts β_j for the combination in $m_T^W \otimes |\eta(\ell)|$ using the nominal or the varied electron multijet. The error bars represent the reduction of the uncertainties by the combination. All systematic shifts are shown in the appendix in Figure B.22.

two different combinations. Thus, no significant improvements could be achieved. Finally, the systematic shifts are also very similar.

In conclusion, the finer $|\eta(e)|$-binning of the fake efficiencies did not improve either the combination or the unfolded results. Therefore, it was decided to keep the previous binning for the fake efficiencies.

4.6.2 Different loose level in the Matrix Method

Another study, that has been carried out concerns the loose lepton level used in the determination of the fake electron background. The default Matrix Method loose level is defined to be equal to the veto level[4] defined in Section 3.2. However, it is also allowed to use a different definition. In principle, this should give a similar result for the multijet background. To test the stability of the Matrix Method, a rather large variation of the loose level was chosen. The new Matrix Method loose level requires the `TightLH` identification, while no isolation criterion is used. Thus, the lepton identification level was increased and the lepton isolation level was reduced. For technical reasons, it was also necessary to change the veto level, when lowering the isolation criterion. The new one requires a `MediumLH` identification, but no isolation. This change had no significant effect on the number of data events considered. In the case of the $t\bar{t}$-background, the event yield was reduced by $\sim 0.4\%$. Thus, the new veto level is slightly lower than the previous one, i.e. more leptons satisfy the requirement, and more events are vetoed.
Comparing the two loose levels of the Matrix Method, the new one is tighter than the previous one. This results in $\sim 13\%$ less data events containing a lepton that satisfies this requirement. To save computational effort, this study was carried out only for apart of the dataset, namely the mc16d period.

The resulting real and fake efficiencies for both levels are given in Figure 4.24. Here only the last $|\Delta\phi|$-bin, in which most of the data events contribute, of the fake efficiencies is shown, all other bins can be found in the appendix (Appendix B.4). In general, it can be seen that both the real and fake efficiencies are larger for the new loose level. This is expected because, as explained above, the varied level has tighter criteria than the nominal one. Therefore, an object that has to pass the varied loose level is more likely to pass the tight level than if it only had to pass the nominal loose level. This holds for both real and fake leptons. Furthermore, the statistical uncertainties of the real efficiencies are reduced, while those of the fake efficiencies are increased. The latter can be explained by the fact that less events pass the loose level of the varied Matrix Method.

Figure 4.25 presents a comparison between the multijet estimates for the measurement variable $m_T^W \otimes |\eta(e)|$ obtained with the two different approaches. It can be seen that the difference between the two estimates is quiet large. It varies in the order of $\sim 50\%$. A tendency towards a larger multijet background is observed if the Matrix Method with a tighter loose level is used. In addition, there are more bins with negative bin contents, which are unphysical, when using the varied efficiencies, such as the first $|\eta(e)|$-bin in the first measurement bin. This is probably related to the fact that the new loose level is closer to the tight level. The Matrix Method weights are proportional to $\frac{1}{\epsilon_R - \epsilon_F}$ (see Equation 3.6 in Section 3.1) and become thus unstable, when the difference $\epsilon_R - \epsilon_F$ is close to zero. Since the real efficiencies are usually close to one,

[4] `LooseAndBLayerLH+FCLoose`

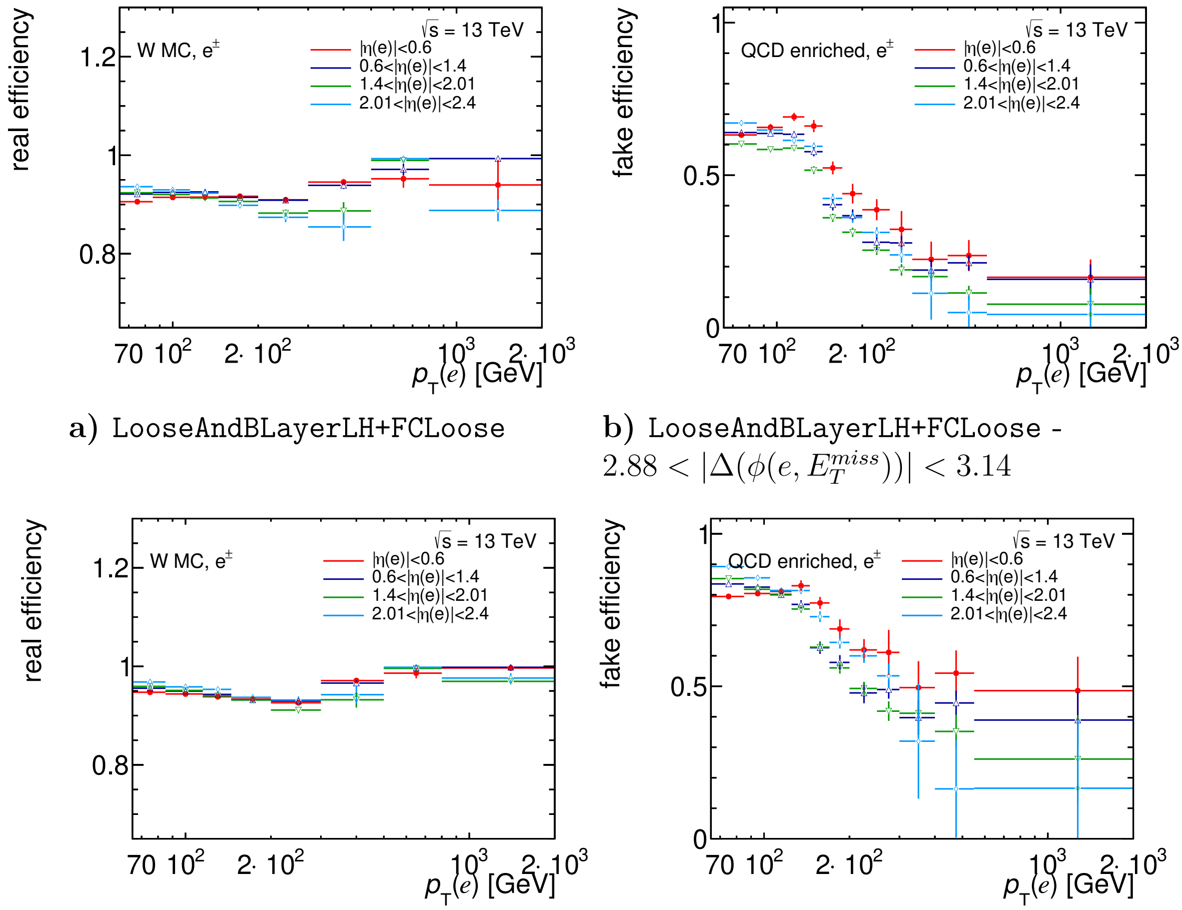

a) `LooseAndBLayerLH+FCLoose`

b) `LooseAndBLayerLH+FCLoose` - $2.88 < |\Delta(\phi(e, E_T^{miss}))| < 3.14$

c) `TightLH`

d) `TightLH` - $2.88 < |\Delta(\phi(e, E_T^{miss}))| < 3.14$

Figure 4.24: Real and fake efficiencies using the nominal (top row) and the varied (bottom row) loose level. Only the last $|\Delta\phi|$-bin ($2.88 < |\Delta(\phi(e, E_T^{miss}))| < 3.14$) of the fake efficiency is shown. All other plots can be found in Appendix B.4.

this happens in particular if the fake efficiencies become large as well. When the two levels of the Matrix Method are relatively close to each other, even a fake electron is likely to pass the tight level selection when it has already passed the loose level selection.

Unfolded cross sections were determined using the two different multijet backgrounds. These are given in Figure 4.26. The ratio between the unfolded result and the theory prediction shows a different behaviour between the two loose levels. The varied multijet leads to significantly more fluctuations in this ratio. In particular, the bins that already showed deviations with the nominal multijet have even greater deviations between the data and the prediction. These are especially the bins at high $|\eta(e)|$ ($2.2 < |\eta(e)| < 2.4$) and before the LAr-crack ($1.2 < |\eta(e)| < 1.4$). There are discrepancies in other bins as well. An example of this are the bins covering the region $1.4 < |\eta(e)| < 1.8$. This behaviour is slightly more pronounced in the e^--channel. Given the multijet estimates shown in Figure 4.25, these observations are to be expected. In most of the problematic bins, the unfolded cross section was already smaller than the predicted one. Thus, the increasing multijet estimate leads to a significantly worse agreement between data and theory.

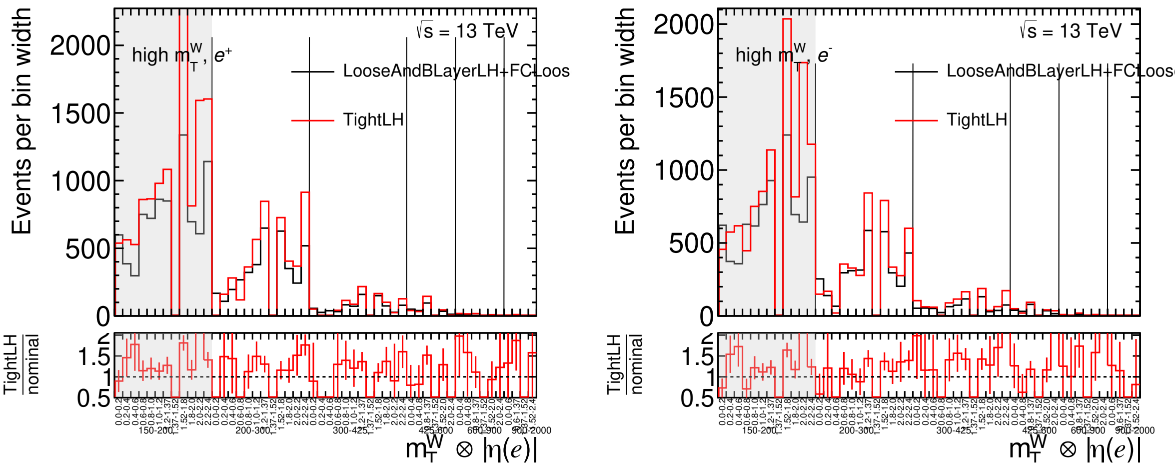

a) $m_T^W \otimes |\eta(e)|$ - e^+ b) $m_T^W \otimes |\eta(e)|$ - e^-

Figure 4.25: Comparison of the multijet estimates using the nominal and the varied loose level. Shown is the measurement variable in $m_T^W \otimes |\eta(e)|$ in both the e^+- and e^--channel.

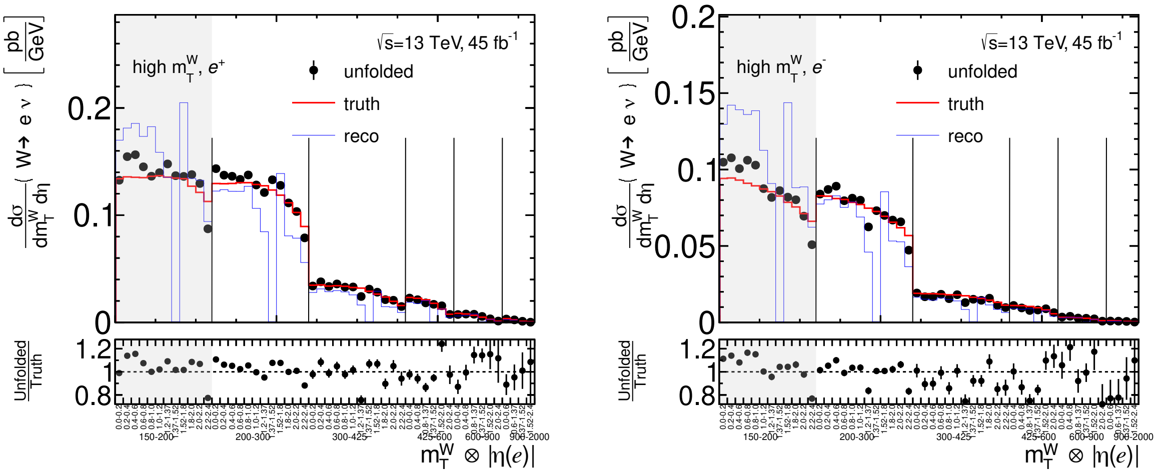

a) e^+ - LooseAndBLayerLH+FCLoose b) e^- - LooseAndBLayerLH+FCLoose

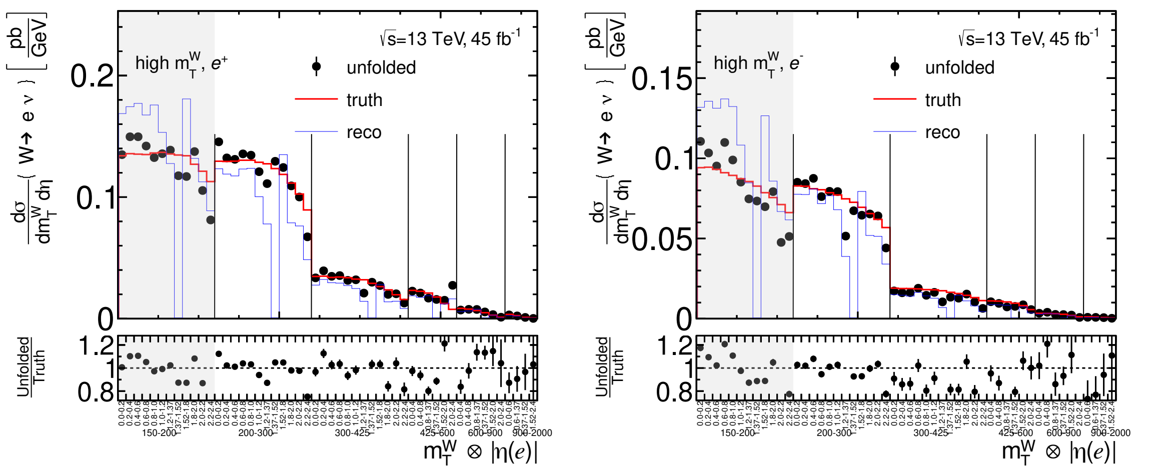

c) e^+ - TightLH d) e^- - TightLH

Figure 4.26: Unfolded cross section in $m_T^W \otimes |\eta(e)$ using the nominal (top row) and the varied (bottom row) loose level. The bottom panel shows the ratio between unfolded cross section and the theory prediction.

Finally, a ratio of the unfolded cross sections in electron and muon channel is calculated to estimate the effect of the different Matrix Method loose levels on the combination, see Figure 4.27. Substantial fluctuations are visible in all ratios. A significant fraction of the bins are not compatible with one, especially in the measurement region. Thereby, it is important to mention that only statistical uncertainties are taken into account here. In principle, this is to be expected, since the combination in $m_T^W \otimes |\eta(\ell)|$ shows that the electron and muon channel are not perfectly in agreement. However, these observations hold for both the nominal and the varied Matrix Method loose level. Thus, one cannot identify any of the different loose levels as giving the better electron-muon-agreement. For this reason, an additional χ^2-compability test was performed. Thereby, the shadow bin was not considered in the calculation. The results of this test are shown in Table 4.2. In general, the χ^2-values are very high, which is probably caused by the fact that only statistical uncertainties are considered in this test. The comparison of the different χ^2 values, especially of the ℓ^+ channel using the varied Matrix Method loose level, shows a very poor agreement between the electron and muon channels. However, also the ℓ^--channel using the varied level shows a significantly higher χ^2 than the corresponding test with the nominal one. Thus, the latter leads to a better agreement between electrons and muons. This is also in line with what is seen before, since the unfolded results in the electron channel show a significantly better agreement between data and prediction for the nominal loose level.

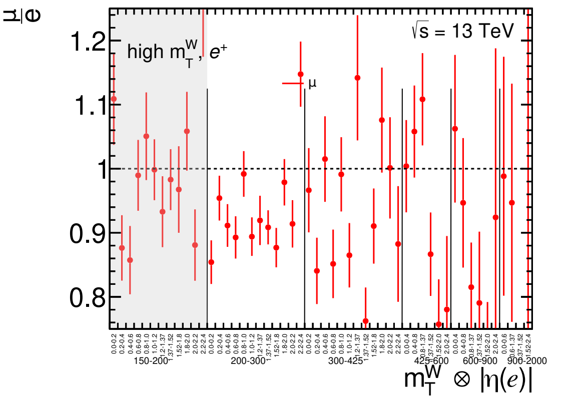

a) ℓ^+ - `LooseAndBLayerLH+FCLoose`

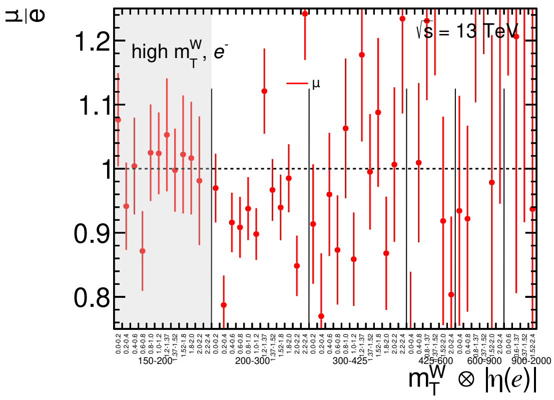

b) ℓ^- - `LooseAndBLayerLH+FCLoose`

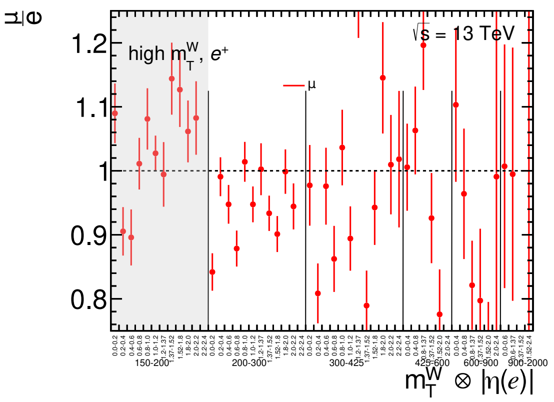

c) ℓ^+ - `TightLH`

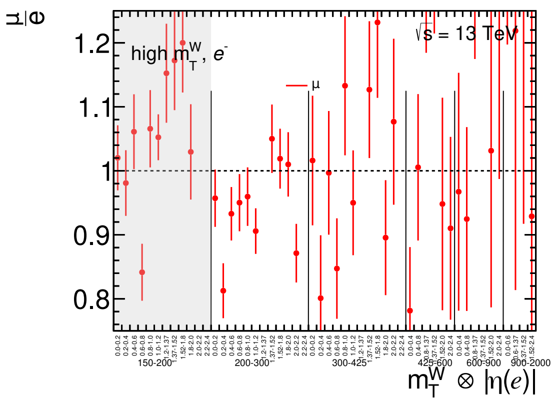

d) ℓ^- - `TightLH`

Figure 4.27: Electron-muon ratios of the unfolded cross section in $m_T^W \otimes |\eta(e)|$ using the nominal (top row) and the varied (bottom row) loose level in the electron channel. Only statistical uncertainties are taken into account.

Table 4.2: Chi-squared compability test between each of the two obtained electron cross sections with the muon channel cross section. The nominal Matrix Method loose level corresponds to `LooseAndBLayerLH+FCLoose` and the varied loose level to `TightLH`. Only statistical uncertainties are taken into account.

loose level	channel	χ^2	NDF	χ^2_{red}
nominal	ℓ^+	103.45	39	2.65
	ℓ^-	100.59	39	2.58
varied	ℓ^+	679.63	39	17.43
	ℓ^-	173.30	39	4.44

In conclusion, neither the unfolded result nor the electron-muon agreement could be improved by varying the Matrix Method loose level and its chosen to stay with the nominal. However, it was also found that the multijet estimate differs substantial when the loose level of the Matrix Method is changed.

4.7 Studies regarding the systematic uncertainties

In principle, a large shift of a systematic uncertainty indicates that its central value has not been correctly estimated. However, since many systematics are significantly shifted, it is also possible that none of them sufficiently fits to the differences between electrons and muons. This is underlined, by the fact that the χ^2 is not perfect despite the large systematic shifts. For this reason, several studies have been carried out to investigate the behaviour of the different crucial systematics.

4.7.1 Variation of the phase space of the MJ EL MET systematic

One of the uncertainties that gets a substantial shift in the combination is the MJ EL MET systematic. It refers to the E_T^{miss} range that is taken into account when calculating the fake efficiencies. Therefore, the whole E_T^{miss} range (0 GeV $< E_T^{miss} <$ 65 GeV) is divided into a low E_T^{miss} (0 GeV $< E_T^{miss} <$ 30 GeV) and a high E_T^{miss} (30 GeV $< E_T^{miss} <$ 65 GeV) region as systematic uncertainty. In this study, the definition of the high and low E_T^{miss} region is varied.

Figure 4.28 shows the resulting systematic uncertainties normalised to the signal cross section. Beside the default uncertainty (dark blue & green), the variations for 0 GeV $< E_T^{miss} <$ 20 GeV (light blue) and 40 GeV $< E_T^{miss} <$ 65 GeV (red) are presented. Comparing them, it can be seen that the trends observed for the default variations are more pronounced in the two new E_T^{miss} variations. In principle, these observations are to be expected, since the new E_T^{miss}-regions correspond to slightly more extreme variations of the nominal MJ EL MET systematic. The shape of the different multijet variations is very similar. Therefore, the choice of the E_T^{miss} cut does not hide a different behaviour of the multijet.

A fit was done for all possible combinations of a low-E_T^{miss} and a high-E_T^{miss} variation (beside the nominal). The one with 0 GeV $< E_T^{miss} <$ 20 GeV and 30 GeV $< E_T^{miss} <$ 65 GeV is shown in Figure 4.29 with the important shifts in Figure 4.30. A complete overview of all systematic shifts is given in the appendix (Figure B.8c).
This average gives the lowest χ^2/NDF (by $\sim$ 3) of all three combinations. The other two combinations can be found in the appendix in Figure B.6 and Figure B.7. Comparing the obtained averaged cross sections with the one using the nominal E_T^{miss}-variations for the MJ

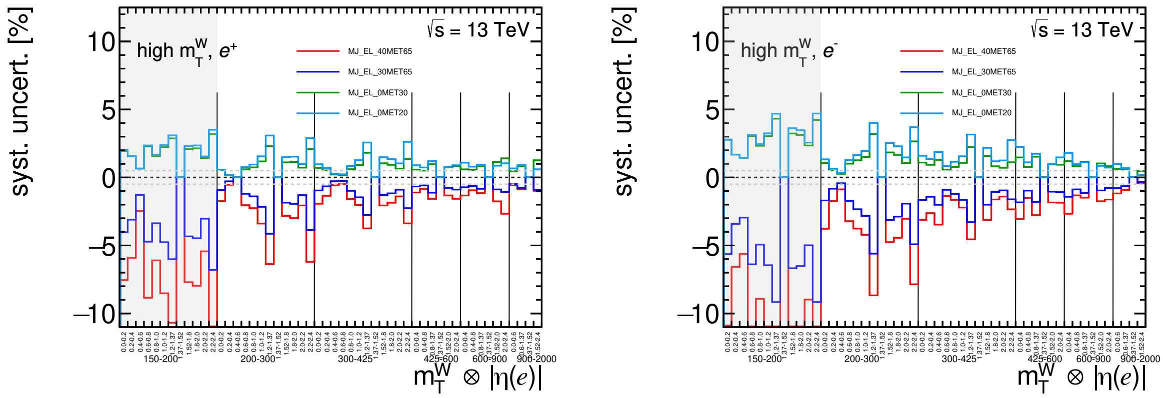

a) e^+-channel **b)** e^--channel

Figure 4.28: MJ EL MET systematic normalised to the signal cross section for different cuts applied on the E_T^{miss}. The final systematic is composed out of a low E_T^{miss} and a high E_T^{miss} variation.

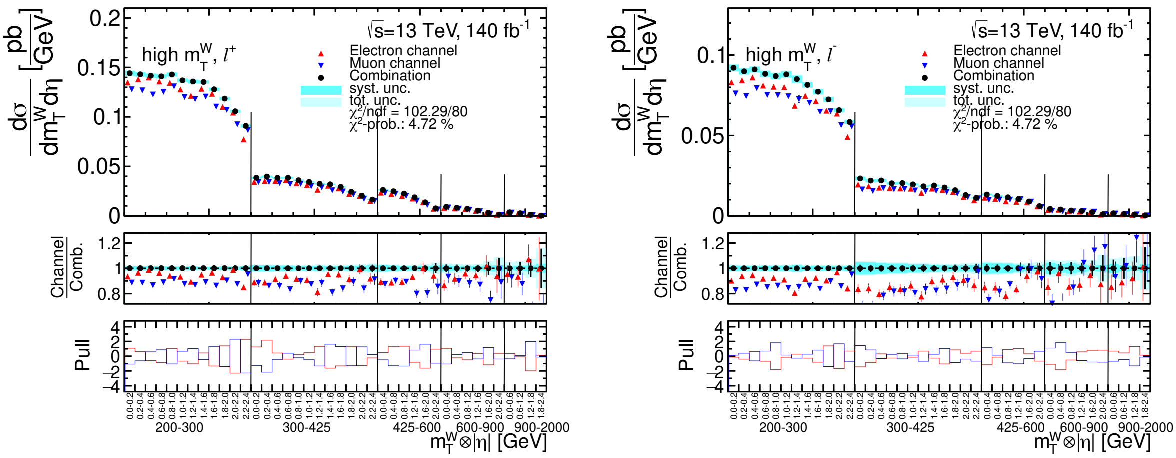

a) e^+-channel **b)** e^--channel

Figure 4.29: Averaged cross section (black) in $m_T^W \otimes |\eta(\ell)|$ together with the input cross sections of electron (red) and muon (blue) channel when using 0 GeV $< E_T^{miss} <$ 20 GeV and 30 GeV $< E_T^{miss} <$ 65 GeV as up- and down-variation of the MJ EL MET systematic. The combinations using the other variations of the MJ EL MET systematic are shown in the appendix (Figure B.6 and Figure B.7). The blue (light blue) uncertainty band gives the systematic (total) uncertainty. The error bars represent the statistical uncertainty. The middle panel shows the ratio with respect to the combined cross section. The bottom panel shows the pulls of the electron (red) and muon (blue) channel, according to Equation 4.6.

EL MET uncertainty, no significant differences can be observed. This is also underlined by the $\chi^2/NDF = 102.29/80$, which is only slightly reduced compared to the default fit (105.82/80). A few more differences show the systematic shifts. While MJ EL MET provides no substantial change (1.52 vs. 1.55), other systematics are more affected. The shifts related to the electron multijet tend to decrease, while the ones related to the the muon multijet only increase. This is observed for the MJ MC SCALING (which is reduced by $\sim 0.5\sigma$) and MJ MU MET and MJ MU D0CUT (which are increased by $\sim 0.2\sigma$) uncertainties. One can explain this behaviour by the shape of the MJ EL MET systematic. Figure 4.7a and 4.7b show that MJ EL MET has the largest effects in the same bins as MJ MC SCALING. Since the MJ EL MET uncertainty

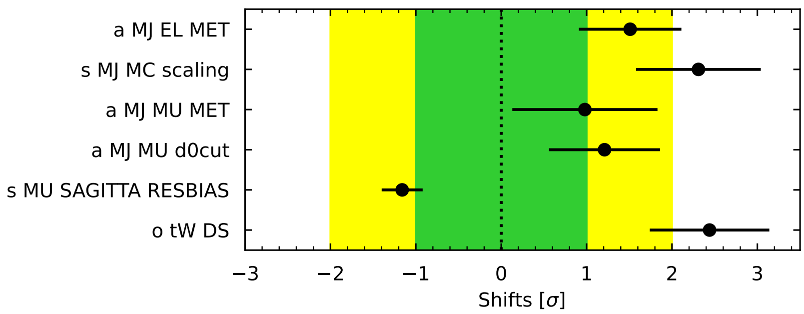

Figure 4.30: Important systematic shifts β_j for the combination in $m_T^W \otimes |\eta(\ell)|$ when using 0 GeV $< E_T^{miss} <$ 20 GeV and 30 GeV $< E_T^{miss} <$ 65 GeV as up- and down-variation of the MJ EL MET systematic. The error bars represent the reduction of the uncertainties by the combination. All systematic shifts are shown in the appendix in Figure B.8c.

is increased, a smaller shift of the MJ MC SCALING systematic is sufficient. This also reduces the effect of the MJ MC SCALING uncertainty on the muon channel cross section, because the systematic is correlated between the lepton flavours, which is then compensated by the MJ MU D0CUT and the MJ MU MET systematic.

Overall, varying the MJ EL MET uncertainty has no significant effect on the combination. On the other hand, reducing the range in which the systematic is defined is also associated with a higher risk of statistical fluctuations. For this reason, it was decided to keep the previous definition of the MJ EL MET systematic.

4.7.2 Adding a new MJ shape uncertainty

This study was conducted at an earlier state of the analysis, where, in particular, the tW DS systematic was not included in the combination. This systematic had a rather large effect on the combination. In addition, two bugs were found concerning the trigger scale factors and the MU SAGITTA RESBIAS systematic was decorrelated between charges, which had a smaller influence on the combination. The nominal combination before adding the tW DS systematic and correcting the trigger scale factor bugs can be found in the appendix (Appendix B.3).

Another uncertainty, which is substantially shifted, is the MJ MC SCALING systematic. It is correlated between the electron and muon channel and represents an uncertainty in the cross section of the MC samples used to determine the fake efficiencies. To determine this systematic, the MC processes are scaled by $\pm 6\%$ before subtracting them from the data and the resulting fake efficiencies are used to calculate the systematically varied multijet. However, this variation does not account for uncertainties in the shape of the MC processes. An alternative $W \to \ell\nu$ MC is available, which can be used to define a shape uncertainty for the signal. The alternative MC uses SHERPA2.2.11 for both the matrix element and the showering and is based on the NNPDF3.0 PDF. Electroweak corrections to next-to-leading order are applied. The shape uncertainty is defined in the following way. First, the Sherpa MC in the fake enriched region is rescaled, so that its integral is equal to the one of the nominal signal MC. This removes effects due to different normalisations in the two MC's. The Sherpa MC is then used instead of the nominal MC to calculate the real and fake efficiencies. The resulting multijet template provides a one-sided systematic on the multijet. Since the contribution of the background processes in the fake enriched region is relatively small, no shape uncertainties for the backgrounds are taken into account. This uncertainty is calculated in both the electron and muon channel.

Figure 4.31 presents the obtained MJ Sherpa Shape systematic in comparison with the other multijet systematics considered in the electron and muon channel, exemplarily for the measurement binning in $m_T^W \otimes |\eta(\ell)|$. The ℓ^+- and ℓ^--channel are shown for both an electron and a muon final state after the unfolding.
In the electron channel (top row), the MJ EL Sherpa Shape systematic extends to $\sim 3\%$ at small $|\eta(e)|$ and small m_T^W in the e^--channel. In this range, it is the largest multijet systematic. For higher pseudorapidities and transverse masses the magnitude of the systematic decreases with respect to the other multijet uncertainties. Starting at $|\eta(e)| > 0.6$ in the first m_T^W bin, the other multijet systematics are dominant. In contrast to the MJ EL MET and MJ EL MC scaling variations, no peaks are observed in the bin before the LAr-crack and at high $|\eta(e)|$. In almost all bins, the new systematic increases the multijet and thus reduces the cross section.
In the muon channel (Figure 4.31c and Figure 4.31d), the behaviour of the uncertainty is a bit different. The sherpa shape systematic is relatively small ($\lesssim 2\%$ in all bins) compared to the other systematics. Thereby, it reduces the cross section for small $|\eta(\mu)|$ and increases it at high $|\eta(\mu)|$.

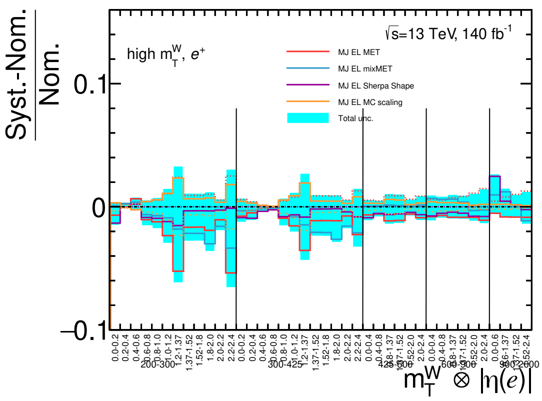

a) e^+-channel

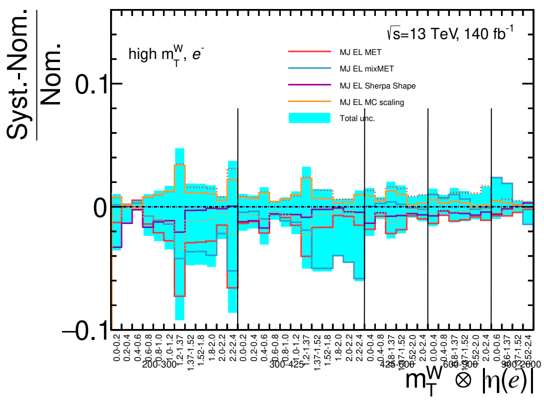

b) e^--channel

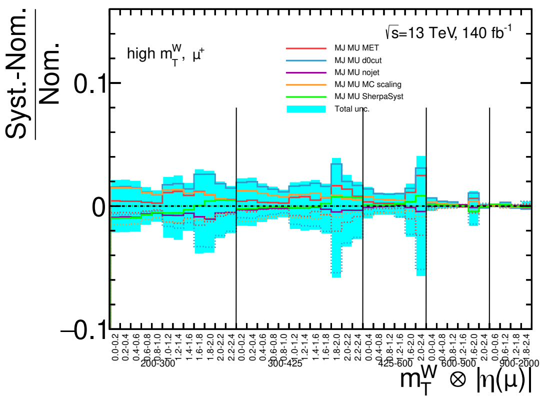

c) μ^+-channel

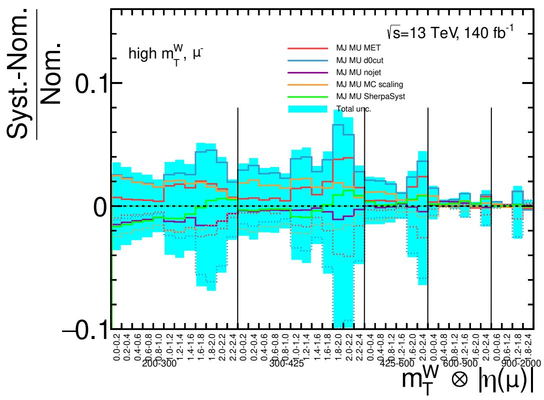

d) μ^--channel

Figure 4.31: MJ EL/MU Sherpa Shape Syst in comparison to the other multijet systematics normalised to the signal cross section. In the top row, the electron channel is shown, while in the bottom row the muon channel is presented.

Combinations of the electron and muon channel measurements with and without the MJ EL/MU Sherpa Shape Syst were performed. This systematic was treated decorrelated between the electron and muon channel. In Figure 4.32, the resulting averaged cross sections are shown. The corresponding most important shifts are presented in Figure 4.33 with a complete overview of all shifts in Figure B.22 in the appendix.

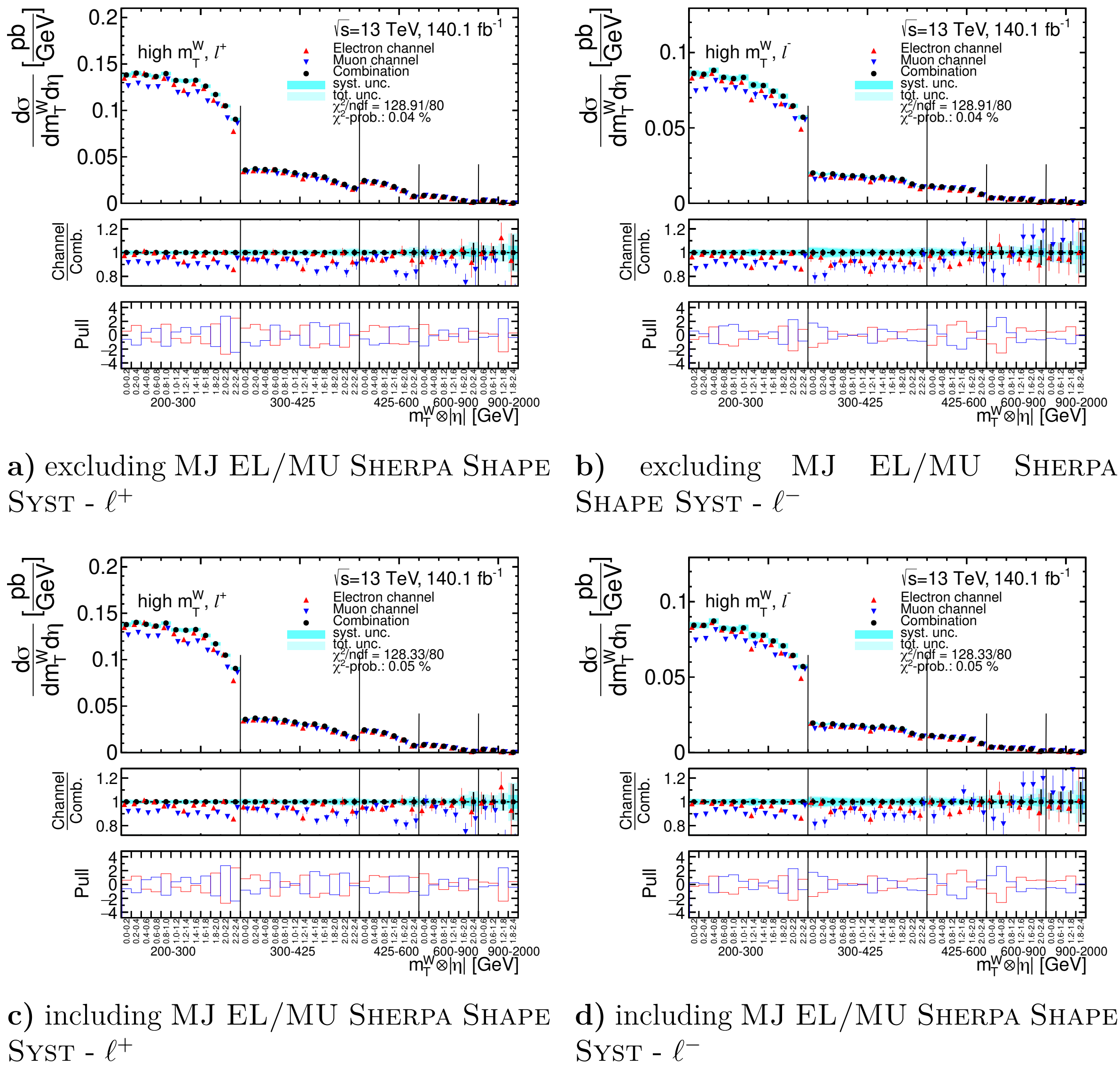

a) excluding MJ EL/MU Sherpa Shape Syst - ℓ^+

b) excluding MJ EL/MU Sherpa Shape Syst - ℓ^-

c) including MJ EL/MU Sherpa Shape Syst - ℓ^+

d) including MJ EL/MU Sherpa Shape Syst - ℓ^-

Figure 4.32: Averaged cross section (black) in $m_T^W \otimes |\eta(\ell)|$ together with the input cross sections of electron (red) and muon (blue) channel including and excluding the Sherpa Shape systematic. The blue (light blue) uncertainty band gives the systematic (total) uncertainty. The error bars represent the statistical uncertainty. The middle panel shows the ratio with respect to the combined cross section. The bottom panel shows the pulls of the electron (red) and muon (blue) channel, according to Equation 4.6.

Only a very small reduction in the χ^2/NDF ($128.91/80 \to 128.33/80$) is obtained, thus the MJ EL/MU Sherpa Shape Syst systematics have no relevant impact on the combination. Consequently, the shape of the new systematic does not fit to the deviations between electron and muon channel very well. Furthermore, no major changes in the ratio and the pulls of the central values are visible. The total shift of the averaged cross section is very slightly reduced, as can be seen, for example, in the first two $|\eta(\ell)|$-bins of the second m_T^W-bin in the ℓ^--channel.

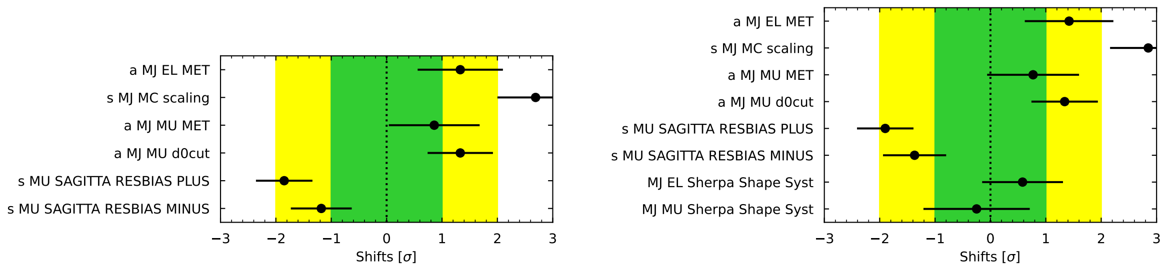

a) excluding MJ EL/MU Sherpa Shape Syst **b)** including MJ EL/MU Sherpa Shape Syst

Figure 4.33: Important systematic shifts β_j for the combination in $m_T^W \otimes |\eta(\ell)|$ including and excluding the Sherpa Shape systematic. The error bars represent the reduction of the uncertainties by the combination. All systematic shifts are shown in the appendix in Figure B.22.

A similar picture show the pulls of the central values. Only a few bins with already small pulls have slightly smaller pulls. These observations are also consistent with the changes in the systematic shifts. Most of the shifts that were remarkably large in the previous combination change only in the order of $\sim 0.1\sigma$. The newly introduced systematics have small systematic shifts. In the muon channel, this shift is -0.25σ. Thus, it points in the direction of the down variation of this systematic, which is zero per definition of a one-sided uncertainty. According to Equation 4.2, this leads to a reduction in the magnitude of the uncertainty, because it is a one-sided systematic. Thus, the effect of the shift on the cross section becomes even smaller. In the electron channel, the shift of $+0.58\sigma$ points into the same direction as the systematic. Therefore it is not further reduced. However, the effect on the cross section is still negligible compared to the systematics with the largest shifts.

Overall, the systematics have no significant effect on the combination. Only a tiny reduction in the χ^2/NDF could be achieved. The systematic shifts, the pulls of the central values and the ratio $\frac{\sigma_{e/\mu}}{\sigma_{aver}}$ also shows no substantial improvement. Finally, the systematics themselves are not significantly shifted. Therefore, it was decided not to include them in the combination.

4.7.3 Smoothing of electron MJ systematics

Because of large fluctuations in the systematic uncertainties, especially at high m_T^W, they are smoothed using the standard `ROOT` smoothing algorithm. For the $m_T^W \otimes |\eta(\ell)|$ distribution, a separate smoothing is applied across the $|\eta(\ell)|$-distribution per m_T^W-bin. However, such a smoothing can also remove or reduce real parts of the shape. In the case of the electron multijet uncertainties, peaks are observed in the bins before the crack and at high $|\eta(e)|$ (see Figure 4.34a and Figure 4.34b). These may have been reduced by the smoothing. Therefore, the effect of the smoothing needs to be studied.

A comparison of the smoothed and unsmoothed multijet systematics is shown in Figure 4.34. One can see that especially the MJ EL mixMET systematic has several peaks that are fully smoothed, e.g. $1.52 < |\eta(e)| < 1.8$ for 200 GeV $< m_T^W <$ 300 GeV and 300 GeV $< m_T^W <$ 425 GeV. However, the other systematics also show changes due to the smoothing. Both the peaks before the LAr-crack ($1.38 < |\eta(e)| < 1.52$) and in the last $|\eta(e)|$-bin ($2.2 < |\eta(e)| < 2.4$) are slightly reduced by the smoothing. Here, the effect is slightly more pronounced for the bin before the crack. In general, these changes are smaller than for the MJ EL MIXMET systematic.

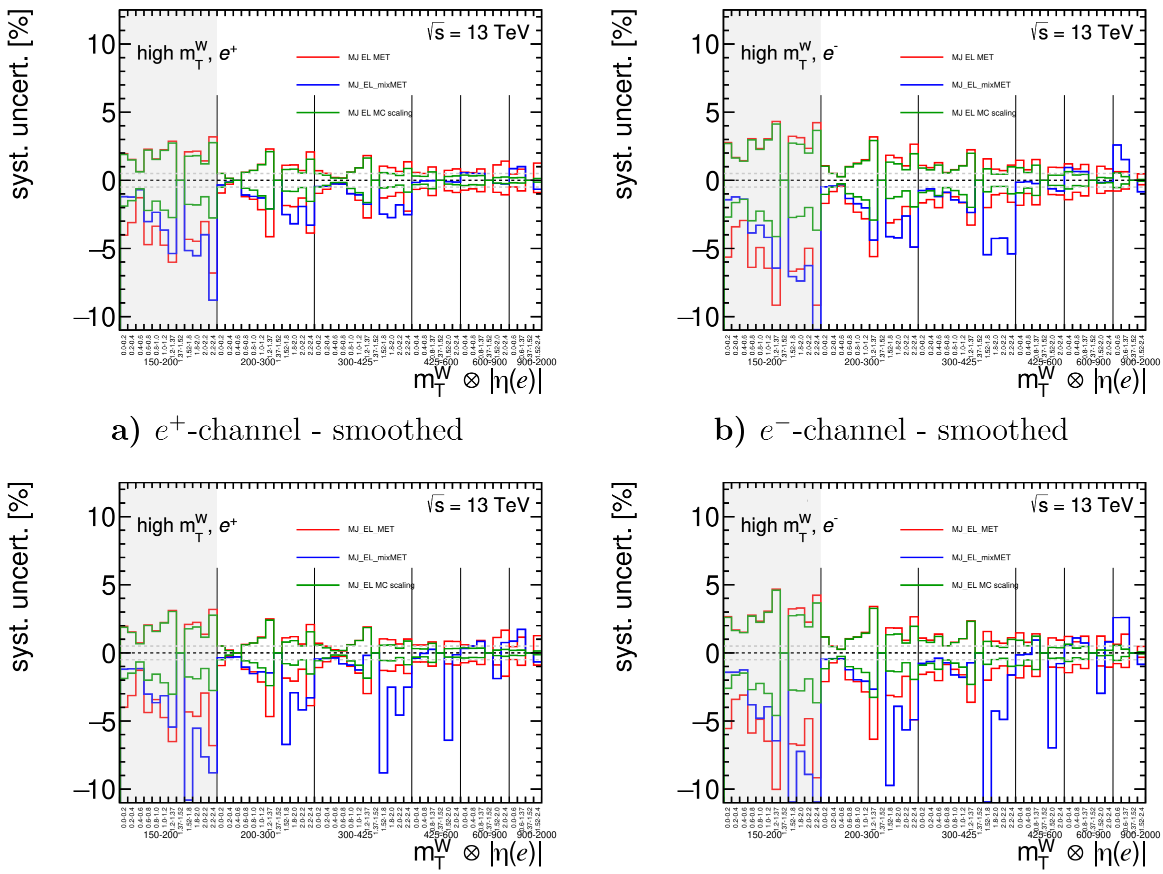

a) e^+-channel - smoothed b) e^--channel - smoothed

c) e^+-channel - unsmoothed d) e^--channel - unsmoothed

Figure 4.34: Multijet systematics that are considered in the combination normalised to the signal cross section. In the top row, a smoothing algorithm is applied, which is not done in the bottom row. The MJ EL MC SCALING systematic is symmetrised in both cases.

The resulting combination using the unsmoothed electron multijet uncertainties with the most important shifts can be seen in Figure 4.35 and Figure 4.36. All other systematic shifts are shown in Figure B.9a in the appendix. The χ^2/NDF of 100.14/80 is better than that of the default combination. This is also underlined by its probability, which increases from 2.83% to 6.34%. In addition, the pulls of the central value have changed slightly. In the ℓ^--channel, several intermediate pulls are reduced when using the unsmoothed electron multijet systematics. Moreover, the pull for $0.8 < |\eta(\ell)| < 1.0$ in the first m_T^W bin is significantly reduced ($1.9 \rightarrow 1.3$). On the other hand, only very few bins show a slightly increased pull. All in all, this is in line with the expectations arising from the better χ^2/NDF. Lastly, the total shift of the combined cross section is also a bit smaller. This can be seen, for example, in the first two $|\eta(\ell)|$-bins of the second m_T^W-bin in the ℓ^--channel. Comparing the systematic shifts, several differences can be observed. The MJ EL MET, the MJ MC SCALING and the tW DS systematic show small differences. Here, the shifts of the two multijet systematics are increased by about $\sim 0.1\sigma$, while the tW DS shift is reduced by $\sim 0.1\sigma$. Thus, the shifts of the unsmoothed systematics are not reduced. It is likely that the unsmoothed systematics fit the divergences between electrons and muons better, so that a shift gives a greater benefit to the combination than for the smoothed uncertainties. Therefore, a larger shift is accepted due to its disproportionate benefit to the combination. This is also underlined by the fact that the shifts of the MJ MU MET ($0.79\sigma \rightarrow 0.57\sigma$) and the MJ MU D0CUT ($0.95\sigma \rightarrow 0.37\sigma$) are significantly reduced. Probably, their effect is now already covered by the MJ MC SCALING systematic.

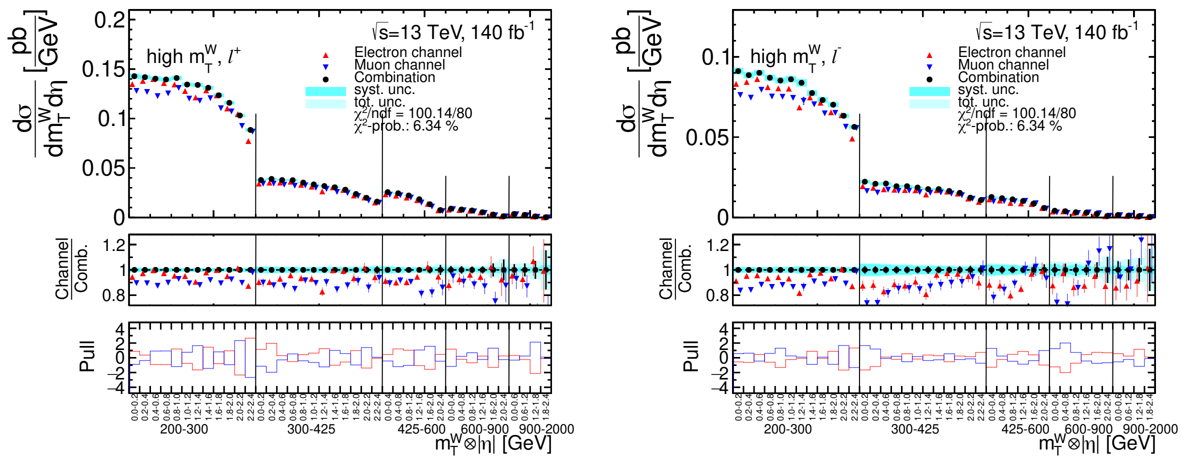

a) e^+-channel **b)** e^--channel

Figure 4.35: Averaged cross section (black) in $m_T^W \otimes |\eta(\ell)|$ together with the input cross sections of electron (red) and muon (blue) channel when the electron multijet systematics are not smoothed. The blue (light blue) uncertainty band gives the systematic (total) uncertainty. The error bars represent the statistical uncertainty. The middle panel shows the ratio with respect to the combined cross section. The bottom panel shows the pulls of the electron (red) and muon (blue) channel, according to Equation 4.6.

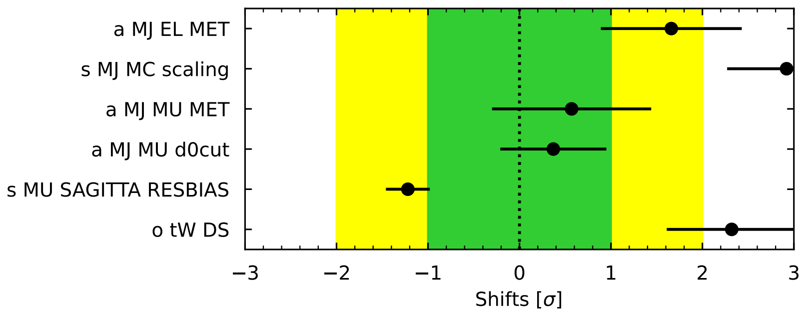

Figure 4.36: Important systematic shifts β_j for the combination in $m_T^W \otimes |\eta(\ell)|$ when the electron multijet systematics are not smoothed. The error bars represent the reduction of the uncertainties by the combination. All systematic shifts are shown in the appendix in Figure B.9a.

In general, it can be said that removing the smoothing for the electron multijet systematics leads to a small but notable improvement of the obtained average, between electron and muon channel. Thereby, it should be mentioned that there are still statistical fluctuations at high m_T^W, which are then not smoothed. A smaller improvement could thus be achieved by a more sophisticated smoothing. However, neither the large total shift of the averaged cross section nor the large systematic shifts are expected to be completely vanished. This can be explained by the fact that these are initially triggered by deviations between electrons and muons, which remain unaffected.

4.7.4 Barrel-end-cap-decorralation of MU SAGITTA RESBIAS uncertainty

The different variations of the phase space of the combination presented in Section 4.5 show an interesting behaviour of the shift of the MU SAGITTA RESBIAS systematic: It is much more pronounced when considering the high-$\eta(\ell)$ region, while it becomes very small at small $\eta(\ell)$. Thus, a decorrelation of the MU SAGITTA RESBIAS systematic could bring a significant improvement in the combination. In this study, the systematic was decorrelated for $|\eta(\mu)| < 1.01$ and $|\eta(\mu)| > 1.01$ on reconstruction level (i.e. before the unfolding), which refers to the transition between the barrel and the end-caps of the Muon Spectrometer. This choice is reasonable, since the barrel and the end-caps are in principle different detectors. Furthermore, the determination of this systematic suffers from less statistics in the high-$p_T(\mu)$ and high-$\eta(\mu)$ region.

Figure 4.37 and Figure 4.38 show the combination using the decorrelated MU SAGITTA RESBIAS uncertainty with the main systematic shifts, while an overview of the other shifts is given in the appendix (see Figure B.9b).

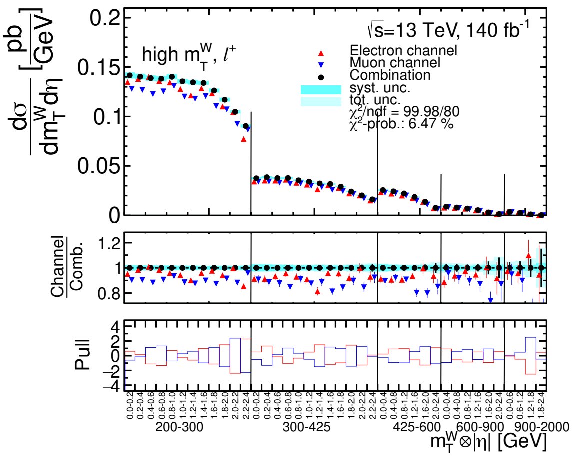

a) e^+-channel

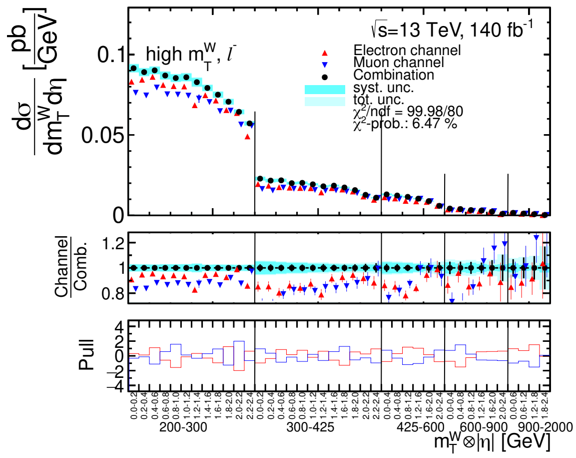

b) e^--channel

Figure 4.37: Averaged cross section (black) in $m_T^W \otimes |\eta(\ell)|$ together with the input cross sections of electron (red) and muon (blue) channel when the MU SAGITTA RESBIAS systematic is decorrelated between MS barrel and end-cap. The blue (light blue) uncertainty band gives the systematic (total) uncertainty. The error bars represent the statistical uncertainty. The middle panel shows the ratio with respect to the combined cross section. The bottom panel shows the pulls of the electron (red) and muon (blue) channel, according to Equation 4.6.

The $\chi^2/NDF = 99.98/80$ indicates a small but significant improvement. The largest differences are seen in the shifts of the MU SAGITTA RESBIAS systematic, which is now separated into MU SAGITTA RESBIAS BARREL ($|\eta(\mu)| < 1.0$) and MU SAGITTA RESBIAS ENDCAP ($|\eta(\mu)| > 1.0$). While the shift in the barrel is almost zero, the shift in the end-caps is about $\sim -1.5\sigma$. This is in line with the previous studies, where no substantial shifts were observed in the barrel region (see Section 4.5.3). The increase of the shift in the end-caps can

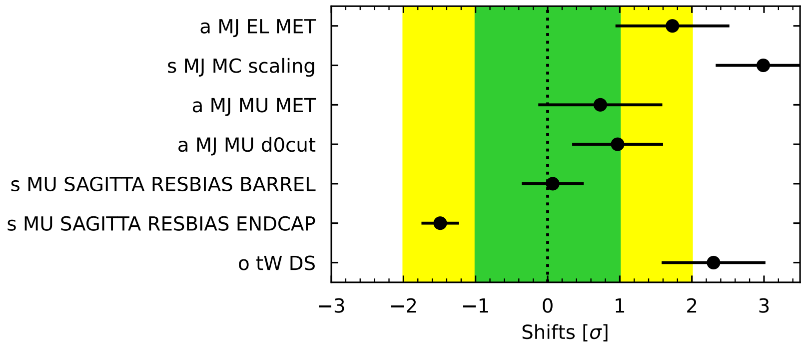

Figure 4.38: Important systematic shifts β_j for the combination in $m_T^W \otimes |\eta(\ell)|$ when the MU SAGITTA RESBIAS systematic is decorrelated between MS barrel and end-cap. The error bars represent the reduction of the uncertainties by the combination. All systematic shifts are shown in the appendix in Figure B.9b

.

be explained by the fact that the shift of the previous MU SAGITTA RESBIAS systematic was constrained by the effects at low $|\eta(\mu)|$. The differences in the other shifts are smaller. The shifts of MJ EL MET and MJ MC SCALING are increased by $\lesssim 0.2\sigma$ and that of TW DS is reduced by $\sim 0.1\sigma$. Small changes are also observed in the ratio $\frac{\sigma_{e/\mu}}{\sigma_{aver}}$. In particular, opposite effects can be seen for the different lepton charges as well as for the MS barrel and end-cap region. On the one hand, the total shift of the averaged cross section is slightly increased for a positively charged lepton with $|\eta(\ell)| > 1.0$ and a negatively charged lepton with $|\eta(\ell)| < 1.01$. On the other hand, it is decreased for a positively charged lepton with $|\eta(\ell)| < 1.01$ and a negatively charged lepton with $|\eta(\ell)| > 1.01$. This behaviour can be identified with the MU SAGITTA RESBIAS systematic. It causes a shift to smaller cross sections, i.e. a smaller total shift of the averaged cross section, in the ℓ^--channel and a shift to larger cross sections in the ℓ^+-channel. These effects are reduced for $|\eta(\ell)| < 1.01$ and increased for $|\eta(\ell)| > 1.01$ after the decorrelation. Thus, the total shift becomes larger for $|\eta(\ell)| < 1.01$ in the ℓ^--channel and $|\eta(\ell)| > 1.01$ in the ℓ^+-channel. For $|\eta(\ell)| > 1.01$ in the ℓ^--channel and $|\eta(\ell)| < 1.01$ in the ℓ^+-channel the total shift is smaller. Lastly, the pulls of the central values are also slightly changed. In particular, most of the bins with an intermediate pull have a smaller pull after the decorrelation. The largest pulls remain almost unchanged.

It can be concluded from this study that the different behaviour of the sagitta bias systematics in the MS barrel and end-caps has a notable effect on the combination. Some improvements can be achieved by decorrelating the MU SAGITTA RESBIAS systematic between the barrel and the end-caps. Based on this study and several other studies done by this analysis team, the Muon Combined Performance Group has developed a new scheme for the MU SAGITTA RESBIAS systematic using three different nuisance parameters. One of them is defined only for the MS end-caps and high-p_T muons. This scheme gives similar results in the combination as the decorrelation of the MU SAGITTA RESBIAS systematic presented here.

4.8 Summary of the combination and the further studies

A combination of the unfolded electron and muon channel cross section was done for both the single-differential measurement in m_T^W and the double-differential measurement in $m_T^W \otimes |\eta(\ell)|$. Thereby, the considered systematic uncertainties were treated correlated between the two lepton charges. Furthermore, uncertainties affecting both electrons and muons were treated correlated between the lepton flavours.

The combination of the single-differential measurements (see Figure 4.1) shows a very good agreement between the electron and muon channel. This can be seen in particular in the low χ^2/NDF of 11.04/22. The fact that the reduced χ^2 is smaller than one indicates that the uncertainties in these measurements might be overestimated. The good agreement is further underlined by the observation that the initial electron and muon channel measurements agree in most of the bins with the obtained average cross section within the uncertainties. The pulls of the central values in this combination are mostly smaller than one and thus relatively small. Furthermore, the sign of these small pulls often fluctuates, indicating that the differences between electrons and muons are mainly due to statistical fluctuations rather than systematic effects. Overall, this picture is also drawn by the systematic shifts. The only two uncertainties with a notable shift are the MJ EL MIXMET systematic and the MU SAGITTA RESBIAS systematic. Thereby, the shift on the MJ EL MIXMET uncertainty indicates that the multijet template using the mixed E_T^{miss} scheme might be better for the single-differential measurements. The shift of the MU SAGITTA RESBIAS underlines the observations that were already made at high m_T^W in the unfolded muon channel cross sections: It seems that the sagitta bias correction does not give perfect results, so that the corresponding systematic has to correct for this.

A χ^2/NDF of 105.82/80 is obtained by combining the double-differential measurements (see Figure 4.5). In principle, this still shows a relatively good agreement between the electron and muon channel. However, the combination shows one striking behaviour at small m_T^W: The combined cross section is larger than both the initial measurements in almost all bins. This behaviour might be unintuitive, but it can happen if the initial measurements are significantly shifted in the same direction due to large systematic shifts. Indeed, several uncertainties are significantly shifted, in particular the MJ MC SCALING ($\sim 2.8\sigma$) and the TW DS ($\sim 2.4\sigma$) systematic. These uncertainties are also among the largest at low to intermediate m_T^W. The effect of the MJ MC SCALING systematic is most pronounced in the bins before the LAr-crack ($1.37 < |\eta(e)| < 1.52$) and in the last $|\eta(e)|$ bin ($2.2 < |\eta(e)| < 2.4$). These are also the bins with the largest deviations between the unfolded data and the theory prediction in the electron channel, which indicates that these deviations might trigger the large shift. The shift that is applied to the TW DS indicates that the DS scheme might be more suitable for this analysis to remove the $t\bar{t}$-tW-interference. However, this would correspond to a shift of 1σ, whereas the observed shift does not correspond to any provided scheme. Finally, the MU SAGITTA RESBIAS systematic is substantially shifted as well. This again reflects the discrepancies seen at high $|\eta(\mu)|$ and high m_T^W in the unfolded muon cross sections, which are probably related to the sagitta bias correction.
The combination of the summed $\ell^{\pm}$-channel also gives insights into the behaviour of the systematic uncertainties. The multijet systematics are still significantly shifted, showing that they are not caused by charge-anticorrelated effects. On the other hand the shift of the TW DS systematic is reduced to $\sim 1\sigma$. This suggests that the DS scheme might be helpful although it does not directly correspond to the shift seen in the default combination.

The overall shift of the combined cross section, as well as the large systematic shifts observed in the 2D-combination, might be driven by the individual regions or correlations between different

regions. To investigate this, the combination was decorrelated several ways (see Section 4.5).
At first, a decorrelation between the lepton charges was done. Thereby, the combination for a ℓ^- final state showed a much better agreement between the electron and muon channel measurements. This is particularly evident in the large difference in χ^2/NDF (48.82/40 vs. 71.11/40). Consequently, the systematic uncertainties fit better to the discrepancies between electrons and muons for the ℓ^--channel. However, substantial systematic shifts and thus differences between the input measurements are observed for both charges.
In addition, the combination was performed separately for the low, intermediate and high m_T^W-region. Thereby, the systematic shifts show a different behaviour in the three regions. While the multijet systemtics are very important at small m_T^W, the shift of the MU SAGITTA RESBIAS systematic is dominant at high m_T^W. The fact that the obtained χ^2 decreases with larger m_T^W thus indicates that the differences at high m_T^W are well covered by the MU SAGITTA RESBIAS systematic.
Besides the decorrelation in m_T^W, a decorrelation between central ($|\eta(\ell)| < 1.0$) and forward ($|\eta(\ell)| > 1.0$) $|\eta(\ell)|$ is done as well. The resulting combination shows a much better agreement for the central region than for the forward region. This is consistent with the fact that most of the observed deviations between data and prediction are present at $|\eta(\ell)| > 1.0$, e.g. the discrepancies before the LAr-crack in the electron channel or due to the sagitta bias correction in the muon channel.
Since the effects of the shifts of the electron multijet uncertainties might be driven by individual bins with a poor agreement between data and prediction, bins, which showed such a poor agreement were excluded from the combination. This results in a very good χ^2/NDF of 64.96/64. Thus, these bins are indeed the ones with the worst electron-muon agreement. However this combination still provides significant shifts, which shows that there are also bins that cause the large systematic shifts.
Finally, the combination is done separately per data taking period. Thereby, none of the three periods showed a substantial better or worse agreement between the electron and the muon channel measurements.

The fact that the multijet uncertainties are significantly shifted in the combination suggests, that the multijet estimate might be not optimal. Therefore, two studies are done to investigate the multijet in the electron channel (see Section 4.6).
First, the fake efficiencies were calculated using a finer binning in $|\eta(\ell)|$. This leads only to small changes in the multijet in the order of $\lesssim 10\%$. Since the total multijet contribution is also in the order of $\sim 5\%$, the impact on the unfolded cross section and thus the combination is negligible small.
Furthermore, a new loose level is tested for the Matrix Method. This change has substantial effects on the estimated multijet background, which is varied by $\sim 50\%$ in several bins. However, the unfolded cross sections using the varied template show larger fluctuations than those for the nominal multijet and the χ^2-compability test between the electron and muon channel cross sections also underlines that the agreement between the electrons and muons is worse with the varied multijet template.

Finally, the systematic uncertainties considered are further investigated as well (see Section 4.7). One of the uncertainties with a significant shift is the MJ EL MET systematic. Therefore, different variations and their effect on the combination are tested. These variations lead to negligible changes in the obtained χ^2/NDF. Consequently, it was decided to keep the default systematic uncertainty.

Furthermore, a new shape uncertainty is introduced, to cover uncertainties in the shapes of the MC processes in the determination of the fake efficiencies. However, this new uncertainty is not significantly shifted in the fit so that its effect on the combination is negligible.
As the systematic uncertainties are smoothed, it is possible that real parts of the shape of the uncertainties might be removed by the smoothing algorithm. To test this effect, the combination was performed using unsmoothed multijet systematics for the electron channel. This results in small but still notable improvement in the χ^2 of about ~ 5. However, some of the systematics also show statistical fluctuations, which should be smoothed. Consequently, smaller improvements in the combinations could be gained by a more sophisticated smoothing procedure.
Finally, the MU SAGITTA RESBIAS systematic was decorrelated between the barrel and the end-cap region of the MS. This was done because a significantly different behaviour of this uncertainty was seen, when the combination was decorrelated between central and forward $|\eta(\ell)|$. The resulting combination showed that the MU SAGITTA RESBIAS systematic is shifted only in the end-cap region. Additionally, an improvement in the χ^2 could be achieved, which is similar as for the combination using the unsmoothed multijet systematics.

Chapter 5

Conclusions and outlook

This thesis is part of a measurement of the $W \to \ell\nu$ cross section at high transverse masses, i.e. $200\,\text{GeV} < m_T^W < 2000\,\text{GeV}$, which is done single-differentially in m_T^W and double-differentially in $m_T^W \otimes |\eta(\ell)|$. The measurement is performed in the electron and muon decay channels, while both charges are measured separately. It is based on *pp*-collision data taken with the ATLAS detector at a centre-of-mass energy of $\sqrt{s} = 13$ TeV. The dataset corresponds to an integrated luminosity of $\mathcal{L} = (140.1 \pm 1.2)$ fb^{-1}. Statistical and systematic uncertainties are considered in the measurement. Thereby, a precision of $\sim 5\%$ at small m_T^W and $\sim 20\%$ (electron channel) and $\sim 30\%$ (muon channel) at large m_T^W is achieved. This measurement has several applications. It can provide constraints on parton distribution functions of the proton as it explores regions with high PDF uncertainties. Furthermore, the measurement is sensitive to the running of the electroweak coupling constant and to effective field theories. Finally, it provides a test of the principle of lepton universality.

The main subject of this thesis was a combination of the electron and muon channel measurements. Due to the better statistics when using both electron and muon channel data, this can provide a more precise cross section measurement. Additionally, the combination gives a test of the lepton universality, since it quantifies the agreement between the electron and muon channel measurements. The combination was done using the HAverager tool. It uses a χ^2-minimisation method to calculate an average of different measurements. Thereby, statistical and systematic uncertainties are considered. All systematic uncertainties were treated correlated between lepton charges. Furthermore, uncertainties which are assigned to both electron and muon channel measurements are treated correlated between the lepton flavours.
The combination of the single differential measurements shows a very good agreement between electrons and muons with a $\chi^2/NDF = 11.04/22$. The fact that the reduced χ^2 is smaller than one, indicates that the uncertainties in this measurement are overestimated. The systematic shifts of this combination are small, underlining the good agreement between the electron and muon channel. This is also supported by the fact that the electron and muon channel measurements agree with the combined measurement within the statistical and systematic uncertainties in most of the bins.
The double-differential combination in $m_T^W \otimes |\eta(\ell)|$ results in a χ^2/NDF of 105.82/80, which still indicates a relatively good electron-muon-agreement. The central values of several systematic uncertainties were significantly ($> 1\sigma$) shifted by the combination. This concerns in particular the systematics related to the data-driven multijet background, the systematics covering the sagitta bias correction in the muon channel and the systematics covering the $t\bar{t}$-tW-interference. The fact that in particular the shifts on the multijet systematics and the uncertainties covering the $t\bar{t}$-tW-interference shift to about $\sim 10\%$ larger cross sections, leads to an interesting

behaviour of the obtained average: At low m_T^W, the combined cross section is larger than both the initial cross sections of the electron and muon channel.

In order to understand the large shifts of the systematic uncertainties as well as the overall shift of the combined cross section with respect to the initial measurements, the combination of the double-differential measurements was analysed in more detail. First, the phase space considered in the combination was varied in different ways. The combination was decorrelated in small ($200\,\mathrm{GeV} < m_T^W < 300\,\mathrm{GeV}$), intermediate ($300\,\mathrm{GeV} < m_T^W < 425\,\mathrm{GeV}$) and high ($425\,\mathrm{GeV} < m_T^W < 2000\,\mathrm{GeV}$) m_T^W, central ($|\eta(\ell)| < 1.0$) and forward ($|\eta(\ell)| > 1.0$) $|\eta(\ell)|$ and in the charge of the lepton. If the behaviour of the systematic uncertainties differs strongly between the different regions, a correlation between these regions could cause the observed shifts, since the modelling of the systematics in the different regions does not fit together well. It was seen that the correlations over the lepton charge as well as over m_T^W and $|\eta(\ell)|$ are responsible for the overall shift of the averaged cross section. However, none of them initially causes this shift. In addition, several bins with significant deviations between the unfolded data and the theory prediction were removed in the combination. The resulting χ^2/NDF of $64.96/64$ showed a very good agreement between the electron and muon channel, although there were still substantial systematic shifts in the order of 2σ on the systematic uncertainties covering the multijet and the $t\bar{t}$-tW-interference. Consequently, these bins are one main reason for the enhanced χ^2/NDF with respect to the 1D-combination, but they are not the only reason for the large systematic shifts.
It was seen that the shifts of the electron multijet systematics are relatively large and, in addition, strongly pronounced in bins with a comparatively large differences between the unfolded result and the theory prediction. For this reason, the multijet estimate in the electron channel was further investigated. Thereby, no significant improvements of the electron-muon-agreement were obtained.
Finally, some systematic uncertainties considered were investigated in more detail. At first, an uncertainty which covers the considered E_T^{miss}-range in the multijet estimation was varied. In addition, a new multijet shape systematic was introduced. However, none of this changes was found to improve the combination. To get rid of statistical fluctuations, the systematic uncertainties of the initial electron and muon channel measurements are smoothed. Since this smoothing can also remove parts of the shape of the uncertainties, it was tested to use the unsmoothed electron multijet systematics. This results in a reduction of the χ^2/NDF by ~ 6. Furthermore, a decorrelation of the uncertainties covering the sagitta bias correction between the MS barrel and end-cap led to a similar improvement of the electron-muon-agreement.

There are still some aspects in the underlying analyses, which probably improve the combination. First of all, the group responsible for the muon calibration has developed a new scheme for the systematic uncertainties covering the sagitta bias correction. In contrast to the nominal systematic using one nuisance parameters, it is based on three nuisance parameters, one of which is defined only for high-p_T-muons and in the end-caps of the MS. Moreover, a more sophisticated smoothing of the systematic uncertainties could improve the combination, as the current smoothing algorithm is very rough. The shift of the uncertainty covering the $t\bar{t}$-tW-interference suggests that a different scheme to remove this interference might be more suitable for this analysis. In addition, new recommendations are provided to remove the $t\bar{t}$-tW-interference, which have not been implemented in the analysis so far. Finally, systematic uncertainties of the unfolding procedure are not taken into account yet. These can also lead to a smaller χ^2 in the combination.

Appendix A

Supplemental material for the underlying measurements

A.1 Real and fake efficiencies

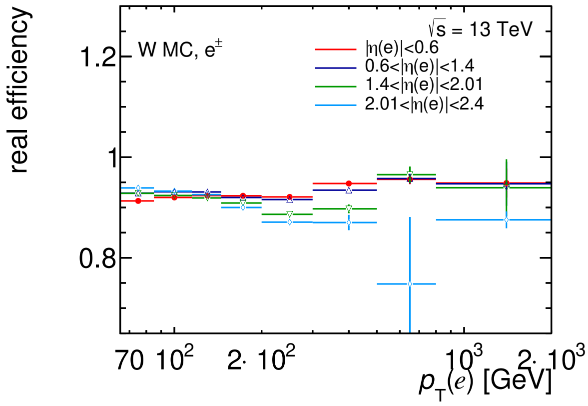

Figure A.1: Real electron efficiency used for the determination of the multijet background. The plot is binned in $p_T(e)$, each colour corresponds to on $|\eta(e)|$-bin.

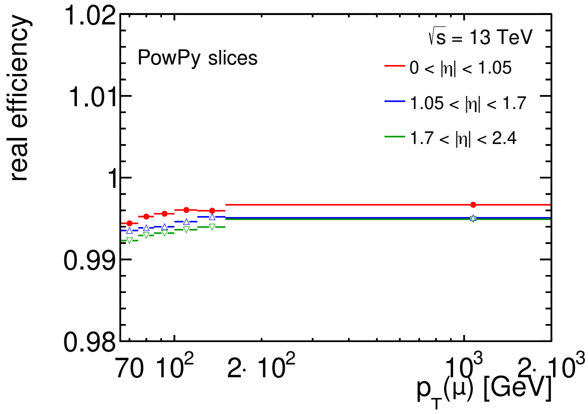

Figure A.2: Real muon efficiency used for the determination of the multijet background. The plot is binned in $p_T(\mu)$, each colour corresponds to on $|\eta(\mu)|$-bin [5].

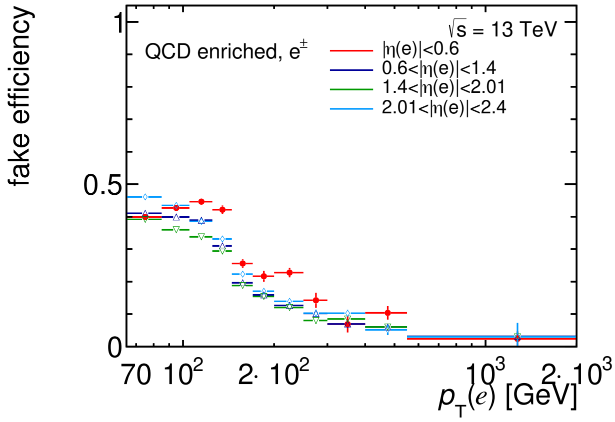

a) $0 < |\Delta\Phi(e, E_T^{miss})| < 0.26$

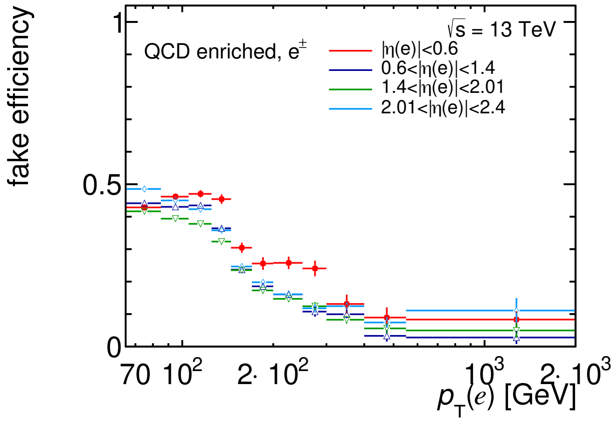

b) $0.26 < |\Delta\Phi(e, E_T^{miss})| < 0.52$

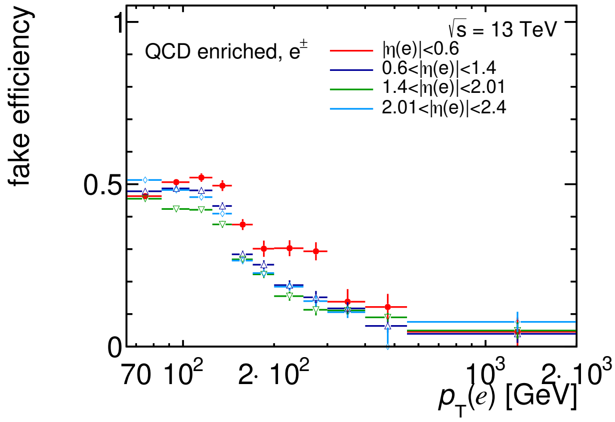

c) $0.52 < |\Delta\Phi(e, E_T^{miss})| < 0.78$

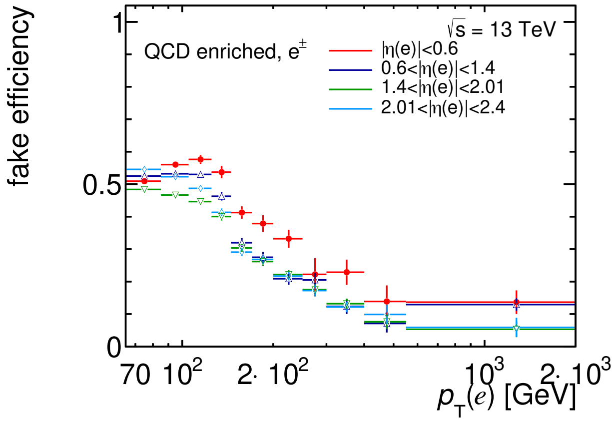

d) $0.78 < |\Delta\Phi(e, E_T^{miss})| < 1.05$

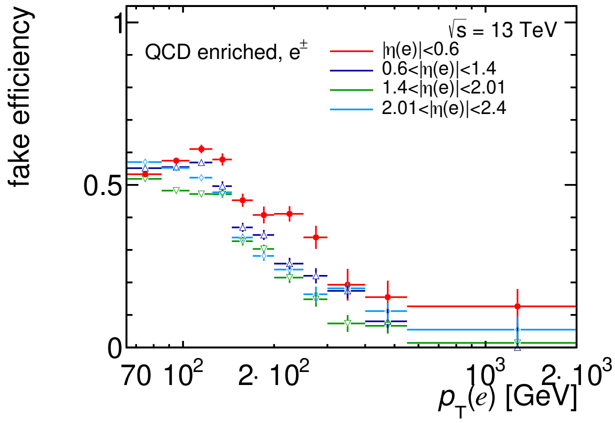

e) $1.05 < |\Delta\Phi(e, E_T^{miss})| < 1.31$

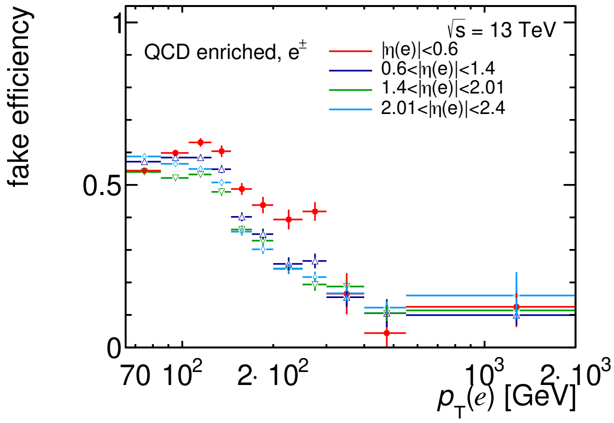

f) $1.31 < |\Delta\Phi(e, E_T^{miss})| < 1.57$

Figure A.3: Fake electron efficiency used for the determination of the multijet background. Each plot corresponds to a $|\Delta\phi(e, E_T^{miss})|$-bin. The plot is binned in $p_T(e)$, each colour corresponds to on $|\eta(e)|$-bin. The first six $|\Delta\phi(e, E_T^{miss})|$-bins are shown.

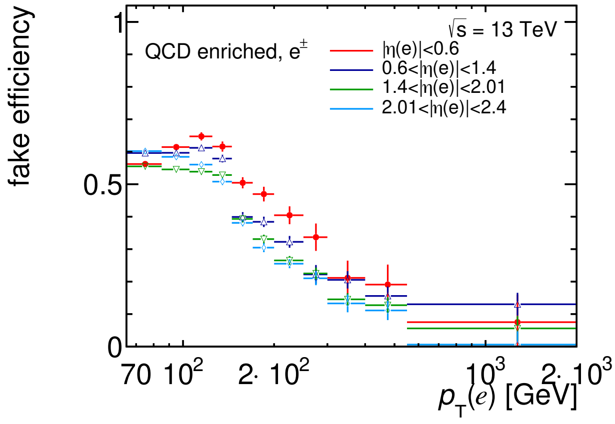

a) $1.57 < |\Delta\Phi(e, E_T^{miss})| < 1.83$

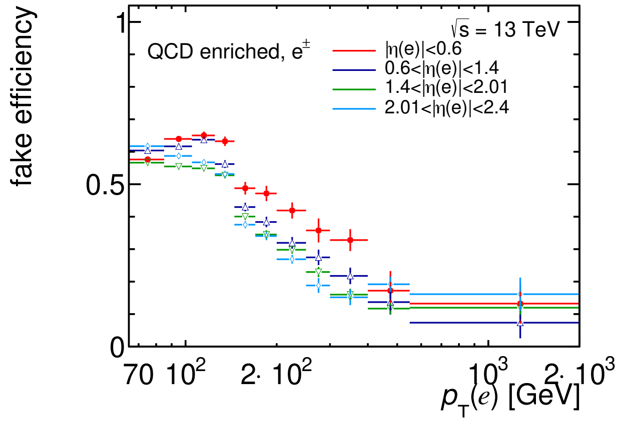

b) $1.83 < |\Delta\Phi(e, E_T^{miss})| < 2.09$

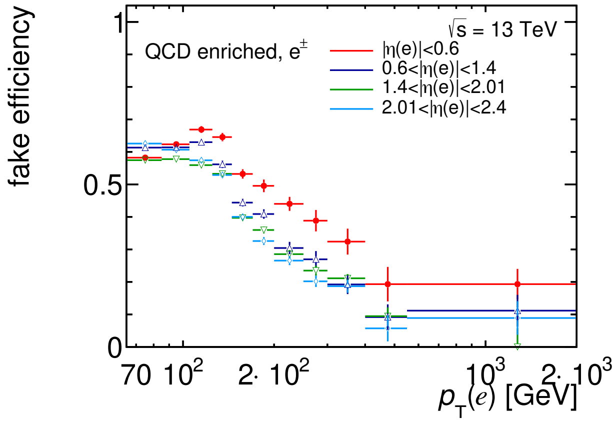

c) $2.09 < |\Delta\Phi(e, E_T^{miss})| < 2.36$

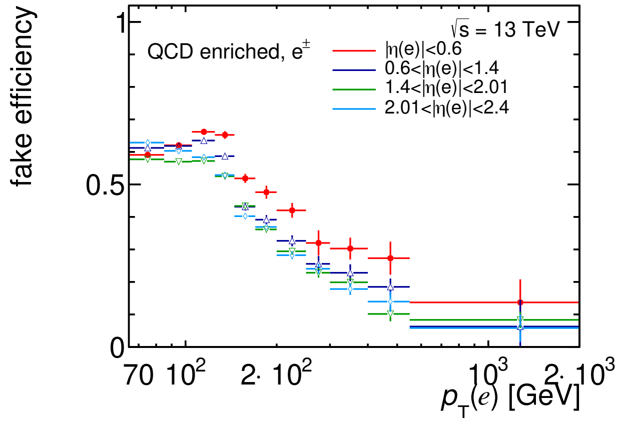

d) $2.36 < |\Delta\Phi(e, E_T^{miss})| < 2.62$

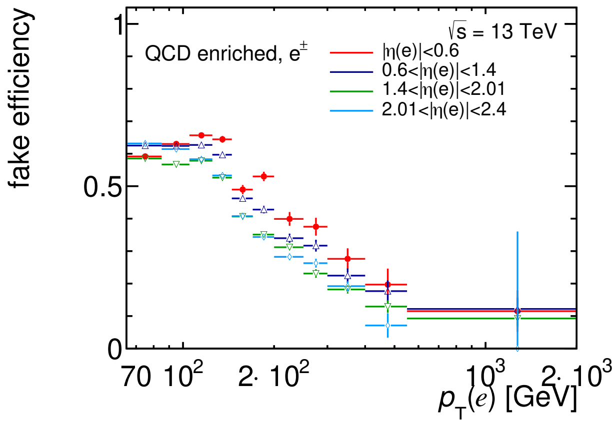

e) $2.62 < |\Delta\Phi(e, E_T^{miss})| < 2.88$

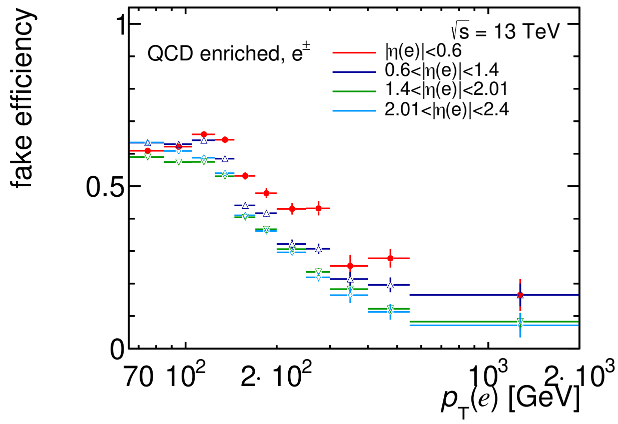

f) $2.88 < |\Delta\Phi(e, E_T^{miss})| < 3.14$

Figure A.4: Fake electron efficiency used for the determination of the multijet background. Each plot corresponds to a $|\Delta\phi(e, E_T^{miss})|$-bin. The plot is binned in $p_T(e)$, each colour corresponds to on $|\eta(e)|$-bin. The last six $|\Delta\phi(e, E_T^{miss})|$-bins are shown.

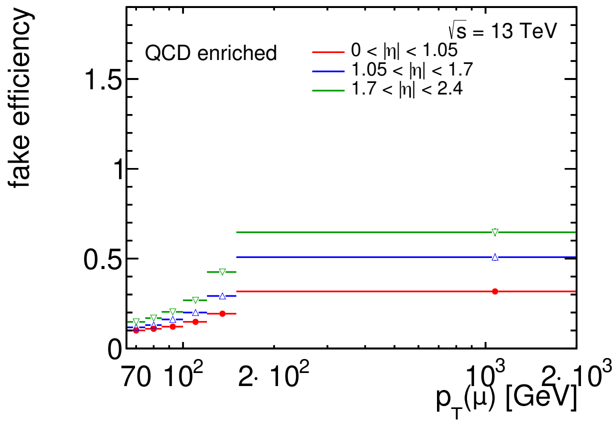

a) $0 < |\Delta\Phi(\mu, E_T^{miss})| < 0.525$

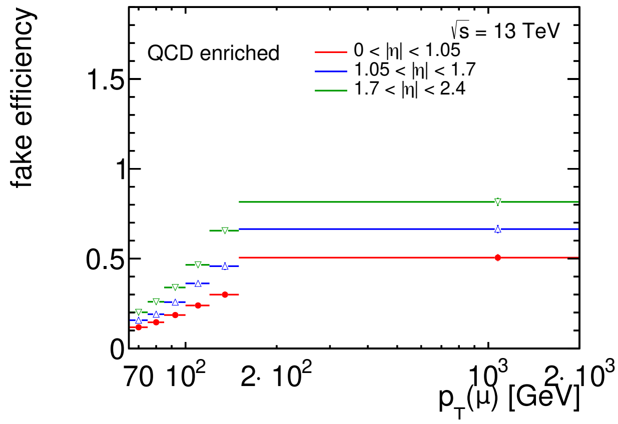

b) $0.525 < |\Delta\Phi(\mu, E_T^{miss})| < 1.05$

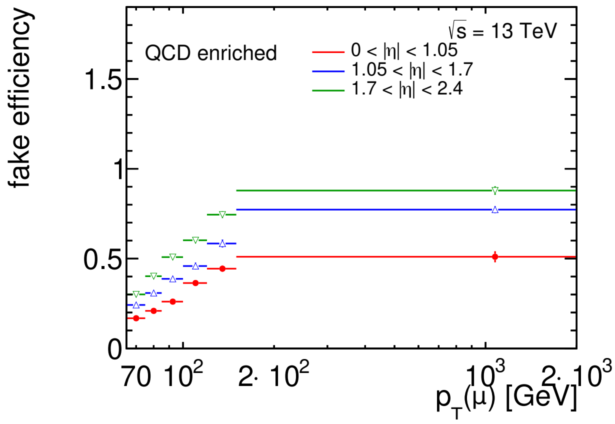

c) $1.05 < |\Delta\Phi(\mu, E_T^{miss})| < 1.575$

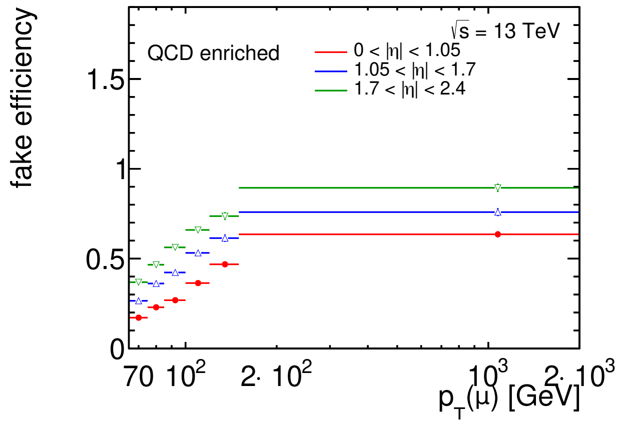

d) $1.575 < |\Delta\Phi(\mu, E_T^{miss})| < 2.1$

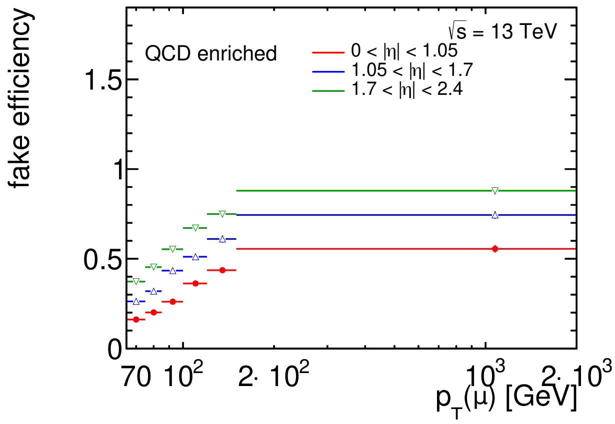

e) $2.1 < |\Delta\Phi(\mu, E_T^{miss})| < 2.625$

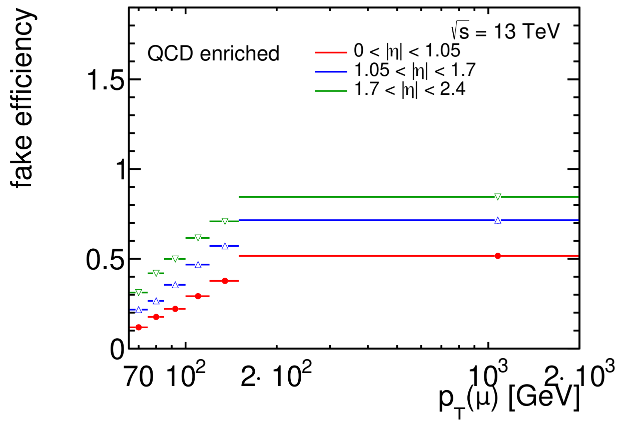

f) $2.625 < |\Delta\Phi(\mu, E_T^{miss})| < 3.15$

Figure A.5: Fake muon efficiency used for the determination of the multijet background. Each plot corresponds to a $|\Delta\phi(, E_T^{miss})|$-bin. The plot is binned in $p_T(\mu)$, each colour corresponds to on $|\eta(\mu)|$-bin [5].

A.2 Measurement distributions in $m_T^W \otimes |\eta(\ell)|$ per m_T^W-bin

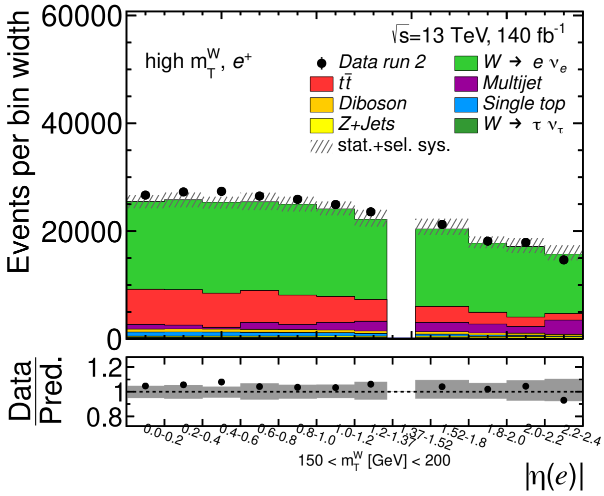

a)

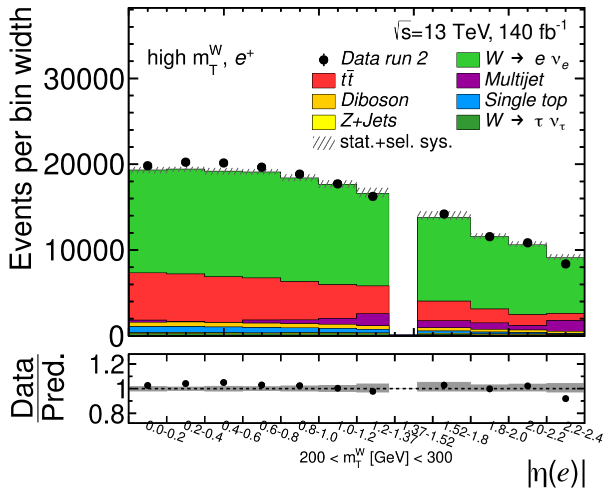

b)

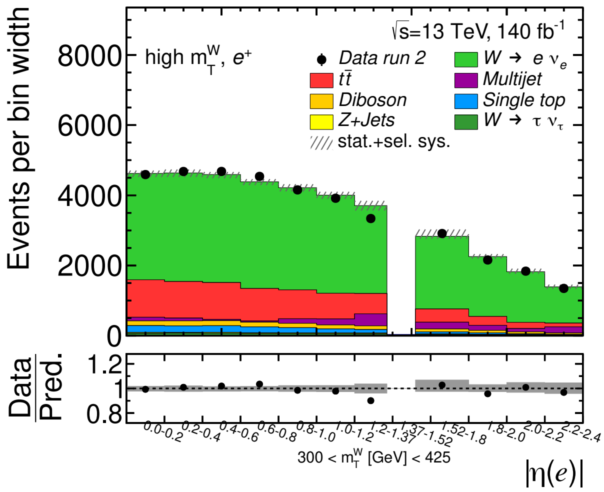

c)

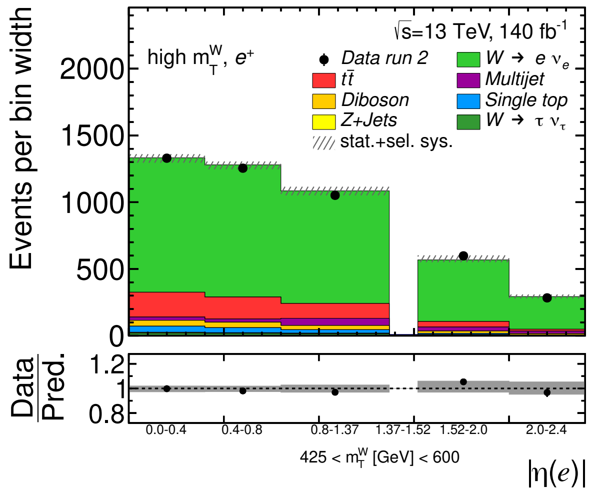

d)

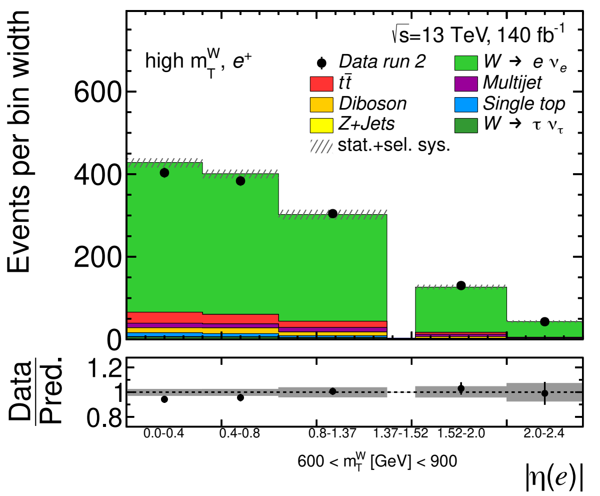

e)

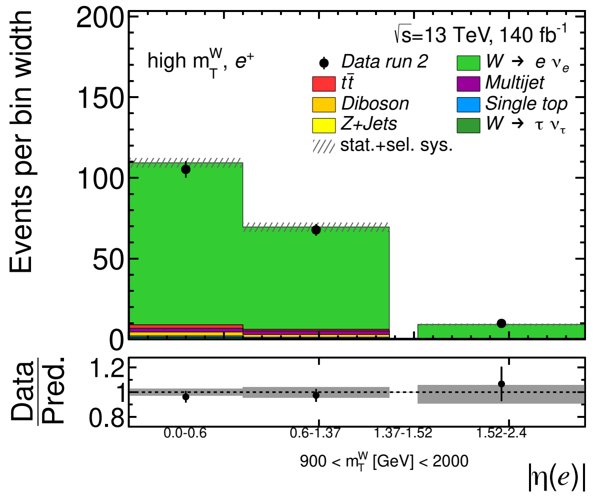

f)

Figure A.6: MC-data comparisons in the signal region for the measurement variable in $m_T^W \otimes |\eta(e)|$ in the e^+-channel. Each plot correspond to a m_T^W-bin. The uncertainty band includes all uncertainties with a contribution of at least 0.5% in one bin of any measurement distribution.

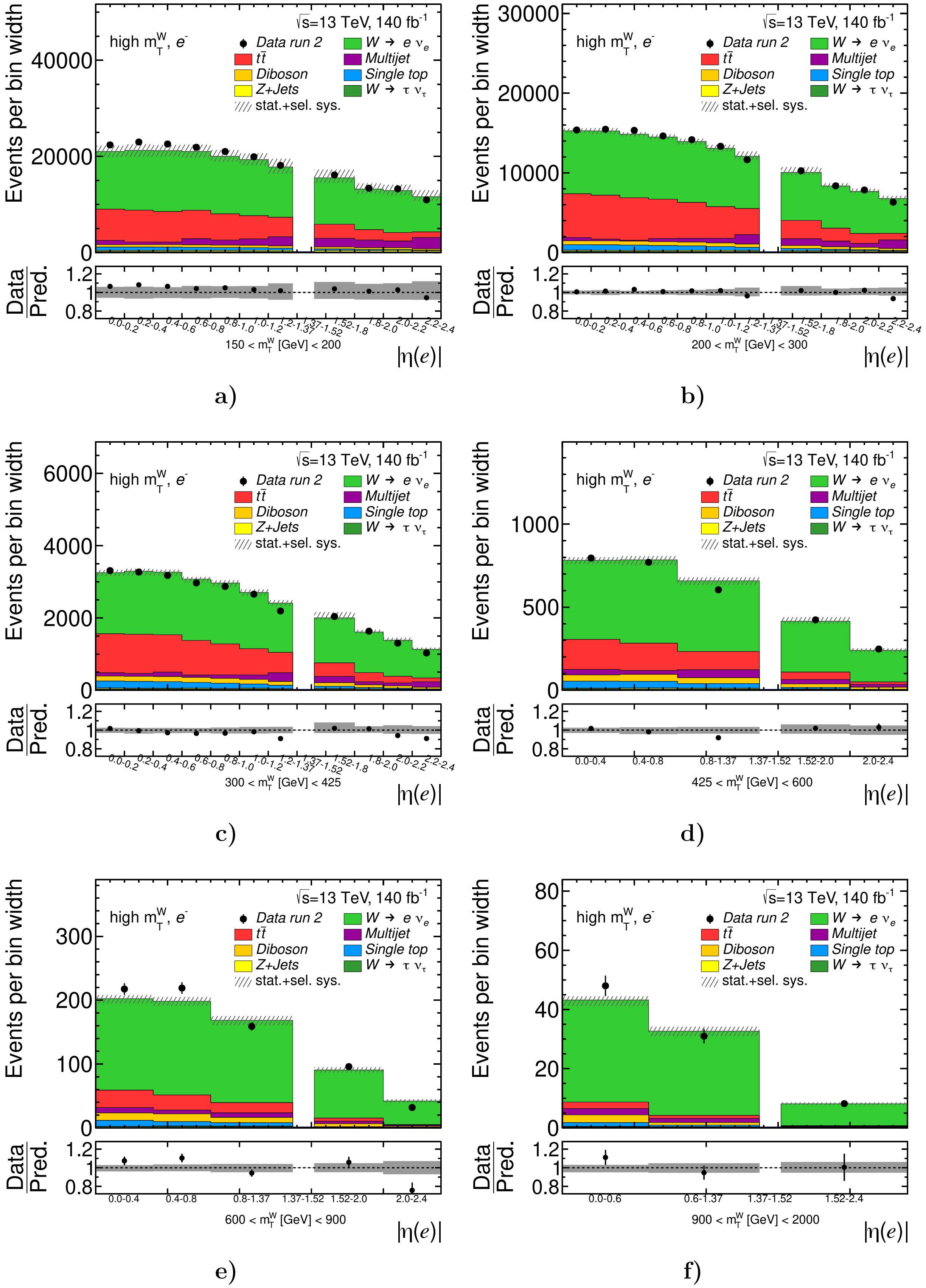

Figure A.7: MC-data comparisons in the signal region for the measurement variable in $m_T^W \otimes |\eta(e)|$ in the e^--channel. Each plot correspond to a m_T^W-bin. The uncertainty band includes all uncertainties with a contribution of at least 0.5% in one bin of any measurement distribution.

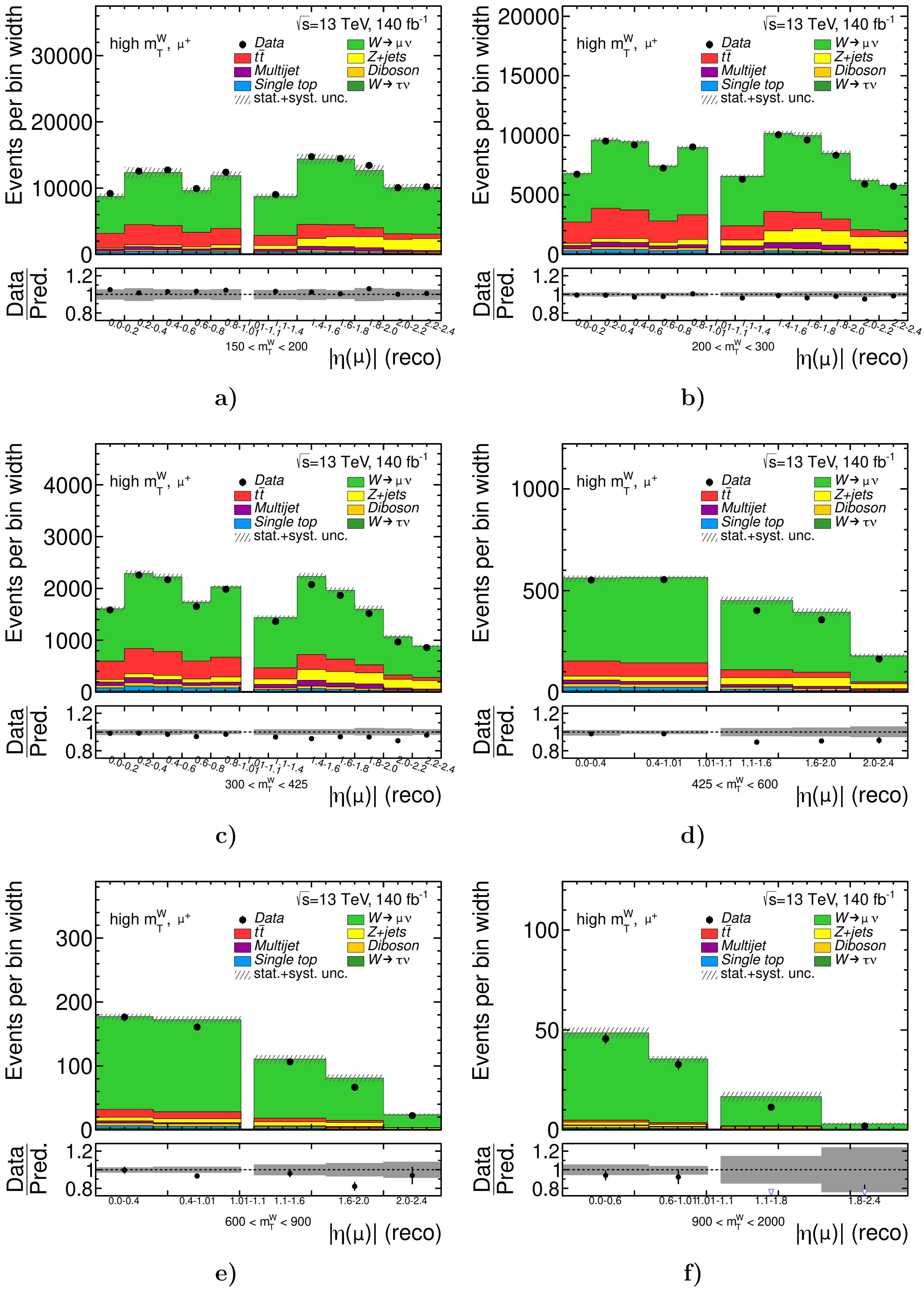

Figure A.8: MC-data comparisons in the signal region for the measurement variable in $m_T^W \otimes |\eta(\mu)|$ in the μ^+-channel. Each plot correspond to a m_T^W-bin. The uncertainty band includes all uncertainties with a contribution of at least 0.5% in one bin of any measurement distribution [5].

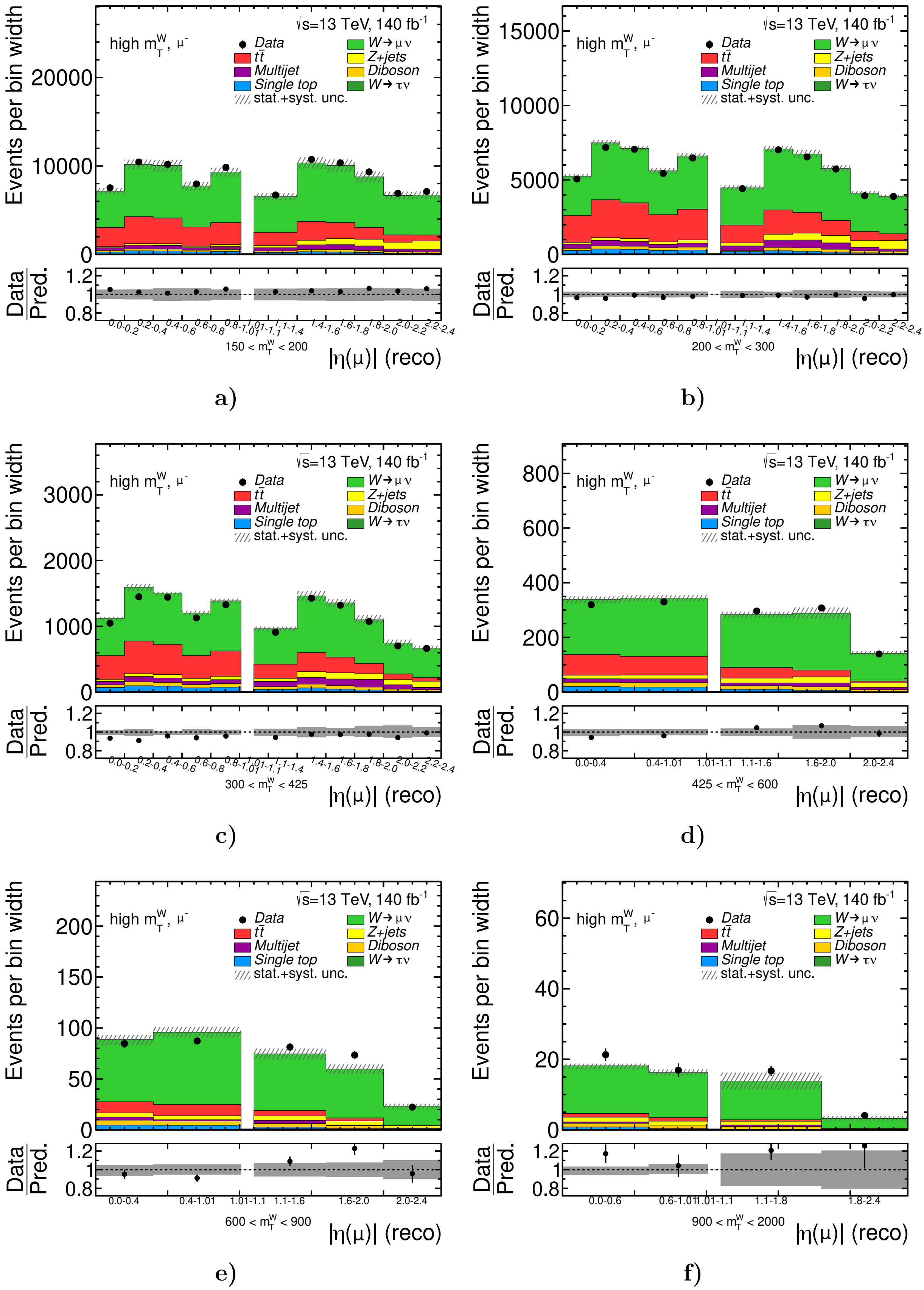

Figure A.9: MC-data comparisons in the signal region for the measurement variable in $m_T^W \otimes |\eta(\mu)|$ in the μ^--channel. Each plot correspond to a m_T^W-bin. The uncertainty band includes all uncertainties with a contribution of at least 0.5% in one bin of any measurement distribution [5].

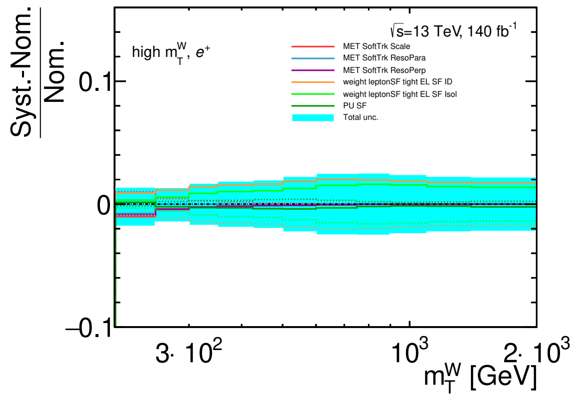

a) e^+-channel

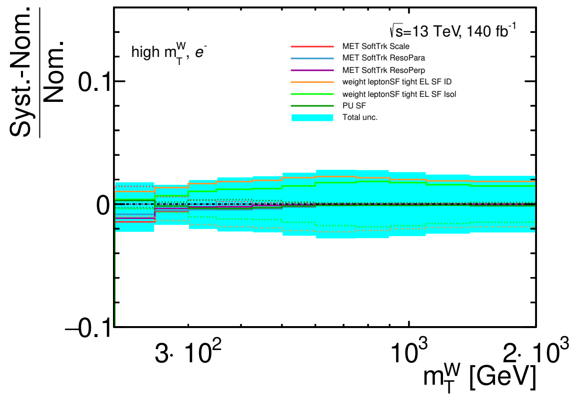

b) e^--channel

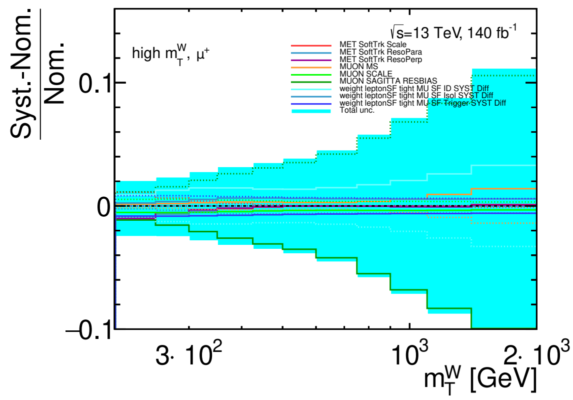

c) μ^+-channel

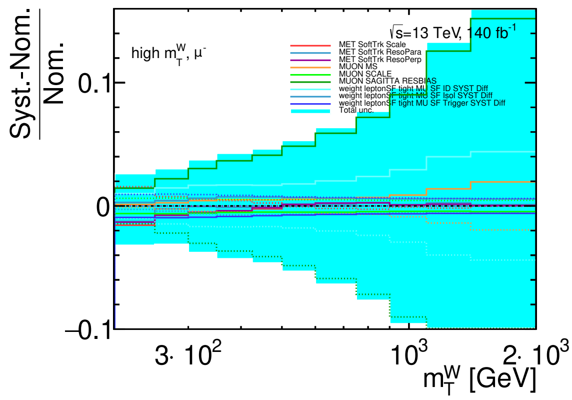

d) μ^--channel

Figure A.10: Electron/muon and MET systematics in the measurement variable in m_T^W. Shown are the systematic uncertainties after the unfolding normalised to the unfolded cross section [5].

A.3 Systematic uncertainties after the unfolding

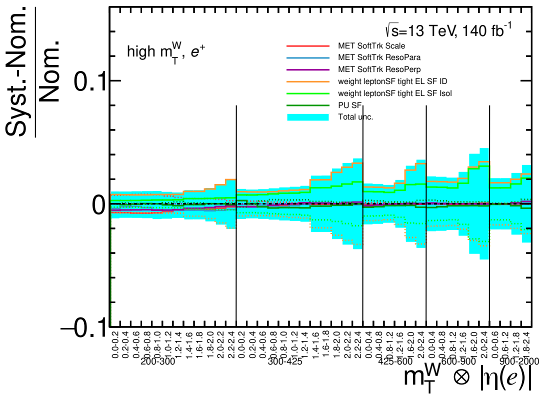

a) e^+-channel

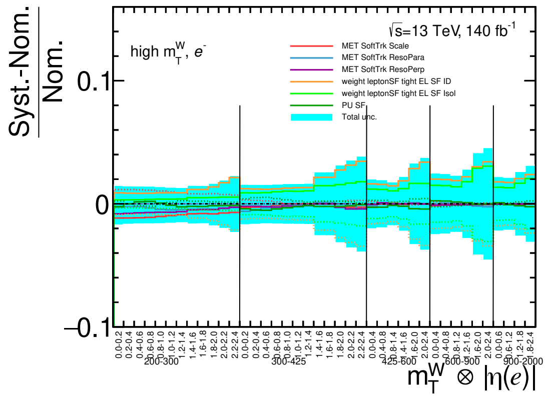

b) e^--channel

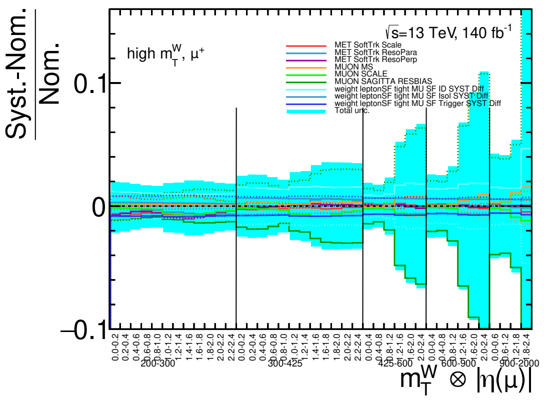

c) μ^+-channel

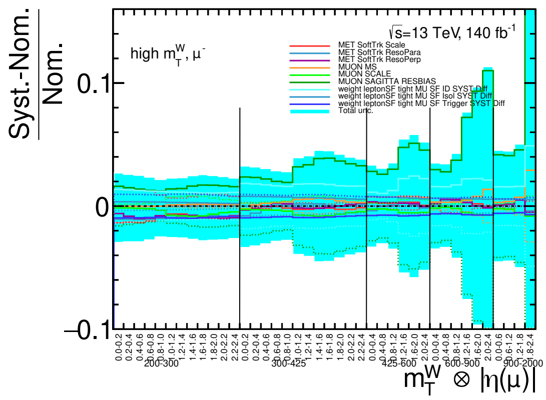

d) μ^--channel

Figure A.11: Electron/muon and MET systematics in the measurement variable in $m_T^W \otimes |\eta(\ell)|$. Shown are the systematic uncertainties after the unfolding normalised to the unfolded cross section [5].

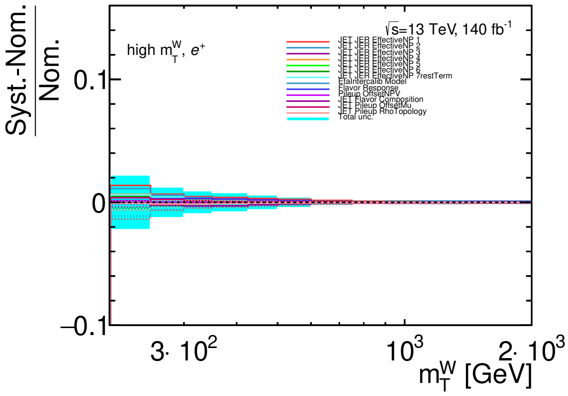

a) e^+-channel

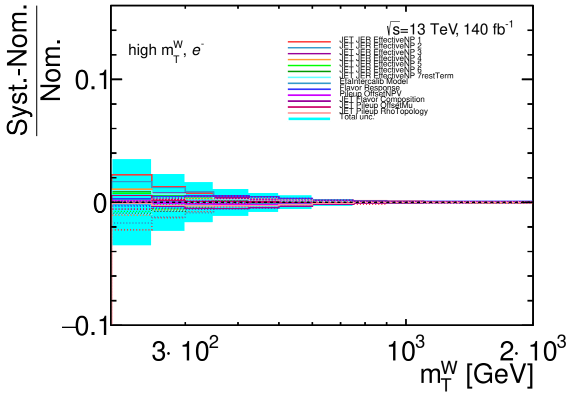

b) e^--channel

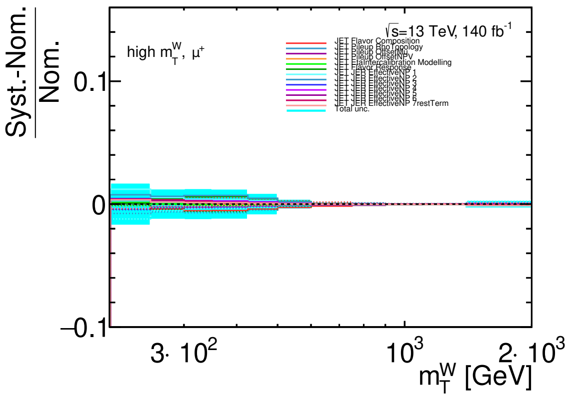

c) μ^+-channel

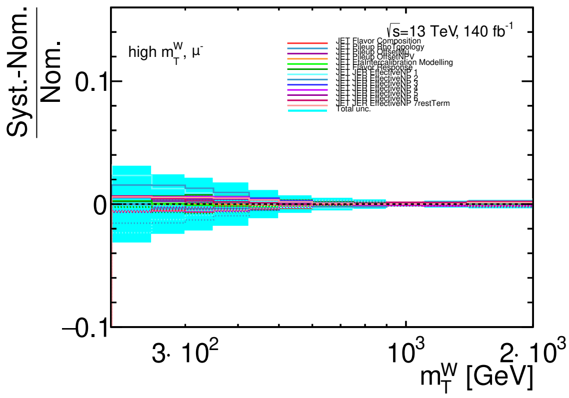

d) μ^--channel

Figure A.12: JET systematics in the measurement variable in m_T^W. Shown are the systematic uncertainties after the unfolding normalised to the unfolded cross section [5].

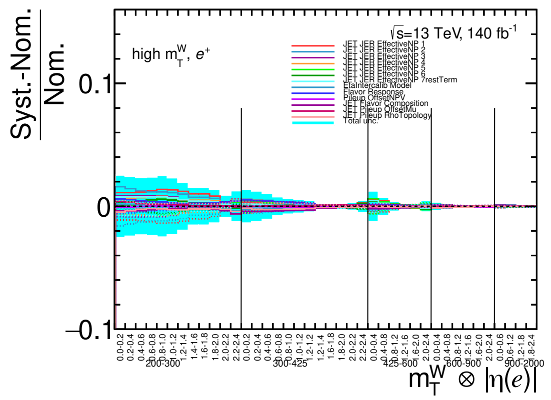

a) e^+-channel

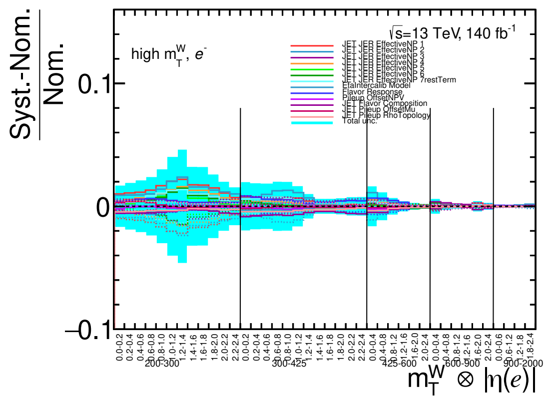

b) e^--channel

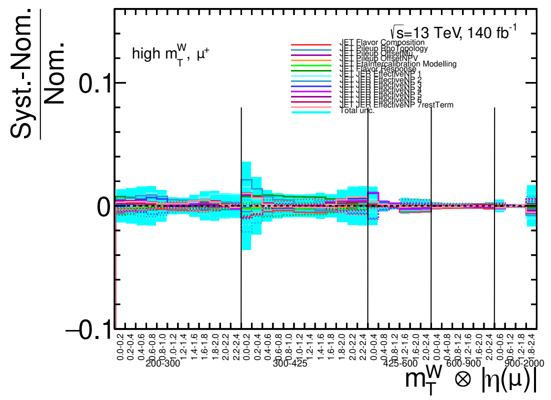

c) μ^+-channel

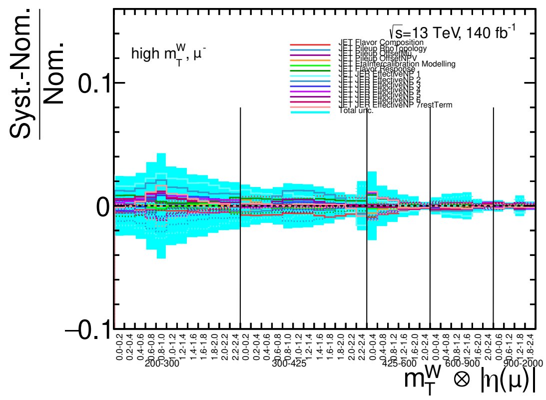

d) μ^--channel

Figure A.13: JET systematics in the measurement variable in $m_T^W \otimes |\eta(\ell)|$. Shown are the systematic uncertainties after the unfolding normalised to the unfolded cross section [5].

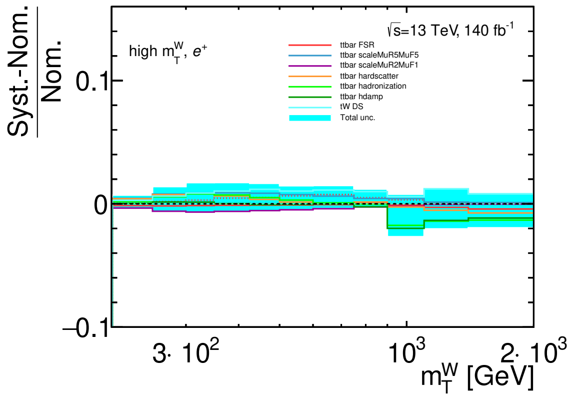

a) e^+-channel

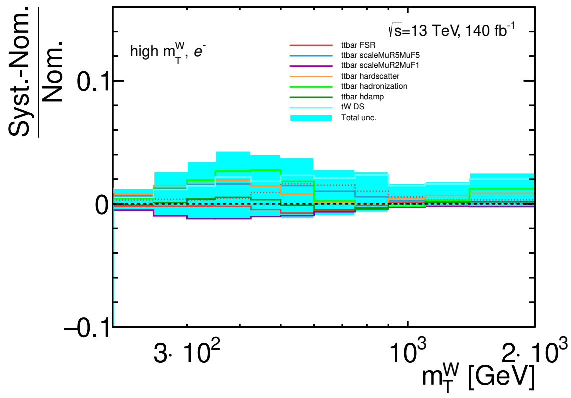

b) e^--channel

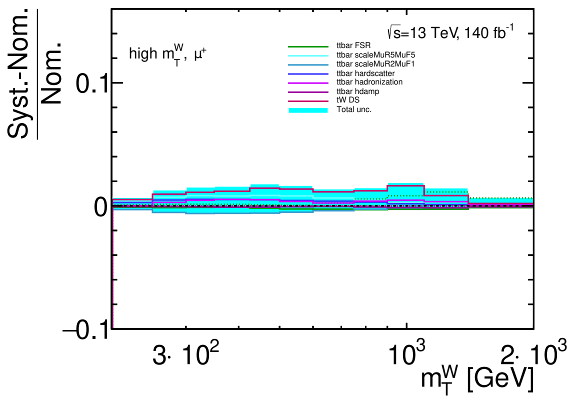

c) μ^+-channel

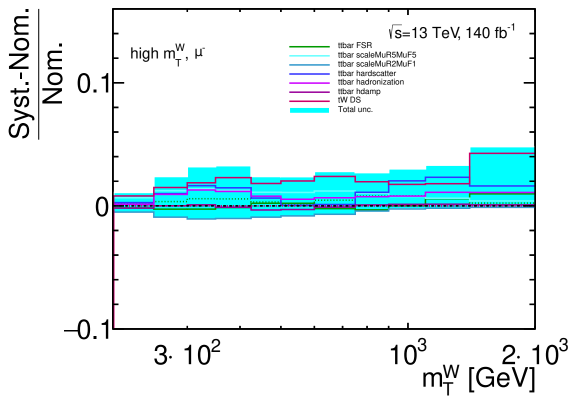

d) μ^--channel

Figure A.14: Theory systematics in the measurement variable in m_T^W. Shown are the systematic uncertainties after the unfolding normalised to the unfolded cross section [5].

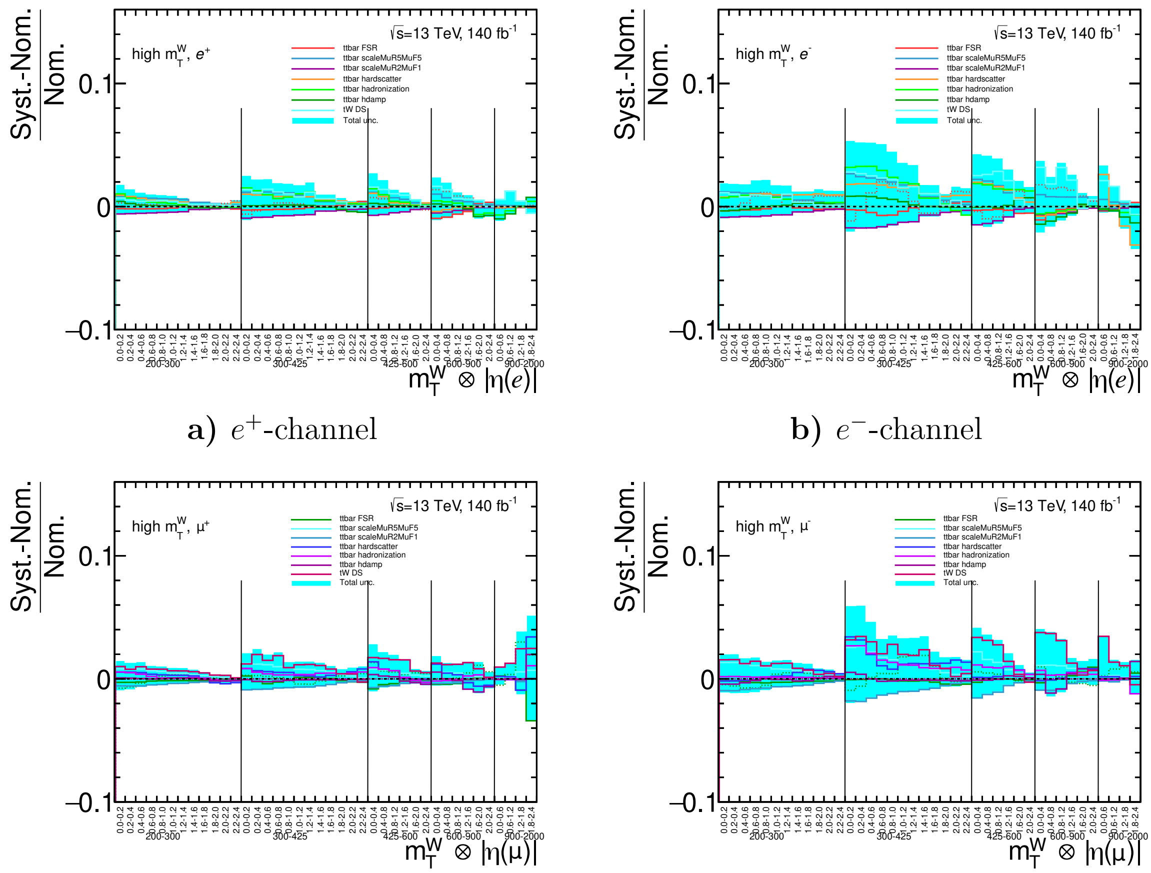

a) e^+-channel

b) e^--channel

c) μ^+-channel

d) μ^--channel

Figure A.15: Theory systematics in the measurement variable in $m_T^W \otimes |\eta(\ell)|$. Shown are the systematic uncertainties after the unfolding normalised to the unfolded cross section [5].

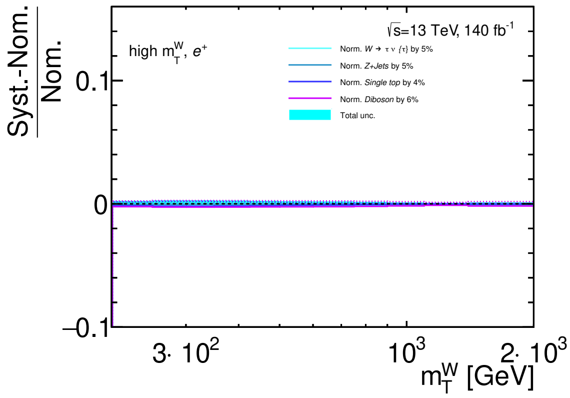

a) e^+-channel

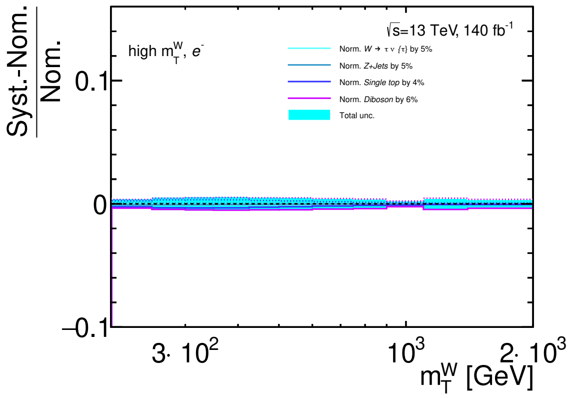

b) e^--channel

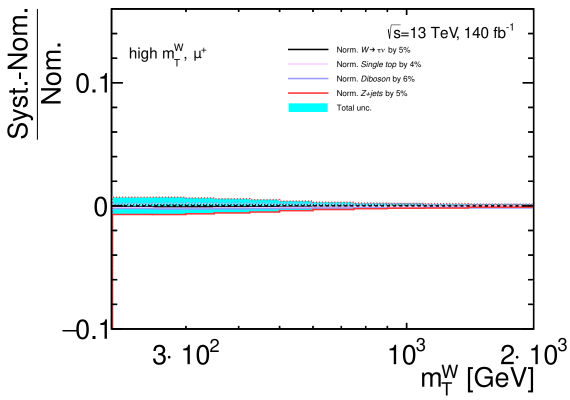

c) μ^+-channel

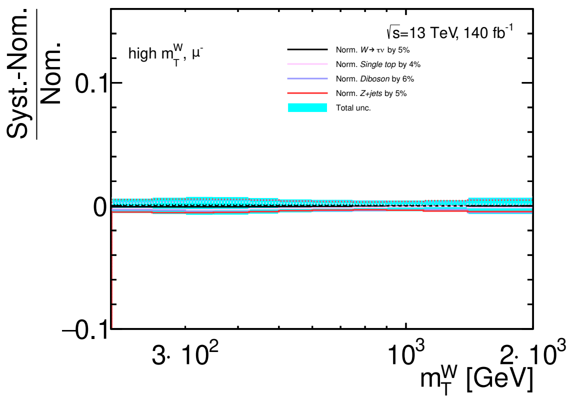

d) μ^--channel

Figure A.16: Flat cross section uncertainties in the measurement variable in m_T^W. Shown are the systematic uncertainties after the unfolding normalised to the unfolded cross section [5].

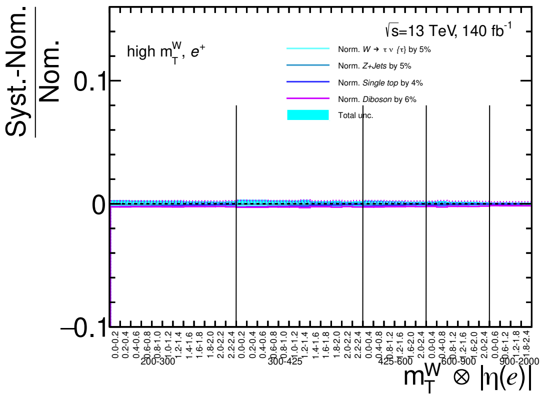

a) e^+-channel

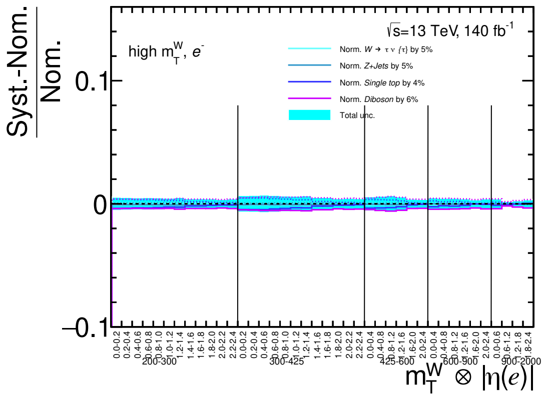

b) e^--channel

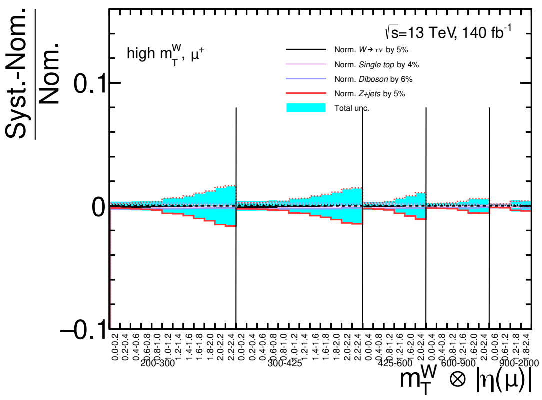

c) μ^+-channel

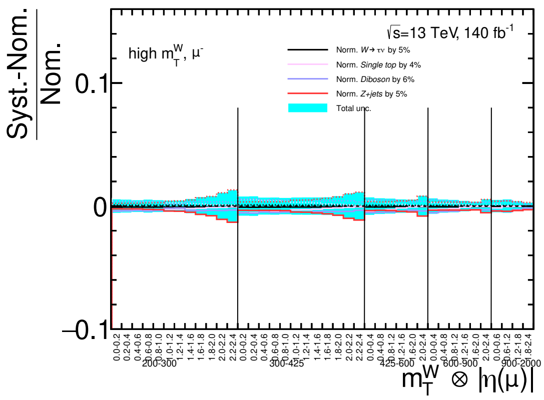

d) μ^--channel

Figure A.17: Flat cross section uncertainties in the measurement variable in $m_T^W \otimes |\eta(\ell)|$. Shown are the systematic uncertainties after the unfolding normalised to the unfolded cross section [5].

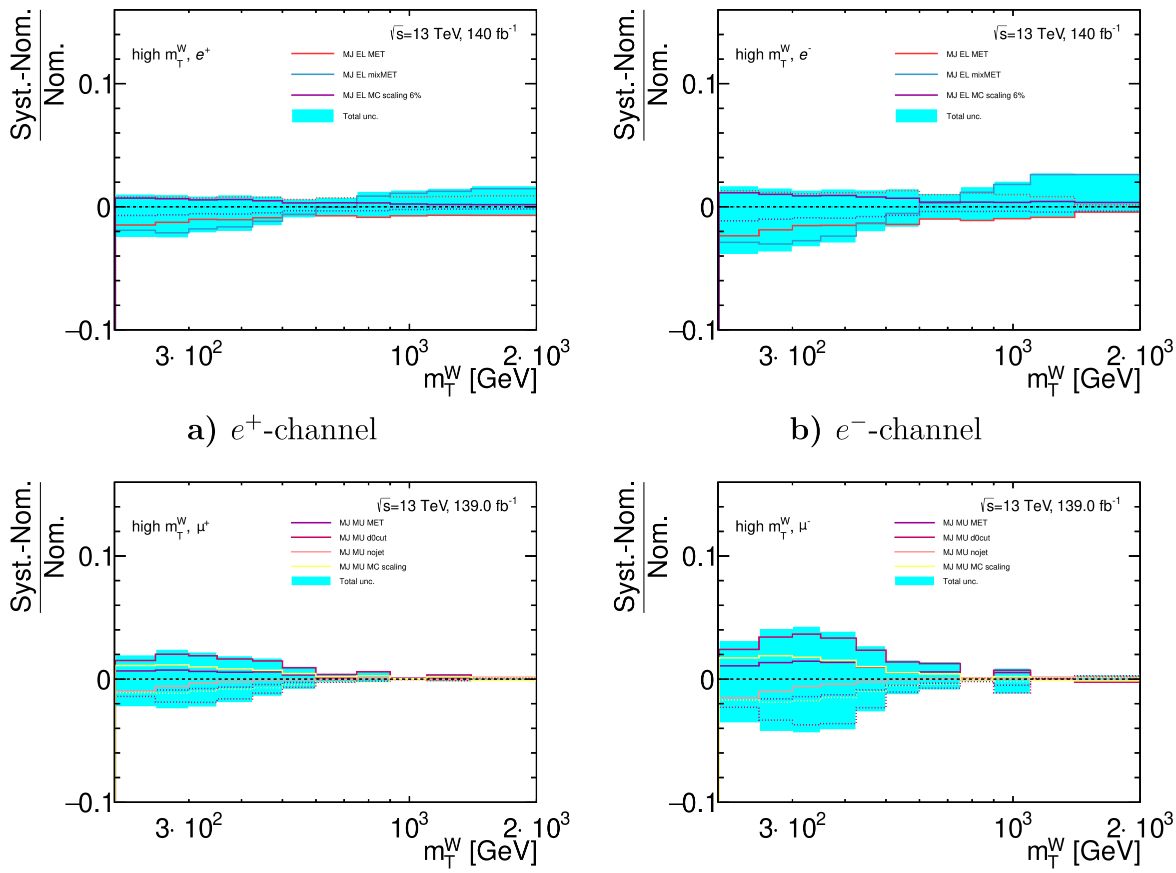

a) e^+-channel **b)** e^--channel **c)** μ^+-channel **d)** μ^--channel

Figure A.18: Uncertainties associated to the fake lepton background in the measurement variable in m_T^W. Shown are the systematic uncertainties after the unfolding normalised to the unfolded cross section [5].

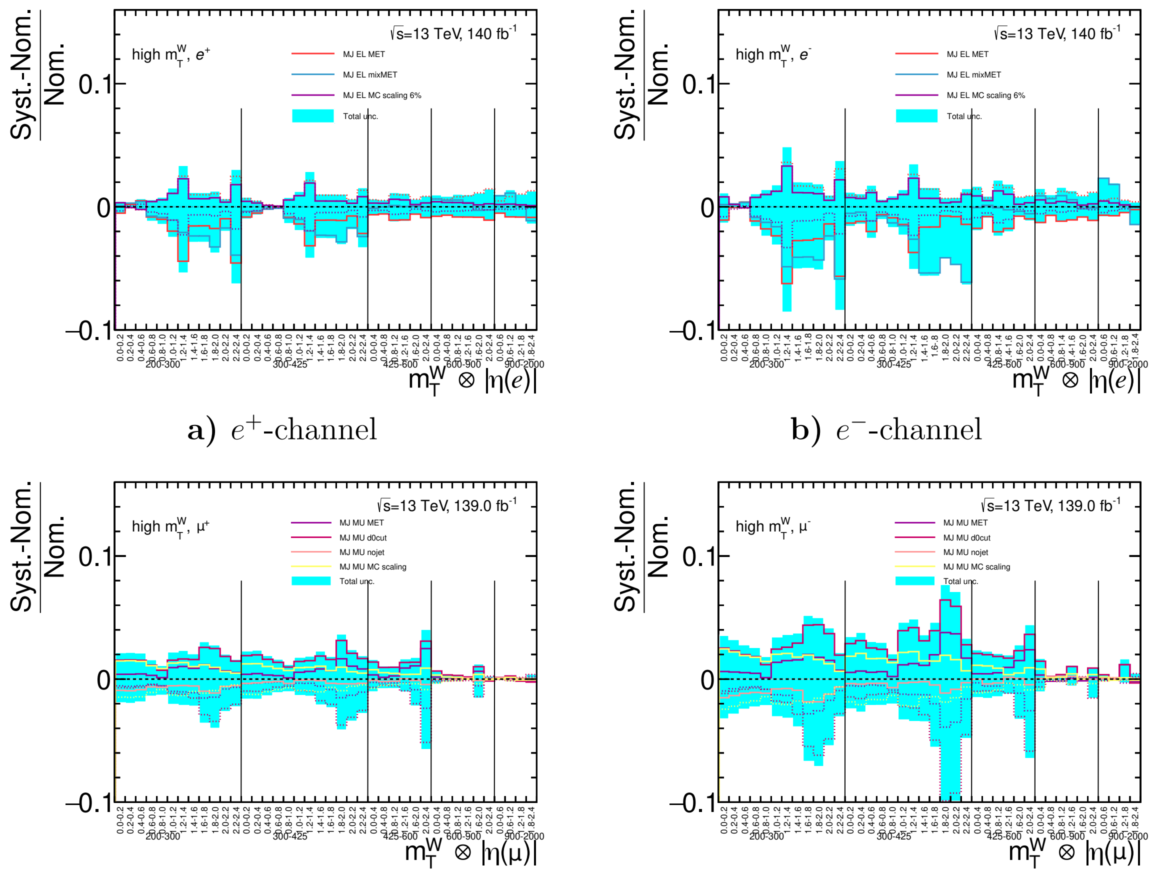

a) e^+-channel

b) e^--channel

c) μ^+-channel

d) μ^--channel

Figure A.19: Uncertainties associated to the fake lepton background in the measurement variable in $m_T^W \otimes |\eta(\ell)|$. Shown are the systematic uncertainties after the unfolding normalised to the unfolded cross section [5].

Appendix B

Supplemental material for the combination

B.1 Sum of pulls per bin

Lets consider a bin i of a combination with two contributing measurements, i.e. $W_{i,e} = 1$ for exact two $e \in \{1, \cdots N_e\}\}$. W.l.o.g. let these e be 1 and 2. We calculate the sum of the pulls of the initial central values $p^{i,1} + p^{i,2}$. For simplicity, the index i is relaxed in the following. The denominator of Equation 4.7 can be written as:

$$\sqrt{\Delta_e^2 - \Delta_{aver}^2} = \sqrt{\Delta_e^2 - \frac{1}{\frac{1}{\Delta_1^2} + \frac{1}{\Delta_2^2}}} = \sqrt{\frac{\Delta_e^2(\Delta_1^2 + \Delta_2^2) - \Delta_1^2\Delta_2^2}{\Delta_1^2 + \Delta_2^2}} \tag{B.1}$$

$$= \sqrt{\frac{\Delta_e^2\Delta_1^2 + \Delta_e^2\Delta_2^2 - \Delta_1^2\Delta_2^2}{\Delta_1^2 + \Delta_2^2}} = \sqrt{\frac{\Delta_e^4}{\Delta_1^2 + \Delta_2^2}} \tag{B.2}$$

$$= \frac{\Delta_e^2}{\sqrt{\Delta_1^2 + \Delta_2^2}}. \tag{B.3}$$

By defining $\mu_e^S := \mu_e + \sum_{j=1}^{N_s} \Gamma_e^j \beta_j$, Equation 4.4 becomes to:

$$\mu_{aver} = \frac{\sum_{e=1}^{N_e} \left(\mu_e + \sum_{j=1}^{N_s} \Gamma_e^j \beta_j\right) \frac{W_e}{\Delta_e^2}}{\sum_{e=1}^{N_e} \frac{W_e}{\Delta_e^2}} \tag{B.4}$$

$$= \Delta_{aver}^2 \sum_{e=1}^{N_e} \left(\mu_e + \sum_{j=1}^{N_s} \Gamma_e^j \beta_j\right) \frac{W_e}{\Delta_e^2} \tag{B.5}$$

$$= \Delta_{aver}^2 \sum_{e=1}^{2} \frac{\mu_e^S}{\Delta_e^2}, \tag{B.6}$$

and Equation 4.7 becomes to:

$$p^e = \frac{\mu_{aver} - \left(\mu_e + \sum_{j=1}^{N_s} \Gamma_e^j \beta_j\right)}{\sqrt{\Delta_e^2 - \Delta_{aver}^2}} \tag{B.7}$$

$$= \frac{\sqrt{\Delta_1^2 + \Delta_2^2}}{\Delta_e^2} \left(\mu_{aver} - \left(\mu_e + \sum_{j=1}^{N_s} \Gamma_e^j \beta_j\right)\right) \tag{B.8}$$

$$= \frac{\sqrt{\Delta_1^2 + \Delta_2^2}}{\Delta_e^2} \left(\mu_{aver} - \mu_e^S\right) \tag{B.9}$$

$$= \frac{\sqrt{\Delta_1^2 + \Delta_2^2}}{\Delta_e^2} \left(\Delta_{aver}^2 \left(\frac{\mu_1^S}{\Delta_1^2} + \frac{\mu_2^S}{\Delta_2^2}\right) - \mu_e^S\right). \tag{B.10}$$

This leads to:

$$p^1 + p^2 = \sqrt{\Delta_1^2 + \Delta_2^2} \left[-\frac{\mu_1^S}{\Delta_1^2} + \frac{\Delta_{aver}^2}{\Delta_1^2} \left(\frac{\mu_1^S}{\Delta_1^2} + \frac{\mu_2^S}{\Delta_2^2}\right) - \frac{\mu_1^S}{\Delta_1^2} + \frac{\Delta_{aver}^2}{\Delta_1^2} \left(\frac{\mu_1^S}{\Delta_1^2} + \frac{\mu_2^S}{\Delta_2^2}\right)\right] \tag{B.11}$$

$$= \sqrt{\Delta_1^2 + \Delta_2^2} \left[-\left(\frac{\mu_1^S}{\Delta_1^2} + \frac{\mu_2^S}{\Delta_2^2}\right) + \left(\frac{\mu_1^S}{\Delta_1^2} + \frac{\mu_2^S}{\Delta_2^2}\right) \underbrace{\Delta_{aver}^2 \left(\frac{1}{\Delta_1^2} + \frac{1}{\Delta_2^2}\right)}_{=1}\right] \tag{B.12}$$

$$= \sqrt{\Delta_1^2 + \Delta_2^2} \left[-\left(\frac{\mu_1^S}{\Delta_1^2} + \frac{\mu_2^S}{\Delta_2^2}\right) + \left(\frac{\mu_1^S}{\Delta_1^2} + \frac{\mu_2^S}{\Delta_2^2}\right)\right] = 0. \tag{B.13}$$

Thus, as long as only two measurements contribute to bin i, the sum over the pulls in this bin equals 0.

B.2 Supplemental material for the additional studies

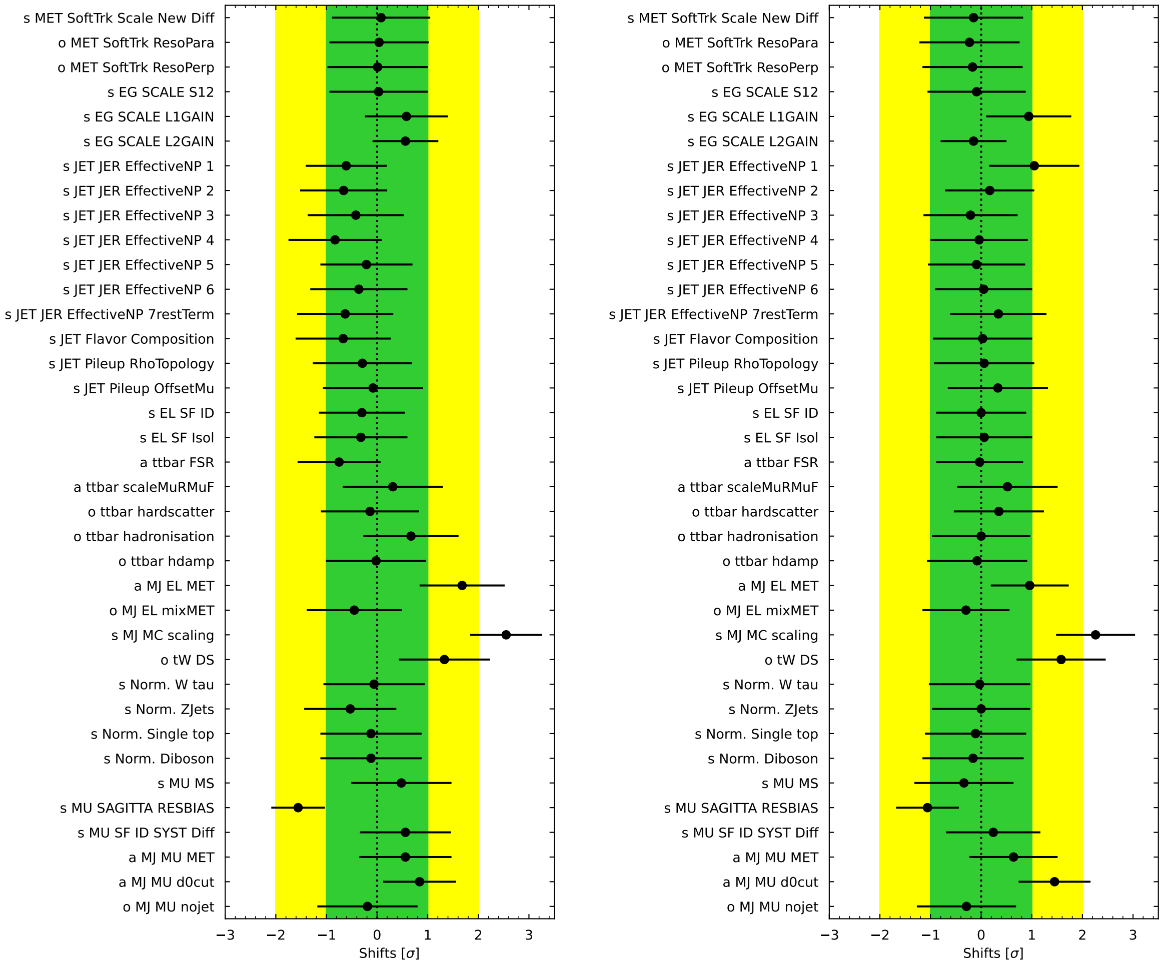

a) ℓ^+-channel b) ℓ^--channel

Figure B.1: All systematic shifts β_j for the charge decorrelated combination of ℓ^+- (a)) and ℓ^--channel (b)) in $m_T^W \otimes |\eta(\ell)|$ (See Figure 4.9). The error bars represent the reduction of the uncertainties by the combination.

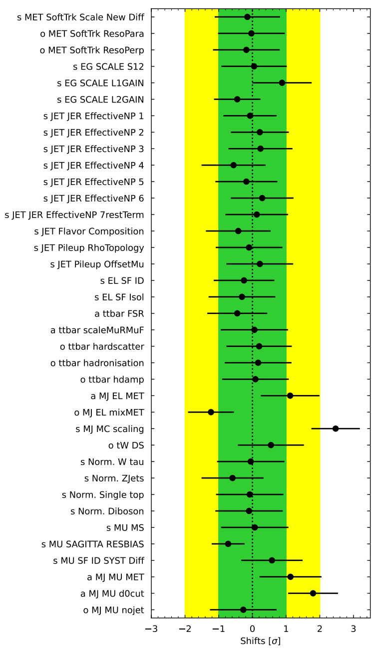

a) 200 GeV $< m_T^W <$ 300 GeV

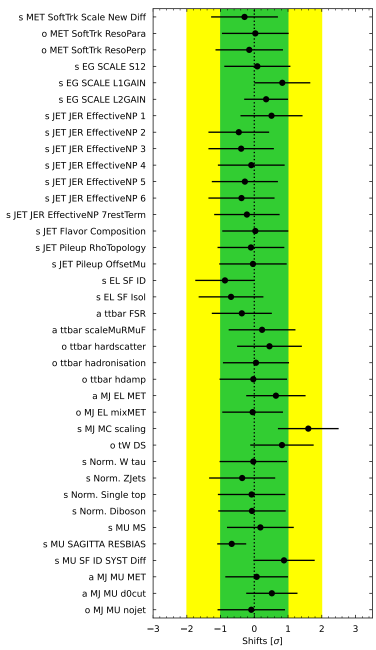

b) 300 GeV $< m_T^W <$ 425 GeV

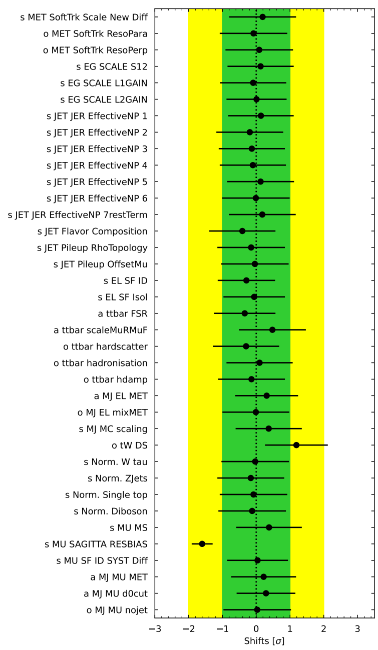

c) 425 GeV $< m_T^W <$ 2000 GeV

Figure B.2: All systematic shifts β_j for the combination per m_T^W-bin in $m_T^W \otimes |\eta(\ell)|$ (See Figure 4.11). The error bars represent the reduction of the uncertainties by the combination.

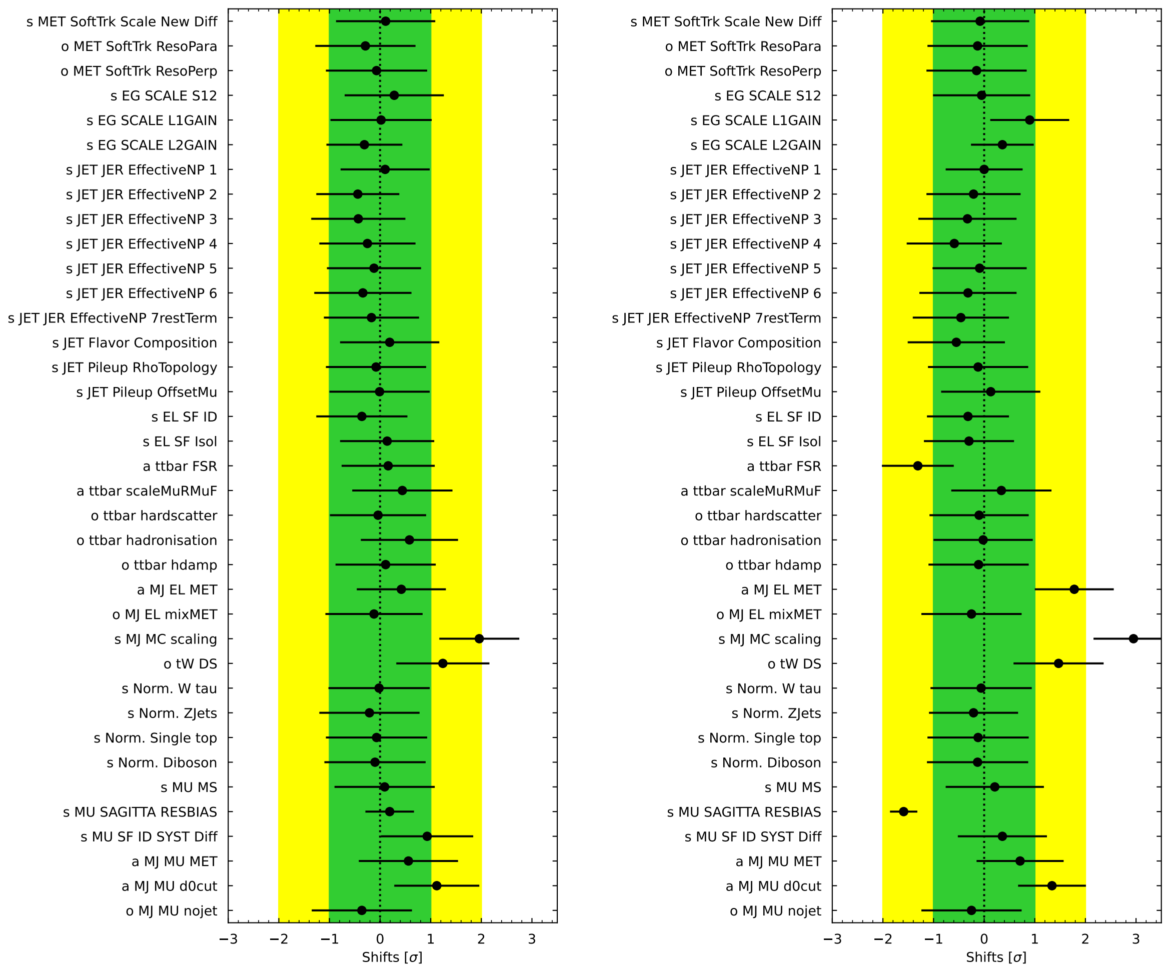

a) $|\eta(\ell)| < 1.0$ **b)** $|\eta(\ell)| > 1.0$

Figure B.3: All systematic shifts β_j for the combination decorrelated at $|\eta(\ell)| = 1.0$ in $m_T^W \otimes |\eta(\ell)|$ (See Figure 4.13). The error bars represent the reduction of the uncertainties by the combination.

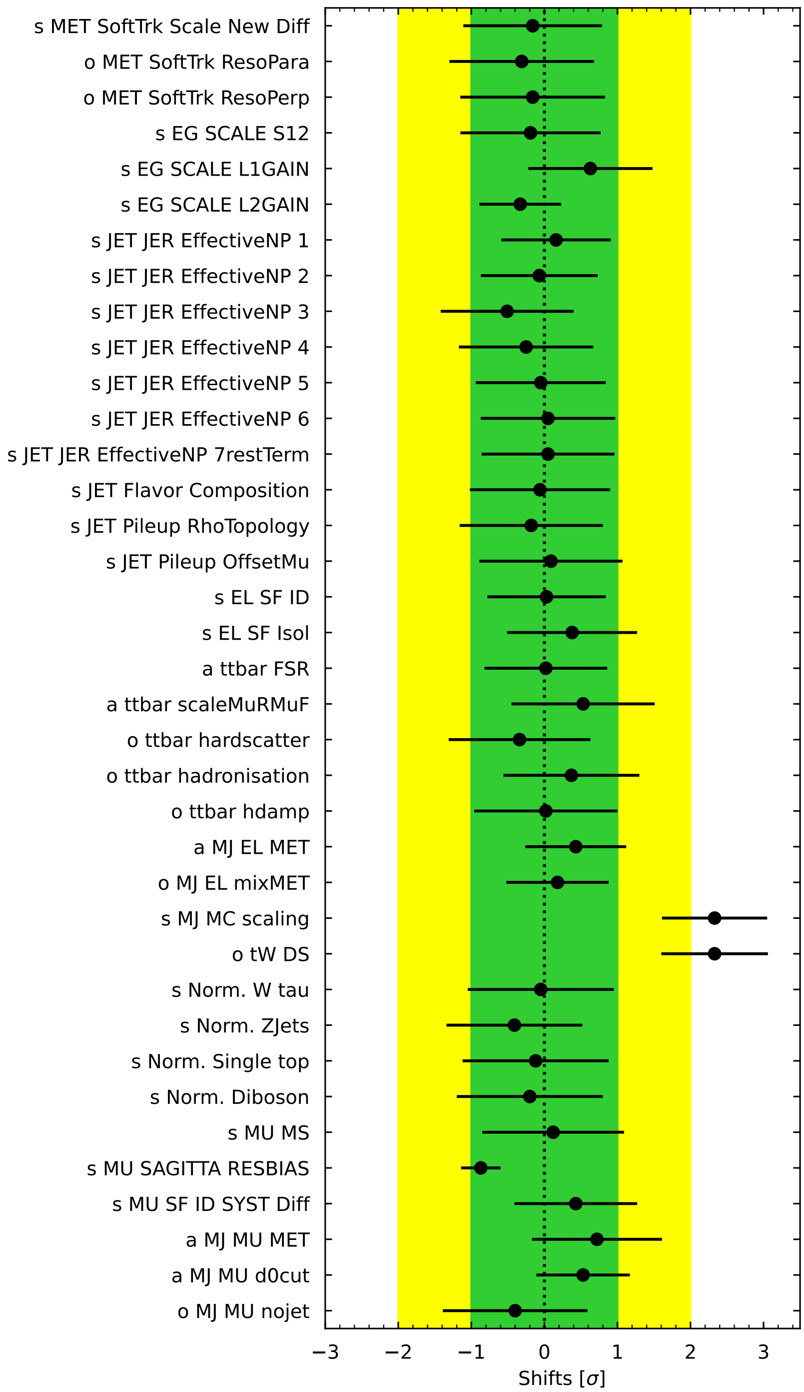

Figure B.4: All systematic shifts β_j for the combination in $m_T^W \otimes |\eta(\ell)|$ when some single bins are ignored in the combination (See Figure 4.15). The error bars represent the reduction of the uncertainties by the combination.

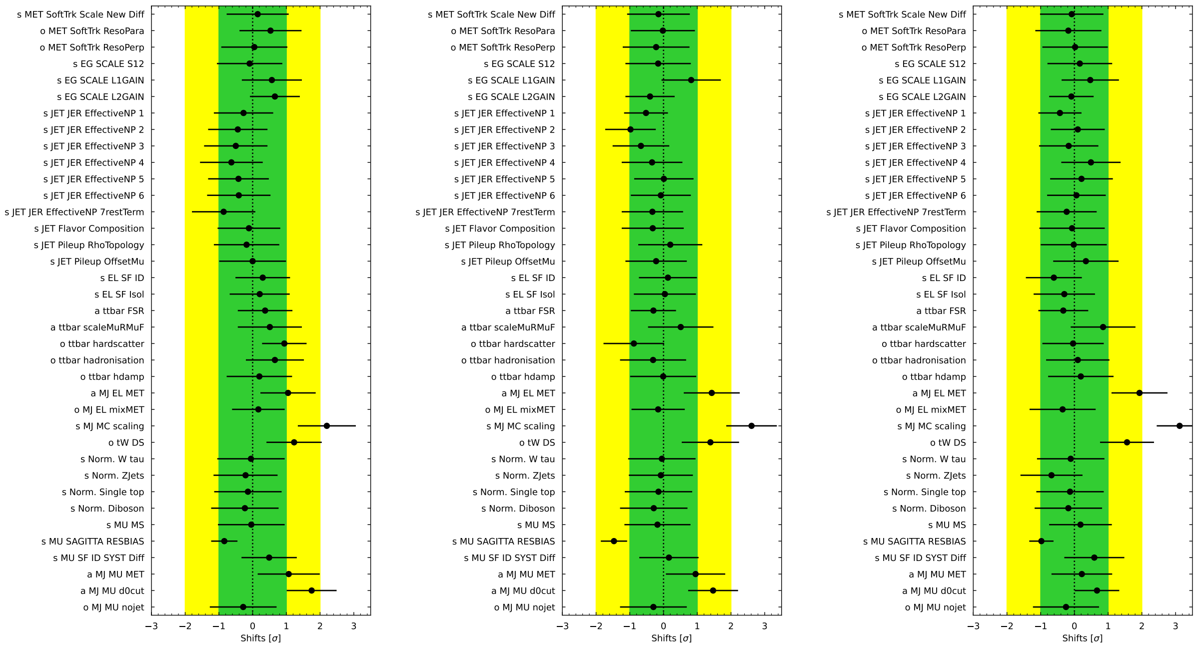

a) mc16a **b)** mc16d **c)** mc16e

Figure B.5: All systematic shifts β_j for the combination in $m_T^W \otimes |\eta(\ell)|$ separated per data taking period (See Figure 4.18). The error bars represent the reduction of the uncertainties by the combination.

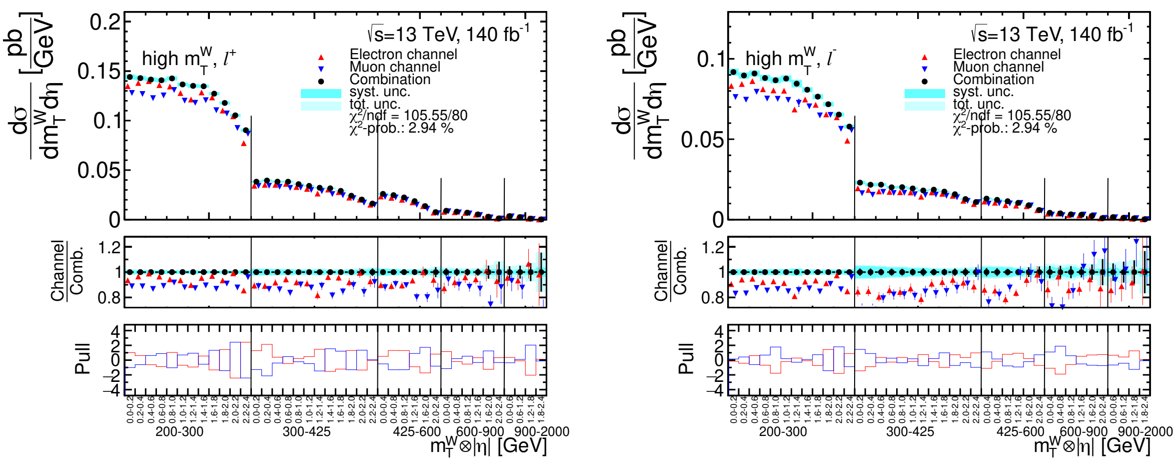

a) e^+-channel **b)** e^--channel

Figure B.6: Averaged cross section (black) in $m_T^W \otimes |\eta(\ell)|$ together with the input cross sections of electron (red) and muon (blue) channel when using 0 GeV $< E_T^{miss} <$ 30 GeV and 40 GeV $< E_T^{miss} <$ 65 GeV as up- and down-variation of the MJ EL MET systematic. The blue (light blue) uncertainty band gives the systematic (total) uncertainty. The error bars represent the statistical uncertainty. The middle panel shows the ratio with respect to the combined cross section. The bottom panel shows the pulls of the electron (red) and muon (blue) channel, according to Equation 4.6. The corresponding systematic shifts are presented in Figure B.8a.

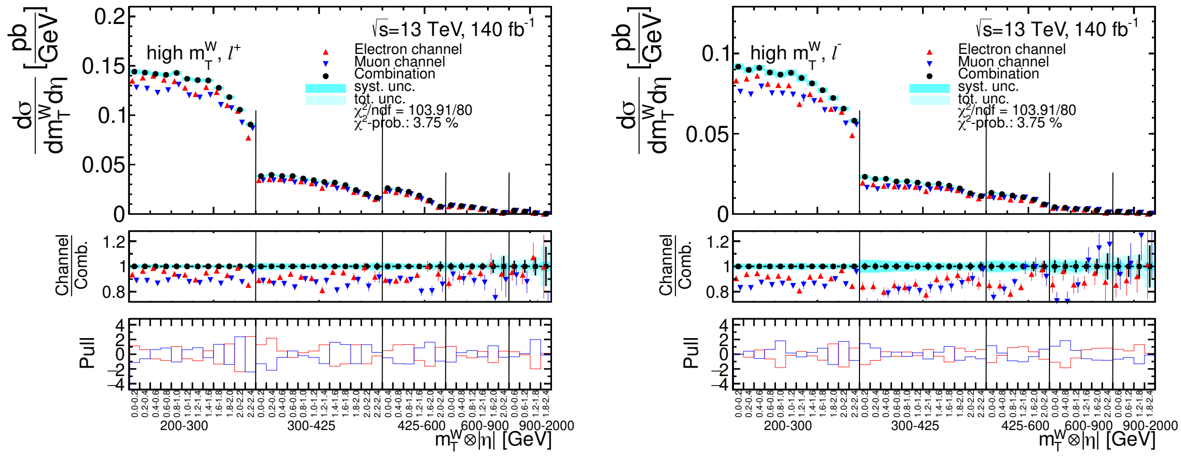

a) e^+-channel **b)** e^--channel

Figure B.7: Averaged cross section (black) in $m_T^W \otimes |\eta(\ell)|$ together with the input cross sections of electron (red) and muon (blue) channel when using 0 GeV $< E_T^{miss} <$ 20 GeV and 40 GeV $< E_T^{miss} <$ 65 GeV as up- and down-variation of the MJ EL MET systematic. The blue (light blue) uncertainty band gives the systematic (total) uncertainty. The error bars represent the statistical uncertainty. The middle panel shows the ratio with respect to the combined cross section. The bottom panel shows the pulls of the electron (red) and muon (blue) channel, according to Equation 4.6. The corresponding systematic shifts are presented in Figure B.8b.

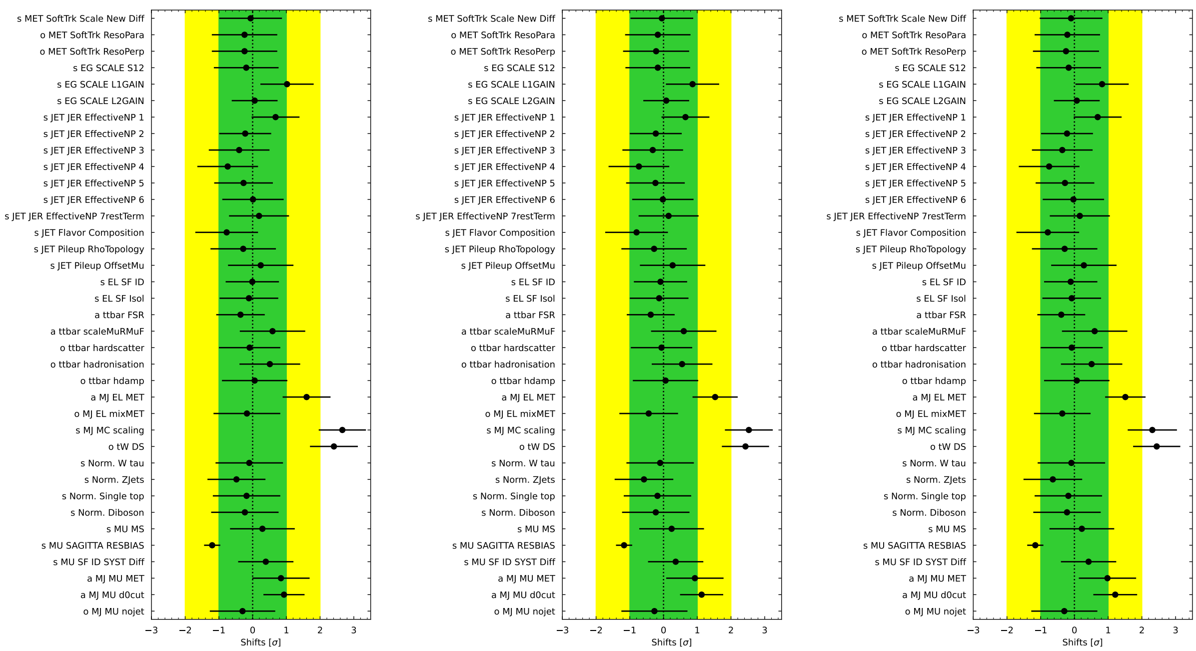

a) 0 GeV $< E_T^{miss} <$ 30 GeV & 40 GeV $< E_T^{miss} <$ 65 GeV **b)** 0 GeV $< E_T^{miss} <$ 20 GeV & 40 GeV $< E_T^{miss} <$ 65 GeV **c)** 0 GeV $< E_T^{miss} <$ 20 GeV & 30 GeV $< E_T^{miss} <$ 65 GeV

Figure B.8: All systematic shifts β_j for the combination in $m_T^W \otimes |\eta(\ell)|$ using different definitions of the MJ EL MET uncertainty (See Figure B.6, Figure B.7 Figure 4.29). The error bars represent the reduction of the uncertainties by the combination.

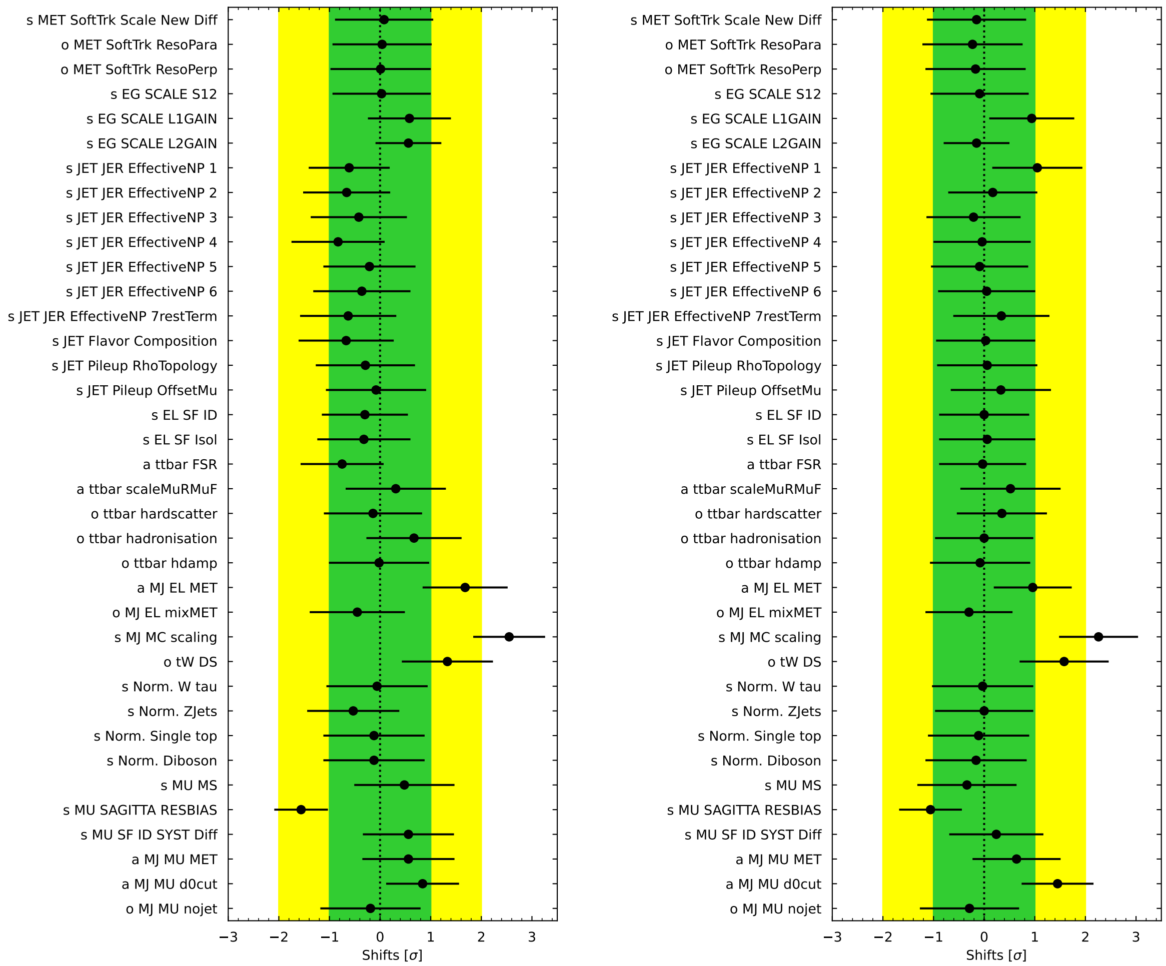

a) unsmoothed electron-MJ systematics

b) decorrelated MU SAGITTA RESBIAS systematic

Figure B.9: All systematic shifts β_j for the combination of with unsmoothed electron-multijet systematics (a), see Figure 4.35) and a decorrelated MU SAGITTA RESBIAS (b), see Figure 4.37) systematic in $m_T^W \otimes |\eta(\ell)|$. The error bars represent the reduction of the uncertainties by the combination.

B.3 Earlier state of the analysis

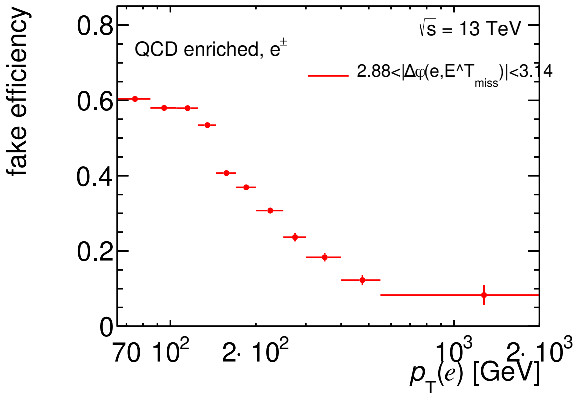

a) nominal: $1.4 < |\eta(\ell)| < 2.0$

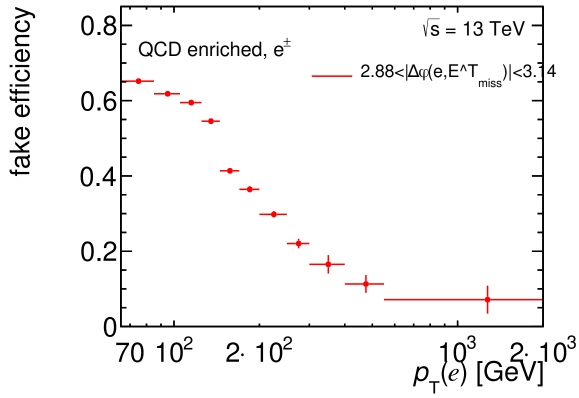

b) nominal $2.0 < |\eta(\ell)| < 2.4$

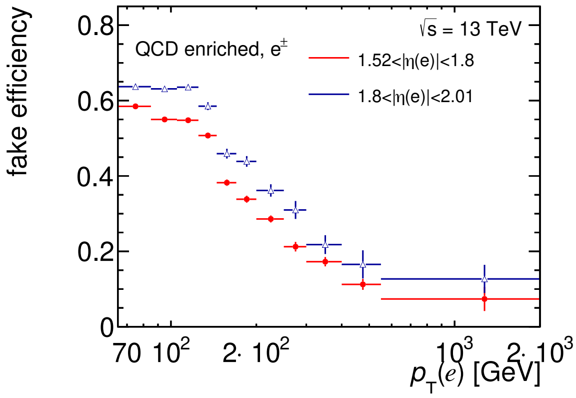

c) finer bins: $1.4 < |\eta(\ell)| < 2.01$

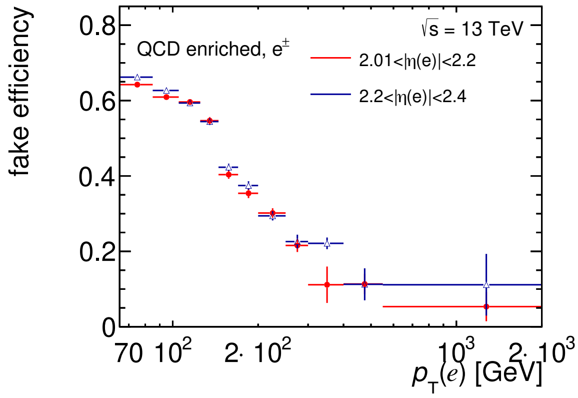

d) finer bins: $2.01 < |\eta(\ell)| < 2.4$

Figure B.10: Fake efficiencies in the nominal (top row) and the finer (bottom row) $|\eta|$-binning (see Section 4.6.1). Only the last $|\Delta\phi|$-bin ($2.88 < |\Delta(\phi(e, E_T^{miss}))| < 3.14$) and the region $|\eta(e)| > 1.4$ is shown.

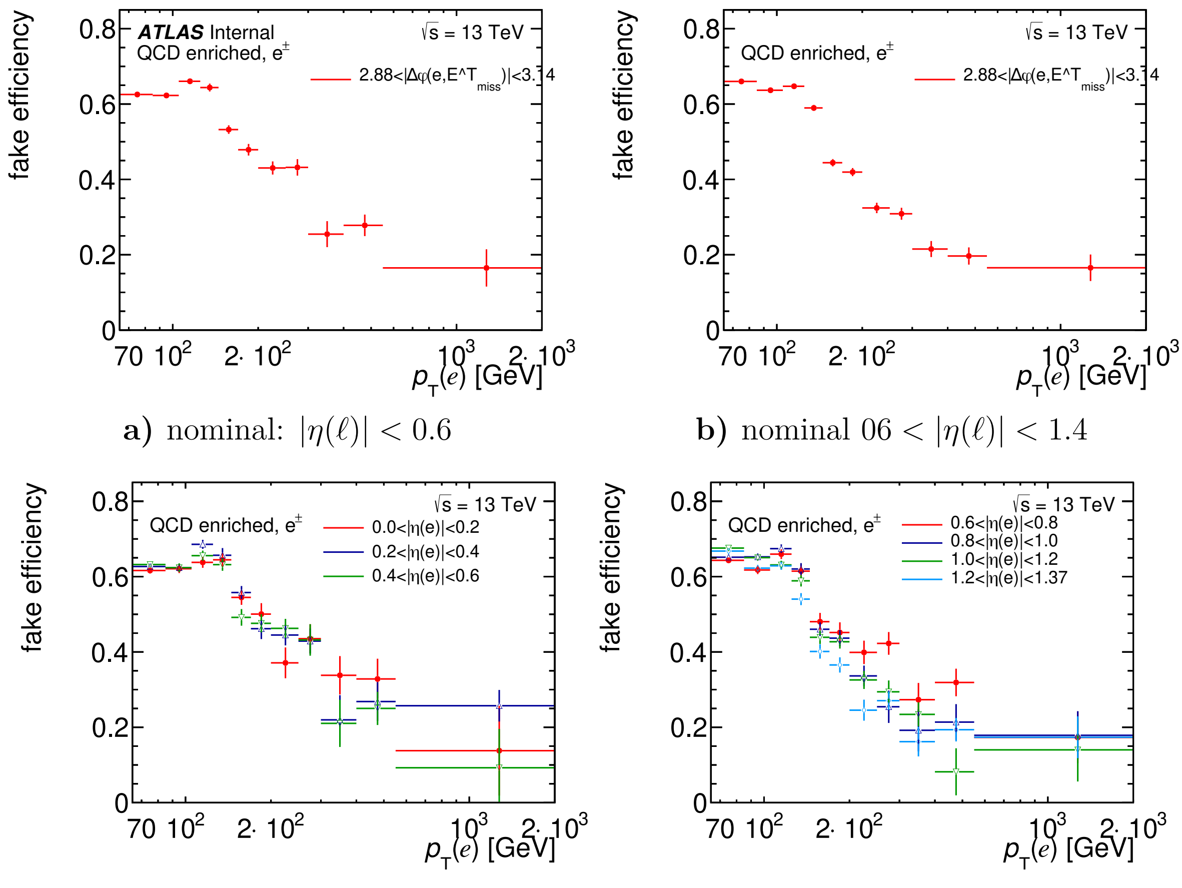

a) nominal: $|\eta(\ell)| < 0.6$ **b)** nominal $06 < |\eta(\ell)| < 1.4$

c) finer bins: $|\eta(\ell)| < 0.6$ **d)** finer bins: $0.6 < |\eta(\ell)| < 1.37$

Figure B.11: Fake efficiencies in the nominal (top row) and the finer (bottom row) $|\eta|$-binning (see Section 4.6.1). Only the last $|\Delta\phi|$-bin $(2.88 < |\Delta(\phi(e, E_T^{miss}))| < 3.14)$ and the region $|\eta(e)| < 1.4$ is shown.

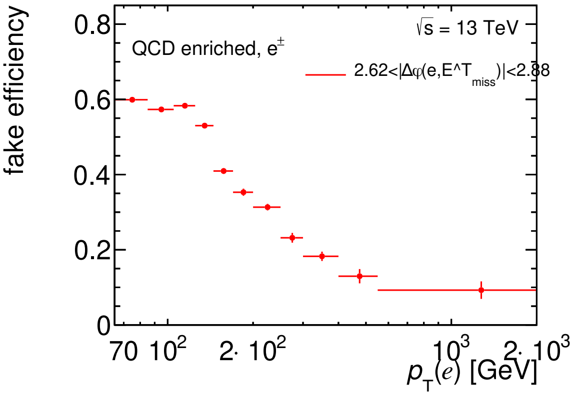

a) nominal: $1.4 < |\eta(\ell)| < 2.0$

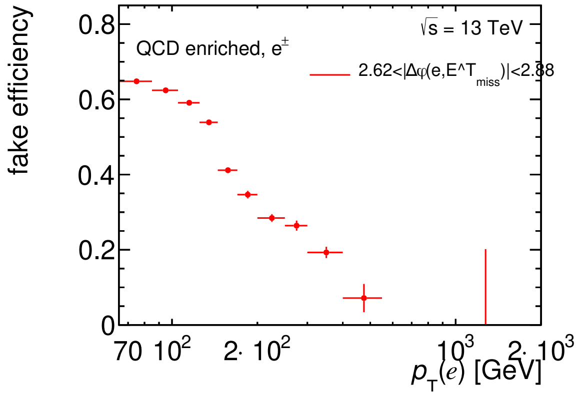

b) nominal $2.0 < |\eta(\ell)| < 2.4$

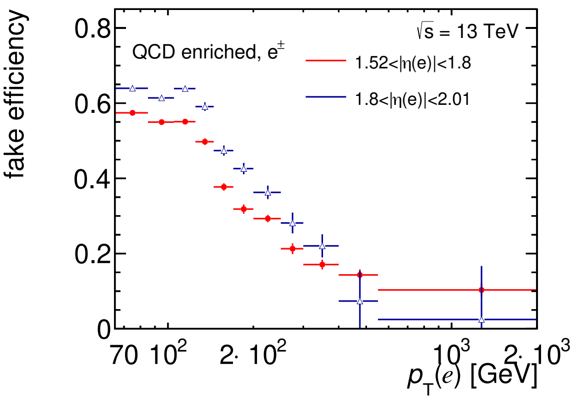

c) finer bins: $1.4 < |\eta(\ell)| < 2.01$

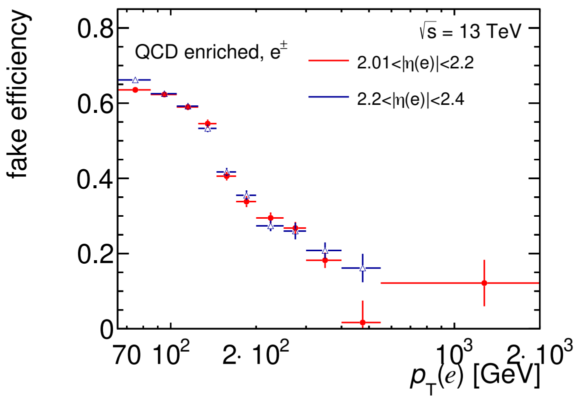

d) finer bins: $2.01 < |\eta(\ell)| < 2.4$

Figure B.12: Fake efficiencies in the nominal (top row) and the finer (bottom row) $|\eta|$-binning (see Section 4.6.1). Only the fourth $|\Delta\phi|$-bin ($2.62 < |\Delta(\phi(e, E_T^{miss}))| < 2.88$) and the region $|\eta(e)| > 1.4$ is shown.

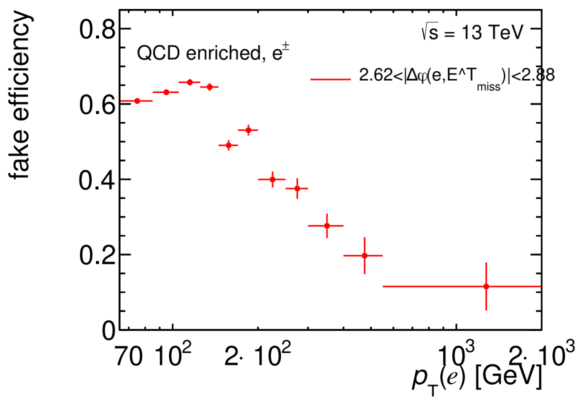

a) nominal: $|\eta(\ell)| < 0.6$

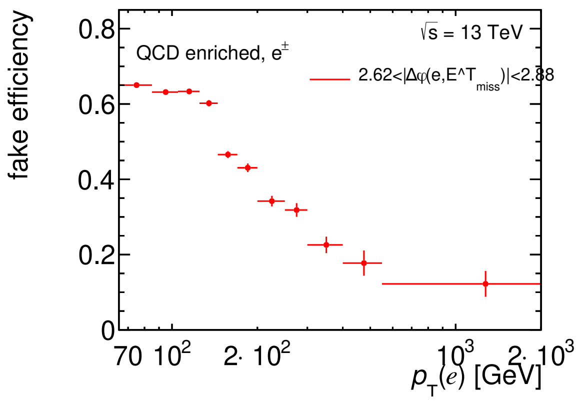

b) nominal $06 < |\eta(\ell)| < 1.4$

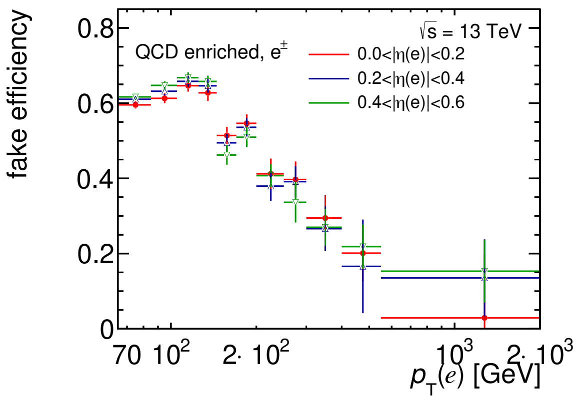

c) finer bins: $|\eta(\ell)| < 0.6$

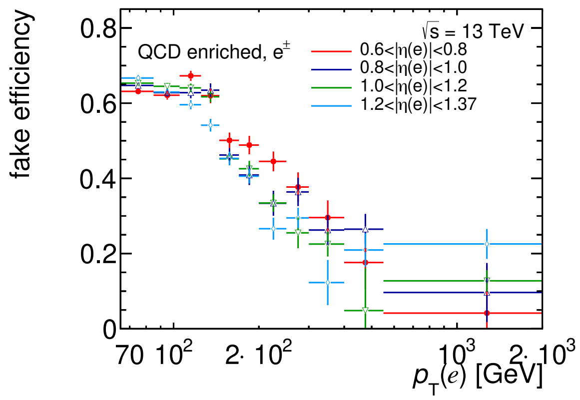

d) finer bins: $0.6 < |\eta(\ell)| < 1.37$

Figure B.13: Fake efficiencies in the nominal (top row) and the finer (bottom row) $|\eta|$-binning (see Section 4.6.1). Only the fourth $|\Delta\phi|$-bin $(2.62 < |\Delta(\phi(e, E_T^{miss}))| < 2.88)$ and the region $|\eta(e)| < 1.4$ is shown.

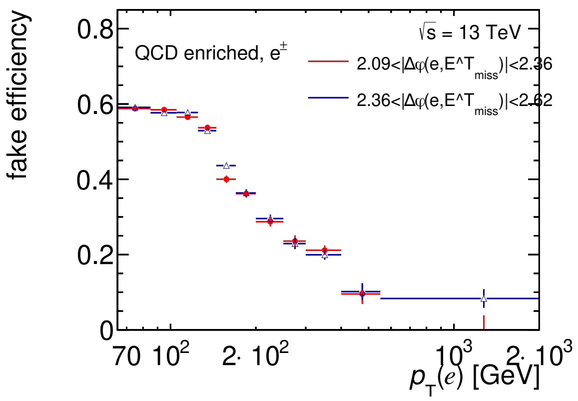

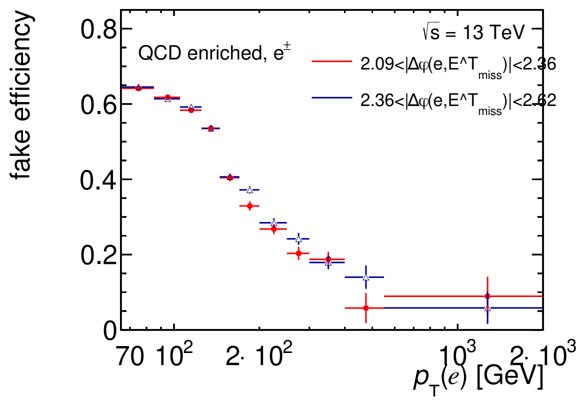

a) nominal: $1.4 < |\eta(\ell)| < 2.0$

b) nominal $2.0 < |\eta(\ell)| < 2.4$

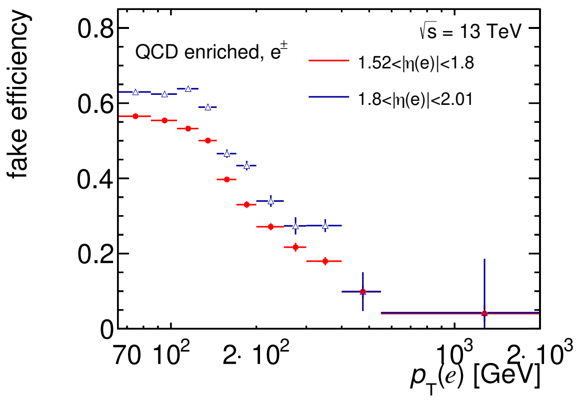

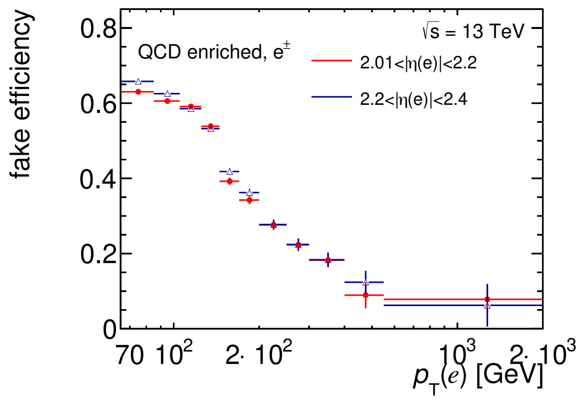

c) finer bins: $1.4 < |\eta(\ell)| < 2.01$

d) finer bins: $2.01 < |\eta(\ell)| < 2.4$

Figure B.14: Fake efficiencies in the nominal (top row) and the finer (bottom row) $|\eta|$-binning (see Section 4.6.1). Only the third $|\Delta\phi|$-bin $(2.09 < |\Delta(\phi(e, E_T^{miss}))| < 2.62)$ and the region $|\eta(e)| > 1.4$ is shown.

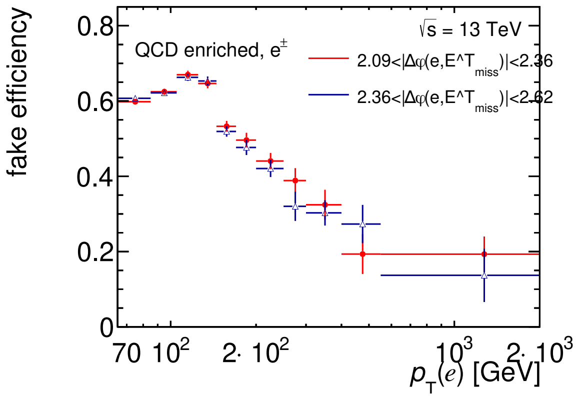

a) nominal: $|\eta(\ell)| < 0.6$

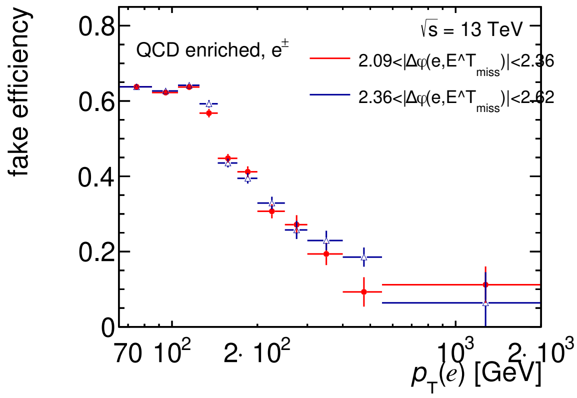

b) nominal $06 < |\eta(\ell)| < 1.4$

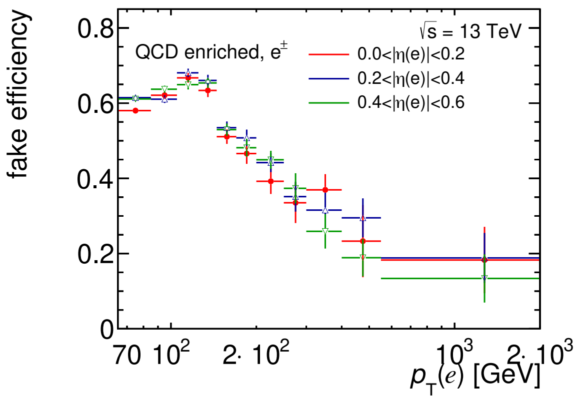

c) finer bins: $|\eta(\ell)| < 0.6$

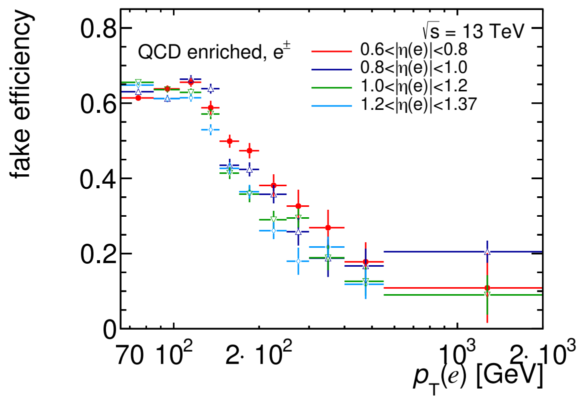

d) finer bins: $0.6 < |\eta(\ell)| < 1.37$

Figure B.15: Fake efficiencies in the nominal (top row) and the finer (bottom row) $|\eta|$-binning (see Section 4.6.1). Only the third $|\Delta\phi|$-bin ($2.09 < |\Delta(\phi(e, E_T^{miss}))| < 2.62$) and the region $|\eta(e)| < 1.4$ is shown.

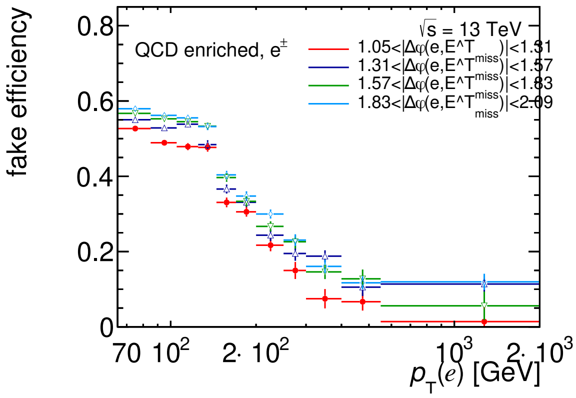

a) nominal: $1.4 < |\eta(\ell)| < 2.0$

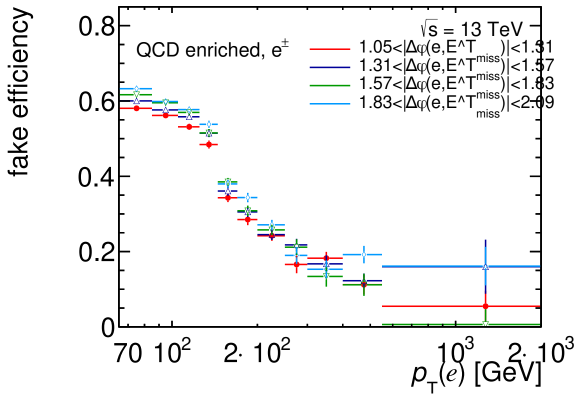

b) nominal $2.0 < |\eta(\ell)| < 2.4$

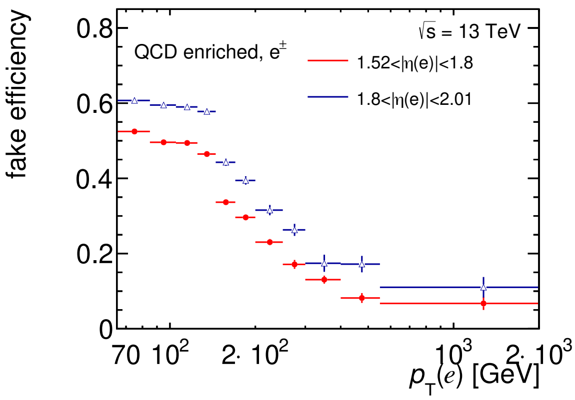

c) finer bins: $1.4 < |\eta(\ell)| < 2.01$

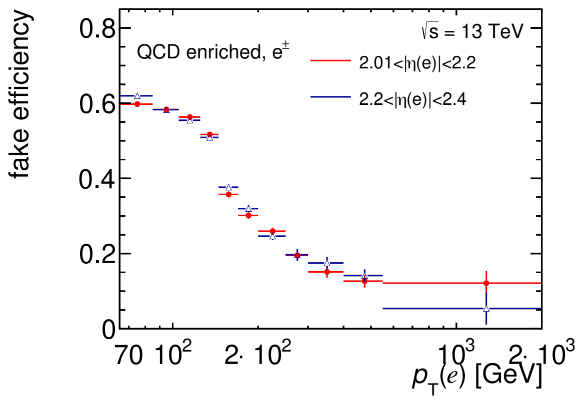

d) finer bins: $2.01 < |\eta(\ell)| < 2.4$

Figure B.16: Fake efficiencies in the nominal (top row) and the finer (bottom row) $|\eta|$-binning (see Section 4.6.1). Only the second $|\Delta\phi|$-bin ($1.05 < |\Delta(\phi(e, E_T^{miss}))| < 2.09$) and the region $|\eta(e)| > 1.4$ is shown.

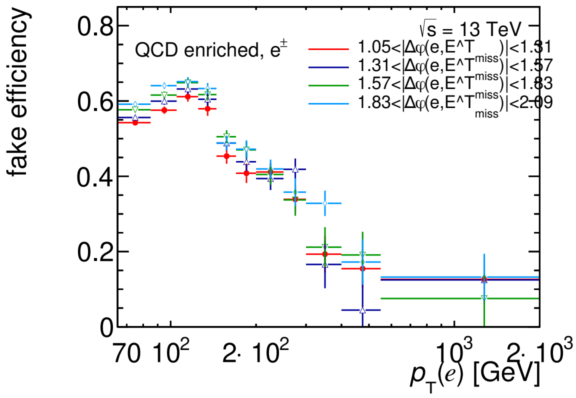

a) nominal: $|\eta(\ell)| < 0.6$

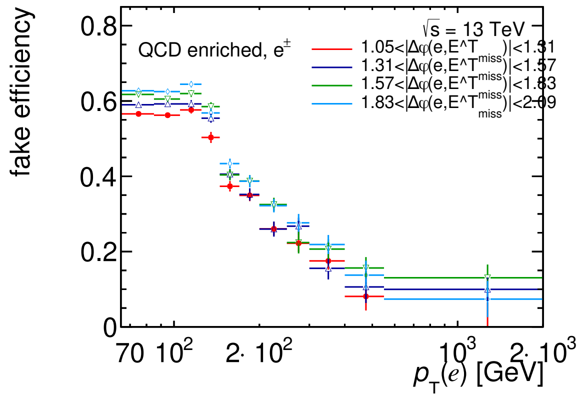

b) nominal $06 < |\eta(\ell)| < 1.4$

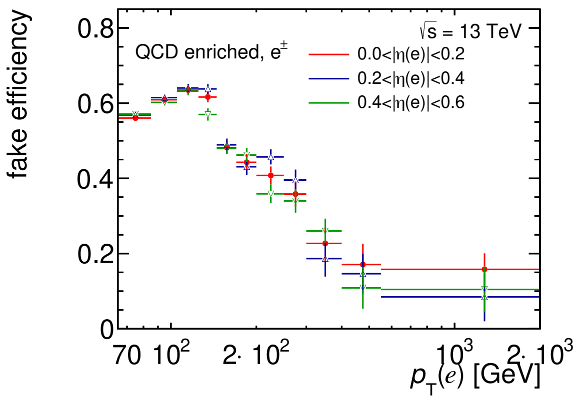

c) finer bins: $|\eta(\ell)| < 0.6$

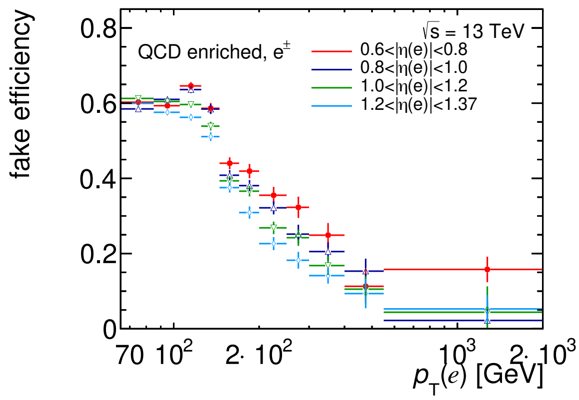

d) finer bins: $0.6 < |\eta(\ell)| < 1.37$

Figure B.17: Fake efficiencies in the nominal (top row) and the finer (bottom row) $|\eta|$-binning (see Section 4.6.1). Only the second $|\Delta\phi|$-bin ($1.05 < |\Delta(\phi(e, E_T^{miss}))| < 2.09$) and the region $|\eta(e)| < 1.4$ is shown.

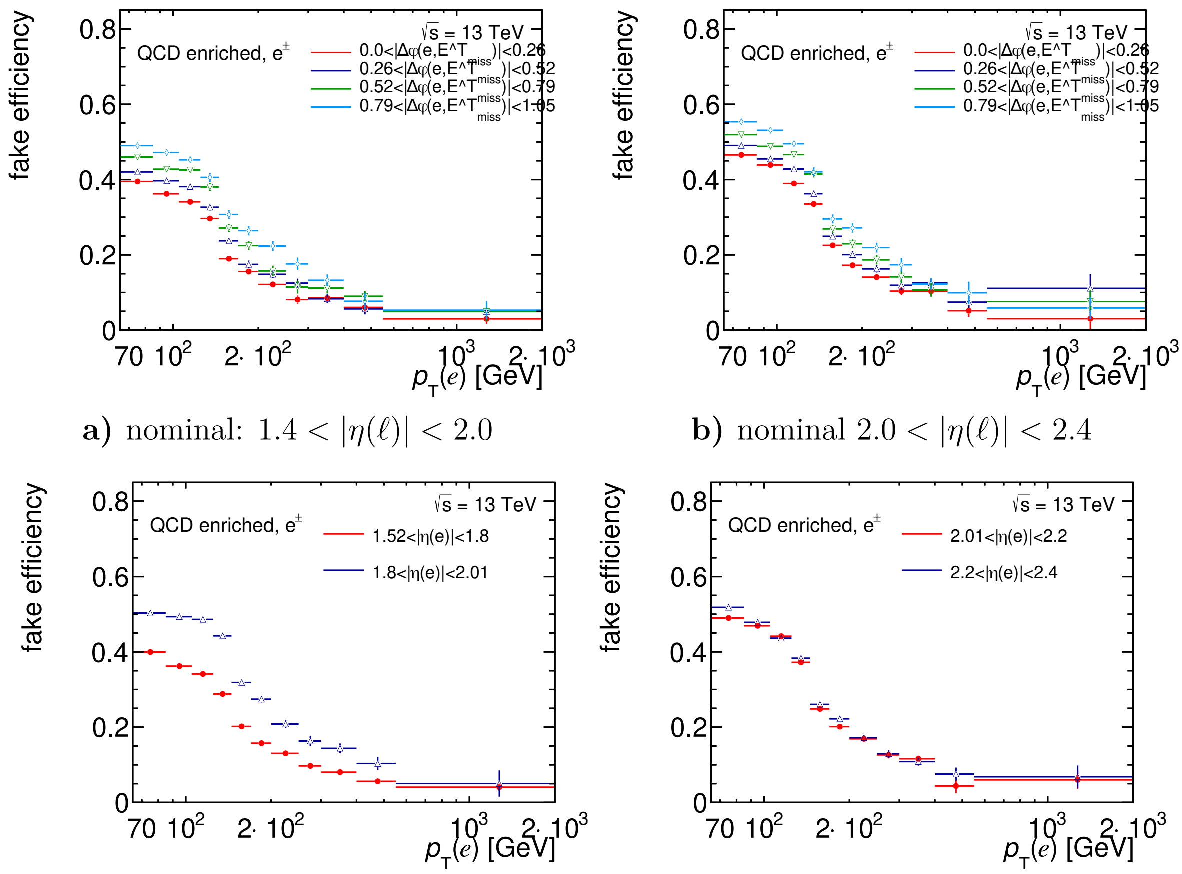

a) nominal: $1.4 < |\eta(\ell)| < 2.0$

b) nominal $2.0 < |\eta(\ell)| < 2.4$

c) finer bins: $1.4 < |\eta(\ell)| < 2.01$

d) finer bins: $2.01 < |\eta(\ell)| < 2.4$

Figure B.18: Fake efficiencies in the nominal (top row) and the finer (bottom row) $|\eta|$-binning (see Section 4.6.1). Only the fist $|\Delta\phi|$-bin ($|\Delta(\phi(e, E_T^{miss}))| < 1.05$) and the region $|\eta(e)| > 1.4$ is shown.

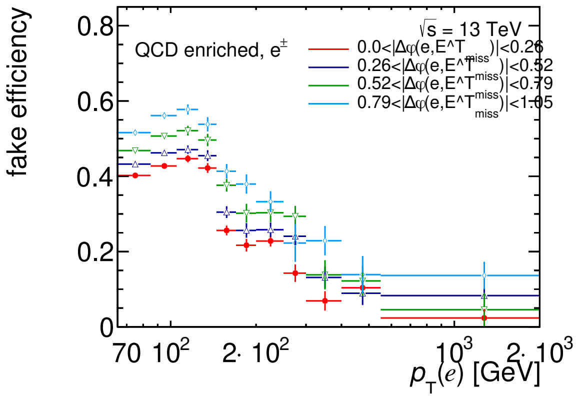

a) nominal: $|\eta(\ell)| < 0.6$

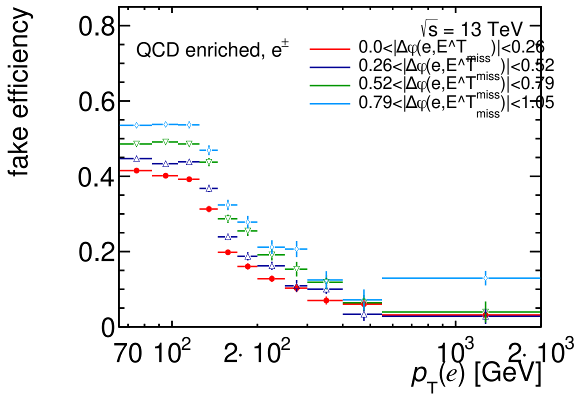

b) nominal $06 < |\eta(\ell)| < 1.4$

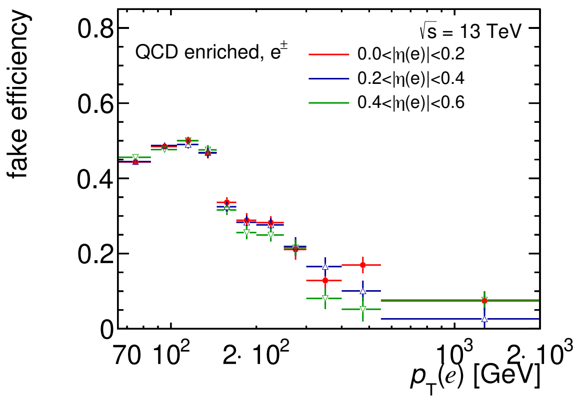

c) finer bins: $|\eta(\ell)| < 0.6$

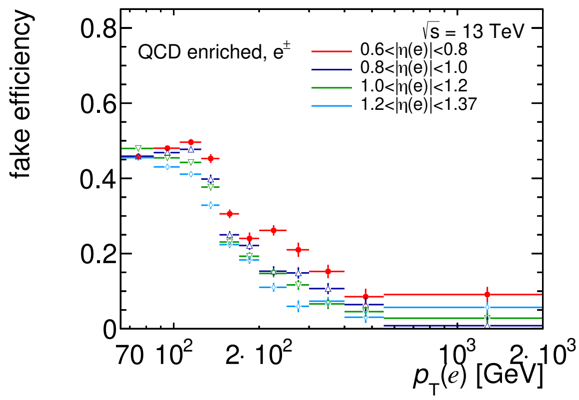

d) finer bins: $0.6 < |\eta(\ell)| < 1.37$

Figure B.19: Fake efficiencies in the nominal (top row) and the finer (bottom row) $|\eta|$-binning (see Section 4.6.1). Only the first $|\Delta\phi|$-bin ($|\Delta(\phi(e, E_T^{miss}))| < 1.05$) and the region $|\eta(e)| < 1.4$ is shown.

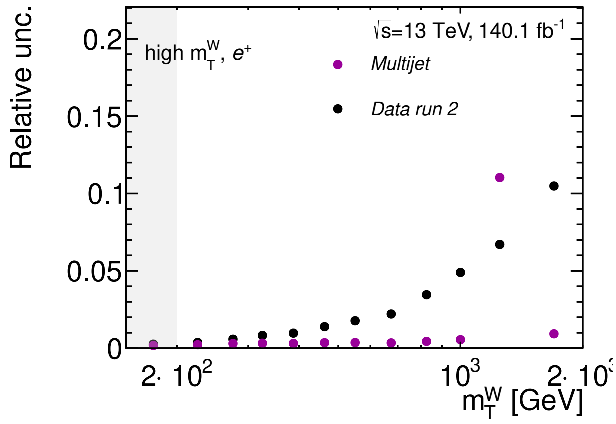

a) m_T^W - e^+

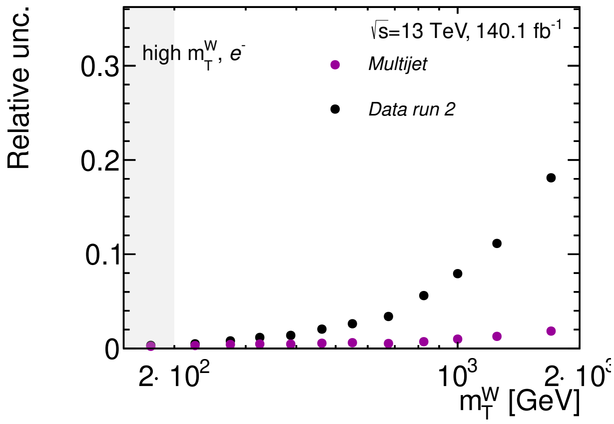

b) m_T^W - e^-

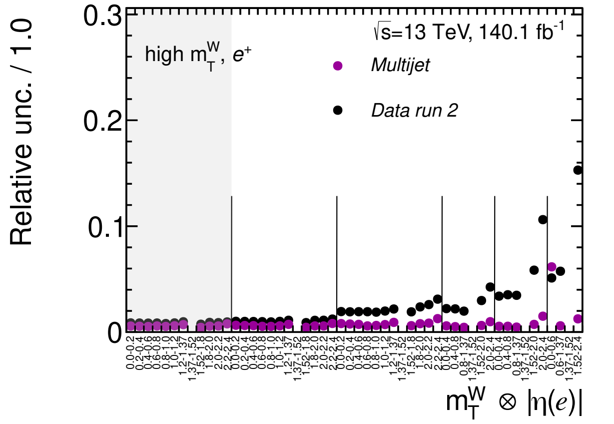

c) $m_T^W \otimes |\eta(e)|$ - e^+

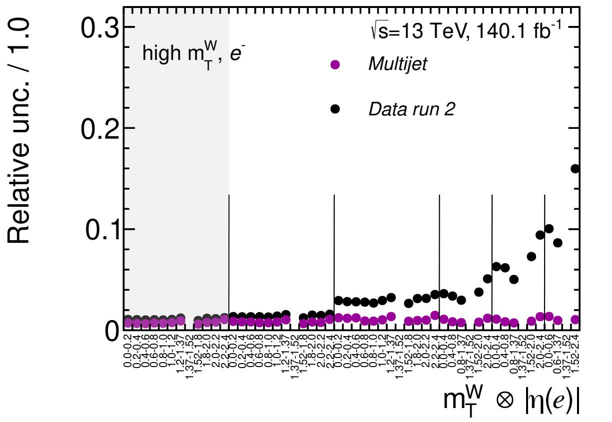

d) $m_T^W \otimes |\eta(e)|$ - e^-

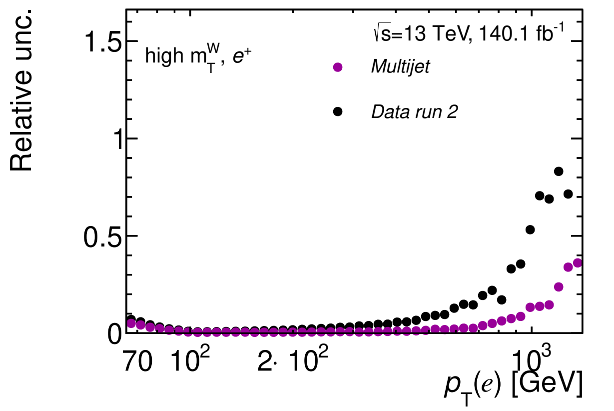

e) $p_T(e)$ - e^+

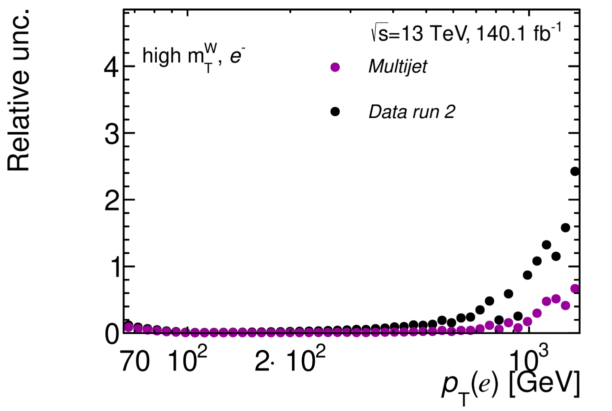

f) $p_T(e)$ - e^-

Figure B.20: Statistical uncertainties of the multijet and the data using the nominal fake efficiencies. The measurement distributions in m_T^W and $m_T^W \otimes |\eta(e)|$ as well as the $p_T(e)$-distribution are shown for both the e^+- and the e^--channel.

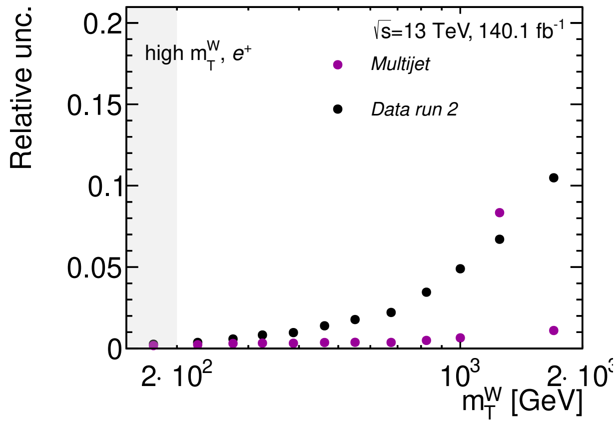

a) m_T^W - e^+

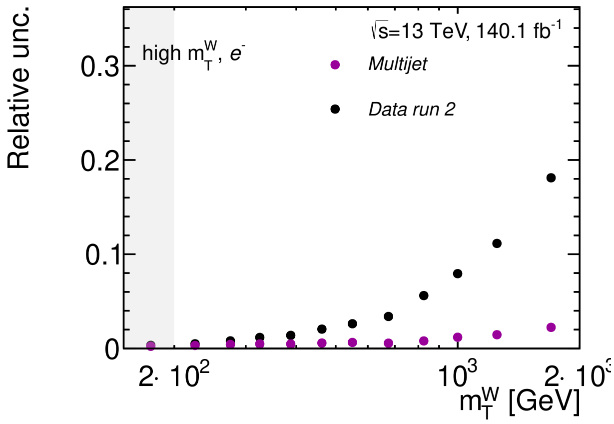

b) m_T^W - e^-

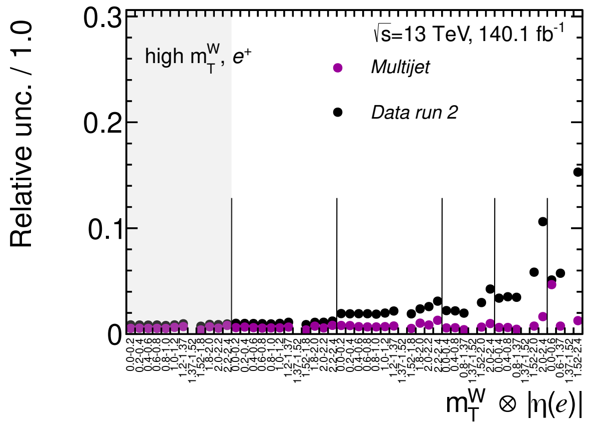

c) $m_T^W \otimes |\eta(e)|$ - e^+

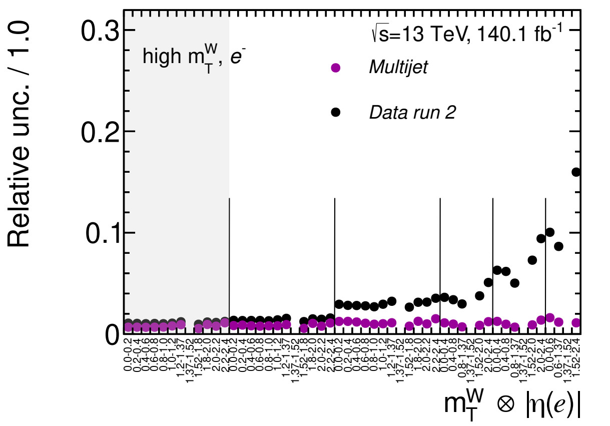

d) $m_T^W \otimes |\eta(e)|$ - e^-

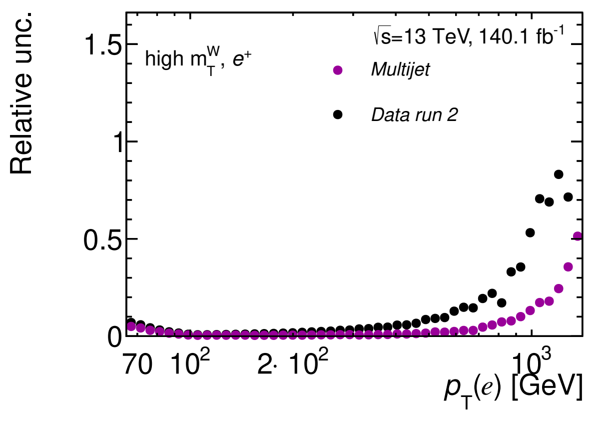

e) $p_T(e)$ - e^+

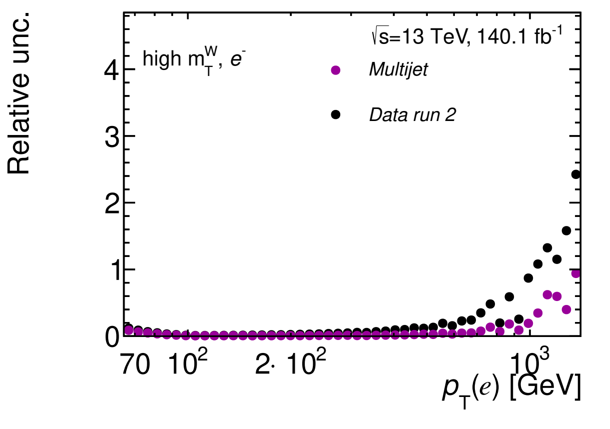

f) $p_T(e)$ - e^-

Figure B.21: Statistical uncertainties of the multijet and the data using the finer binned (in $|\eta(e)|$) fake efficiencies. The measurement distributions in m_T^W and $m_T^W \otimes |\eta(e)|$ as well as the $p_T(e)$-distribution are shown for both the e^+- and the e^--channel.

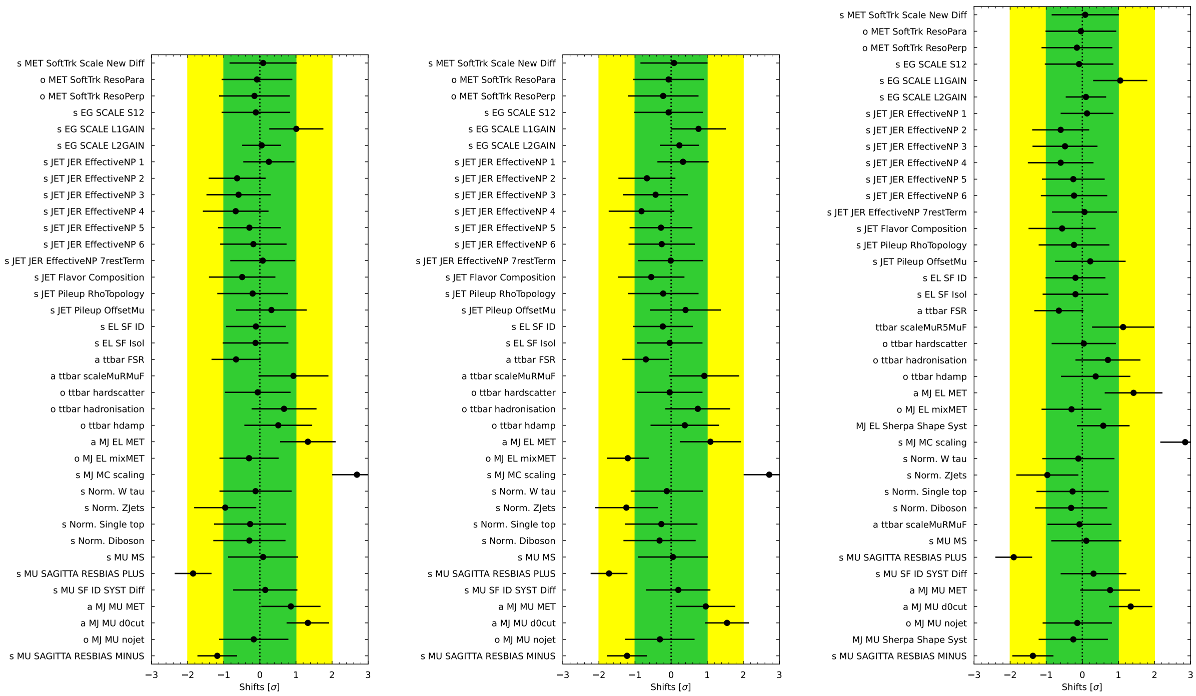

a) nominal multijet

b) varied multijet

c) including MJ EL/MU SHERPA SHAPE SYST

Figure B.22: All systematic shifts β_j for the combination using the nominal or the varied electron multijet in $m_T^W \otimes |\eta(\ell)|$ (See Figure 4.22). In c), the shifts for the combination with the additional Sherpa shape systematic (See Figure 4.32) are shown. The error bars represent the reduction of the uncertainties by the combination.

B.4 Real and fake efficiencies for mc16d

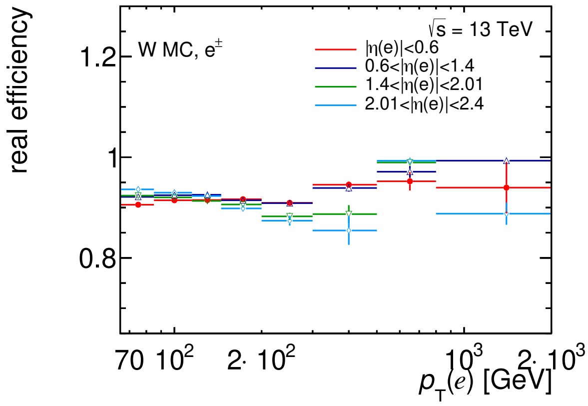

Figure B.23: Real electron efficiency used for the determination of the multijet background for mc16d only. The plot is binned in $p_T(e)$, each colour corresponds to on $|\eta(e)|$-bin. The presented efficiencies correspond to the nominal Matrix Method loose level (`LooseAndBLayerLH+FCLoose`).

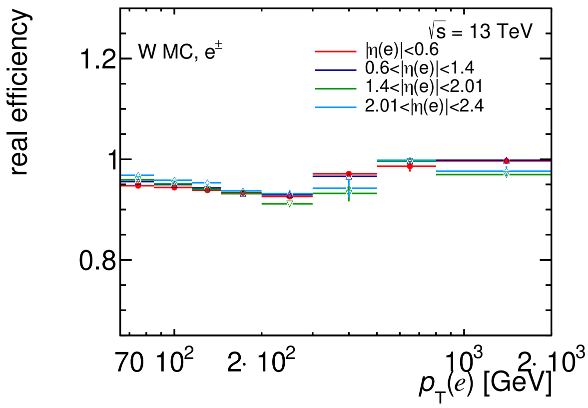

Figure B.24: Real muon efficiency used for the determination of the multijet background for mc16d only. The plot is binned in $p_T(\mu)$, each colour corresponds to on $|\eta(\mu)|$-bin. The presented efficiencies correspond to the varied Matrix Method loose level (`TightLH`).

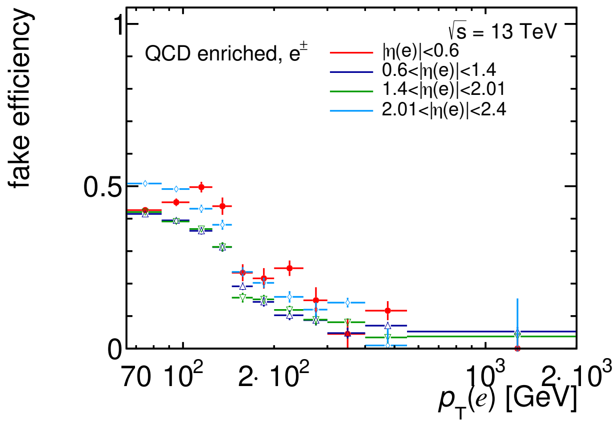

a) $0 < |\Delta\Phi(e, E_T^{miss})| < 0.26$

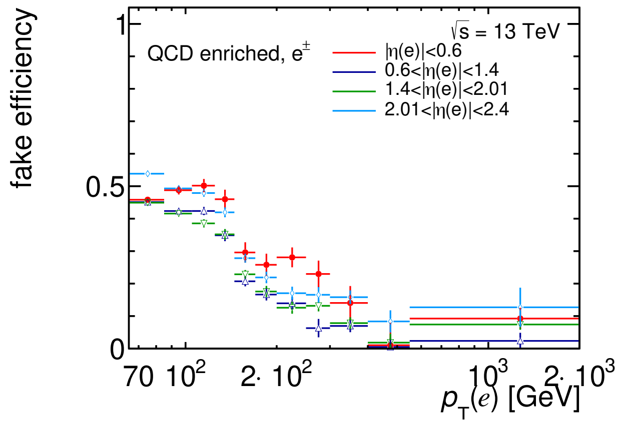

b) $0.26 < |\Delta\Phi(e, E_T^{miss})| < 0.52$

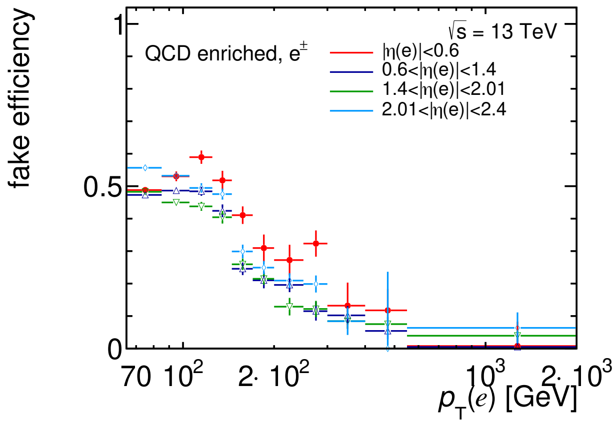

c) $0.52 < |\Delta\Phi(e, E_T^{miss})| < 0.78$

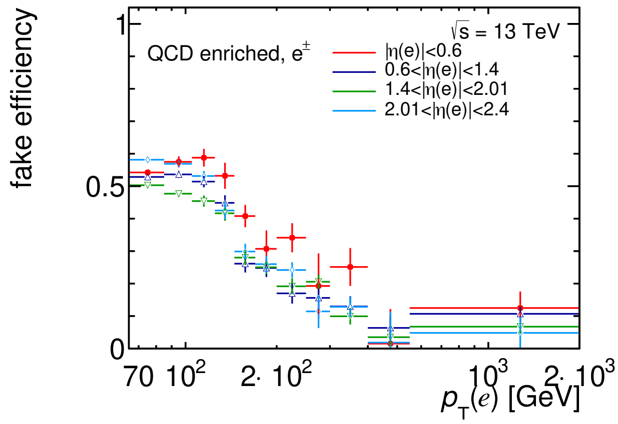

d) $0.78 < |\Delta\Phi(e, E_T^{miss})| < 1.05$

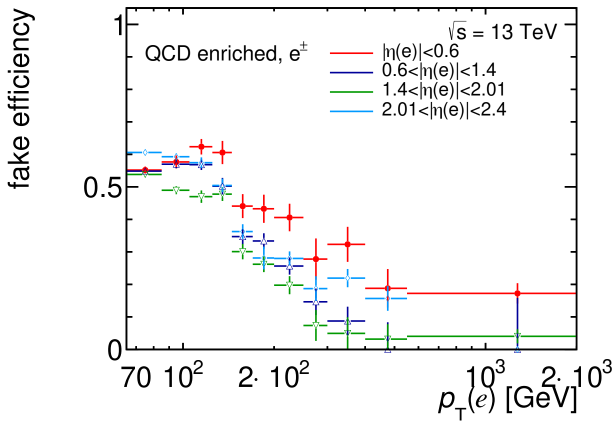

e) $1.05 < |\Delta\Phi(e, E_T^{miss})| < 1.31$

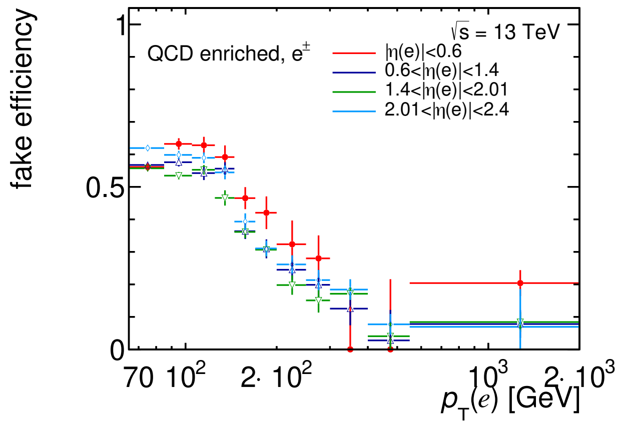

f) $1.31 < |\Delta\Phi(e, E_T^{miss})| < 1.57$

Figure B.25: Fake electron efficiency used for the determination of the multijet background for mc16d only. Each plot corresponds to a $|\Delta\phi(e, E_T^{miss})|$-bin. The plot is binned in $p_T(e)$, each colour corresponds to on $|\eta(e)|$-bin. The first six $|\Delta\phi(e, E_T^{miss})|$-bins are shown. The presented efficiencies correspond to the nominal Matrix Method loose level (`LooseAndBLayerLH+FCLoose`).

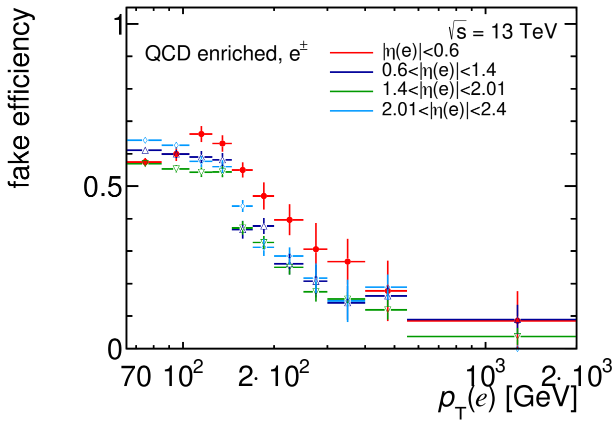

a) $1.57 < |\Delta\Phi(e, E_T^{miss})| < 1.83$

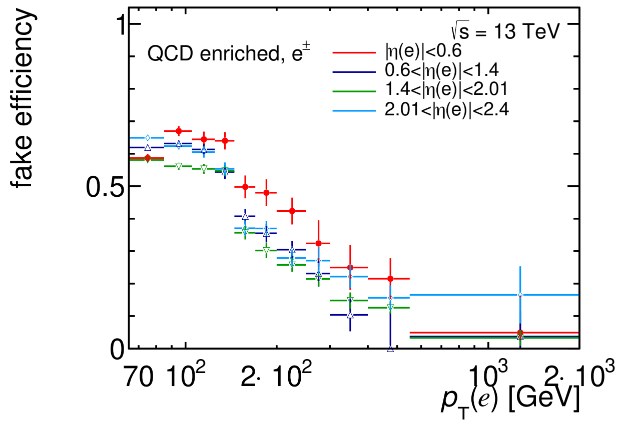

b) $1.83 < |\Delta\Phi(e, E_T^{miss})| < 2.09$

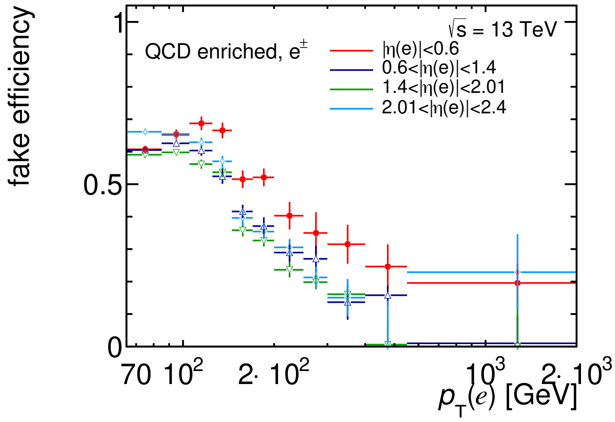

c) $2.09 < |\Delta\Phi(e, E_T^{miss})| < 2.36$

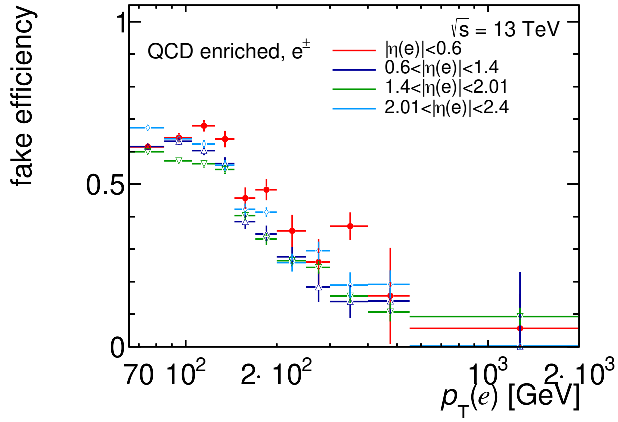

d) $2.36 < |\Delta\Phi(e, E_T^{miss})| < 2.62$

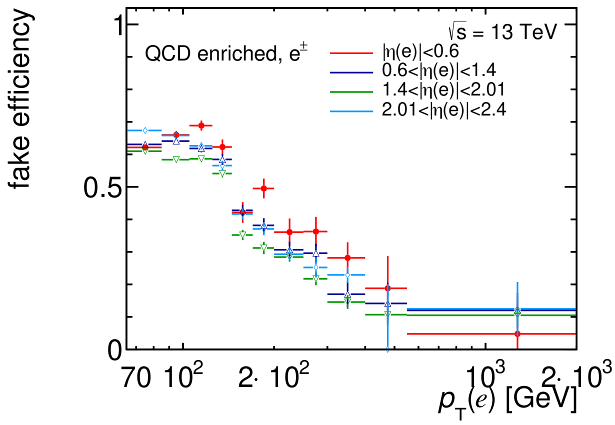

e) $2.62 < |\Delta\Phi(e, E_T^{miss})| < 2.88$

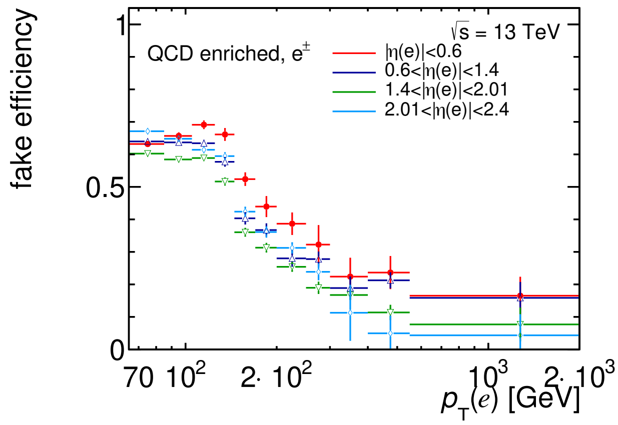

f) $2.88 < |\Delta\Phi(e, E_T^{miss})| < 3.14$

Figure B.26: Fake electron efficiency used for the determination of the multijet background for mc16d only. Each plot corresponds to a $|\Delta\phi(e, E_T^{miss})|$-bin. The plot is binned in $p_T(e)$, each colour corresponds to on $|\eta(e)|$-bin. The last six $|\Delta\phi(e, E_T^{miss})|$-bins are shown. The presented efficiencies correspond to the nominal Matrix Method loose level (`LooseAndBLayerLH+FCLoose`).

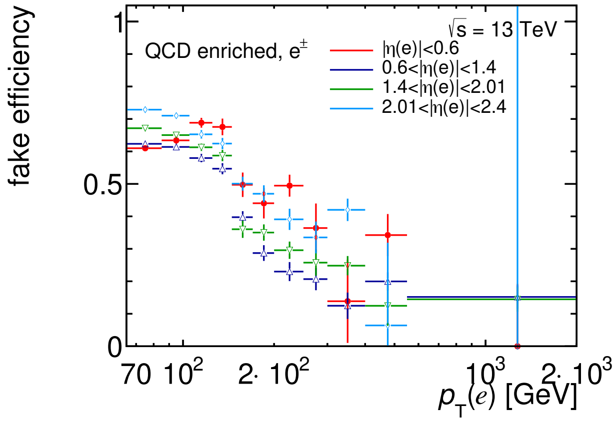

a) $0 < |\Delta\Phi(e, E_T^{miss})| < 0.26$

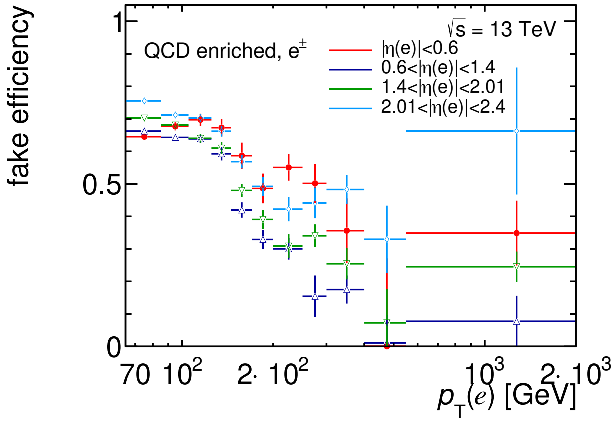

b) $0.26 < |\Delta\Phi(e, E_T^{miss})| < 0.52$

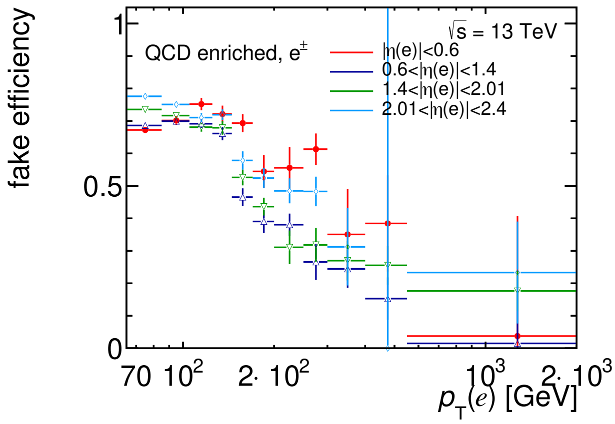

c) $0.52 < |\Delta\Phi(e, E_T^{miss})| < 0.78$

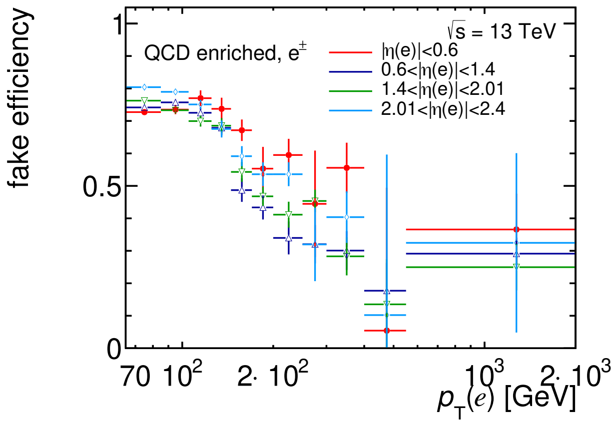

d) $0.78 < |\Delta\Phi(e, E_T^{miss})| < 1.05$

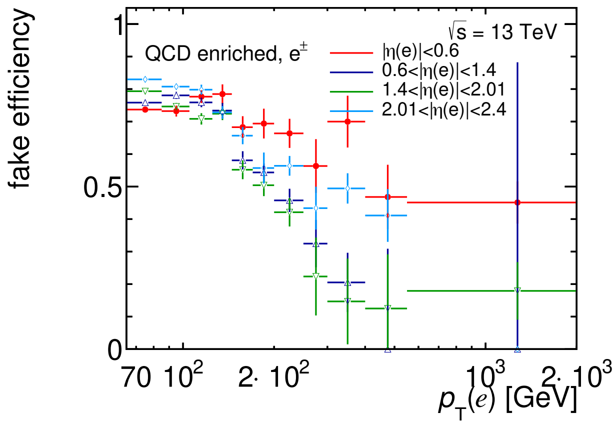

e) $1.05 < |\Delta\Phi(e, E_T^{miss})| < 1.31$

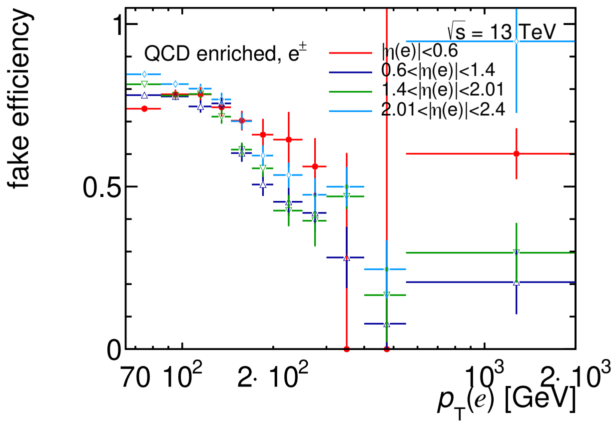

f) $1.31 < |\Delta\Phi(e, E_T^{miss})| < 1.57$

Figure B.27: Fake electron efficiency used for the determination of the multijet background for mc16d only. Each plot corresponds to a $|\Delta\phi(e, E_T^{miss})|$-bin. The plot is binned in $p_T(e)$, each colour corresponds to on $|\eta(e)|$-bin. The first six $|\Delta\phi(e, E_T^{miss})|$-bins are shown. The presented efficiencies correspond to the varied Matrix Method loose level (`TightLH`).

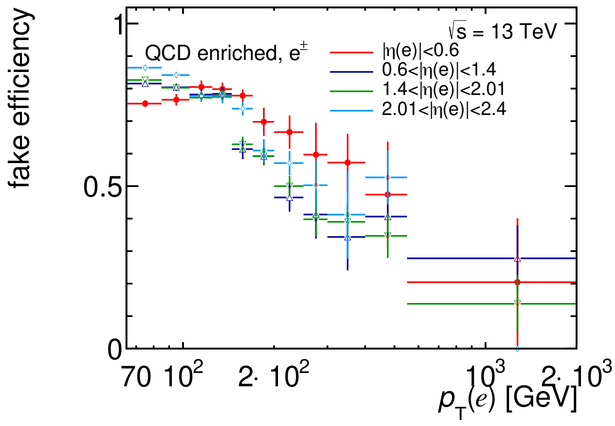

a) $1.57 < |\Delta\Phi(e, E_T^{miss})| < 1.83$

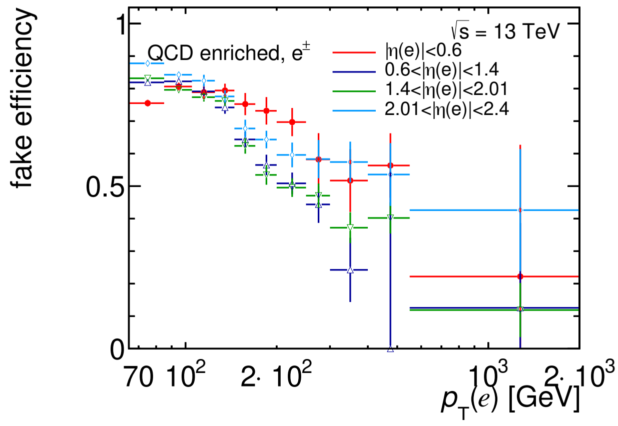

b) $1.83 < |\Delta\Phi(e, E_T^{miss})| < 2.09$

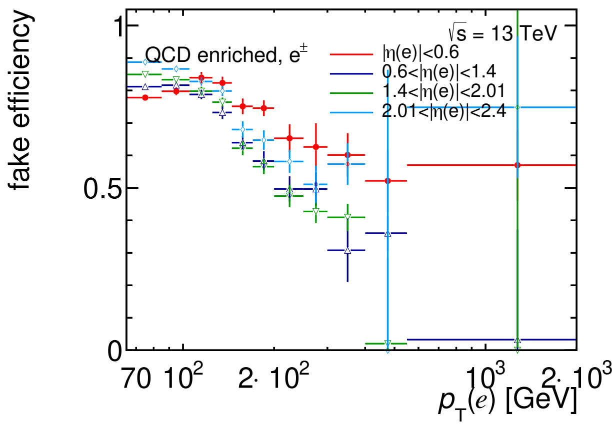

c) $2.09 < |\Delta\Phi(e, E_T^{miss})| < 2.36$

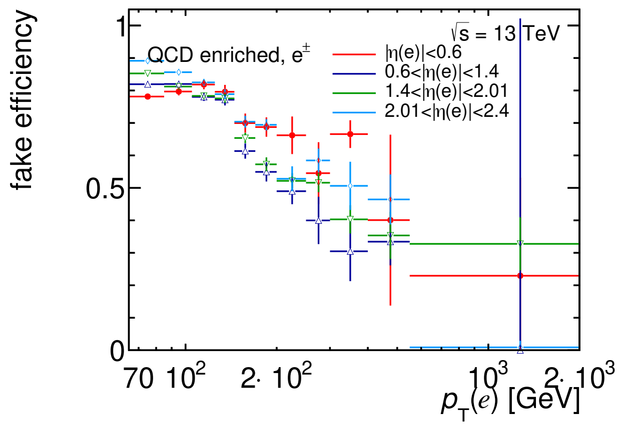

d) $2.36 < |\Delta\Phi(e, E_T^{miss})| < 2.62$

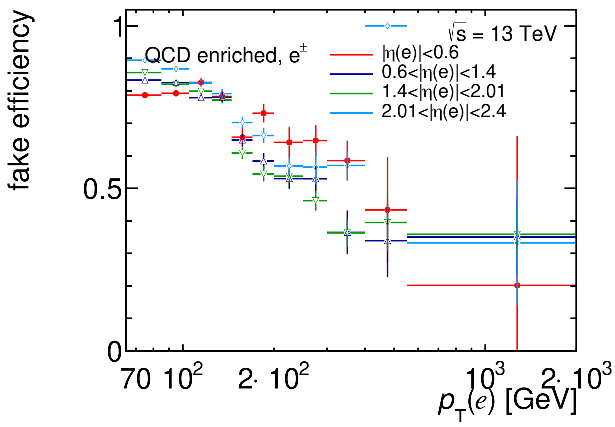

e) $2.62 < |\Delta\Phi(e, E_T^{miss})| < 2.88$

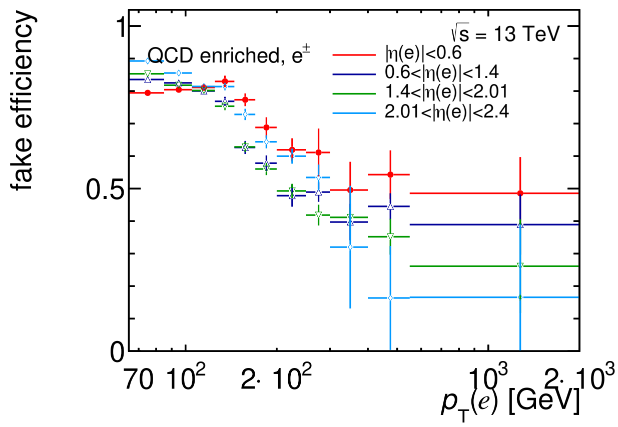

f) $2.88 < |\Delta\Phi(e, E_T^{miss})| < 3.14$

Figure B.28: Fake electron efficiency used for the determination of the multijet background for mc16d only. Each plot corresponds to a $|\Delta\phi(e, E_T^{miss})|$-bin. The plot is binned in $p_T(e)$, each colour corresponds to on $|\eta(e)|$-bin. The last six $|\Delta\phi(e, E_T^{miss})|$-bins are shown. The presented efficiencies correspond to the varied Matrix Method loose level (`TightLH`).

Appendix C

Bug in electron reconstruction scale factor

Due to a bug in the provided electron reconstruction scale factors, the reconstruction scale factor for mc16a was also applied in mc16d and mc16e. The unfolded cross section separated per data taking period was calculated for both the correct and incorrect scale factors, so that the effect on the underlying electron channel analysis could be tested. The correct scale factors were taken directly from the updated root-files[1]. In Figure C.1 and Figure C.2, one can see the ratios of the unfolded cross sections obtained with the correct and incorrect scale factors for the for both the single and double differential measurements. Since the bug affects only mc16d and mc16e, no differences are expected in mc16a. However rounding erros can arise when the new scale factors are applied. These can explain the tiny differences observed in mc16a. As can be seen from the ratios in mc16d and mc16e, the influence of the reconstruction scale factor bug in the underlying analysis is rather small. All observed differences are smaller than 0.5%, with the exception of two single bins in the 2D-mc16e distribution (with deviations $< 0.9\%$). In order to save the computational effort of re-running all systematic uncertainties, it was therefore decided to keep the previous uncorrected scale factors.

[1] /cvmfs/atlas.cern.ch/repo/sw/database/GroupData/ElectronEfficiencyCorrection/2015_2018/rel21.2/Precision_Summer2020_v4/offline/efficiencySF.offline.RecoTrk.root

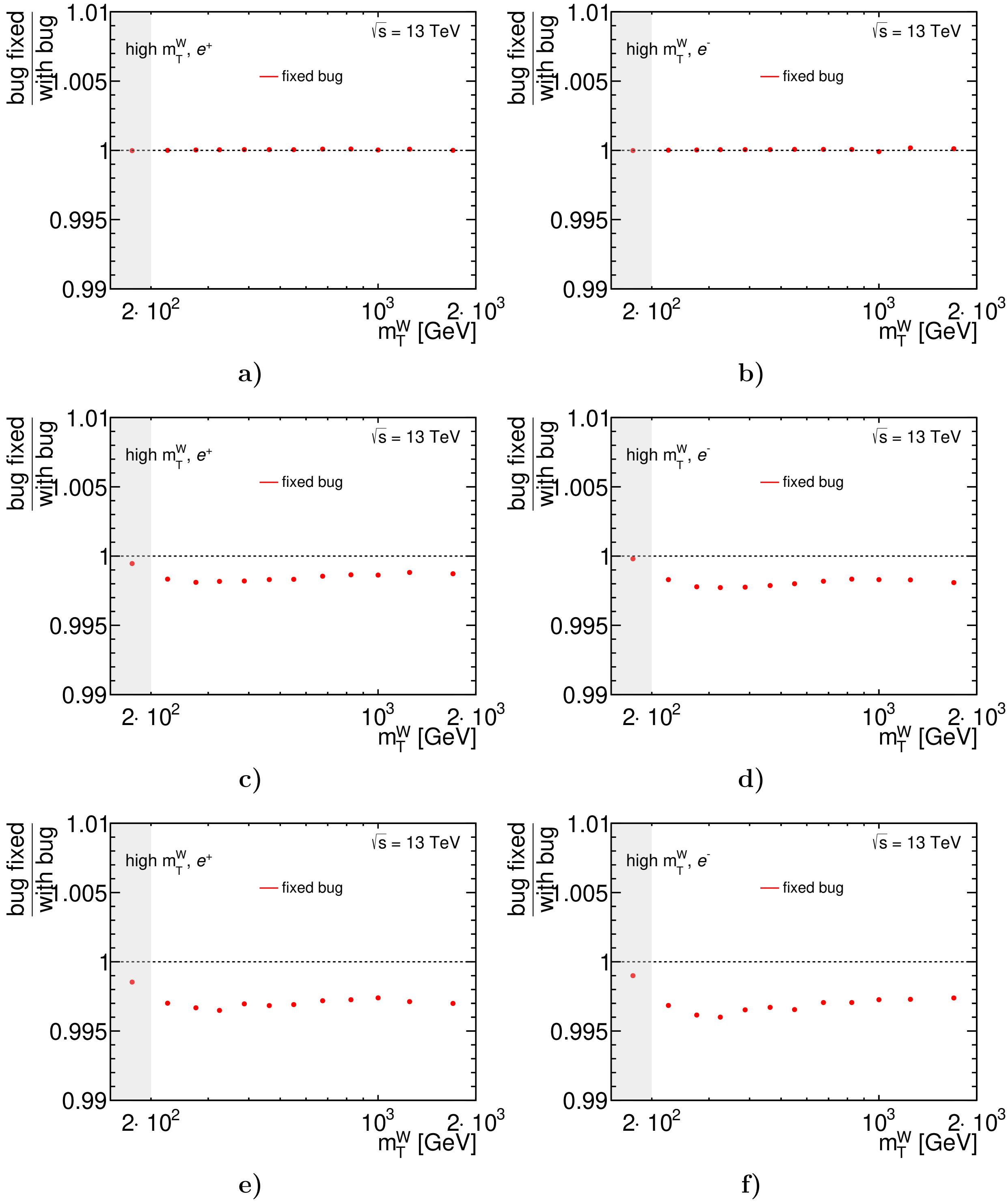

Figure C.1: Direct comparison of the unfolded cross sections before and after the reconstruction scale factor bugfix for the measurement distribution in m_T^W. Top row: mc16a, middle row: mc16d, bottom row: mc16e. Left column: e^+-channel, right column: e^--channel.

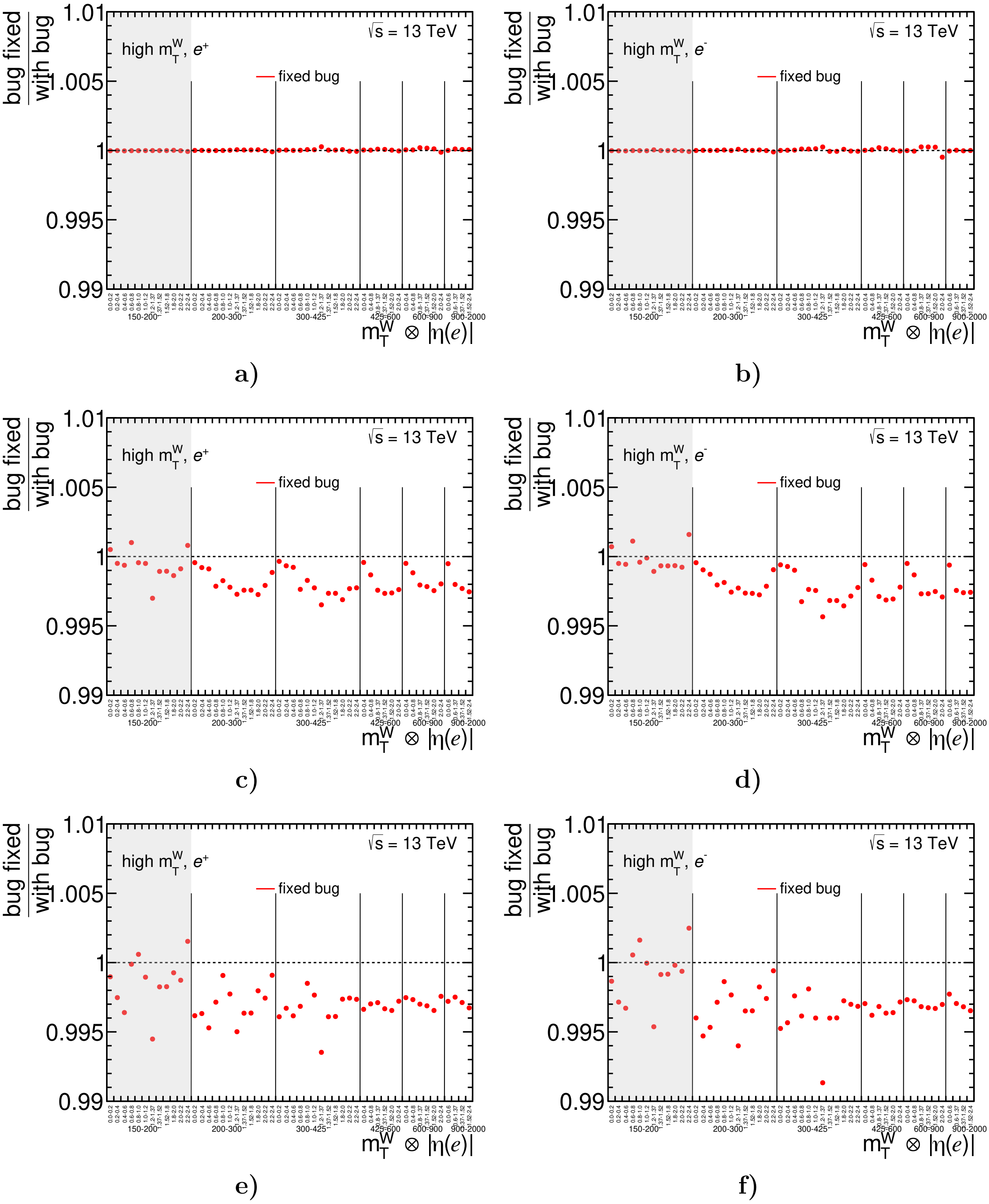

Figure C.2: Direct comparison of the unfolded cross sections before and after the reconstruction scale factor bugfix for the measurement distribution in $m_T^W \otimes |\eta(e)|$. Top row: mc16a, middle row: mc16d, bottom row: mc16e. Left column: e^+-channel, right column: e^--channel.

Bibliography

[1] Y. et al Fukuda. “Evidence for Oscillation of Atmospheric Neutrinos”. In: *Phys. Rev. Lett.* 81 (8 Aug. 1998), pp. 1562–1567. DOI: 10.1103/PhysRevLett.81.1562. URL: https://link.aps.org/doi/10.1103/PhysRevLett.81.1562.

[2] Q. R. et al Ahmad. “Direct Evidence for Neutrino Flavor Transformation from Neutral-Current Interactions in the Sudbury Neutrino Observatory”. In: *Phys. Rev. Lett.* 89 (1 June 2002), p. 011301. DOI: 10.1103/PhysRevLett.89.011301. URL: https://link.aps.org/doi/10.1103/PhysRevLett.89.011301.

[3] Lars Bergström. “Cosmology and the dark matter frontier”. In: *Physica Scripta* T158 (Dec. 2013), p. 014014. ISSN: 1402-4896. DOI: 10.1088/0031-8949/2013/t158/014014. URL: http://dx.doi.org/10.1088/0031-8949/2013/T158/014014.

[4] Lyndon R Evans and Philip Bryant. “LHC Machine”. In: *JINST* 3 (2008). This report is an abridged version of the LHC Design Report (CERN-2004-003), S08001. DOI: 10.1088/1748-0221/3/08/S08001. URL: http://cds.cern.ch/record/1129806.

[5] Frank Ellinghaus et al. *Charged-current Drell-Yan cross sections at high transverse masses in pp collisions at $\sqrt{s} = 13$ TeV*. Tech. rep. Geneva: CERN, 2020. URL: https://cds.cern.ch/record/2711872.

[6] Sidney D. Drell and Tung-Mow Yan. “Massive Lepton-Pair Production in Hadron-Hadron Collisions at High Energies”. In: *Phys. Rev. Lett.* 25 (5 Aug. 1970), pp. 316–320. DOI: 10.1103/PhysRevLett.25.316. URL: https://link.aps.org/doi/10.1103/PhysRevLett.25.316.

[7] Sidney D. Drell and Tung-Mow Yan. “Massive Lepton-Pair Production in Hadron-Hadron Collisions at High Energies”. In: *Phys. Rev. Lett.* 25 (13 Sept. 1970), pp. 902–902. DOI: 10.1103/PhysRevLett.25.902.2. URL: https://link.aps.org/doi/10.1103/PhysRevLett.25.902.2.

[8] The ATLAS Collaboration. “Precision measurement and interpretation of inclusive W^+, W^- and Z/γ^* production cross sections with the ATLAS detector.” In: *Eur. Phys. J. C* 77.6 (2017), p. 367. DOI: 10.1140/epjc/s10052-017-4911-9. arXiv: 1612.03016. URL: https://cds.cern.ch/record/2238565.

[9] ATLAS Collaboration. *Luminosity determination in pp collisions at $\sqrt{s} = 13$ TeV using the ATLAS detector at the LHC*. 2022. arXiv: 2212.09379 [hep-ex].

[10] The ATLAS Collaboration. “Search for a heavy charged boson in events with a charged lepton and missing transverse momentum from *pp* collisions at $\sqrt{s} = 13$ TeV with the ATLAS detector”. In: *Phys. Rev. D* 100 (2019), p. 052013. DOI: 10.1103/PhysRevD.100.052013. arXiv: 1906.05609 [hep-ex].

[11] Daniele S. M. Alves et al. “Running electroweak couplings as a probe of new physics”. In: *Journal of High Energy Physics* 2015.2 (Feb. 2015). DOI: 10.1007/jhep02(2015)007. URL: https://doi.org/10.1007%2Fjhep02%282015%29007.

[12] Steven Weinberg. "A Model of Leptons". In: *Phys. Rev. Lett.* 19 (21 Nov. 1967), pp. 1264–1266. DOI: 10.1103/PhysRevLett.19.1264. URL: https://link.aps.org/doi/10.1103/PhysRevLett.19.1264.

[13] Sheldon L. Glashow. "Partial Symmetries of Weak Interactions". In: *Nuclear Physics* 22 (1961), pp. 579–588. URL: https://doi.org/10.1016/0029-5582(61)90469-2.

[14] Abdus Salam. "Weak and Electromagnetic Interactions". In: *Conf. Proc. C* 680519 (1968), pp. 367–377. DOI: 10.1142/9789812795915_0034.

[15] Gerard 't Hooft and M. J. G. Veltman. "Regularization and Renormalization of Gauge Fields". In: *Nucl. Phys. B* 44 (1972), pp. 189–213. DOI: 10.1016/0550-3213(72)90279-9.

[16] Wikipedia. *Standard Model of Elementary Particles.* Sept. 17, 2019. URL: https://en.wikipedia.org/wiki/File:Standard_Model_of_Elementary_Particles.svg#/media/File:Standard_Model_of_Elementary_Particles.svg (visited on 05/04/2023).

[17] Mark Thomson. *Modern Particle Physics.* Cambridge University Press, 2013. DOI: 10.1017/CBO9781139525367.

[18] F. Englert and R. Brout. "Broken Symmetry and the Mass of Gauge Vector Mesons". In: *Phys. Rev. Lett.* 13 (1964). Ed. by J. C. Taylor, pp. 321–323. DOI: 10.1103/PhysRevLett.13.321.

[19] Peter W. Higgs. "Broken Symmetries and the Masses of Gauge Bosons". In: *Phys. Rev. Lett.* 13 (1964). Ed. by J. C. Taylor, pp. 508–509. DOI: 10.1103/PhysRevLett.13.508.

[20] G. S. Guralnik, C. R. Hagen, and T. W. B. Kibble. "Global Conservation Laws and Massless Particles". In: *Phys. Rev. Lett.* 13 (1964). Ed. by J. C. Taylor, pp. 585–587. DOI: 10.1103/PhysRevLett.13.585.

[21] The ATLAS Collaboration. "Observation of a new particle in the search for the Standard Model Higgs boson with the ATLAS detector at the LHC". In: *Physics Letters B* 716.1 (Sept. 2012), pp. 1–29. DOI: 10.1016/j.physletb.2012.08.020. URL: https://doi.org/10.1016%2Fj.physletb.2012.08.020.

[22] The CMS Collaboration. "Observation of a new boson at a mass of 125 GeV with the CMS experiment at the LHC". In: *Physics Letters B* 716.1 (Sept. 2012), pp. 30–61. DOI: 10.1016/j.physletb.2012.08.021. URL: https://doi.org/10.1016%2Fj.physletb.2012.08.021.

[23] R. L. Workman et al. "Review of Particle Physics". In: *PTEP* 2022 (2022), p. 083C01. DOI: 10.1093/ptep/ptac097.

[24] Makoto Kobayashi and Toshihide Maskawa. "CP Violation in the Renormalizable Theory of Weak Interaction". In: *Prog. Theor. Phys.* 49 (1973), pp. 652–657. DOI: 10.1143/PTP.49.652.

[25] CERN. *CERN's accelerator complex.* URL: https://home.cern/science/accelerators/accelerator-complex (visited on 06/18/2023).

[26] Ewa Lopienska. "The CERN accelerator complex, layout in 2022. Complexe des accélérateurs du CERN en janvier 2022". In: (2022). General Photo. URL: https://cds.cern.ch/record/2800984 (visited on 05/01/2023).

[27] The ATLAS Collaboration. "The ATLAS Experiment at the CERN Large Hadron Collider". In: *JINST* 3 (2008). Also published by CERN Geneva in 2010, S08003. DOI: 10.1088/1748-0221/3/08/S08003. URL: https://cds.cern.ch/record/1129811.

[28] The CMS collaboration. “The CMS experiment at the CERN LHC. The Compact Muon Solenoid experiment”. In: *JINST* 3 (2008). Also published by CERN Geneva in 2010, S08004. DOI: 10.1088/1748-0221/3/08/S08004. URL: https://cds.cern.ch/record/1129810.

[29] The LHCb collaboration. “The LHCb Detector at the LHC”. In: *JINST* 3 (2008). Also published by CERN Geneva in 2010, S08005. DOI: 10.1088/1748-0221/3/08/S08005. URL: https://cds.cern.ch/record/1129809.

[30] The ALICE collaboration. “The ALICE experiment at the CERN LHC. A Large Ion Collider Experiment”. In: *JINST* 3 (2008). Also published by CERN Geneva in 2010, S08002. DOI: 10.1088/1748-0221/3/08/S08002. URL: https://cds.cern.ch/record/1129812.

[31] *ATLAS inner detector: Technical Design Report, 1*. Technical design report. ATLAS. Geneva: CERN, 1997. URL: https://cds.cern.ch/record/331063.

[32] M Capeans et al. *ATLAS Insertable B-Layer Technical Design Report*. Tech. rep. 2010. URL: https://cds.cern.ch/record/1291633.

[33] *ATLAS muon spectrometer: Technical Design Report*. Technical design report. ATLAS. Geneva: CERN, 1997. URL: https://cds.cern.ch/record/331068.

[34] The ATLAS Collaboration. “Performance of the ATLAS trigger system in 2015”. In: *The European Physical Journal C* 77.5 (May 2017). ISSN: 1434-6052. DOI: 10.1140/epjc/s10052-017-4852-3. URL: http://dx.doi.org/10.1140/epjc/s10052-017-4852-3.

[35] John C. Collins, Davison E. Soper, and George Sterman. *Factorization of Hard Processes in QCD*. 2004. arXiv: hep-ph/0409313 [hep-ph].

[36] Sayipjamal Dulat et al. “New parton distribution functions from a global analysis of quantum chromodynamics”. In: *Physical Review D* 93.3 (Feb. 2016). DOI: 10.1103/physrevd.93.033006. URL: https://doi.org/10.1103%2Fphysrevd.93.033006.

[37] Hung-Liang Lai et al. “New parton distributions for collider physics”. In: *Physical Review D* 82.7 (Oct. 2010). DOI: 10.1103/physrevd.82.074024. URL: https://doi.org/10.1103%2Fphysrevd.82.074024.

[38] Simone Alioli et al. “A general framework for implementing NLO calculations in shower Monte Carlo programs: the POWHEG BOX”. In: *Journal of High Energy Physics* 2010.6 (June 2010). DOI: 10.1007/jhep06(2010)043. URL: https://doi.org/10.1007%2Fjhep06%282010%29043.

[39] Torbjörn Sjöstrand, Stephen Mrenna, and Peter Skands. “A brief introduction to PYTHIA 8.1”. In: *Computer Physics Communications* 178.11 (June 2008), pp. 852–867. DOI: 10.1016/j.cpc.2008.01.036. URL: https://doi.org/10.1016%2Fj.cpc.2008.01.036.

[40] S. Agostinelli et al. “GEANT4–a simulation toolkit”. In: *Nucl. Instrum. Meth. A* 506 (2003), pp. 250–303. DOI: 10.1016/S0168-9002(03)01368-8.

[41] Richard D. Ball et al. “Parton distributions for the LHC run II”. In: *Journal of High Energy Physics* 2015.4 (Apr. 2015). DOI: 10.1007/jhep04(2015)040. URL: https://doi.org/10.1007%2Fjhep04%282015%29040.

[42] Enrico Bothmann et al. “Event generation with Sherpa 2.2”. In: *SciPost Physics* 7.3 (Sept. 2019). DOI: 10.21468/scipostphys.7.3.034. URL: https://doi.org/10.21468%2Fscipostphys.7.3.034.

[43] The ATLAS Collaboration. "Electron reconstruction and identification in the ATLAS experiment using the 2015 and 2016 LHC proton-proton collision data at $\sqrt{s} = 13$ TeV". In: *The European Physical Journal C* 79.8 (Aug. 2019). DOI: 10.1140/epjc/s10052-019-7140-6. URL: https://doi.org/10.1140%2Fepjc%2Fs10052-019-7140-6.

[44] The ATLAS Collaboration. "Muon reconstruction and identification efficiency in ATLAS using the full Run 2 pp collision data set at $\sqrt{s} = 13$ TeV". In: *Eur. Phys. J., C* 81 (2021). 64 pages in total, author list starting page 42, auxiliary material starting at page 59, 34 figures, 3 tables. All figures including auxiliary figures are available at https://atlas.web.cern.ch/Atlas/GROUPS/PHYSICS/PAPERS/MUON-2018-03/, p. 578. DOI: 10.1140/epjc/s10052-021-09233-2. arXiv: 2012.00578. URL: http://cds.cern.ch/record/2746302.

[45] Matteo Cacciari, Gavin P Salam, and Gregory Soyez. "The anti-k_t jet clustering algorithm". In: *Journal of High Energy Physics* 2008.04 (Apr. 2008), pp. 063–063. DOI: 10.1088/1126-6708/2008/04/063. URL: https://doi.org/10.1088%2F1126-6708%2F2008%2F04%2F063.

[46] *Expected performance of missing transverse momentum reconstruction for the ATLAS detector at $\sqrt{s} = 13$ TeV*. Tech. rep. All figures including auxiliary figures are available at https://atlas.web.cern.ch/Atlas/GROUPS/PHYSICS/PUBNOTES/ATL-PHYS-PUB-2015-023. Geneva: CERN, 2015. URL: https://cds.cern.ch/record/2037700.

[47] Frederic Schroeder. "Measurement of the charged-current Drell-Yan single- and double-differential cross-sections at high transverse masses at $\sqrt{s} = 13$ TeV with the ATLAS detector". Presented 15-07-2022. 2022. URL: https://cds.cern.ch/record/2825779.

[48] The ATLAS Collaboration. "Study of the material of the ATLAS inner detector for Run 2 of the LHC". In: *Journal of Instrumentation* 12.12 (Dec. 2017), P12009–P12009. DOI: 10.1088/1748-0221/12/12/p12009. URL: https://doi.org/10.1088%2F1748-0221%2F12%2F12%2Fp12009.

[49] ATLAS Jet and Etmiss Combined Performance Group. *JetEtMiss Recommendations for Release 21 MC16 (2015-2018)*. URL: https://twiki.cern.ch/twiki/bin/view/AtlasProtected/JetEtmissRecommendationsR21#Baseline_MET_Recommendations (visited on 06/18/2023).

[50] ATLAS ElectronGamma Group. *EGamma recommendations for Run2 release 21*. URL: https://twiki.cern.ch/twiki/bin/view/AtlasProtected/EGammaRecommendationsR21 (visited on 06/18/2023).

[51] Muon Combined Performance Group. *MCPAnalysisGuidelinesMC16*. URL: https://twiki.cern.ch/twiki/bin/viewauth/AtlasProtected/MCPAnalysisGuidelinesMC16 (visited on 06/18/2023).

[52] ATLAS Jet and Etmiss Combined Performance Group. *METSystematics*. URL: https://twiki.cern.ch/twiki/bin/viewauth/AtlasProtected/MissingETSystematics (visited on 06/18/2023).

[53] Physics Modelling Group. *PmgTopProcesses*. URL: https://twiki.cern.ch/twiki/bin/view/AtlasProtected/PmgTopProcesses (visited on 06/18/2023).

[54] Stefano Frixione et al. "Single-top hadroproduction in association with a W boson". In: *Journal of High Energy Physics* 2008.07 (July 2008), p. 029. DOI: 10.1088/1126-6708/2008/07/029. URL: https://dx.doi.org/10.1088/1126-6708/2008/07/029.

[55] Emanuele Re. “Single-top Wt-channel production matched with parton showers using the POWHEG method”. In: *The European Physical Journal C* 71.2 (Feb. 2011). DOI: 10.1140/epjc/s10052-011-1547-z. URL: https://doi.org/10.1140%2Fepjc%2Fs10052-011-1547-z.

[56] The ATLAS collaboration. “Measurement of W± and Z-boson production cross sections in pp collisions at $\sqrt{s} = 13\,\mathrm{TeV}$ with the ATLAS detector”. In: *Physics Letters B* 759 (Aug. 2016), pp. 601–621. DOI: 10.1016/j.physletb.2016.06.023. URL: https://doi.org/10.1016%2Fj.physletb.2016.06.023.

[57] ATLAS Collaboration. *Multi-boson simulation for* 13 *TeV ATLAS analyses*. ATL-PHYS-PUB-2016-002. 2016. URL: https://cds.cern.ch/record/2119986.

[58] Nikolaos Kidonakis and Nodoka Yamanaka. “Higher-order corrections for tW production at high-energy hadron colliders”. In: *Journal of High Energy Physics* 2021.5 (May 2021). DOI: 10.1007/jhep05(2021)278. URL: https://doi.org/10.1007%2Fjhep05%282021%29278.

[59] Heraverager developers. *Heraverager*. Aug. 11, 2016.

Name, Vorname: ....

Erklärung

gem. § 12 Abs. 7 Prüfungsordnung 2007/2012

Hiermit erkläre ich, dass ich die von mir eingereichte Abschlussarbeit (Bachelor-Thesis) selbständig verfasst und keine anderen als die angegebenen Quellen und Hilfsmittel benutzt sowie Stellen der Abschlussarbeit, die anderen Werken dem Wortlaut oder Sinn nach entnommen wurden, in jedem Fall unter Angabe der Quelle als Entlehnung kenntlich gemacht habe.

....

Datum Unterschrift

Erklärung

Hiermit erkläre ich mich damit einverstanden, dass meine Abschlussarbeit (Bachelor-Thesis) wissenschaftlich interessierten Personen oder Institutionen und im Rahmen von externen Qualitätssicherungsmaßnahmen des Studienganges zur Einsichtnahme zur Verfügung gestellt werden kann.

Korrektur- oder Bewertungshinweise in meiner Arbeit dürfen nicht zitiert werden.

....

Datum Unterschrift